CONSTRUCTION OF A NOVEL CONTINUOUS FLOW REACTOR FOR SOLID-STATE PHOTOCHEMISTRY

Jiarui Gao, BEng, MRes

Thesis submitted to the University of Nottingham

for the degree of Doctor of Philosophy

March 2025

ABSTRACT

Solid-state photoreaction has recently gained more attention due to its high selectivity, which has the potential to design chiral synthesis or shorten the synthesis pathway. One of the limitations of scaling up these solid-state reactions is the lack of a controllable reactor. The existing photoreactors have some problems with mobile particles, including dealing with particle blockage and reducing the attenuation effect of light transport during scaling up.

In this thesis, a swirl-induced pipe is applied to design a multiphase flow tubular photochemical reactor creating a ring distribution of particles, which can reduce particle accumulation and expose particles evenly to light. The particle distribution along the pipe was obtained using the Eulerian method with the k-ω shear stress transport (SST) turbulence model. The radiation transfer equation was solved by the discrete ordinate (DO) model. The absorption coefficient was calculated from the UV-absorption spectrum, and the scattering coefficient was determined by Mie scattering theory.

The results show that the settled particle can be redistributed by the tangential velocity induced by the swirl-induced pipe, showing an anti-blocking effect. Moreover, the local volumetric rate of energy absorbed (LVREA) is increased up to about twice that in the straight pipe due to the increasing retention time caused by the swirl. Different inlet conditions were compared according to their corresponding LVREA and specific radiation absorption (absorbed energy per weight of particles), and the specific absorption has a 5% increase compared to the straight pipe. Meanwhile, the induction of the swirl pipe improves the continuous flow of solid, which facilitates the flow chemistry of solid materials. To further explore the cause affecting the performance of the reactor, factors are defined to describe the particle distribution. A fully expended and compact layer of solid particle can receive more photons. This thesis provides an insight of the insertion of the swirl pipe to the photoreactor design.

Table of Content

List of Figures

List of Tables

Chapter 1 Introduction

1.1 Background

Solid-state photochemical reactions are drawing increasing attention from researchers. The history of solid-state photochemistry started in the late 19th century, when various photoreactions in organic solids were discovered and investigated, such as photodimerization and photochromism (Marckwald, 1899, Ciamician and Silber, 1901, Stobbe, 1922, de Jong, 1923, Senier and Shepheard, 1909). However, the research cannot proceed due to the lack of physical methods to understand the molecular structure of organic solids (Schmidt, 1971). It was back to the concerns of researchers mainly because of two reasons. The first reason was the development of techniques, such as X-ray diffraction (XRD) analysis and Solid-state nuclear magnetic resonance (ssNMR) spectroscopy, which helped to study the solid structure. On the other hand, the higher selectivity of the solid-state photochemical reaction makes it a tool for designing valuable molecules (Cole and Irie, 2016).

Solid-state photochemistry has similar superiorities to typical photochemistry in solution compared to typical hydrothermal reactions, including the selective activation, mild reaction conditions, and green energy sources (Hoffmann, 2008, Menzel et al., 2021, González et al., 2008, Weingarten, 2017). Moreover, the spatial structure of solid crystalline limits the relative position of reactant molecules, and the reaction is restricted to a designed direction to increase the selectivity (Hernandez-Linares et al., 2015, Resendiz et al., 2009, Park et al., 2018). Besides, this mechanism generates special molecules, which rarely occur in solution (Kole and Vittal, 2022). According to this mechanism, the valuable molecules can be selectively designed via chiral synthesis (Genzink et al., 2022, Hernandez-Linares et al., 2015, Evans et al., 1986, Sakamoto et al., 1995, Hernández-Linares et al., 2015) by host-guest solid-state photochemistry. Therefore, many organic synthesis routes have the potential to be modified or shortened, which can reduce the production cost. Moreover, it is a sustainable approach as it is solvent-free, which helps to reduce environmental hazards or pollution (Gui et al., 2020).

1.2 Current Situation and Research Gap

The lack of a suitable and controllable reactor for this solid-state photoreaction is one of the limitations to enlarging the production. The attenuation effect of photon transport prevents the direct dimensional-enlarging method from scaling up the photochemical reactor for the reaction that occurs in either solid-state or solution. To ensure a high conversion, a longer retention time and a more vigorous light intensity may be applied to the reactor, and this over-irradiation results in by-products for the traditional continuous stirring tank.

Currently, the core strategy to reduce the attenuation effect is to shorten the light path and to accelerate the mixing in the continuous flow reactors, such as small tank reactors in series and vortex reactors. However, they are not convenient for enlargement. Moreover, tubular reactors, regarded as the ideal photoreactor (Otake et al., 2018), were also applied in the solid-state photochemical reactions (Hernandez-Linares et al., 2015). However, they are equipped with extra mechanical equipment to create a vortex to reduce the probability of blockage and settlement for a semi-continuous process. The development of a well-designed reactor for solid-state photochemical reactions will contribute to the broadening of the strategy of organic synthesis because of its high selectivity and its unique products, and it has the potential to reduce cost by shortening the organic synthesis route in the industry.

1.3 Core Research Questions

The tubular reactor was regarded as the ideal photoreactor, as it has a short light transport path and a large surface for heat transport. The close system for tubular reactors reduces the unnecessary decomposition of desired chemicals and they are also easy to scale up by increasing the length or the number of tubes. To solve the risks of settlement, such as blockage and over-irradiation and to design a suitable photoreactor based on this tubular reactor, there are several questions required to be solved, including

- What is the relationship between the light intensity and the reaction rate of solid-state reaction.
- How the hydraulic or pneumatic failure can be prevented in particle conveying caused by the settlement.
- How a thin layer of the reactant can be formed to reduce the attenuation effect of the photon transport and then to increase the efficiency of the radiation absorption.
- What the characteristics of the boundary conditions are resulting in a good distribution of particles.

These problems may be solved by inducing a swirl flow. Swirl-induction pipe technology was numerically and experimentally developed (Li et al., 2015), and it promotes solid particle suspension in gas or liquid streams for pneumatic and hydraulic conveying of materials. The insertion of this pipe can provide a shear stress downstream of the swirl pipe and this force can redistribute the particles. Therefore, the main variable in this research is the particle distribution caused by this addition so that the problem can be converted into these core scientific problems, including

- How does the insertion of the swirl pipe redistribute the particle distribution downstream of the swirl pipe.
- How does particle distribution affect the radiation field and the absorption of light.
- How do boundary conditions affect the particle distribution downstream of the swirl pipe.

In this thesis, the performance of the swirl-induced reactor was investigated by using computational fluid dynamics (CFD) simulation.

1.4 Aims and Objectives

This project aims to develop a controllable and well-performed reactor for solid-state photochemical reactions via numerical methods. To design a better reactor, the intrinsic connection is studied among the reaction rate, radiation intensity, particle distributions and boundary conditions. The aims of this thesis are listed below.

- Complete a comprehensive literature survey on the limitations of the current multiphase photoreactor, the fluid dynamic properties of swirl flows and their applications, and the modelling techniques used by current and previous researchers to describe multiphase swirl flow and radiation field.

- Create the 3D geometry of a 4-lobed swirl pipe with different arrangements of swirl pipe and transparent glass pipe and build a suitable mesh for calculation.
- Establish a steady-state CFD model to obtain the averaged value of the geometrically induced swirl flows in terms of particle distribution along the pipe.
- Derive a kinetic model of solid-state photochemical reactions to find the key factors that affect the reaction rates.
- Build a radiation model to determine the radiation distribution along the glass pipe and find the relationship between it and the particle distribution.
- Find how the particle distribution was affected based on the inlet boundary conditions.

1.5 Thesis Outline

This thesis consists of 9 chapters, and a brief introduction to each chapter is shown as follows.

The current chapter, **Chapter 1, Introduction,** gives general background information and the importance of developing a novel continuous photoreactor for solid-state photoreaction. Then, the objective of this thesis is introduced to show how this thesis is divided into different parts to solve the problem. The summary of each chapter is listed at the end of this chapter.

Chapter 2, Literature review, reviews the required knowledge of several aspects. It includes the concepts of computational fluid dynamics (CFD), and how CFD works. The recent research results are discussed on solid-state photoreactions and their applications.

How these reactions undergo both batch and continuous processes is also analysed. The behaviour of the radiation of transfer through the solid flow is also reviewed so that the framework of this thesis can be built. After that, the research progress of the swirl pipe is also presented, to show the potential of how the swirl pipe improves the reaction. Models for determining the flow field, particle distribution and radiation were also reviewed in this chapter.

Chapter 3, Numerical Methodology, describes the models to simulate geometry, turbulence, multiphase, radiation, reaction models and corresponding general boundary conditions. To solve the governing equation, different solution methods are compared and. An efficient way is selected based on simple test or literature, to meet the requirement of simulating solid-state photoreaction.

Chapter 4, Characteristics of the Multiphase Swirling Flow, illustrates the basic characteristics of downstream swirling flow with particle flows. Different inlets with different distributed particles was tested and the resulting distribution was analysed in this section. Factors were defined to assess the distribution such as radial factor and angular factor.

Chapter 5, Chemical Reaction Kinetics and Derivation, presents the current models describing the solid-state photoreactions and it contains a description of how the solid-state chemistry kinetics is derived. The model was verified by experimental data from the literature.

Chapter 6, Radiation Field Characteristics, displays the reactor's performance in terms of radiation field. This chapter studies how the distribution of particles affects the distribution of radiation. Moreover, several factors are defined to describe the particle distribution, which helps the understanding of the relationship between the particle distribution and the radiation distribution.

Chapter 7, Flow Field Simulation, examines different inlet boundary conditions, including the initial velocity, inlet particle distribution, particle load, and geometry, and how they affect the particle distribution, which is presented in this chapter.

Chapter 8, Discussion, summarizes the main findings. This chapter also explains the expectation of the result, the limitations, and the significance of this project.

Chapter 9, Conclusions and Future Work concludes this thesis and the implication of present findings. The possible further work to improve or to broaden this research is proposed in this chapter as well.

Chapter 2 Literature Review

2.1 Introduction

Sunlight is a renewable and abundant source of energy that can be utilized for the synthesis of valuable molecules. Among the various types of light-driven reactions, solid-state photoreaction is a highly selective and environmentally friendly reaction which does not require any solvent. To enhance the efficiency and yield of this reaction, a well-designed solid-state reactor is essential. This chapter provides a comprehensive overview of six topics:

- The principles and applications of solid-state photochemistry,
- Current status and challenges of solid-state photoreactors,
- The development and function of swirl-induced pipe for particle redistribution,
- the use and validation of computational fluid dynamics (CFD) simulation for the flow field,
- the use and validation of CFD simulation for radiation distribution
- the use and validation of (CFD) simulation for the reaction rate distribution.

The section on solid-state photochemistry introduces the basic concepts and mechanisms of solid-state reaction and highlights its advantages and applications in organic synthesis, purification, and new energy development. The section also discusses the main challenges and limitations in developing solid-state photoreaction, such as low quantum yield, poor light penetration, and complex reaction kinetics.

The section on the current designs and challenges of solid-state photoreactors reviews the existing types and designs of reactors for solid-state photoreaction and evaluates their performance and drawbacks. The section also analyses the common problems encountered in solid-state reactors, such as particle deposition, fouling, uneven irradiation, and heat transfer.

The section on the development and function of swirl-induced pipe presents a potential device for improving particle redistribution in solid-state reactors. It demonstrates that the swirl-induced pipe can effectively solve the problem of particle deposition and fouling by creating a swirling flow that enhances the mixing and suspension of particles.

The design of the photoreactor was first based on simulation, so the computational models were reviewed. To determine the reactor's performance, the particle distribution and the reaction rate were required to be determined. Because the particle distribution affects the radiation field related to the reaction rate, the models to calculate the flow field, radiation field, and reaction rate field were all reviewed.

The section on computational fluid dynamics (CFD) simulation for flow field discussed various turbulence models combined with multiphase models. The section presented the performance of these models and compared the accuracy and reliability of CFD simulation with experimental data.

The section on radiation simulation reviewed the phenomenon of radiation transfer and methods to estimate the radiation field. Due to the lack of experimental data and correlations, the Mie calculation was reviewed to determine the optical properties of solid particles. The section also discussed the performance of these models.

The section on reaction simulation reviewed the mechanisms of solid-state chemistry and photochemistry, which are important to develop a model for designing a photoreactor. The section also reviewed models for species transport, especially their accuracy and reliability.

2.2 Solid-State Photochemistry and Their Applications

2.2.1 Photochemistry

Photochemistry is a branch of chemistry that studies chemical reactions caused by the absorption of ultraviolet (wavelength from 100 to 400 nm), visible light (400–750 nm) or infrared radiation (750–2500 nm). It studies how light can initiate, accelerate, or modify chemical reactions, as well as how light can affect the physical properties and behaviour of matter.

When molecules absorb light and reach an excited state, their electronic distribution changes, which alters their reactivity. This enables the formation of products that are inaccessible by thermal activation (Hoffmann, 2008). Moreover, photochemical reactions can often simplify the synthetic routes of complex organic molecules by reducing the number of steps required (Karkas et al., 2016). Photochemical reactions also have other advantages, such as mild reaction conditions, low by-product formation, and renewable energy sources (sunlight) (Hoffmann, 2008). These advantages have led to a wide range of applications of photochemistry in various fields, such as pharmaceuticals (Otake et al., 2018, Oelgemoeller, 2012), polymers (Junkers and Wenn, 2016, Chatani et al., 2014), nanoparticles (Freitas de Freitas et al., 2018, Sakamoto et al., 2009), water treatment (De Lasa et al., 2005, Miklos et al., 2018, Byrne et al., 2018), hydrogen production (Kudo and Miseki, 2009), and light-responsive devices (Irie et al., 2014, Ceroni et al., 2010).

One of the advantages of photochemistry over thermal reactions is that photochemistry can access different reaction pathways by exciting the reactants to higher energy states that are otherwise inaccessible by thermal activation. This enables photochemistry to induce bond cleavage or formation that is thermodynamically or kinetically unfavourable in thermal reactions (Menzel et al., 2021, González et al., 2008). Another advantage of photochemistry is that it can control the reaction's selectivity and yield by tuning the light source's wavelength and intensity. The wavelength determines which orbital of the reactant is populated by the photon, and thus which reaction channel is activated (González et al., 2008). The intensity determines how many photons are absorbed by the reactant, and thus how much of the reactant is converted to the product (Menzel et al., 2021).

Unlike thermal reaction, which relies on heat energy and often requires chemical activators or harsh conditions, photochemistry uses light energy and can exploit sunlight as a renewable and environmentally benign energy source (Weingarten, 2017). This allows green photochemistry to achieve selective and efficient transformations of natural materials into useful compounds with minimal waste and toxicity (Albini, 2016). Photochemistry is therefore a valuable application of green chemistry principles (Anastas and Kirchhoff, 2002) for the synthesis of chemicals from natural materials, which can enhance the value and sustainability of the substrates (Crisenza and Melchiorre, 2020).

2.2.2 Solid-State Photochemistry and Its Applications

Solid-state photochemistry is a field of research that explores the intermolecular interactions and geometrical constraints of the solid state (Schmidt, 1971). By using light as an energy source and avoiding organic solvents, solid-state photochemistry can achieve a green and sustainable synthesis of various organic compounds with high selectivity and stereo-control. Moreover, solid-state photochemistry can also create functional materials that exhibit photochromic or photomechanical behaviour, which have potential applications in sensors, actuators, and memory devices (Cole and Irie, 2016). Furthermore, solid-state photochemistry can also enable photo-redox catalysis, activating challenging redox reactions by using light-induced electron transfer (Shaw et al., 2016). Therefore, solid-state photochemistry is a valuable and versatile tool for developing new materials and reactions.

The history of solid-state photochemistry dates back to the late 19th century was called the heroic era. Pioneers like Marckwald (1899), Ciamician and Silber (1901), Stobbe (1922), de Jong (1923), Senier and Shepheard (1909) discovered and investigated various photoreactions in organic solids, such as photodimerization and photochromism. However, this research phase ended due to the lack of physical methods to understand the molecular structure of organic solids (Schmidt, 1971).

It was not until the mid-20th century that X-ray crystallography and other techniques became available to reveal the intermolecular interactions and packing arrangements in organic crystals. This enabled researchers like Schmidt (Schmidt, 1971), Desiraju and Parshall (1989), and Ramamurthy (1991) to rationalize and control the photoreactivity of solid compounds based on their crystal structures and supramolecular assemblies.

With the development of crystal engineering, the goal was to design and synthesize organic solids with specific intermolecular geometries and orientations that favour certain photoreactions (Ramamurthy and Sivaguru, 2016). This led to the development of new synthetic methods, new photochemical transformations, and new applications of solid-state photochemistry in areas like chiral synthesis (Evans et al., 1986, Sakamoto et al., 1995, Hernández-Linares et al., 2015, Genzink et al., 2022), molecular switches and sensors, (Krysanov and Alfimov, 1982, Irie et al., 2002, Safin et al., 2016, Jiao et al., 2022), and photomechanical materials (Kitagawa et al., 2016, Norikane et al., 2016, Bushuyev et al., 2016).

Apart from crystal engineering, the current phase of development includes nano-engineering. The focus is on exploring the photophysical and photochemical properties of nanostructured materials, such as thin films (Manjavacas et al., 2017), nanoparticles (Wang et al., 2023), nanotubes (Maeda et al., 2016, Wang et al., 2020), nanowires (Wang et al., 2022), quantum dots (Xu et al., 2020, Bai et al., 2022), etc. These materials offer new possibilities for manipulating light-matter interactions at the nanoscale and creating novel functional devices.

It includes photoisomerization (Kole and Vittal, 2022), photocycloaddition (Hu et al., 2014, Pandolfi et al., 2021, Ramamurthy and Sivaguru, 2016), photodecarbonylation (Park et al., 2018, Hernández-Linares et al., 2015), and photoinduced electron transfer.

Meanwhile, heterogeneous photocatalytic reactions (Wang et al., 2022, Wang et al., 2020) or host-guest reactions can be considered to be applied in the photoreactor. These reactions are valuable in medicine (Sommerwerk et al., 2016), energy production (Hassan et al., 2023), biochemical production (Chen et al., 2008, Liu et al., 2022), material science (topochemistry, morphology control and crystal growth inhibition, etc.)(Cole and Irie, 2016), asymmetric synthesis (Fernandes and Levendis, 2004, Genzink et al., 2022, Scheffer and Xia, 2005), and supramolecular design (Yu et al., 2019, Kole and Mir, 2022).

2.2.3 Advantages of Solid-State Photochemistry

Apart from the general advantages of photochemical reactions compared to traditional thermal reactions mentioned in section 2.2.1, solid-state chemical reactions have specific superiorities to those which occur in the solution. The advantages of them are listed below:

- High selectivity
- Specific product
- Potential to shorten the synthesis route
- Solvent-free

Solid-state photoreactions often show a higher selectivity. As crystals have a unique structure, reactant molecules are limited in the framework by the intermolecular force. These molecules cannot move flexibly, which results in the reaction occurring selectively. Chemists use this characteristic to improve selectivity or to create new synthesis routes.

Hernandez-Linares et al. (2015) compared the selectivity of photodecarbonylation of the acyclic, homochiral, hexasubstituted(+)-(2R,4S)-2-carbomethoxy-4-cyano-2,4-diphenyl-3-pentanone in three different media, dry solid, benzene solution, and the nanocrystalline suspension. This reaction generates six combination products, four disproportionation products and trace polymerization products (Figure 2.1). Although this reaction has 100% conversion in the benzene solution, a modest 18% yield of combination products with circa (ca.) 77% enantiomeric excess (ee.) was achieved. This is in accord with 80% ee. for a similar reaction. (Resendiz et al., 2009). By contrast, this reaction occurs in the dry solid and presents a 96% yield of combination products with ca.100% ee., while the occurrence in the nanocrystalline suspensions presents a 100% yield and 100% ee., which are much higher than that in the solution. The slightly lower yield of dry solid is due to some melting.

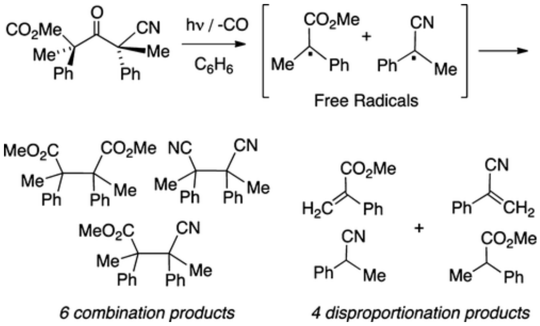

Figure 2.1 Presentation of the products of photodecarbonylation. (Hernandez-Linares et al., 2015)

Park et al. (2018) also displayed different products of decarbonylation of the ketone derivatives with different substitutions. This scheme presents all products generated from the reaction in a solid crystal or solution and shows that the intermolecular force from the solid structure affords a much higher selectivity.

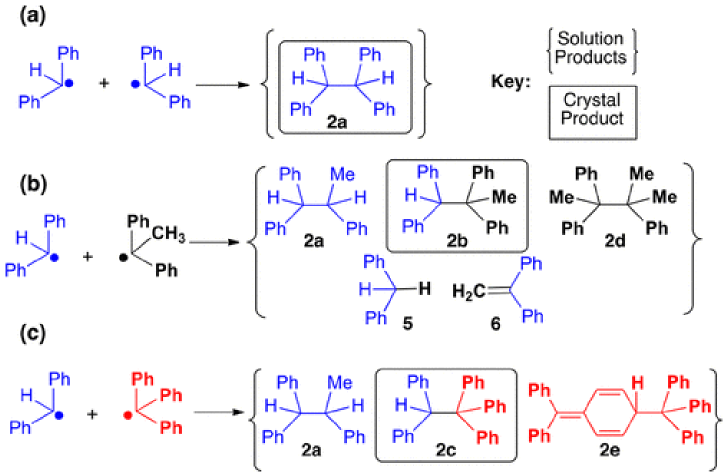

Figure 2.2 Presentation of the products of photodecarbonylation. (Park et al., 2018)

In the meantime, solid-state photochemical reactions have their potential special products. Kole and Vittal (2022) reviewed the literature on the isomerization of pyridyl-substituted cyclobutane ligands and their salts in coordination polymers and metal-organic frameworks (MOFs) in the solid state and solution. Cyclobutane compounds are a class of compounds that can be synthesized in the solid state by photochemical [2 + 2] cycloaddition reactions. The rctt-isomer (or the syn-dimer) is the exclusive form obtained in the solid state, which can isomerize to the thermodynamically more stable rtct-form (or the anti-dimer) by heating in both the solution and solid state. This rctt-isomer also proves the selectivity for solid-state photochemistry caused by the supramolecular interaction. This shows a potential to shorten the route in organic synthesis.

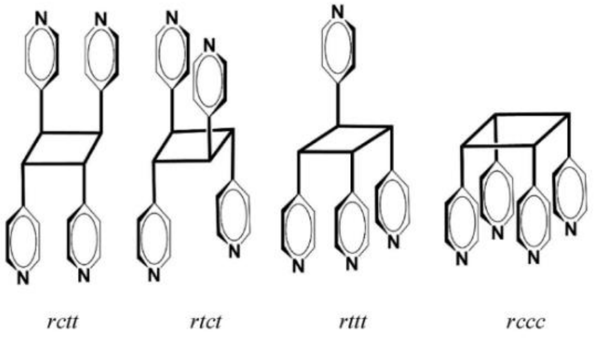

Figure 2.3 Four *regio*-isomers of *tetrakis*(4-pyridyl)cyclobutane. (*r=regio, c=cis, and t=trans)*

The solid-state photoreaction is solvent-free. They minimize the production of by-products or waste by avoiding conventional volatile organic solvents. This helps to minimize environmental hazards or pollution and is a sustainable approach (Gui et al., 2020). Solvent-free synthesis has several advantages over the classical method of synthesis. It provides a neat reaction with easy separation, workup, and purification (Anastas and Warner, 1998).

It has huge economic potential as solid-state photochemistry may shorten a long organic synthesis path. However, it remains to be developed such as the reaction kinetics and the suitable equipment.

2.2.4 Limitations on Development of Solid-State Photochemistry

Despite the many advantages of solid-state chemistry, it has not been widely used industrially. This is caused by that there are some application limitations listed below,

- Temperature sensitive
- Mechanism remained to be studied
- Lack of suitable equipment

The intramolecular force provided by the solid structure increase the selectivity. It is sensitive to temperature. When the temperature increases to some extent (partially melted), the selectivity of the reaction decreases due to the weakened intermolecular forces. Avoiding the breakage of the force (lower temperature) may result in a slower reaction rate to maintain higher selectivity if the crystal has a low melting point.

Fernandes and Levendis (2016) tested three different types of polymorphs and changed the structure by increasing the temperature. They found 100% α-truxillic acid yielded at 343K by a two-stage mechanism, where the α-polymorph undergoes a phase change to α'-polymorph and stabilized at 343K. The reaction occurred in α-polymorph, α'-polymorph at 293k and 343K and showed a lower conversion of 66.7% for α'-polymorph at 293K (Figure 2.4 b) (Fernandes and Levendis, 2004). The conversion and the reaction speed are all improved with higher temperature, and it also shows that the effect of the crystal structure on the selectivity or conversion of the reaction. Although these studies showed the potential of rapid response of the solid-state photoreaction, it still requires more experimental data to promote and prove the finding.

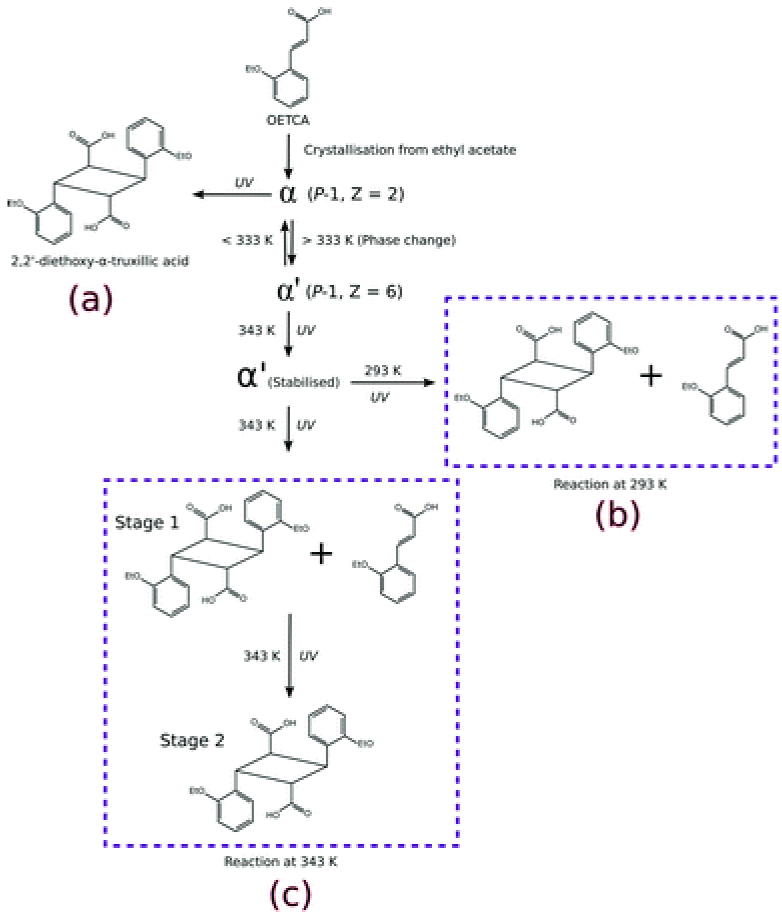

Figure 2.4 Reaction route of photodimerization of a derivative of cinnamic acid under different polymorph formed under different temperature. (Fernandes and Levendis, 2004)

Therefore, the difficulty of controlling the reaction conditions limits the development of the-solid state photoreactions from lab scale to larger scale. Apart from the temperature, the control of radiation intensity is also important. The over-irradiation and poor heat exchange rate may result in undesired side reactions. The high energy of photons may result in an unwanted decomposition directly (Inkinen et al., 2015) or breaking the solid structure indirectly by converting it to heat (Bertoni et al., 2016).

Another limitation is that the general rules or models to predict the photochemical behaviour of different solid-state systems are still under research. The photochemical behaviour of different solid-state systems depends on many factors, such as the molecular structure, crystal packing, light wavelength, light intensity, and duration. These factors can vary widely among different systems and affect the rate and outcome of the photochemical reactions (Akhtaruzzaman et al., 2023, Kim et al., 2012, Peedikakkal and Vittal, 2010). Therefore, it may be difficult to find general rules or models that can capture all the complexity and diversity of photochemical phenomena in solid-state systems (Menzel et al., 2021).

The lack of the equipment for solid-state photochemistry also limits the development of them. Not only do they need uniform incident radiation, but they also require controllable process in handling solids and controlling temperature. The next section is going to analyse the status of photoreactors and the limitation for being applied to the solid-state photochemistry.

2.2.5 Summary of Comparison of Different Reactions

Table 2-1 General comparisons among traditional reactions (hydrothermal), photochemistry in solution and solid-state photochemistry

	Traditional reactions	Photochemistry in solution	Solid-state photochemistry
Temperature	As high as possible	Mild temperature. Sometimes low temperatures are required;	Not required
Pressure	Related to reaction temperature. Gaseous reactions need higher pressure;	Normally not required. Gaseous reactions need higher pressure;	Not required
Radiation	Not required	UV-visible light	UV-visible light
Selectivity	low	High	Higher (than that in solution)
Stability of Products	Relatively stable	Temperature sensitive	Temperature sensitive Rare molecules
Solvent	Yes	Yes	Not required
Catalyst	Metal/organic	Semiconductor	Not required. Specific design: host-guest synthesis

2.3 Photoreactors

Continuous flow chemistry is one of the possible solutions for facilitating solid-state reactions in academic and industrial applications. The main motivations for advancing this field are safety, controllability, feasibility and the ability to rapidly access complex chemical structures. The advent of new innovative reactor designs in recent years provides a powerful way to increase the practicality and productivity of modern photochemical reactors in a reproducible and automatable manner (Donnelly and Baumann, 2021). Although there are many good continuous-flow photoreactors, whether homemade or from commercial suppliers, allowing for the creation of valuable molecules, these reactors are not compatible with solid-state photoreactions in scalability. In this review section, the key achievements in this field were highlighted.

2.3.1 Case Study of Multiphase Photoreactors

At present, multiphase photoreactors have been reported at various scales, from laboratory to commercial applications, while most of them are designed for gas-liquid or liquid-liquid systems. In this section, multiphase photochemical reactors are reviewed focusing on those for solid-state photochemical reactions or which can be applied to these reactions. In this section, (a) batch reactors, (b) continuous stirred-tank reactors and (c) thin film reactors are studied. In addition to these reactors, linear reactors can be also applied to reactions with solids. They are introduced separately in section 2.3.3 for their specific characteristics after analysing the ideal features of a photoreactor in section 2.3.2.

(a) Batch reactors for solid-state photochemical reaction

The traditional solid-state reactor in the lab is simple. Normally it consists of a glass slip and a slide or a Petri dish in the focus of the radiation, where particles are evenly distributed in a thin layer for a small dose experiment (Khan et al., 2008). Because of the temperature sensibility of the solid-state reaction, the glass slide was upgraded with cooling water shown in Figure 2.5 (Hu et al., 2014). These reactors are simple and easy to operate, which are suitable for small-scale experiments. However, the productivity for them is dozens of milligrams per hour and they are hard to scale up.

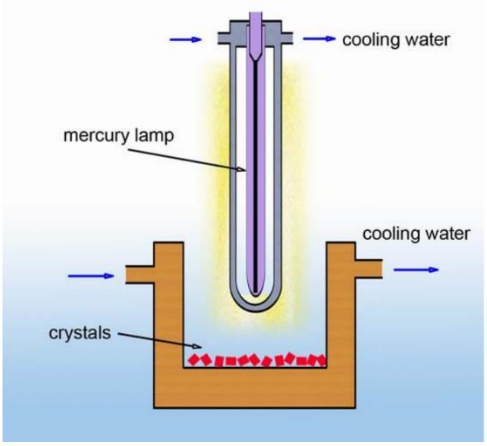

Figure 2.5 Batch reactor in the lab scale (Hu et al., 2014)

Another typical batch reactor is the continuous stirring tank reactor, for example, the photo-fermentation reactor for biohydrogen production shown in Figure 2.6 (Chen et al., 2008). They provide external and internal light sources as shown in this figure, mixing with magnetic stirring rods. This setup provides a competitive yield (7.1 mol H_2/hexose) from other studies from 2.4-7.1 mol H_2/hexose (Asada et al., 2006, Redwood and Macaskie, 2006, Oh et al., 2004, Özgür et al., 2010). This process can be also operated continuously.

However, it is not suitable for continuous crystal-to-crystal reactions. Because the solids (bacteria) are only staying in the reactor and the gas is the main product, there is no auxiliary equipment for conveying particles in the pipe whereas particles are products required to transport out from the reactor except that the following step of this process is dissolve these solid products. The scale-up is also still a problem in that the dimension of the reactor cannot be increased directly.

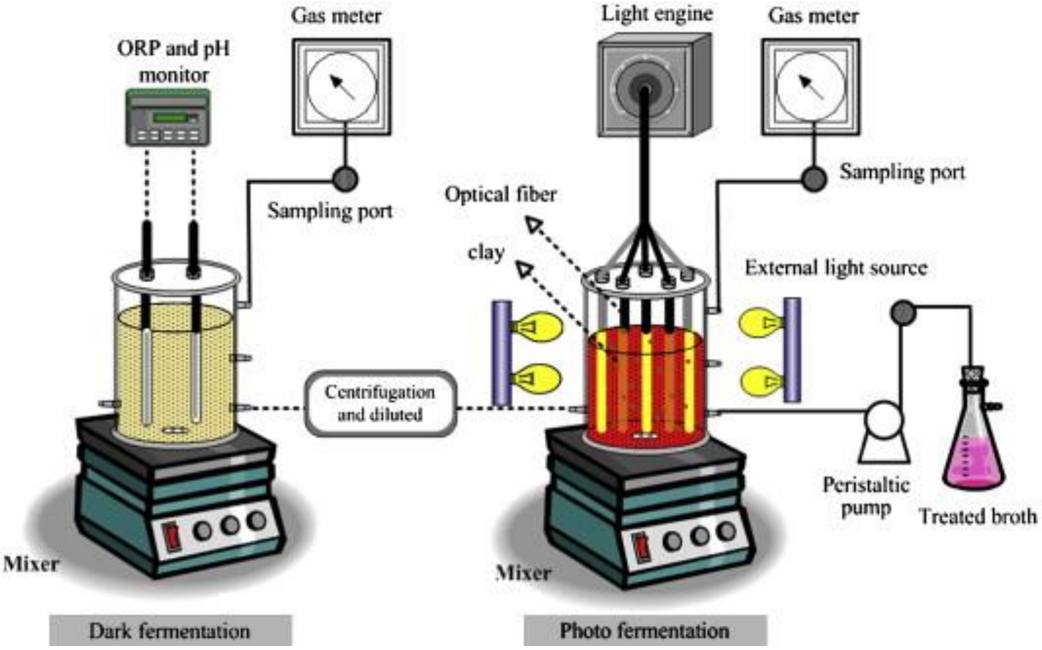

Figure 2.6 Fermentation reactor system for dark reaction and photo reaction. (Chen et al., 2008)

(b) CSTR in series

The Jensen group (Pomberger et al., 2019) reported a continuous stirred-tank reactor (CSTR) system for photochemical reactions. The reaction reported by the MacMillan group (Liang et al., 2018, Shaw et al., 2016) required the presence of an insoluble inorganic base, which is typically incompatible with carrying out reactions in a continuous mode due to reactor blocking and fouling. The CSTR could mitigate this issue through careful reactor design. Previously, the Jensen group (Mo and Jensen, 2016) had reported the design of a CSTR cascade used for heterogeneous reactions, which was adapted for this photochemical reaction.

The reactor consisted of five single chambers (total volume 5.3 mL) connected by a drilled channel, which could be irradiated through a glass window (Figure 2.7 a). Mixing was achieved using magnetic stir bars which could be operated using a conventional magnetic stirring plate. Meanwhile, the problem of the clogging was not found in this design. Using this setup, in combination with a slurry pump, the heterogeneous mixture could be administered to the reactor while maintaining an inert atmosphere.

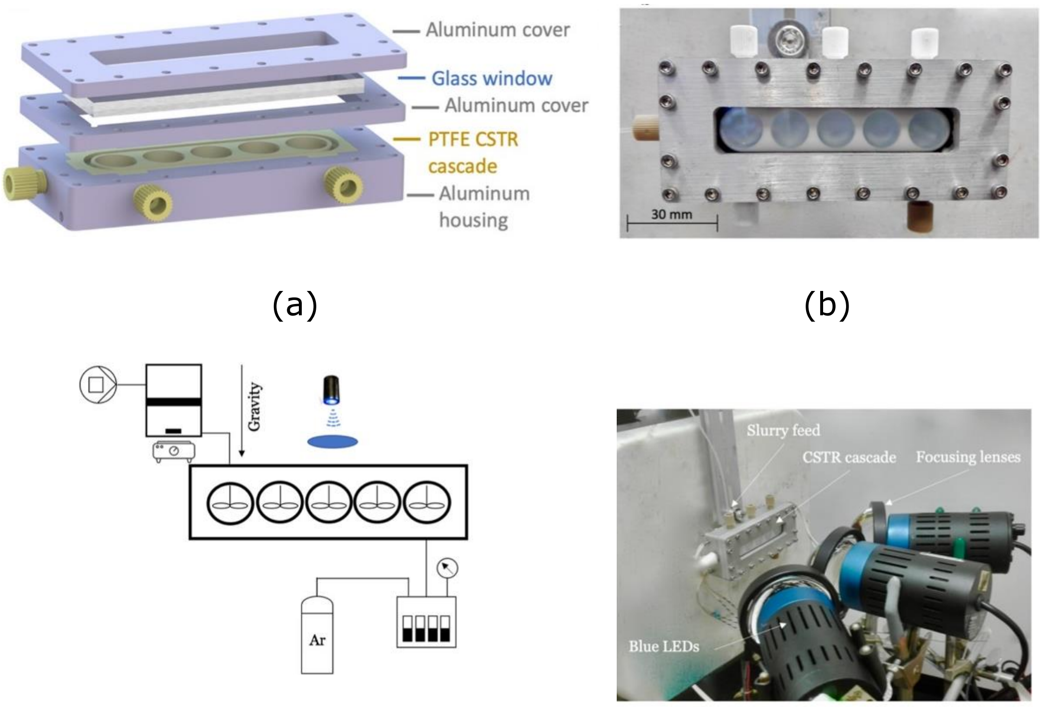

(a) (b)

(c) (d)

Figure 2.7 CSTR in series for photoreaction (a) Exploded-view drawing of the CSTR cascade for solid-containing photochemical reactions. (b) Picture of the assembled CSTR cascade. (c) Flow diagram of solid-flow CSTR including the slurry pump. (d)Image of the lamps and reactor. (Pomberger et al., 2019)

Under these conditions facilitating direct transfer of the previous batch method to continuous flow was possible, eliminating the need for re-optimisation to incorporate a soluble organic base. The flow system was then used to synthesise the product on a gram scale in 13 h (77 mg/ h) with similar yields to the batch process (77% in flow, 80% in batch). While the application of flow chemistry to this reaction did not offer an improvement in yield, as is sometimes the case, it offered significantly shorter reaction times (30-min residence time vs 15 h in batch) and higher productivity than a batch reactor of similar size. Based on the reactor design this productivity could be further improved by a relatively straightforward increase in reactor size. However, there still is a limitation when enlargement is performed.

Whether the light can penetrate in the middle of the reactor is still a problem when increasing the volume of the reactor. For this small vessel, the change of the light intensity can be ignored while the increasing path of the radiation transport results in an ununiform distribution of light. Meanwhile, the mixing becomes a problem when the volume increases. If the enlargement is not available, several sets of this reactor are required to increase the production.

(c) Thin film reactor

Clark et al. (2018) reported that the high productivities, equivalent to 170.5 g/h were obtained for the intramolecular [2+2] photocycloaddition of Cookson’s dione from a semi-continuous operation. They modified a conventional rotary evaporator by adding inlet and outlet tubes as well as the light source shown in Figure 2.8, as well as the gas cylinder which is adapted for gas-liquid reaction or as a protecting environment. This set was called

PhotoVap. Due to its simple structure, its productivity is comparable to the batch operation in the same apparatus, which is 198.7 g/h. Although continuous operation has a lower production rate, it is convenient that it is unnecessary to disassemble it and clean it after each batch. This simple adaption is cost and time saving, which is suitable for larger production in the lab.

This difference is caused by imprecise retention time control according to the experimental procedures. The semi-continuous manner was operated by the peristatic pump. This process was then repeated multiple times until all the reaction solutions had been processed. Before running a reaction specific volume timing for the pumps were determined to dispense a known volume into the flask. This operation cannot ensure every molecule receives the same number of photons. Meanwhile, this reactor requires additional auxiliary equipment to prevent the stuck if it is applied for solid-state photochemical reaction.

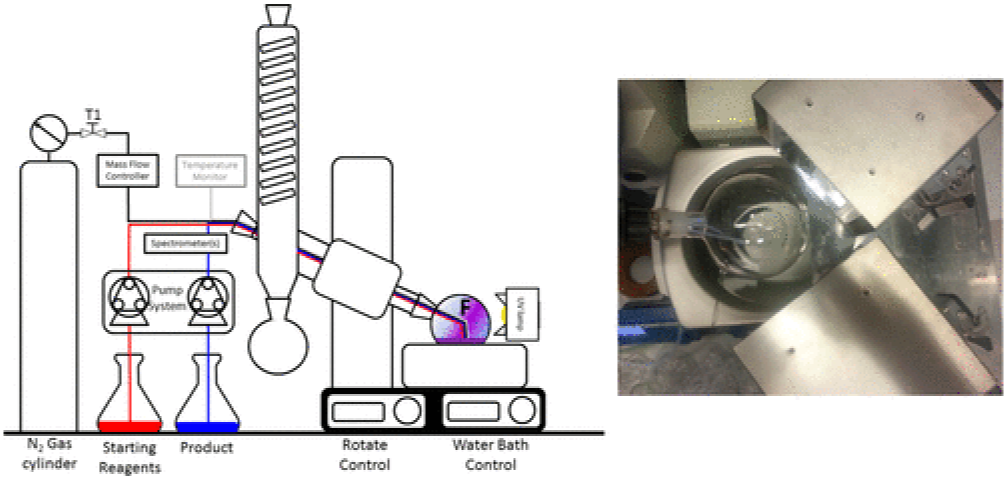

Figure 2.8 Thin film reactor called PhotoVap, modified from a conventional rotary evaporator. The left is the sketch of this system while the right is the picture of the irradiated round bottom flask reactor. (Clark et al., 2018)

Lee et al. (2017) developed a vortex reactor (Taylor reactor). It uses a rotating structure with a stationary outer. It is similar to the smaller scale they have reported using a stationary bored rod (DeLaney et al., 2017). This new design consists of a suspended bored stainless-steel rod (18 mm diameter) that functions as the rotor. The rod is placed inside a custom jacketed glass tube (20 mm ID) and the annular space between these (~1 mm) functions as the irradiated volume (8 mL), irradiated by three blocks equipped with 5 white LEDs each (total input power ~ 195 W) (Figure 2.9 a, b). The liquid was fed into the system through the narrow bore inside the rod, and the required gaseous phase was drawn in by the lower pressure region caused by the rotation of this rod. Therefore, no additional gas feed was necessary, which was made possible by keeping the top of the reactor open to air (Figure 2.9c). The rotating rod caused high shear rates and generated Taylor−Couette vortices (Figure 2.9d) in the liquid, finely dispersing the gas phase as bubbles into the liquid and providing rotating-dependent mixing.

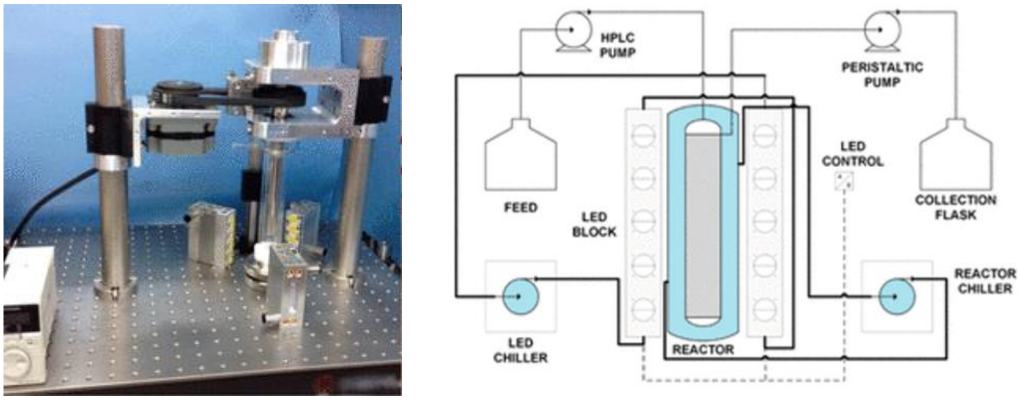

(a) (b)

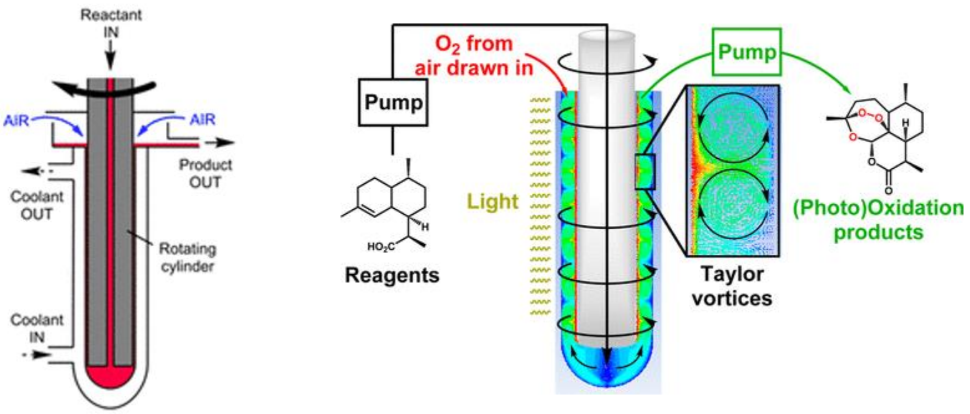

(c) (d)

Figure 2.9 (a) Picture of the deconstructed reactor with the motor and its control box. A drive belt connects the motor and the rotating cylinder. During operation, a protective housing (not shown) contains the motor, belt, and moving parts. (b) showing the pipe and partial instruments diagram of the system. (c) indication of the flow in the Tayler reactor and (d) showing the flow vortex in the reactor coloured by the magnitude of velocity determined by CFD. (Lee et al., 2017)

The production of ascaridole was used as a benchmark gas−liquid photochemical reaction (Figure 2.10), where the rotational speed was varied and found to be optimal at 3000 rpm. At higher speeds, the competing oxidation to p-cymene was promoted and the yield of ascaridole dropped. A flow rate of 0.5 mL·min−1 (0.1M α-terpinene in ethanol) at 3000 rpm resulted in a productivity of 2.73 mmol·h−1 (11.0 g·day^{-1}) with 91% yield of ascaridole.

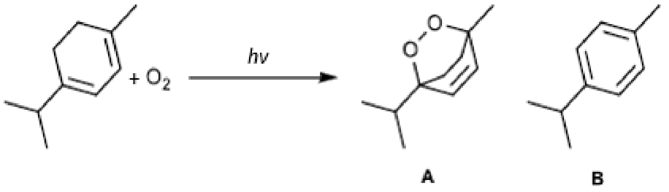

Figure 2.10 Scheme of the production of ascaridole.

Starting from the small-scale vortex reactor, they developed a scaled-up version of this reactor concept (Lee et al., 2020). Instead of the air being drawn in, a gaseous flow into the reactor was implemented to allow for more precise control of the gas feed. The rotor was changed from a suspended stainless-steel rod to a polyether ether ketone (PEEK) rod (96 mm diameter) that was attached to both the reactor base and cap, to ensure mechanical stability. This rod was placed inside an open-ended jacketed glass filter tube (100 mm ID) that was closed off by the base and cap (Figure 2.11). Both the liquid- and gas-inlets were placed at the base, whereas the outlets were located inside the cap. Irradiation of the annular space (~2 mm, 280 mL) was provided by two curved white LED blocks for visible light (totalling 720 W input power), and one or two medium-pressure mercury arc lamps for UV-light (1.4 or 2.0kW input power). Because the tangential velocity (angular velocity multiplied by the radius) of a rotating object increases with an increasing radius, the larger-sized rotor required lower rotational speeds to provide the same Taylor−Couette vortex behaviour as the small-scale reactor (1300 vs 4000 rpm). This large-scale reactor showed a maximum projected productivity of 7.5 $kg \cdot day^{-1}$ (2 × 2.0 kW).

Although these reactors perform well in gas-liquid photoreactions, these reactors still show problems with fouling, and additional mechanical instruments are required. Meanwhile, this design did not fully use the light. Only one side of the reactant was irradiated, and the light was not effectively used. To create this Taylor−Couette vortex, the space in the annulus is limited, and the space utilization rate is not high.

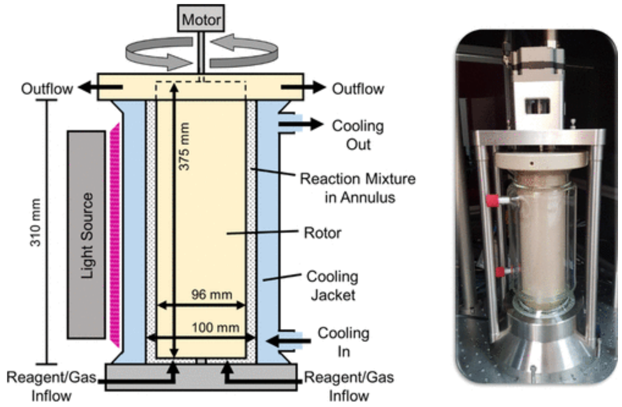

Figure 2.11 Representation of a large scale Taylor reactor. The left is the structure of this reactor, while the right is the picture without scale. (Lee et al., 2020)

2.3.2 Ideal Features of the Continuous Reactor for Solid-State Photochemical Reactions

An ideal solid-state reactor has several necessary characteristics to meet the requirement of production. A good reactor can help the reaction reach a high conversion and a high selectivity in a safe and controllable way. These characteristics are listed below, and they are analysed in the following sub-sections.

- Particles need sufficient irradiation without exceed (melting)
- Continuous operation with closure system
- Feasible scale-up with high quality production
- Precise temperature control
- Mixing
- Safety

(a) Appropriate irradiation

Photochemical reactions require the absorption of photons. As a result, sufficient exposure to the radiation for the reactants inside a photoreactor is important to obtain a high yield and a high selectivity. A homogeneous radiation distribution promotes the absorption of reactants. Based on the Beer-Lambert Law, the distribution will not be even in a reactor due to the extinction effect.

$$A = \log_{10} T = \log_{10} \frac{I_0}{I} = \varepsilon c l \tag{2-1}$$

This equation clearly shows the correlation between the absorbance (A), transmittance (T) and the depth of the reactor (l), where c is the concentration, and the ε is the extinction coefficient. When the concentration is a constant, the relationship is shown in Figure 2.12**.** With the concentration increase, the higher the concentration, the shorter the light path, which restricts the size of the reactor.

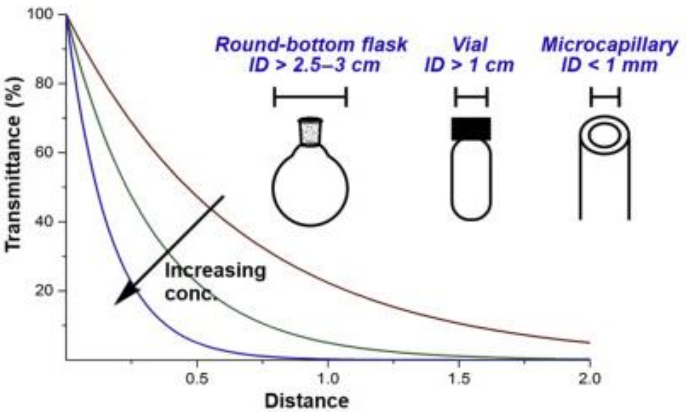

Figure 2.12 the correlation between distance and light transmittance (Sambiagio and Noël, 2020)

This attenuation effect of photons is one of the key problems limiting the expansion of production. When the light path or the diameter of the reactor increases, there are several bad effects on the performance of the photoreactor. Firstly, the light cannot penetrate every place with the increasing dimension of the reactor, so the reactant molecules in the area away from the light source cannot receive sufficient photons. To ensure every molecule gets even radiation, increasing incident radiation intensity and strengthening mixing are the regular strategies. Higher radiation intensity results in local strong radiation, which leads to the occurrence of side reactions. This over-irradiation can also increase the temperature of the materials and drive the reaction in an unexpected direction. On the other hand, the traditional stirring method to increase mixing is getting weaker with the increasing size of the reactor. Therefore, the key problem for scaling up the photoreactor is to ensure every molecule receives sufficient and equal photons.

The quantum yield is an important parameter to assess the efficiency of the photochemical reactions, shown as in Equation 2-2. It is typically between 0 and 1 for no chain mechanism (Studer and Curran, 2016). The quantum yield can be determined by carrying out photon flux measurements and subsequently performing the reaction in the same setup.(Ziegenbalg et al., 2016)

$$\phi = \frac{number\ of\ molecules\ of\ product}{number\ of\ photons\ absorbed\ by\ reactant} \tag{2-2}$$

(b) Reliable Scale-up

A reliable scale-up is important to photoreactor design because it allows for the exploitation of the benefits of photochemical reactions on a larger scale, such as faster reaction rates, higher yields, and lower environmental impact. There are two main strategies to scale up, increasing the total volume of the reactor and increasing the flow rate. It is a straightforward way to increase the flow rate resulting in changes in the hydrodynamics, the heat transfers and pressure drop. In this section, the strategy of increasing the total volume was discussed as there are limitations to increasing the flow rate.

The traditional method to increase the volume by increasing the dimensions of the batch reactor is no longer reliable because it leads to a decrease in the efficiency and selectivity of the reactions due to the attenuation effect of photon transport resulting in nonuniform energy profiles. Over-radiation was a regular operation in the traditional scale-up scale to ensure the conversion of the reaction. This causes side reactions, decomposition, and waste generation, which reduce the quality and yield of the product.

Compared to direct enlargement, a more reliable method is numbering up. The numbering-up method can be divided into external and internal numbering up (Dong et al., 2021). The difference between these two is whether every parallel reactor uses the individual equipment, for example, pumps and controllers. The external numbering up uses individual pumps and controllers so that productivity can be achieved by adding the units. The main disadvantage of this setup is the high investment cost. In the internal numbering up, these reactors multiplied several times itself and they share the same single inlet, collection, and monitoring system. At mean time, the equal flow distribution over the different reactors should be take care of because the different pressure difference results in maldistribution. Therefore, an advanced and reliable scale-up technique has yet to be developed especially for managing solid in the photoreactor.

(c) Continuous operation

In mean time, the continuous operation is preferred ideally, due to its continuity and closure. The chemicals being treated or unstable intermediates have less chance to decompose, such as singlet oxygen, diazonium salts, azides (Gutmann et al., 2015, Müller and Wirth, 2015). For these multi-step chemical processes, continuous operation reduces manual handling, and saves operating cost and time. The combination with inline spectroscopic tools, self-optimization protocols and automation are also applied to the continuous process. This combination can further reduce the human interaction (Fabry et al., 2016, Fabry et al., 2014, Ley et al., 2015).

(d) Fast heat exchange

Solid-state photochemical reactions are sensitive to temperature. The intermolecular force can be easily broken by increasing temperature, which decrease the selectivity of the reaction. Meanwhile, the increasing temperature can also result in acceleration of the undesired reaction (Chizhik et al., 2018). For photochemical process, temperature in the reactor increases due to the heating from the irradiation and the exothermic reactions (Gemoets et al., 2016). Therefore, the fast heat exchange rate is significant to the reaction process. When designing this reactor, the key is the material (U) and the area (A) to volume ratio if the temperature difference keeps the same.

$$Q = UA\Delta T \tag{2-3}$$

where U is the overall heat transfer coefficient, A is the area for heat transfer, and ΔT is the temperature difference.

(e) Fast mixing

Diffusion across a concentration gradient is the main mechanism for mass transport in the reactor. The mass transport is slow without mechanical stirring, especially for tank reactor, which results in a slower rate for diffusion-controlled reaction. For tubular reactors, the smaller diameter of the reactor reduces the path for molecules to diffuse form the centre to the wall of the reactor, resulting in fast mixing to a uniform reactant across the reactor without additional mechanical devices.

(f) Safety operation and controllable

Increasing the operational safety of hazardous reactions is one of the main arguments for the chemical industry to switch to a continuous-flow protocol. Reactors have small dimensions which reduces the total inventory of hazardous chemicals and thus avoids any safety risks associated with its handling. Furthermore, the impact of an explosion is directly related to the total amount of explosive materials present in the reactor to the power of 1/3. Despite the advantages of microreactors, one must still be careful as explosions can propagate into the neighbouring storage vessels which might contain larger amounts of explosive material. This also demonstrates the need of suitable quenchers at the reactor outlet, which can prevent explosion propagation (Liebner et al., 2012).

Due to the increased safety, reaction conditions which are impossible to carry out in batch are now accessible in flow microreactors. This is especially true for photochemical reactions involving singlet oxygen. It is known that pure oxygen results into higher reaction rates and, in flow, such processing conditions become accessible. However, if particles are injected to or generated in the tubular reactor, there is a risk of hydraulic failure, which would be discussed in the following section.

2.3.3 Linear Tubular Reactors

The microreactor is regarded as the ideal technology for the photoreactor (Cambié et al., 2016). This acknowledgement is mainly based on that the attenuation effect of the radiation transfer through the pipe can be solved due to the small channels of them. The design of the microreactor provide a large contact area for either receiving photons or exchanging heat. These performances are highly coincident with the ideal feature described before.

Compared to the different batch, vessel, plate and rotating reactors described in the section 2.3.1, the linear tubular reactor has many advantages. Cambié et al. (2016) reviewed the applications of microreactors and raised nine advantages listed below. This section summarized the characteristics of the microreactor and then show how these reactors meet the ideal requirement of photochemical reactor. In this section, the performance of the microreactor was discussed in terms of the feature before. After that, the limitation for this reactor applied to solid-state photochemistry was discussed.

- Improved irradiation of the reaction mixture
- Fast mixing
- Reliable scale-up
- Fast heat exchange
- Multiphase chemistry
- Multi-step reaction sequence
- Immobilized catalysts
- Improved reaction selectivity and increased reproducibility
- Increased safety of operation

(a) Appropriate irradiation in microreactors

Improved irradiation of the reaction mixture is an important feature of the microflow photoreactor. Aillet et al. (2014) have compared the photon flux for a flow reactor and batch reactors. At the wavelength at the 365nm, the batch reactor and the flow reactor received 0.033 einstain/(m^3s) and 5.02 einstain/(m^3s). 1 einstain is the energy of 1 mol photon and this unit is widely used in the photochemistry for easier calculation. However, this unit cannot be converted to joule as different wavelengths of radiation has different energy. Therefore, SI unit was applied in this design for engineering convenience.

Another important definition for photochemical process is called photonic efficiency, which is defined as equation 2-4.

$$\xi = \frac{reaction\ rate}{photon\ flux} \tag{2-4}$$

It was reported that the photonic efficiency in batch process is about 0.0086-0.0042 (Jamali et al., 2013), while that in the microflow reactor is up to 0.66 (Su et al., 2015). This improvement results from the small channels which represents the short light path receiving photons evenly (as shown in Figure 2.12).

(b) Reliable Scale-up for microreactors

For tubular reactor, the volume can be increased by increasing the diameter or the length of the channels so that the resident time can be determined accurately and precisely. This also means that every starting molecule can receive sufficient photons equally. Another straightforward method to tubular reactor is the numbering-up method (Figure 2.13).

There are many successful examples for scaling-up by using the tubular reactor. For instance, Hsieh et al. (2018) use a Vapourtec UV-150 continuous flow reactor dramatically increases the productivity form 0.125mmol/16h, with yield of 91% to 0.5 mmol/20min with a higher yield of 94% (Figure 2.14a). The productivity in the tubular reactors was increased from dozens of grams per day (Figure 2.14b) (Blanco-Ania et al., 2016) to hundreds of grams per day (Figure 2.14c) (Abdiaj et al., 2019, Abdiaj et al., 2018) even more than a kilogram per day (Figure 2.14d) (Beaver et al., 2020). They proved that the tubular reactor was a reliable model to scale up.

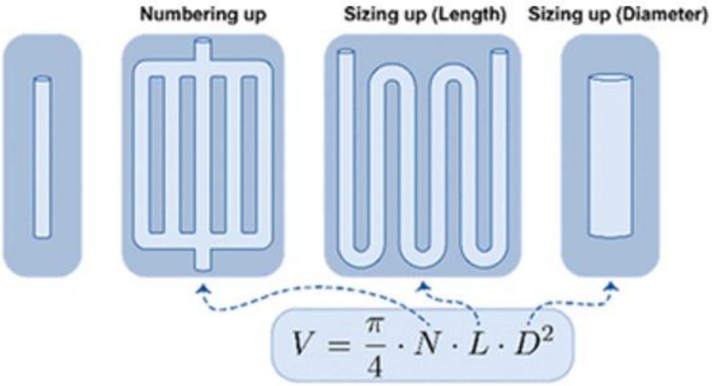

Figure 2.13 Scaling up method for tubular reactors. (Buglioni et al., 2022)

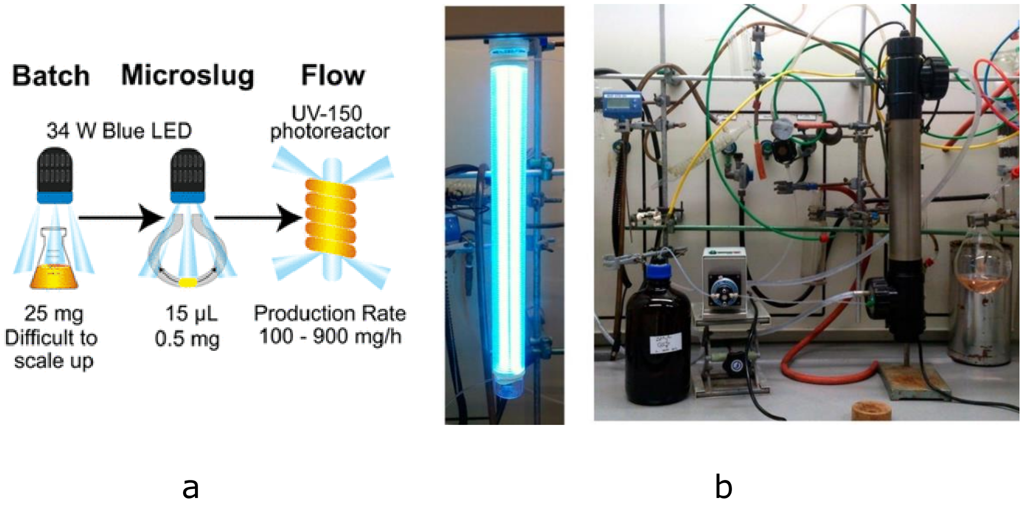

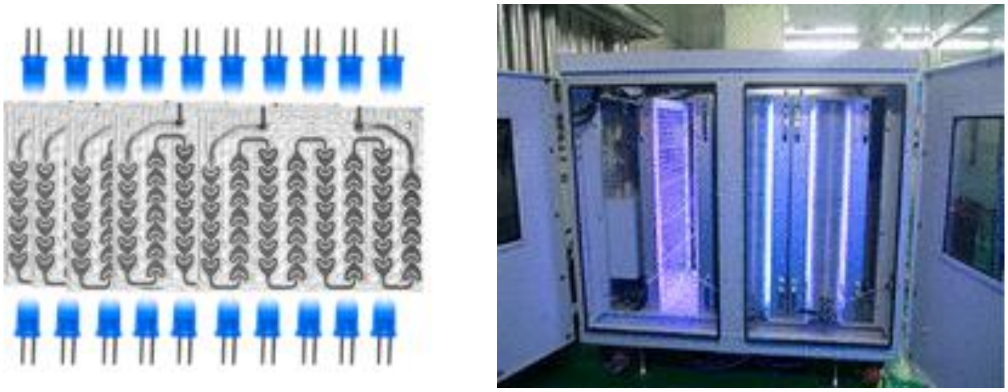

c

d

Figure 2.14 Tubular photoreactors for different scales from (a) mg to grams per day (Hsieh et al., 2018), (b) dozens of grams per day (Blanco-Ania et al., 2016), (c) hundreds of grams per day (Abdiaj et al., 2019), and (d) kilograms per day (Beaver et al., 2020).

(c) Continuous operation for microreactors

A tubular reactor is a one attractive technology to facilitate multistep reaction sequences. It allows several reactions and purification steps to be combined in one continuous streamlined flow process. Webb and Jamison (2010) reviewed the continuous multi-step processes in the organic synthesis and showed that continuous multi-step organic synthesis is a burgeoning and exciting area of research. In this review, there are many examples involving microflow reactors. Usutani et al. (2007) use series of microreactors to proceed the reactions of *o*-dibromobenzene (Figure 2.15). This process eliminates the formation of the benzyne by precise residence time control and precise temperature control, to which the highly instable intermediate is decompose very quickly at -78°C. Compared to the batch process which use lower temperature (-100°C) to reduce the decomposition and it still occurs during the transfer. These multistep processes in the microflow system reduce the requirement of operating temperature and the loss of the unstable intermediate and it was applied to many multistep processes (Herath et al., 2010, Bogdan et al., 2009, Ye et al., 2022).

(d) Fast Heat Exchange for microreactors

The tubular reactor can fasten heat exchange because it has high surface-to-volume ratio. For traditional tank reactor, direct enlargement reducing the surface-to-volume ratio for jacket type tank reactor, while the insert coil tubing for heat exchange in the tank reactor reduce the light absorption. By contrast, the design of tubular reactor has a high surface-to-volume ratio, which meet the requirement of irradiation in satisfying higher heat exchange rate.

The typical material for constructing tubular reactors includes PFA, FEP, glass and silicon (Frank, 2008). Among these, the thermal conductivity of silicon is about 149 ($Wm^{-1}K^{-1}$) where stainless steel is about 45 ($Wm^{-1}K^{-1}$). This higher the thermal conductivity, the faster heat transfer from the mixture to the coolant. These materials are commercially available, inexpensive, chemically stable, and provide optimal transparency properties; however, they have a low thermal conductivity (PFA: 0.195, FEP: 0.19–0.24, glass:1).

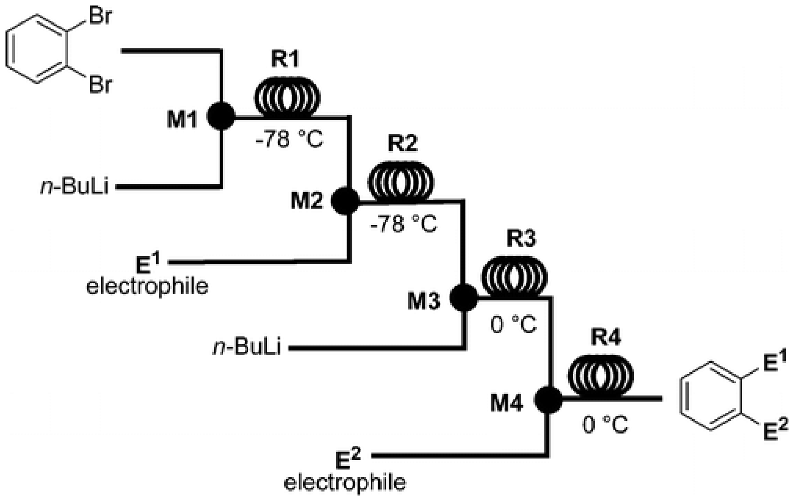

Figure 2.15 Indication of multistep synthesis of *o*-Bromophenyllithium using microflow reactor system. (Usutani et al., 2007)

(e) Fast Mixing for microreactors

As state before, the laminar flow in small channels of micro-scaled is observed. It reduced the path for molecules diffuse form the centre to the wall of the reactor, resulting in fast mixing to a uniform reactant across the reactor.

In addition, there are also some special designs of the microreactors. For example, capturing capsules (Quevedo et al., 2005), SIMM-V2 micro-mixer (Hu et al., 2010), combined nozzle type succeeding tangential mixing elements structure (Kockmann et al., 2011), and heart-shaped microreactors (Wu et al., 2015) (Figure 2.16). These structures strengthen the mixing, and then the molecules, which close to the light source receiving more photons, can mixed with unreacted reactant at the cross-section to reduce the over-irradiation. Meanwhile, the enhanced mixing improves the mass transport between phases, increasing the rate for diffusion-controlled process.

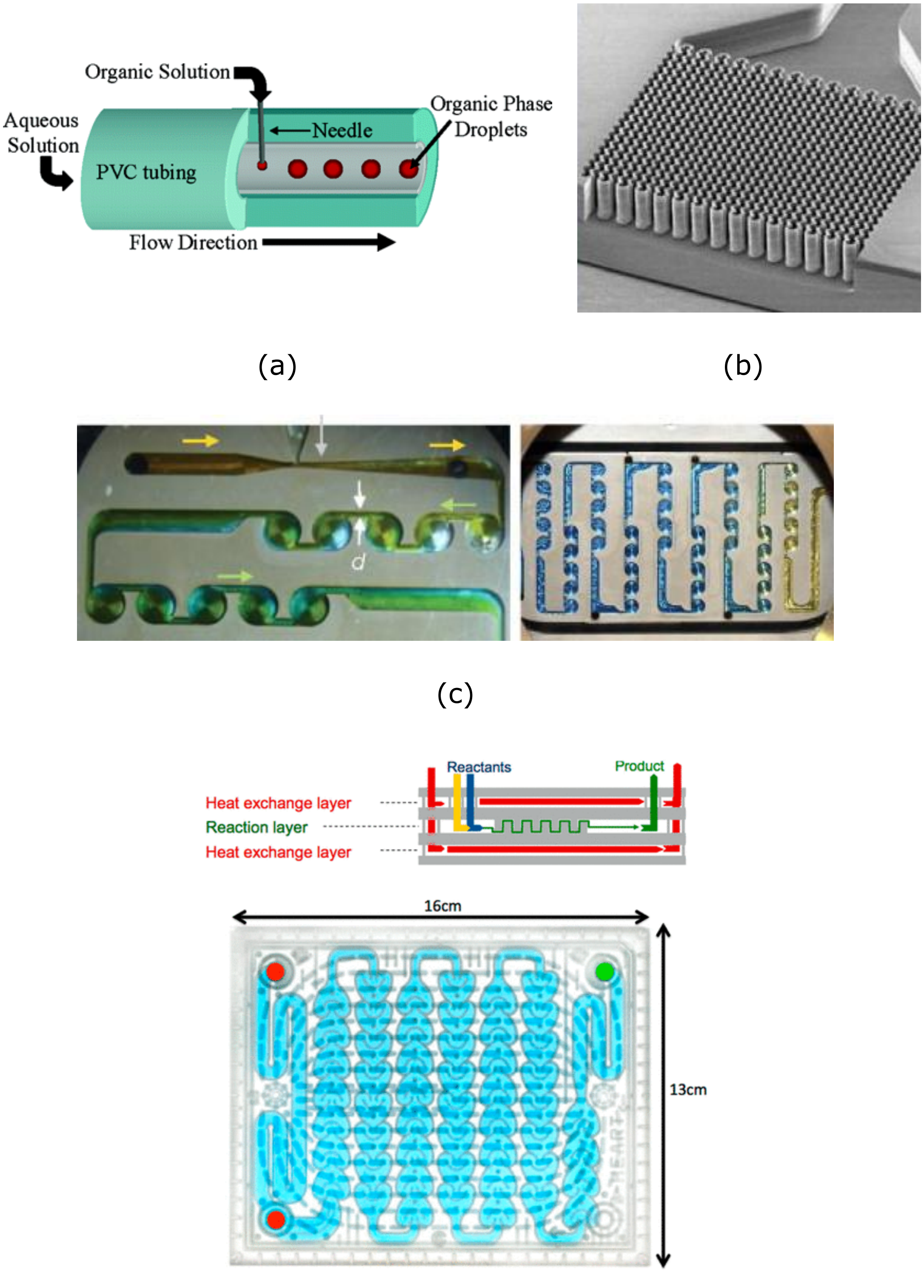

(a) (b)

(c)

(d)

Figure 2.16 special design of the microreactors, (a) capturing capsules (Quevedo et al., 2005), (b) SIMM-V2 micro-mixer (Hu et al., 2010), (c) combined nozzle type succeeding tangential mixing elements structure (Kockmann et al., 2011), and (d) heart-shaped microreactors (Wu et al., 2015)

(f) Safety operation and controllable for microreactors

The flow reactor can deal with a smaller amount of the chemicals which can reduce the safety risks associated with its handling. However, it is still a problem in the process in which particles are involved. The manipulation of solids, both as reagents and products, is still largely an unsolved problem and 'clogging' plagues much of the flow-based research being conducted (Horie et al., 2010, Sedelmeier et al., 2010, Poe et al., 2006).

(g) Limitation of the microreactor for solid-state reactions

The limitation comes from handling solid in the microreactors. It is possible that solids can be blocked in the small channel, which reduce the safety and continuity of the process. The radiation field is also affected by the particle distribution. A poor distribution of the particle with high extinction coefficient can form a shield preventing the incident radiation to internal particles. Therefore, it is essential to study the mechanism of the failure and the regular treatment.

The following section is going to introduce the mechanisms of the hydraulic failure caused by solid and strategies to deal with the solid in the reactor. However, it is still a problem especially for the enlargement of the solid-state photoreactions. For the pneumatic conveying system, there are problems with high specific power consumption, particle attrition and high wear. Meanwhile, a pile of the particles formed in the tube leads to a bad residence time control, which result in an unstable irradiation.

2.3.4 Failure Mechanisms in Solids Handling

The issue of solids handling in continuous reactor systems has gained considerable attention in recent years as the evolution from traditional batch processing to continuous flow continues to impact the fine chemicals industry. 86 different reactions were surveyed in 2005 (Roberge et al., 2005). This survey concluded that 50% of the reactions would benefit from a cost analysis by switching to a continuous process from batch and 63% of these benefited reactions involved the use of solids.

Three hydrodynamic mechanisms can lead to plugging in laminar flow: (1) constriction (Elimelech, 1998, Ramachandran and Fogler, 1998) (2) bridging (Ramachandran and Fogler, 1999, Hartman et al., 2010), and (3) the random detachment of deposits (Lee et al., 2008). In this section each of the three mechanisms was discussed from the perspective of flow and reaction within a continuous flow tubular reactor.

(a) Constriction

Insoluble by-product or recrystallization of the reactant may nucleate (1) on equipment surfaces, (2) in the bulk fluid and undergo deposition (Elimelech, 1998, Ramachandran and Fogler, 1998, Ryde et al., 1991) or (3) a combination of both leading to the constriction of flow paths within a continuous process. For example, the NaCl formed during the Pd-catalysed amination was found to reduce the cross-sectional diameter, even in a fluoropolymer capillary (Figure 2.17a) (Hartman et al., 2010, Noël et al., 2011, Kockmann et al., 2008). For scenarios (2) and (3), internal plugging is possible when the flow-induced deposition of particles onto a surface occurs. As an example, the deposition of stable colloidal particles appears near a flow constriction (Figure 2.17 b and c). The inertial impaction of a stable particle onto a surface can lead to deposition.

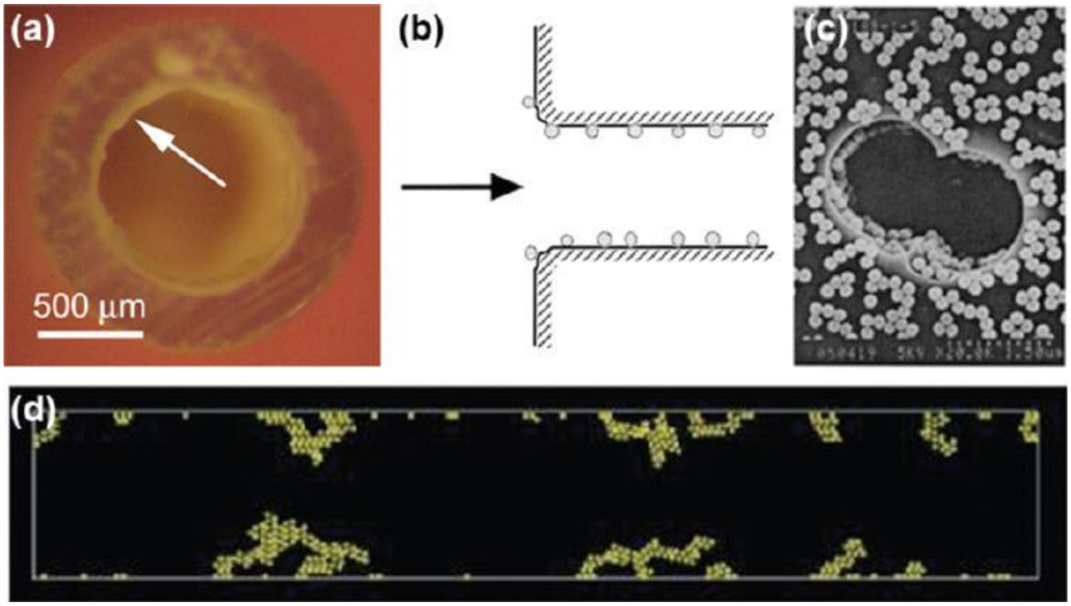

Figure 2.17 Examples of particle deposition and growth on surfaces exposed to laminar flow. (a) The generation of NaCl by-product formed during palladium-catalysed amination can lead to constriction (Hartman et al., 2010). (b) and (c) The flow-induced deposition of stable, colloidal particles near a constriction (Ramachandran and Fogler, 1999) (d) Dendrite formation or the retention of flowing particles on previously deposited particles, simulated for asphaltene deposition on microchannel walls (Boek et al., 2008).

Multilayer layer deposition eventually constricts the flow path via dendrite formation. Dendrite formation, or the retention of flowing particles on previously deposited particles, is illustrated in Figure 2.17d for asphaltene deposition on channel surfaces (Boek et al., 2008). The plugging by a gradual constriction of the flow path is possible in any of the aforementioned scenarios, especially during the continuous manufacturing of fine chemicals.

Identifying a potential constriction problem in a continuous reactor is made possible through the monitoring of the pressure losses. When the pressure drops changes with respect to the residence time (i.e., $\frac{d(\Delta P)}{d\tau} \neq constant$), there exists the potential for the process shutdown and the remediation of accumulated material. Overall, there remain numerous opportunities for the development of such models as synthetic methodologies often utilize different reaction components with varying thermodynamic and kinetic parameters.

The Stokes number, St, a quantity useful in characterizing the risk of internal plugging via inertial impaction, is the ratio of the viscous to the inertial forces acting on a flowing particle, which is defined as Equation 2-5 and it can be adapted to Equation 2-6. In other words, Stokes number is the characteristic time spent by a particle near the wall to the time required for the particle to be transported to the wall's surface.

$$St = \frac{\rho_p d_p^2}{18\mu_f} \cdot \frac{u_0}{l_0} \tag{2-5}$$

$$St = \frac{2}{9}\left(\frac{D}{d}\right)^2 \frac{\rho_p}{\rho_f} Re \tag{2-6}$$

where ρ_p and ρ_f are the particle and the fluid densities, respectively, D is the diameter of the pipe, d is the diameter of the particle dimeter, μ_f is the dynamic viscosity of the fluid, u_0 is the velocity away from the obstacles, and l_0 is the characteristic length of the obstacles. For $St < 1$, the convective forces acting on a stable particle (i.e., no attraction) in a microreactor are likely to prevent the particle itself from undergoing inertial impaction. For $St > 1$, inertial impaction is simply a matter of time (Ramachandran and Fogler, 1998).

(b) Bridging

Particles traveling along streamlines in laminar flow have the potential to contact one another when the flow path cross-section is reduced (Type I) or particle growth occurs (Type II). The potential is a serious consideration that must be made when designing reduced length scale flow reactors or the flow and reaction through a packed bed.

The bridging of particles across the flow path (i.e., hydrodynamic bridging) takes place by the simultaneous arrival of stable particles whose sizes are smaller than the cross-section, as illustrated in Figure 2.18 a and b for stable colloidal particles (0.25 $\mu\mathrm{m}$ latex spheres) entering a pore throat (Ramachandran and Fogler, 1999). At a sufficiently high flow velocity, hydrodynamic forces can overcome particle-to-particle and particle-to-surface repulsion, resulting in the formation of a stable bridge across the flow path entrance (Ramachandran and Fogler, 1999). The flow is thus constrained, and pressure losses occur. For example, fluid flow through a microfluidic device has been characterized by the design of constriction and expansion microchannels (Figure 2.18c). Here, latex microspheres (shaded red) bridge during the flow through parallel channels and within seconds (e.g., 38 s), constraining fluid flow and shown by the absence of any microspheres (shaded yellow).

Type I bridging in laminar flow reactors can be expected at unions, reducers, or virtually any other change in the cross-sectional geometry. Type II bridging has been shown to occur during the formation of NaCl in microchannels, generated from palladium-catalysed aminations, as seen in Figure 2.18d (Hartman et al., 2010, Kockmann et al., 2008). In either Type I or II, blockages are expected for aspect ratios (i.e., the ratio of the flow path length scale to the particle size, W/D) of less than 3−4, or 33% of the flow path cross-sectional dimension (Ramachandran and Fogler, 1999). This general rule only considers particle-to-particle or particle-to-wall repulsion. In practice, aspect ratios that do not result in hydrodynamic bridging are greater than 10 because attraction is common in fine chemical mixtures (Hartman et al., 2010). Hydrodynamic bridging can cause severe, unexpected plugging of continuous flow paths. Consequently, estimation of the aspect ratio for a laminar flow reactor is critically necessary to avoid a possible shutdown scenario.

The axial velocity of fluid flow is an important consideration when the aspect ratio is favourable for hydrodynamic bridging. For microreactor internal volumes from 100 μL to 100 mL and τ= 1 to 10 min, the average velocity can range from 0 to 10 cm/s. Ramachandran and Fogler (1999) showed that increasing the velocity from 0.012 to 0.6 cm/s results in an increase in the normalized pressure drop across the porous membrane of Figure 2.18b.

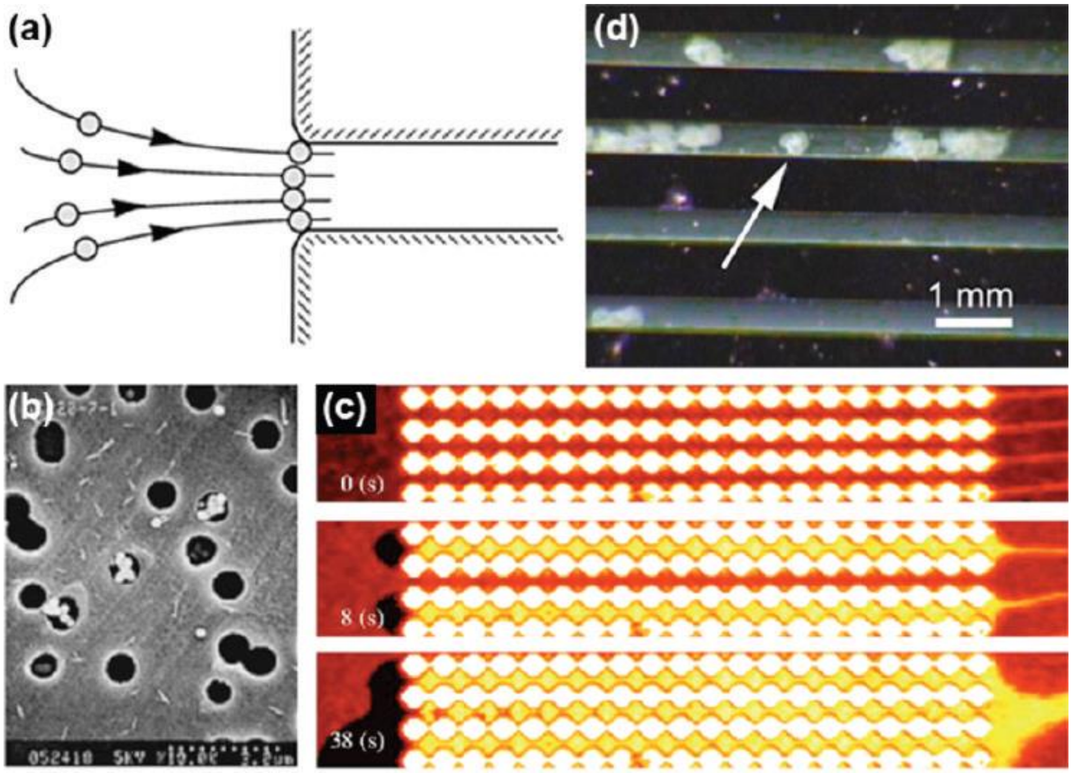

Figure 2.18 Mechanisms that result in the blockage of laminar flow paths. (a,b) Type I hydrodynamic bridging the bridging of stable colloids by the simultaneous arrival of particles at a constriction point (Ramachandran and Fogler, 1999) (c) The rapid hydrodynamic bridging of latex microspheres (shaded red) within parallel microfluidic channels, constraining fluid flow as shown by the absence of any microspheres (shaded yellow) (Wyss et al., 2006) (d)Type II hydrodynamic bridging the reactive bridging of NaCl crystals generated from palladium-catalysed transformations (Hartman et al., 2010)

(c) Random detachment by adhesive or cohesive failure

The formation of compounds on microreactor surfaces creates the potential for the random detachment, or breaking, of the material in the presence of shear stress. If the material becomes mobile, then there exists the opportunity for it to undergo bridging downstream within a reactor, transfer tubing, or other unit operations. The inherent random nature of such breaking makes it virtually impossible to forecast with a predictive model. Instead, understanding the detachment mechanism can yield insight on how to manage it. A wall deposit, either amorphous or crystalline, can fail under shear stress by adhesive or cohesive failure (Lee et al., 2008, Venkatesan et al., 2005), Adhesive failure is defined as the detachment of the material at the deposit-wall interface. Surface chemistry modification, manipulation of the roughness, and externally applied forces (e.g., acoustics) are strategies that limit the formation of any deposits that in turn undergo adhesive failure. Cohesive failure, however, is the breakage of the deposit within its own amorphous or crystalline network. Correlating the deposit thickness to a cohesive failure event is an important step in understanding how to manage it. Laboratory experiments that examine cohesive and adhesive failure are made possible using a parallel plate apparatus, which has been demonstrated for paraffin deposition on metal surfaces (Lee et al., 2008, Venkatesan et al., 2005). In fine chemical synthesis, salt by-product presents the opportunity for deposition and/or growth. One must therefore consider the potential for nucleation and growth in addition to the deposition of particles from the bulk fluid.

2.3.5 Solid Management Strategies of Flow Reactors

To reduce these failures caused by the solid during the convey, researchers developed many techniques to handle solids involved in the process. They can be classified into the following five strategies, including

- Hydrophilicity and hydrophobicity
- Fluid velocity and residence time
- Reactor design
- Immobilization
- Active technic

(a) Hydrophilicity and hydrophobicity

The use of water as a co-solvent is an attractive media to manage halide salt by-product (Naber and Buchwald, 2010, Shaughnessy, 2009). Organic synthetic chemistry has expanded the scope of palladium-catalysed cross-coupling reactions with the design of hydrophilic and water-soluble ligands. (Shaughnessy, 2009, Naber and Buchwald, 2010) Aqueous-based reactions, shown conceptually in Figure 8, can take place in the bulk water (Figure 2.19a), in a surfactant-supported micelle (Figure 2.19b), or at the interface of the immiscible aqueous− organic phases (Figure 2.19c) (Shaughnessy, 2009). The design of catalytic ligands for each of the three scenarios represent passive approaches to managing halide salt by-product. Therefore, the particle generation can be managed by dissolution into the co-solvent.

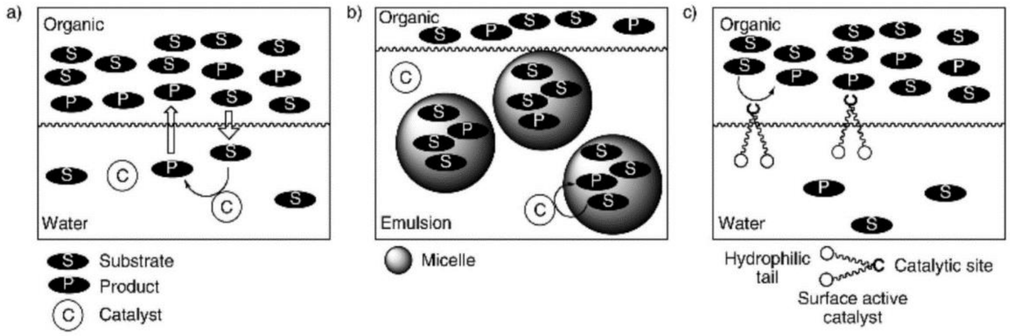

Figure 2.19 Aqueous-based transition metal-catalysed reactions can take place (a) in the bulk water, (b) in a surfactant supported micelle, or (c) at the interface of the immiscible aqueous−organic phases (Shaughnessy, 2009)

A few examples for this design are shown in the Figure 2.20. Microreactor clogging can be eliminated for polymerization reactions by dispersing an organic reaction mixture within an aqueous phase (Figure 2.20 a, b) (Quevedo et al., 2005). The same strategy was applied to make possible the indigo synthesis (123) Protein crystallization, an important problem in biologics and medicinal chemistry, has been carried out in droplets dispersed in a carrier fluid (see Figure 2.20c) (Chen et al., 2005). Polymer products can be dispersed, and hence contact with the microreactor walls eliminated using the same technique (see Figure 2.20d) (Marcati et al., 2010).

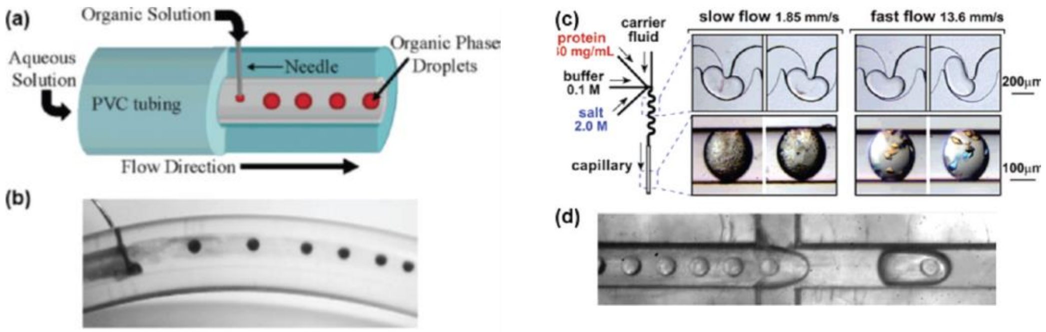

Figure 2.20 Microreactors with co-solvent of water to prevent clogging. (b) polymerization reactions by dispersing an organic reaction mixture within an aqueous phase(a)model indication of this injection reactor. (Quevedo et al., 2005) (c) protein crystallization using stable multiphase flows (Chen et al., 2005), (d) similar approach can be adopted for the dispersion of polymer products (Marcati et al., 2010)

Apart from the dealing with unnecessary generated particles, the solid from the input can be also treated by covering a hydrophobic cap. Baghbanzadeh et al. (2013) developed a continuous-flow synthesis of TiO_2 nanocrystals capped with oleic acid. Such nanoparticles could be efficiently dispersed in toluene, creating concentrated colloidal dispersions. Their photocatalytic activity was tested for the tandem addition cyclization reaction of N-methylmaleimide and *N,N*-dimethylaniline in continuous flow (Figure 2.21). A spiral of PFA capillary (ID 760 μm, 650 μL) was irradiated with UV-LEDs at 365 nm. A solution containing both substrates and the TiO_2 colloidal dispersion was recirculated in the microreactor. The desired tetrahydroquinoline was obtained in 91% yield after 5 h of reaction time.

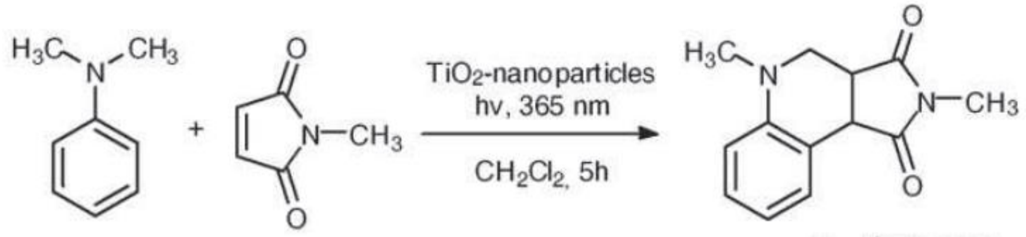

Figure 2.21 Tandem addition–cyclization reaction of N-methylmaleimide and *N,N*-dimethylaniline. (Baghbanzadeh et al., 2013)

This approach is limited by the solubility of the reactants. The good performance of TiO_2 is caused by not only it can be easily dispersed in toluene which is a widely used solvent in organic thesis, but also it is a commonly used photocatalyst. Therefore, this approach can be widely applied for heterogeneous catalysis. However, it is hard to be used for SCSC reactions as the solid structure can be destroyed by solvent and then undesired products appear.

(b) Fluid Velocity and Residence Time

As was shown for hydrodynamic bridging, there exists a critical velocity above which the flow-induced bridging of particles is possible at constriction points (Ramachandran and Fogler, 1999). The Stokes number also elucidates when the deposition of particles is expected, and in turn induce dendrite formation that has the potential for internal plugging. Shear stress at the fluid-wall interface is a critical parameter when the random detachment of deposits occurs, owing to sloughing. Towards this end, the mechanical abrasion of inert particles (or the precipitated material itself) with a reactor's walls has the potential to constrain wall-build ups. Monitoring the growth of particles in the bulk flow can also yield insights on whether enough time has been spent within a reactor to achieve critical aspect ratios. A passive approach to the elimination of particle deposition, constriction, and hydrodynamic bridging is therefore the manipulation of the flow rate, which can be estimated in advance using the guidelines prescribed above combined with laboratory experiments that support predictive models.

(c) Reactor Design

Thus far, the problem of solids handling in the context of continuous flow micro- and mesoscale reactors have been discussed. Continuous stirred-tank reactors (CSTRs) are excellent vessels of choice for solids forming reactions due to their mechanical agitation capabilities. Furthermore, extruders offering utility in the downstream formulation of pharmaceuticals may also substitute upstream reactors when high solids concentrations are necessary. The replacement of laminar flow microreactors with CSTRs or extruders is still challenging especially for large. For example, transfer tubing, peripheral equipment, and downstream unit operations still require a management plan for dealing with the solids formed in such upstream reactors. Moreover, convective heat transfer becomes more important, yet less efficient, than the conductive heat transfer that typically controls microreactors. Meanwhile, the attenuation of the photon transport also becomes a problem during the scale-up as stated before.

(d) Immobilization

Many important reactions in fine chemical and natural product syntheses can be carried out using solid-supported reagents, catalysts, or by-product scavengers (Baumann et al., 2009, Seeberger and Blume, 2007, Baumann et al., 2011). The immobilization of compounds on a polymer support, a useful strategy to eliminate the need for continuous recycling, creates the challenge of the flow and reaction in porous media. The advantage of the reduced-length scales in terms of the mixing and the mass transport are worth the effort to prepare and regenerate a packed bed. It should be noted that reproducible flow profiles through packed bed microreactors are challenging at low velocities due to hydrodynamic anomalies (Hickman et al., 2004). The work of others strengthens the importance of the packing technique(van Herk et al., 2009) and operation at higher flow rates (Hickman et al., 2004) to ensure uniform flow.

To overcome the issues associated with the handling of solid particles in microreactors, for examples clogging or fouling, a solution was found in the immobilization of the TiO_2 nanoparticles on the channel of the microreactor, or on a specific surface such as membranes or filters. Due to the use of microchannels, a large interfacial area can be kept, which compares to the surface area observed for the nanoparticles in suspension. Examples highlighting the use of immobilized TiO_2 include the synthesis of *L*-pipecolinic acid starting from *L*-Lysine (Figure 2.22). (Takei et al., 2005) The reaction was performed in a Pyrex glass chip (770 µm × 3.5 µm) containing a Pt/TiO2 thin film (0.2 wt% of Pt). Irradiation of UV light afforded 87% conversion of the starting material in less than 1 min, with a 70 times higher conversion rate compared to batch. However, no improvement was observed in the ee., which was similar to batch (around 50% in both cases).

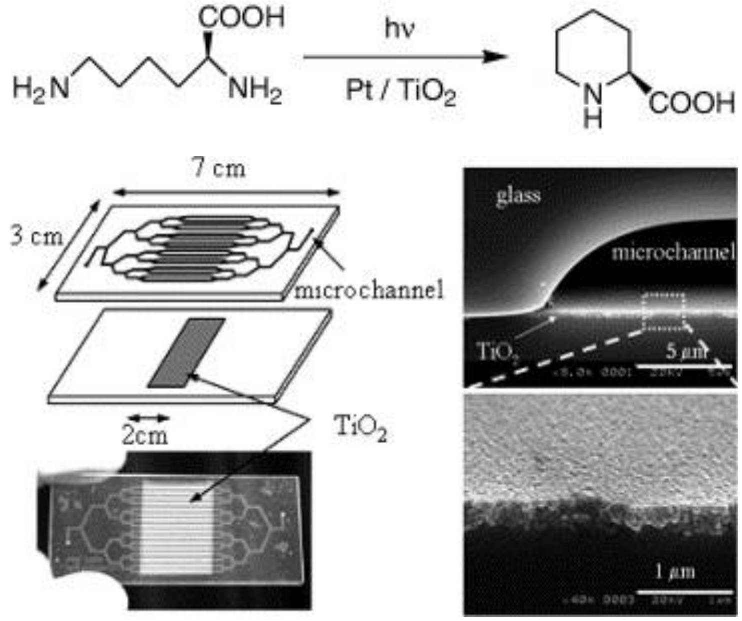

Figure 2.22 TiO_2 modified microchannel chip and cross-sectional SEM images of the channel where the synthesis of L-pipecolinic acid starting from L-Lysin. (Takei et al., 2005)

Hurtado et al. (2016) also developed a tubular multiphase flow reactor with TiO_2 film coated. They compared the performance of the immobile phase reactor, slurry tubular reactor, and traditional CSTR slurry reactor. The photonic efficiency was found to be two orders of magnitude higher in the coated capillary reactor than in the slurry stirred reactor, which are 6.99 and 0.3382 respectively. At meantime, selectivity shows dependence on the form of the catalyst, slurry or the stationary film.

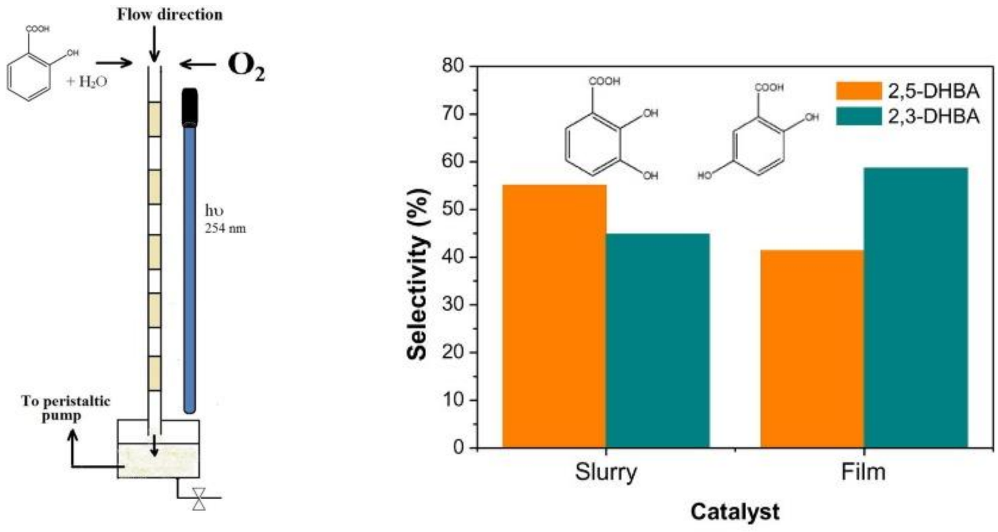

a b

Figure 2.23 coated tubular reactor (a) Capillary reactor system configuration (b) (Hurtado et al., 2016)

Immobilization is a good choice for heterogeneous photo-catalysis. It is obviously not suitable for the solid-state photochemistry as the immobile phase cannot be the input in a continuous process.

(e) Active Technic including Acoustic, Electrophoretic, Magnetic, Mechanical and Oscillatory Force

There are a number of active techniques that have demonstrated utility when passive strategies do not adequately control the flow-induced accumulation of solids (Figure 2.24). The density difference between a particle and the solvent where transport occurs generate a driving force for acoustic forces to displace particulate matter (Bengtsson and Laurell, 2004, Lilliehorn et al., 2005). Thus, the presence of an acoustic standing wave forces particles to position themselves at pressure nodes in laminar flow, which has been demonstrated for the separation of red blood cells from lipids under frequencies of MHz. (Nilsson et al., 2004, Petersson et al., 2007, Petersson et al., 2005)

For example, ultrasonic baths operating in the kilohertz regime have been applied to manage the formation of solids in flow chemistry, as can be seen in. Performing Pd-catalysed C−N bond-forming reactions in an ultrasonic bath prevents the clogging of fluoropolymer capillaries by NaCl formation (Hartman et al., 2010, Alonso et al., 2005, Noël et al., 2011). The working principle has recently been applied to engineer fluoropolymer microreactors sandwiched between a piezoceramic actuator, which delivers on-chip ultrasound to manage the NaCl formation.(Kuhn et al., 2011)

Polymer reaction products, the photodimerization of maleic anhydride has been shown in the Figure 2.24a, also constrain fluid flow in microreactors. In this case, the clogging was mitigated by injecting the reactants into a capillary, coiled around a light source and positioned within an ultrasonic bath (Horie et al., 2010). The use of acoustic forces to manage solids has tremendous potential, as industrial scale ultrasonic baths are available in addition to the engineering of integrated reactor systems.

Mechanical agitation, another active technique, can also ensure the continuous flow of solids. One observes in Figure 2.24b a flow reactor cell (The Coflore ACR) with integrated unbound agitators. The mechanical vibration of the flow cell enabled the production of *N*-iodomorpholinium hydroiodide salt without blockage (Browne et al., 2011). These reservoirs shown emulate a cascade of millilitre-scale CSTRs, and it can be adapted to a photoreactor where the light transfer from the sight glass.

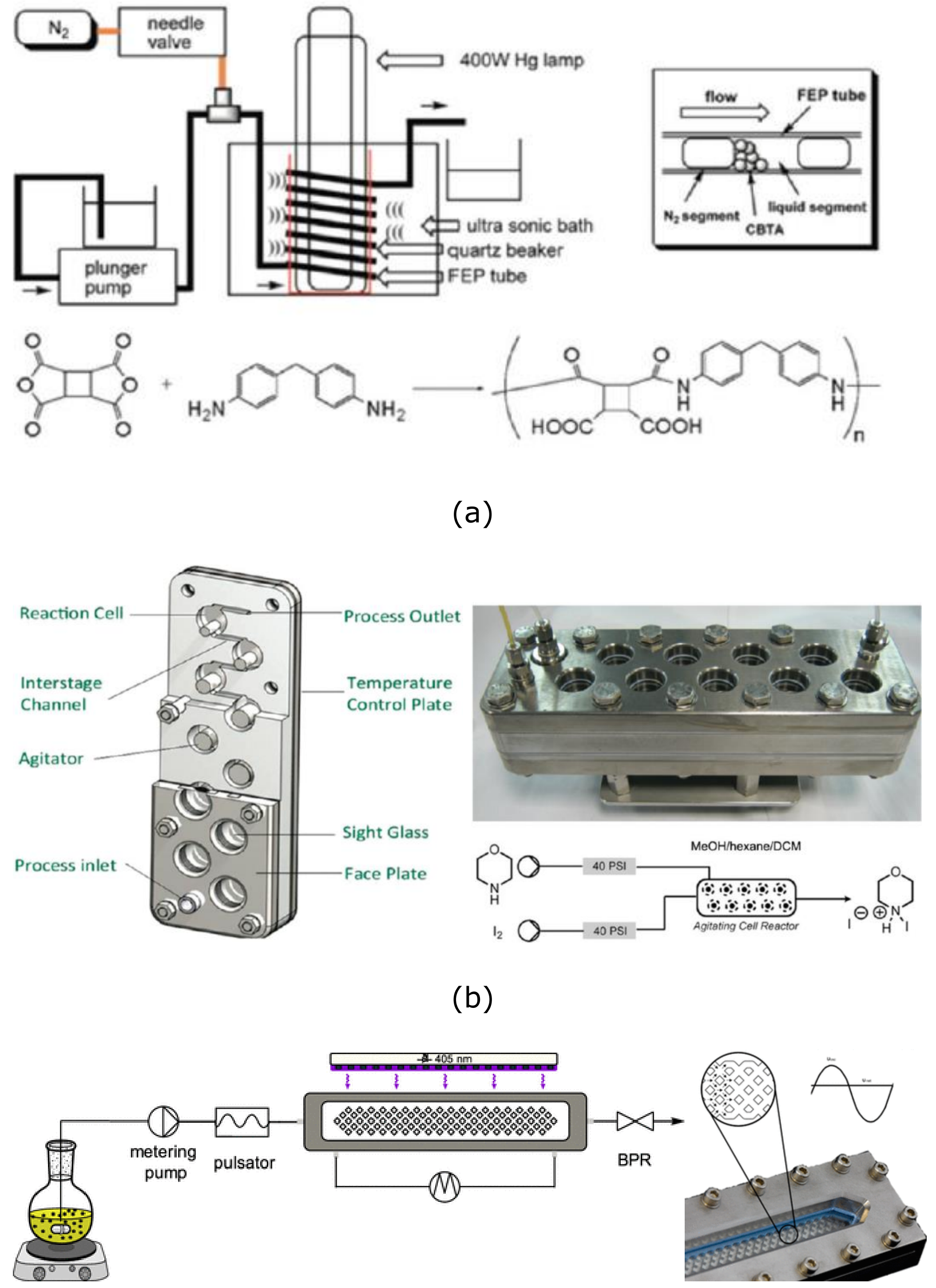

(a)

(b)

(c)

Figure 2.24 Active strategies to handle solid. (a) sonification assistant photoreactor (Horie et al., 2010) (b) Agitating reactor (Browne et al., 2011) (c) Oscillatory reactor (Debrouwer et al., 2020)

More recently the oscillatory flow reactor was applied to the photochemistry (Debrouwer et al., 2020, Rosso et al., 2020). As shown in the Figure 2.24c, HANU HX 15 Reactor was applied to a Ir/Ni heterogeneous photoredox reaction (Debrouwer et al., 2020). This is not a typical tubular reactor but the design of it follows the plug flow reactor model. This reactor is operated with a pulsator, a device that superimposes a periodic oscillation on the net flow generated by a metering pump (Mongeon et al., 2016, Doyle et al., 2020). This oscillatory flow regime and repeated split-and-recombine flow path ensure adequate mixing regardless of the net flow rate. A stable suspension of the photocatalyst can be maintained, and clogging was not found during the 10 cycles (4.5 hours) (Rosso et al., 2020).

In addition to mechanical agitation and oscillatory, electrophoretic (Dürr et al., 2003, Kralj et al., 2006), and magnetic (Gijs, 2004, Rodríguez-Villarreal et al., 2011, Pamme, 2007) particle manipulation, although primarily used in nonreactive microfluidic systems, have the potential for solid control. A challenge towards this end is the application of such techniques to concentrated suspensions where inter-particle and wall interactions are frequent. One must also consider the magnitude of such forces, similar to acoustics, relative to the viscous and the inertial forces (i.e., St number). The delivery of sufficient forces to the flow path may be reduced upon scaling up. Such challenges are promised to overcome by the innovation of novel, unexplored reactor designs.

2.4 Swirl Flow

2.4.1 Introduction to Swirl Flow

Swirl flow in a pipe can be defined as a combination of vortex and axial motions, with helical streamlines (Baker and Sayre, 1974). Swirl flow, which contains a tangential velocity component, is always accompanied by an increase in velocity fluctuations (Fokeer, 2006, Algifri et al., 1988). This tangential component was applied in the previous cases for mixing such as Taylor reactor (Figure 2.9 and Figure 2.11) and the special designed micro-flow reactors (Figure 2.16), which shows that the swirl flow has the potential to solve the mentioned problems such as uneven irradiation caused by fouling and sedimentation in the tubular reactor. Compared to the mentioned strategies to manage solids in the reactor, the swirl pipe does not require additional equipment to offer the mechanical force. Meanwhile, it can be easily inserted into the pipeline to generate the swirl.

Generally, three methods can be employed in order to generate swirl flows in a pipe (Gupta et al., 1984), including rotating cylinder (Figure 2.25a) where the flow pass, fixed blades (vanes) with different angles and shape (Figure 2.25b) and tangential inlet (Figure 2.25c). Downstream of the swirl generator, the previously non-swirling flow is imparted a swirl velocity component known as tangential velocity component.

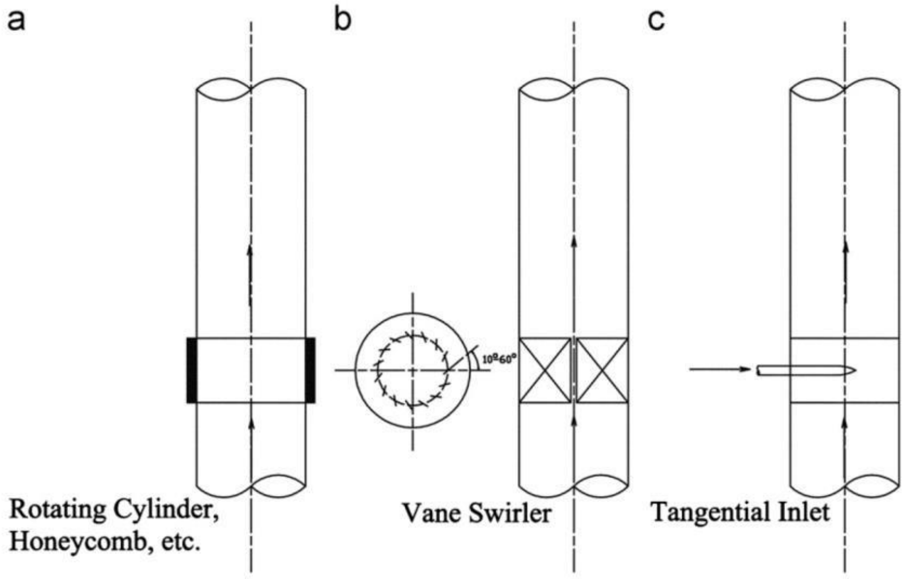

Figure 2.25 Three method to generate swirling flows (Gupta et al., 1984)

It is suggested that the radial distribution of tangential velocities is associated with the swirl generation methods (Kitoh, 1991). Steenbergen and Voskamp (1998) defined three different swirl types according to the radial distribution of tangential velocities as:

- Concentrated Vortex (CV)-rotation concentrated near the pipe centre.
- Solid Body (SB)-almost uniform rotation
- Wall Jet (WJ)-angular momentum concentrated near the wall

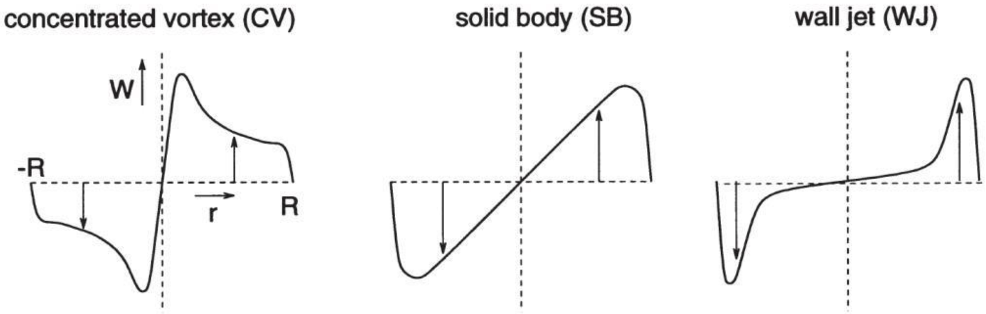

Figure 2.26 Three different swirl types

In addition to the three methods, swirl induction pipes with non-circular cross-sections have been investigated in order to induce swirl into flow passing through them. These included pipes with spiral ribs or fins located within the pipe (Robinson, 1923, Yuille, 1928, Edmund, 1967, Charles et al., 1971, Schriek et al., 1974), pipes with rifles installed inside (Howard, 1941) and tubes with spiral grooves (Frank, 1941). Those swirl induction pipes were applied respectively to mitigate the problem of subsiding and the deposit of particles in the pipe, improve tubular heat exchangers, reduce pipe wear, increase particle conveying efficiency, and save energy. It should be noted that the insertions of ribs, fins, or twisted tape mounted inside the pipe will be subject to direct impact from the particles in the flow giving rise to damage and wear of the pipe.

2.4.2 The Development of Swirl Pipe

At the University of Nottingham, research into helically formed swirl induction pipes can be traced back to 1993, when Jones suggested a new idea to the problem of settling particles in which a pipe section could be given a helical profile to promote suspension of particles at relatively low velocities (Jones, 1997). The idea was investigated later by Raylor (1998) , Ganeshalingam (2002), Tonkin (2005), Ariyaratne (2005) and Fokeer (2006). It should be mentioned that the swirl induction pipes investigated avoid the use of insertions of ribs, fins or vanes inside the pipes. Rather it is the helically shaped geometry of the swirl pipe that force the fluid passing through it to rotate within itself and direct to downstream. A chronological review of their work is given below.

Raylor's experimental investigation was based upon a swirl pipe found in marine boilers which are used to improve heat exchanger efficiency (Raylor, 1998). The pipe, as shown in Figure 2.3.3, has the trade name '*Swirly-Flo* pipe'. Raylor's investigation aimed at pipe induced swirling flow to reduce wear and produce better distribution throughout a bend.

Raylor used commercial CFD software Fluent to examine various pipe shapes and flow fields in swirl inducing pipe. He suggested that when the pitch to diameter ratio in a geodesic pipe decreased, the swirl produced increased with increasing pressure loss. Raylor designed an experimental rig and used water and plastic beads mixture to test the simulation results. He concluded that Swirly-Flo pipe produces an increase in pressure drop across its length compared to a standard pipe. Swirly-Flo pipe induced swirling flow before a bend produced less pressure drop across the bend than non-swirling flow for water and water/plastic beads mixture. Swirling particles before the bend ensured amore even distribution of particles throughout the bend which has the potential to remove the characteristic wear zone.

The pitch to diameter ratio (P:D) is an important parameter defining the character of the twisted swirl induction pipe. Pitch is defined as the axial distance travelled by the rib as it rotates through 360 degrees (Singh and Charles, 1976). This was the basis Raylor used for definition of the pitch of the swirl induction pipe.

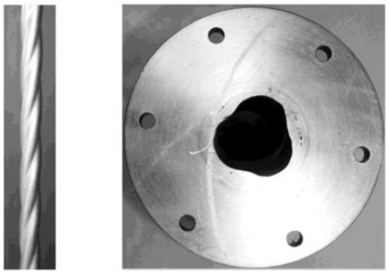

Figure 2.27 *Swirly-Flo* pipe used by Raylor and Ganeshalingham (Ganeshalingam, 2002)

Ganeshalingham continued Raylor's investigation on the '*Swirly-Flo* pipe' and validated the CFD code used with results from Particle Image Velocimetry (PIV), Electrical Resistance Tomography (ERT) and pressure measurements (Ganeshalingam, 2002). Ganeshalingham simulated the radial distribution of tangential velocities downstream of the *Swirly-Flo* pipe and it was shown to fit with 'Wall Jet' swirl type classified by Steenbergen and Voskamp (1998) according to radial distribution of tangential velocity field. An exponential decay of the swirl downstream of a swirl pipe was implied from CFD and the decay was reported to be faster at higher Reynolds number.

Ganeshalingham also carried out further optimisation of the swirl inducing pipe using CFD and continued experimental work on solid -liquid mixture flows. Ganeshalingham tested various cross sections (triangular, square, pentagonal, hexagonal and 2,3,4,5 and 6 lobed cross sections) of pipe and concluded that the 4 lobed cross section was most effective at swirl generation over the others. Ganeshalingham recommended a P:D ratio of 8 and 400mm of length as optimal for the 4-lobed pipe. This optimal swirl inducing pipe is shown in Figure 2.28 with its configuration being as follows, and this 4 lobed near optimal design was further optimized and tested experimentally later by Ariyaratne (2005).

- The swirl pipe has a 4-lobed cross-section.
- The 4-lobed cross-section extends helically around and along the pipe.
- Axial distance travelled by each lobe as it rotates through 360° is 400mm.
- The equivalent diameter of the swirl pipe is 50mm.
- Its pitch to diameter ratio is 8.

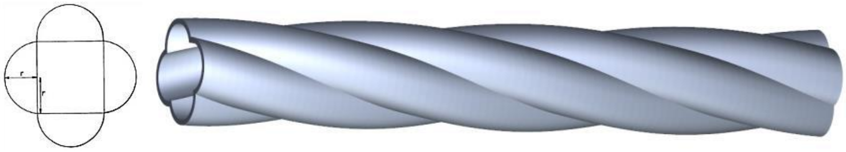

Figure 2.28 Optimal Swirl inducing pipe, 400mm length, P:D=8 (Ganeshalingam, 2002).

Tonkin investigated the application of the4-lobed near-optimal swirl inducing pipe to various pipe configurations, when pumping a range of fluid and fluid/particle mixtures (Tonkin, 2005). Tonkin studied experimentally the effect of the 4-lobednear-optimal swirl inducing pipe on coal-water, sand-water and magnetite-water slurries of various particle sizes. The results showed that swirl induction produced greater benefit for denser slurries and higher concentrations. In addition, the swirl induced into slurries containing larger and denser particles was found to decay more rapidly.

Tonkin also investigated application of swirl inducing pipe to non-Newtonian (shear thinning) carrier liquids. A time independent fluid, CMC (carboxymethyl cellulose) was chosen to avoid changes in rheology as pumping time increased. PIV was used to measure the axial and tangential velocity of swirling flows downstream of the 4-lobed near-optimal swirl pipe with water and CMC. It was concluded that a significant tangential velocity was generated when pumping water in the turbulent regime, however, when the fluid viscosity was increased, leading to laminar flow, no significant tangential velocity was detected.

Ariyaratne further optimized the 4-lobed near-optimal swirl inducing pipe by designing a transition pipe for use as an entry and exit duct with the swirl inducing pipe, providing a gradual transition from circular to lobed cross-section and vice versa (Ariyaratne, 2005). The optimisation was carried out by using single-phase simulation employing CFD. The CFD model was validated by experimental measurements of pressure loss. Transition pipes either before or after the swirl inducing pipe were found to reduce entry and exit pressure losses by providing a gradual transition circular to lobed cross-section. They also increased induced swirl and reduced swirl decay. Ariyaratne concluded that a β type transition with transition multiplier n=0.5 was optimum for both the entry and exit transition from several geometries tested. The configuration of transition pipe, as shown in Figure 2.29, is:

- The transition pipe's cross-section changes from a circular toa4-lobed shape gradually.
- The areas of the cross-sections are constant and equal to that of the swirl pipe.
- The length of the transition pipe is 100mm, and each lobe rotates by 90°.
- Its pitch to diameter ratio is 8.

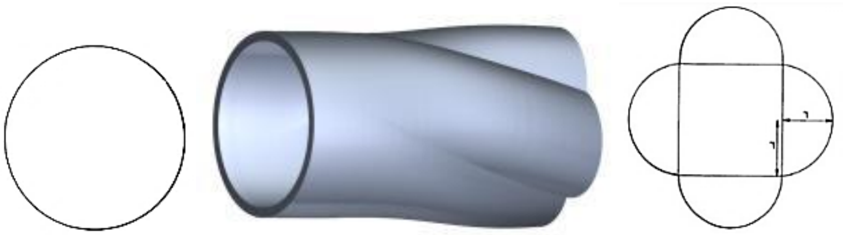

(a)

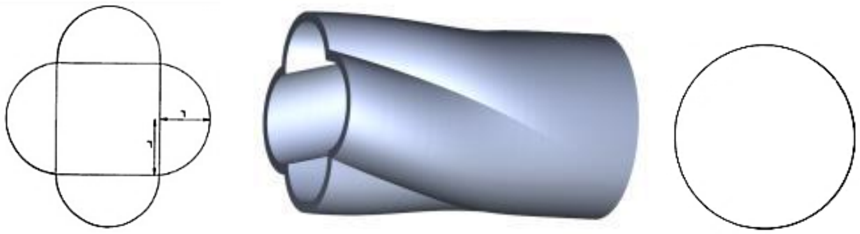

(b)

Figure 2.29 Transition pipes prior/after swirl inducing pipe: (a) Entry transition pipe (b) Exit transition pipe. (Ariyaratne, 2005)

Ariyaratne suggested that the entry and exit transition should be an integral part of the swirl inducing pipe as it results in an efficient swirl induction which reduces energy costs from high pressure losses that otherwise occur due to sudden changes in flow geometry. Ariyaratne carried out settling slurry experiments, which showed that swirl induction resulted in better particle distribution and prevented solids dragging along the bottom of the pipe. This implies reduction in localised erosion and provides an opportunity to operate at lower flow velocities without blockage.

Fokeer investigated the application of geometrically induced swirl by a three lobed helix pipe on a lean phase of particulate suspension in air along a horizontal pipe section (Fokeer, 2006). The research employed high speed photography, Particle Image Velocity (PIV), Laser Doppler Anemometry, and Computational Fluid Dynamics to obtain the characteristic of the air flow behaviour. It was concluded that the swirl pipe imparts a wall jet type swirl to both an air-only flow and a lean pneumatic flow with velocity and momentum shifts from axial to tangential closer to the wall. The swirl was found to decay proportionally with the distance downstream of the swirl pipe and inversely to the flow’s Reynolds number. Additional pressure loss caused by the swirl pipe was found to be proportional to the Reynolds number of the flow and increased further with an addition of particles to the swirling flow.

Based on the suggestion of Ariyaratne (2005), a 400mm length swirl inducing pipe together with 100mm length entry and exit transition pipes at both ends as an integral pipe should be optimized in swirl induction. This optimised swirl pipe has a total length of 600mm (100mm+400mm+100mm). In this study, a further optimised swirl pipe that is comprised of a 100mm length entry transition pipe, half of the 400mm length swirl inducing pipe, and a 100mm length exit transition pipe is proposed. This further optimized swirl pipe has a total length of 400mm (100mm + 200mm + 100mm) which is 200mm shorter than Ariyaratne suggested. This further optimized 4-lobed swirl pipe is found numerically in Li’s work to be more cost-effective in swirl induction and is therefore used in this study (Li, 2016).

Li showed the potential of a swirl flow on improving cleaning in place efficiency (Li, 2016). From the simulation results, swirl pipe would improve the cleaning efficiency of Clean-In-Place procedures in closed processing systems by locally increasing wall shear stress downstream of it without increasing the overall velocity of cleaning fluids, thus potentially reducing time and cost for the company. The beneficial effects of swirl pipe are more obvious in flows with higher velocities where both the effective distance and wall shear stress increase are larger than lower velocities. The swirl pipe is particularly useful in the areas that are most difficult to clean in the pipe system, as the cleaning time is dependent on the degree of cleanliness of such areas. As for the cleaning of straight pipes, proper positioning of the swirl pipe in the pipe system are needed to maintain the increased wall shear stress required for sufficient cleaning.

The development of the swirl pipe illustrate that it can handle the deposition of particles very well, and it can control the construction of the pipe. Moreover, the re-distribution of the particles caused by the swirl can also form a thin film ideally, similarly to the thin film reactor mentioned in 2.3.1(c) .

2.4.3 Terms to Characterize the Swirl Flow

(a) Swirl number S (swirl intensity)

The swirl number S, also termed swirl intensity, is commonly used to quantify the strength of the swirl. It defined as the ratio of the angular momentum flux to the axial momentum flux, multiplied by the hydraulic radius (Li and Tomita, 1994, Steenbergen and Voskamp, 1998, Rocklage-Marliani et al., 2003)

$$S = \frac{\int_0^R u_a u_t r^2 dr}{R \int_0^R u_a^2 r dr} \tag{2-7}$$

where S is the swirl intensity, u_a and u_t are axial velocity and tangential velocity respectively, R is the radius of the pipe, and the r is the local radius of the calculating point.

(b) Swirl decay

Swirl will decay downstream of the swirl pipe which is caused by transport of angular momentum to the pipe wall. To determine the distance over which swirl will prevail in the pipe, several researchers had studied the swirl decay law (Halsey, 1987, Li and Tomita, 1994, Reader-Harris, 1994, Steenbergen and Voskamp, 1998). There was no unanimous agreement on the decay rates in swirling flow, in most reference, the observed swirl intensity fit with exponential decay functions (Equation 2-8), where S_0 is the initial swirl intensity, α is the empirical coefficient, f' is the Moody friction factor, L is the distance along the downstream pipe, and D is the diameter of the pipe.

$$S = S_0 e^{-\alpha f' \frac{L}{D}} \tag{2-8}$$

2.5 Fluid Simulation

Computational fluid dynamics (CFD) is a branch of fluid mechanics, combining of modern fluid mechanics, numerical mathematics, and computer science. It can analyse systems involving fluid flow, heat transfer and associated phenomena by computational simulation. This technic is quite powerful and able to solve many research or industrial problems. It is much cheaper than conducting a real experiment, and it offers an approach to change the model quickly to adapt and to optimize the design. Meanwhile, the analysis from the CFD can be much deeper than the experimental testing, especially for experiments whose important results are hard to obtain.

2.5.1 Turbulence Model

Swirl flow is turbulent and caused considerable degree of anisotropy in stress and dissipation tensor leading to a highly anisotropic eddy viscosity (Kitoh, 1991). Turbulent flows are characterized by fluctuations in velocity and pressure in both space and time (Bhaskaran and Collins, 2003). In modelling swirling flow, turbulence is an important factor (Fluent, 2018).

Many researchers have tried to numerically investigate swirl flow through Reynolds-averaged Navier–Stokes (RANS) approach where an instantaneous quantity is decomposed into its time-averaged and fluctuating quantities (Versteeg and Malalasekera, 2007). There are many RANS models divided by the number of equations. The most used models are two equation models (k-ε

turbulence model and k-ω turbulence model) and seven equations model (Reynolds Stress Model, RSM), which are compatible with two phase simulation (explained in the section 2.5.2 multiphase simulation). For the RSM, the computing cost is very high especially coupled with multiphase models, radiation models, and reactions (Shah et al., 2023, Raeesh et al., 2022). Therefore, the two equations turbulence models were reviewed, and it was found that the accuracy of them were acceptable.

(a) k-ε models

k - ε model includes standard k - ε turbulence model and its variations (Renormalization Group (RNG) k-ε model and realizable k - ε model). The standard k - ε model solves two transport equations, one for the turbulent kinetic energy k, and one for the rate of its dissipation ε. These are then used to calculate the turbulent viscosity, μ_t, to close the Reynolds averaged Navier-Stokes equations (Fluent, 2018).

Launder and Spalding (1974) investigated the applicability of the k-ε model for simulating swirling flow along a twisted tape to impart a swirling motion to a fluid to increase the surface transfer coefficient. The agreement was not very good. The main reason might be that the turbulent viscosity became strongly anisotropic in the complex strain field of the flow. Kobayashi and Yoda (1987) also argued that both k-ε model and its modifications with higher order terms in the Reynolds stress equation are not capable of predicting the axial and tangential velocity profiles in swirl flow because its eddy viscosity components are anisotropic. Similar conclusion was also reported by Nejad et al. (1989) that k-ε model is not successful in solving the velocity field in swirling flows.

Speziale et al. (2000) partially agreed with the above conclusion that traditional two-equation models such as the standard k-ε model with conventional near-wall treatments could not predict two critical effects (the rotationally dependent axial mean velocity and the presence of mean swirl velocity relative to the rotating pipe) associated with turbulent flow in an axially rotating pipe. However, the author argued that at high Reynolds numbers, the traditional two-equation models could be used to predict this only with the implementation of a more sophisticated near-wall treatment that predicts a non-zero Reynolds shear stress $\tau_{r\theta}$. But this was not applicable to cases with low Reynolds number.

Bali (1998) proved that the k-ε turbulent model can successfully predict the weak swirl flow. In his study, the pneumatic swirling flow investigated has a small tangential velocity imparted to the air flow in the pipe using a propeller type swirl generator. The experimental and numerical axial and tangential velocity distributions along the pipe were found to be in good agreement. The standard k-ε model was also used by Ganeshalingam (2002) to investigate swirling flow induced by Swirly-Flo pipes which is a weakly swirling flow. Ganeshalingham stated that RNG k-ε model, Realizable k - ε model and RSM should show substantial improvements in results compared to standard k-ε where the flow features include streamline curvature and rotation, but the accuracy gained is not considerable when the extra time consumed is considered. Similar conclusion was drawn by Ariyaratne (2005) and Fokeer (2006). Ariyaratne (2005) decided to use standard k-ε model for initial work due to the large number of cases to be studied in optimizing the swirl pipe. Fokeer (2006) also decided to first use the k-ε model to obtain a baseline solution, which can then be improved by employing the Reynolds Stress Model.

(b) k-ω models

Apart from the k-ε model, the k-ω model (Wilcox, 2006) is the other commonly used two-equation model. The k-ω model uses the turbulence frequency of the large eddies, ω, to model the turbulence (Rodi, 1993). Initially, this model was proposed by Kolmogorov (1941b), (Kolmogorov, 1941a) and then by Saffman and Whitham (1970) Since then, several modifications and improvements have been made to the model, ultimately resulting in the k-ω model (Wilcox, 2006, Wilcox, 2008). This version models turbulent flow near walls more accurately than the k-εmodel, so it is preferred when correctly simulating the boundary layer is important. The k-ω model has also proven to be more accurate for a wide range of turbulent flows but is sensitive to inflow conditions. The k-ω SST (Menter, 1993) model is a modified model that does not display this sensitivity and is applicable to a broader range of turbulent flows than the standard version.

One advantage of the k-ω shear stress transport (SST) model is that it automatically switches between the k-ω and k-ε models, taking advantage of both and providing accurate results for both near-wall and free-stream regions of the flow (Wilcox, 2006). The k-ω SST model is particularly suitable for external aerodynamics cases. The model is also less sensitive to inflow conditions than the standard k-ω model, allowing it to be applicable to a broader range of turbulent flows (Shah et al., 2023).

SST $k–\omega$ turbulence model has high accuracy in some flow simulations in recent years. Tepe et al. (2020) use this model to accurately predict the average and local Nusselt number distributions on the surface, as it uses theoretical method to treat near wall region. Choi et al. (2021) use the SST k-ω model to simulate the drag and lift coefficients of solar panels under hurricane wind speeds, as it blends the functions of the k-ε and the k-ω models to predict the turbulence flow more precisely. This model was also applied by Amini and Memari (2021) to evaluate the buildings under hurricane wind loads. Their results showed that SST k-ω model has better fitting than the RNG k-ε model. Carloni et al. (2022) analysed five different eddy-viscosity turbulence models to predicting the flow through an elbow pipe. They find that the closure of the SST k-ω is the most appropriate turbulence model to predict the velocity profile in regions of significant streamline curvature, whereas the realizable k - ε is more appropriate in the presence of the high adverse pressure gradient. Zeiny et al. (2023) compared and validate different k-ε and k-ω models to evaluate the thermo-aeraulic behaviour. The results showed that the k-ω models had better performance than k-ε models in predicting the temperature and heat flux caused by the forced convection.

This model also was coupled with different multiphase approaches to simulate the solid flow. Kaushal et al. (2012) investigated the flow characteristics of a sand-water mixture through a pipeline Using the k-ω shear stress transfer (SST) model. They noticed that this model is the best turbulence model for high solid concentrations.

Chou and Liao (2023) uses the SST k-ω turbulence model coupled with Euler-Euler approach to simulate the pneumatic conveying of the dilute phase in a diffuser. Their result shows a good prediction of the fluid velocity as well as the particle velocity. Wan et al. (2023) use the SST k-ω turbulence model coupled with discrete element method (to describe the solid behaviour) to simulate the gas-solid swirling flow characteristics of coaxial jets. From their work, this turbulence model performed well in the swirling flow (Kalt et al., 2002) as well as that in cyclone (Yang et al., 2020). These literature shows that the SST k-ω turbulence model is a good option to simulate the swirling flow.

2.5.2 Multiphase Simulation

In difference of the phase in nature, a phase can be defined as an identifiable class of material in multiphase flow simulation, which has a particular inertial response to and interaction with the flow and the potential field in which it is immersed.

Depending on how to treat the secondary phase, there are two approaches, Euler-Euler and Euler-Lagrange (Chen et al., 2019, Sedrez et al., 2019). In some paper, they have also been called Eulerian-Eulerian and Eulerian-Lagrangian approaches (Mori and Sakai, 2021, Shi et al., 2019a). This name is sometimes confused with a multiphase model derived via Euler-Euler approach called Eulerian (Kaushal et al., 2012), which some researchers also called Eulerian-Eulerian. To make it clear in this thesis, the approach is called Euler-Euler and Euler-Lagrange, while the model is called Eulerian.

The difference between these two models is on how to deal with the secondary phase. The Euler-Lagrange (Lagrangian approach)

approach deals with individual particles and determine the trajectory of each particles separately, while the Euler-Euler approach regard the secondary phase as a partial volume occupied in the limited volume cell and calculates the overall diffusion and convections (Saidi et al., 2014).

The Euler-Lagrange approach observe the motion of the particles and it is good at tracking the particles to visualize the flow. When a large number of the particles injected into the system, it becomes computationally expensive, especially for concentrated particles where a large number of interactions are required to be determined.

As mentioned, Wan et al. (2023) use the SST k-ω turbulence model coupled with discrete element method to simulate swirling flow. This discrete element method (DEM) is a Lagrangian approach to describe the motion. It has been demonstrated as a powerful numerical tool since Cundall and Strack introduced it to study the behaviour of granular material (Cundall and Strack, 1979). Apart from its application on the materials, it can be also used for multiphase flow. Tsuji et al. (1993) use this model to explore the fluidized bed combined with CFD. The CFD is presented to model the fluid flow, while the DEM is to track the motion of solid particles dragged by the fluid. Due to the capacity of the soft-sphere collision model to truly resolve the particle-particle/wall interaction process (Chu et al., 2022, Ismail et al., 2022), the CFD-DEM method has been adopted to simulate the gas-particle swirling flow. Chu et al. (2011) developed the CFD-DEM method to investigate the impact of solid loading ratio on the gas and solid flow structures in a lab-scale cyclone separator. They found that the gas pressure drops versus time showed a first increasing and then decreasing trend when the particles are loaded. The number of turns travelled by the solids in the cyclone, the pressure drop and the tangential velocity of gas phase decrease with increasing solid loading ratio, whereas the width of solid strands increases with enlarging solid loading ratio. Zhou et al. (2018) utilized the CFD-DEM model to optimize the swirling flow generator in the pneumatic conveying technology, obtaining that the three-lobed pipe produces the highest swirl number and fastest decay. Li and Tomita (2000) simulated the large particle behaviour in the swirling flow via the CFD-DEM approach with a discussion of the influence of the swirl number on the flow stability. The results revealed that the particles are most dispersed in the central region of the pipe when the swirl number is in the range of 0.3 to 0.4. The axial velocity and acceleration of the particle slightly decrease with increasing the swirl number. It is generally acknowledged that the addition of particles to the swirling flow can enhance the dispersion efficiency of the particles.

On the contrary, Euler-Euler approach is more suitable to describe dynamic of a field. However, there are approximations resulting in inaccuracy limited by the grid. This approach treated the secondary phases can as a part of volume in a limited element, noted by a volume fraction, named as Euler-Euler approach. Volume of Fraction (VOF), Mixture, and Eulerian are the commonly used models which are derived from this approach.

VOF models simulate stratified flows, free-surface flows, filling, slug flow, and the motion of large bubbles in a liquid. It still has been modified recently to simulate this type of flow (Li et al., 2023, Garoosi et al., 2022, Akhlaghi et al., 2019). For solid involved flow, the Mixture model as well as the Eulerian model were applicable.

Mixture models was applied to simulate the nano-fluid in convective heat transfer (Karimi et al., 2019, Mojarrad et al., 2013, Nuim Labib et al., 2013) as well as in the mass transport (Nandwani et al., 2019). Although this method reduces the calculation time, it overestimates the radial profile of temperature while the Euler-Lagrange approach has the better fitting to the experimental results (Mojarrad et al., 2013). The mixture model was combined with the SST k-ω turbulence model to simulate nano-fluid in a tube with twisted tape (Karimi et al., 2019). Based on their setting and the result shows that the simulation is underestimated the overall heat transfer coefficient under different Reynolds numbers from the experimental result from (Kim et al., 2009), especially for higher Reynolds numbers. This underestimation may be caused by the complex of the geometry (twisted tape) as well where the imperfect quality of the mesh.

Eulerian model consists of more complex equations, which has higher accuracy with a higher computational consumption. This model was also applied to simulate nano-fluid on heat transfer (Monfared et al., 2022). It was validated by comparing the simulation result from the Eulerian model with the experimental results from Zhang et al. (2012) which has a good fitting. It also has a good performance in swirls both in solid-liquid (Shi et al., 2021) and solid-gas system (Liu et al., 2020). They have a good fitting with the experimental result. It was also applied to simulate the multiphase flow in the reactors (Guo et al., 2021), as well as photoreactors (Wang et al., 2019, Ranganathan et al., 2022). Cloete et al. (2012) compared the Eulerian model and the Lagrangian method and the results showed that there are minor differences caused by the formation of delta–shocks. They are all shows that this multiphase model is applicable for the design of this swirl-induced photoreactor for solid state.

2.6 Radiation Simulation

2.6.1 Radiation Transfer Phenomena

Radiative transfer is the physical phenomenon of energy transfer in the form of electromagnetic radiation. UV, visible light, and infrared radiation are types of the electromagnetic radiation with the wavelength from 200 – 400 nm (UV), 400 – 760 nm (visible), and 760-1000 nm, which are commonly used in photochemistry (Bowen and Lind, 1946).

The propagation of radiation through a medium is affected by absorption, emission, and scattering processes as shown in the Figure 2.30. These phenomena are described by a conservation equation, which called radiative transfer equation (RTE) (Chandrasekhar, 1960).

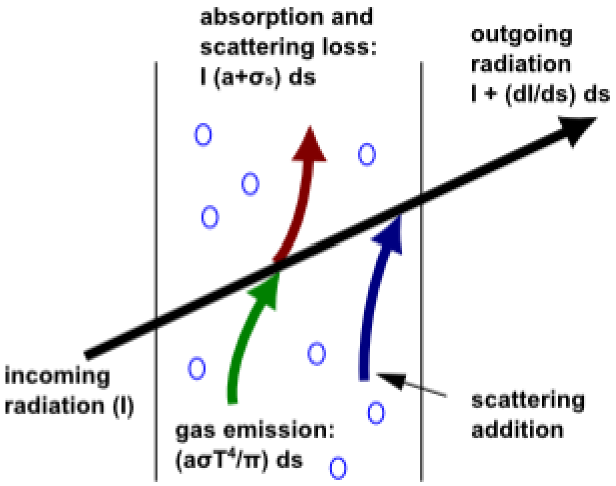

Figure 2.30 Instruction of phenomenon during the radiation transfer process.

Equations of radiative transfer have application in a wide variety of subjects including optics, astrophysics, atmospheric science, and remote sensing (Hubeny and Mihalas, 2014).

$$\frac{dI(\boldsymbol{r},\boldsymbol{s})}{ds}+(a+\sigma_s)I_\lambda(s,\Omega)=an^2\frac{\sigma T^4}{\pi}+\frac{\sigma_s}{4\pi}\int_0^{4\pi}I_v(\boldsymbol{r},\boldsymbol{s})\Phi(\boldsymbol{s}\cdot\boldsymbol{s}')d\Omega \tag{2-9}$$

where there σ_s and α is the scattering coefficient and the absorption coefficient with unit m^{-1}, respectively. $\Phi(\boldsymbol{s}\cdot\boldsymbol{s}')$ is the phase function. The value of it is 1 for isotropic scattering. $\boldsymbol{s}$ is the direction vector, $\boldsymbol{s}'$ is the scattering direction vector, and $\boldsymbol{r}$ is the position vector. n is the refractive index, σ is Stefan-Boltzmann constant, Ω' is the solid angle, T is the local temperature. These phenomena are reviewed in the following sections and the detailed introduction of the RTE in the section 3.4.

2.6.2 Light Absorption

Absorption of the light is how electrons takes the energy from the photons and then transform the electromagnetic energy into internal energy (Kume, 2017). According to the Grotthuss–Draper law, the occurrence of photochemical reactions must be based on the absorption of the light by the reactant. This light transport phenomenon takes an important role in photochemistry that photoexcitation is the first step in a photochemical process where the molecules is elevated to a higher energy state (Calvert and Pitts, 1966).

Absorption spectroscopy is techniques that measure the absorption of the radiation. They are divided into different type according to wavelength of the radiation (Kumar, 2016). The continuous spectrum of electromagnetic wave in the required region of wavelength is used as the light source to irradiate the sample and then determine the relative intensity of light absorption of material molecules. Through the analysis of molecular absorption spectrum, the component in the mixture can be qualitative analysis, and can be based on the Beer-Lambert law (Equation 2-1) of quantitative analysis. The absorbance (A) and transmittance (T) cannot be applied to the RTE directly, the absorption coefficient can be calculated by inverse of the Beer-Lambert law.

$$a = \frac{A}{cl} = -\frac{\log_{10} T}{cl} \tag{2-10}$$

Because of the importance of the light absorption, it becomes a criterium to assess the performance of the photochemical reactor. The local volumetric rate of energy absorption (LVREA) or the local volumetric rate of photon absorption (LVRPA) are used to assess the performance of the reactor in the simulation (Wang et al., 2019).

2.6.3 Scattering

Scattering is another important feature of the light transport. It describes a physical process that moving particles or radiation of some form such as the light and sound are forced to deviate from a straight trajectory by localized non-uniformities in the medium (Ishimaru, 1999). Originally, the term was confined to light scattering (Newton, 1672). As more ray like phenomena were discovered, light scattering and acoustic scattering are connected by Tyndall (1874). Near the end of the 19th century, the scattering of X-rays (1896) was observed and discussed. With the discovery of subatomic particles (Rutherford, 1911) and the development of quantum theory in the 20th century, the sense of this term became broader as it be applied to scattering phenomena in many field and the math framework.

Scattering can be classified into elastic scattering and Inelastic scattering. Inelastic scatterings, such as Brillouin scattering, Raman scattering, inelastic X-ray scattering and Compton scattering, are widely used in analytical chemistry and quantum chemistry (Kargar and Balandin, 2021, Duke and Owens, 1982, Xie et al., 2010, Rostron et al., 2016). It implies that the internal states of the particles change after the collision occurs. In elastic scattering, by contrast, the only change is the moving direction. According to the particle size, the scattering is divided Reyleigh, Mie, and geometrical scattering. This is divided by the size parameter x (Equation 2-11).

$$x = \frac{2\pi r}{\lambda} \tag{2-11}$$

where r is the particle radius and λ is the wavelength of the incident radiation (Mätzler, 2002). Figure 2.31 shows the scattering distribution of the light at different particle sizes and the Table 2-2 presents the criteria and corresponding scattering figure.

Table 2-2 Classification of the Scattering.

Value of size parameter	Scattering type	Corresponding figure
$x \ll 1$	Reyleigh scattering	Figure 2.31A
$x \cong 1$	Mie scattering	Figure 2.31B & C
$x \gg 1$	Geometrical scattering	Figure 2.31D

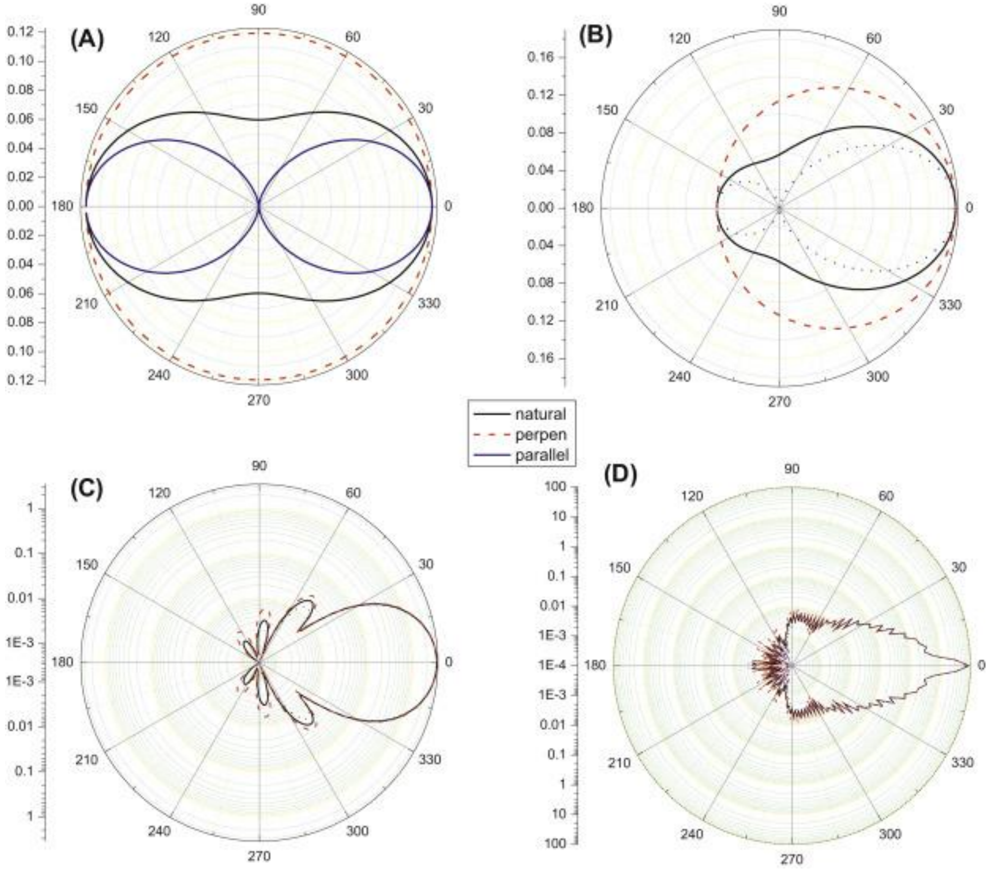

Figure 2.31 Mie simulation of the angular dependence of the intensities for parallel (dot) and perpendicular (dash) orientations of a linearly polarized source beam relative to the polarization orientation of detection and the intensities of total nature light (solid) in medium as prostate cytoplasm at 780 nm scattered by particles with different diameters of (A) 11 nm (x=0.088), (B) 200 nm (x=1.6), (C) 1.2 μm (x=9.7), and (D) 9.3 μm (x=75), respectively. (Pu et al., 2019)

This figure shows the angular dependence of Mie simulation of the particles with different particle parameter. At the Rayleigh scattering range, the Figure 2.31A presents an isotropy scattering intensity when the diameter of the particles much small than the wavelength of the incident radiation. With the increasing size parameter, light prefers more and more forward scattering, which are indicated by the Figure 2.31B-D, and the mode transfer from Mie scattering to geometrical scattering. It shows that the scattering is not always isotropic and then the directionality should be also taken consideration when determining the radiation field.

Therefore, phase functions are applied to estimate the scattering field.

A phase function describes the scattering properties of the materials in terms of the angular distribution of scattered light for a specific wavelength (Zhang, 2019). Its dimensionality and complexity result in the computationally expensive solution of the RTE (Han et al., 2017). The phase function requires several important parameters, including scattering coefficient σ_s and parameters to estimate the scattering distribution such as asymmetry factor, anisotropy factor, weighting factor.

$$\int_0^{4\pi} \Phi(\boldsymbol{s} \cdot \boldsymbol{s}')\, d\Omega = 1 \tag{2-12}$$

Where Φ is the phase function, $\boldsymbol{s}$ is the direction vector of radiation, and $\boldsymbol{s}'$ is the direction vector of scattering.

A general phase function can be simplified using an isotropic scattering first term and a modification term. This is called Linear-Anisotropic phase function (Ozisik, 1973, Mengüç and Iyer, 1988) as Equation 2-13.

$$\Phi_{la}(\theta, \theta') = 1 + \mathrm{g}\mu_0 \tag{2-13}$$

where g is a dimensionless asymmetry factor that can vary between $\pm\infty$. If $\mathrm{g} = 0$ it corresponds to the isotropic phase function. This phase function is rotationally symmetric around the direction of travel of the incident intensity. Integration over all solid angles shows that this phase function is normalized for any value of g.

Apart from the linear-anisotropic phase function A benchmark choice is the Henyey-Greenstein phase function (Henyey and Greenstein, 1941)

$$\Phi_{HG}(\boldsymbol{s}\cdot\boldsymbol{s}') = \frac{1-g_0^2}{4\pi(1+g_0^2-2g_0\cdot\boldsymbol{s}\cdot\boldsymbol{s}')^{3/2}}$$

2-14

where the parameter $g \in (-1, 1)$ is the anisotropy factor of the scattering medium. For isotropic scattering, $g = 0$; for forward scattering, $g > 0$; and for backward scattering, $g < 0$. This phase function can be expanded in the infinite series of (unassociated) Legendre polynomials (Equation 2-15) where L is the L^{th} order moment condition of this function.

$$\Phi_{HG}(\boldsymbol{s}\cdot\boldsymbol{s}') = \sum_{L=0}^{\infty}\frac{2L+1}{4\pi}\Phi_L(\boldsymbol{s}\cdot\boldsymbol{s}')$$

2-15

For reduction of the numerical errors of the moment conditions in the radiation transfer, the expansion form of the phase function (Equation 2-15) is preferred to the original form (Equation 2-14) thanks to the orthogonality of the polynomials. The finite Legendre model approximates the phase function by a finite series of Legendre polynomials up to the order, N.(Morel, 1979, Liu et al., 2002)

$$\Phi_{FL}^{n}(\boldsymbol{s}\cdot\boldsymbol{s}') = \sum_{n=0}^{N}\frac{2n+1}{4\pi}\Phi_L(\boldsymbol{s}\cdot\boldsymbol{s}')$$

2-16

Based on the Henyey-Greenstein phase function, the delta-Eddington (dE) phase function was proposed by Joseph et al. (1976)

$$\Phi_{dE}(\boldsymbol{s}\cdot\boldsymbol{s}') = \frac{1}{4\pi}[(1-f)(1+3g'\boldsymbol{s}\cdot\boldsymbol{s}')+2f\delta(1-\boldsymbol{s}\cdot\boldsymbol{s}')]$$

2-17

where g' is the asymmetry factor of the truncated phase function to modulate the weakly anisotropic scattering, f is the weighting fraction (or factor) of the forward scattering, and δ is the Dirac delta function. This function decomposes the highly forward-peaked phase function into a purely forward-peaked component, expressed by the delta function and other component.

Morel developed the Galerkin quadrature (GQ) method which expands the phase function in a finite series of Legendre polynomials. (Morel, 1989, Morel et al., 2017) In addition, this method conducts the weighting procedure to the highly forward-peaked phase function by requiring that the residual of the scattering integral is orthogonal to the weighting space, spanned by the spherical harmonics. Because the spherical harmonics are eigenfunctions of the analytic scattering operator, the GQ method can construct accurately the discrete scattering integral corresponding to the interpolation of the discrete light intensities with a given quadrature set by the spherical harmonics.

Although the GQ method was shown a higher accuracy than the dE method (Fujii et al., 2020), it has not verified in practical cases. By contrast, the dE method was widely used in simulate the light transport through the cloud with dust and ice particles, and it was verified, which is similar to the particle distribution in this reactor (Shi et al., 2019b, Ren et al., 2020, Cong et al., 2007, Leighton, 1980).Detailed equations of the phase functions are discussed in the section 3.4.5.

2.6.4 Estimation of Important Parameters

To determine the radiation field, many parameters are required to be calculated. Apart from the mentioned absorption coefficient a, the scattering coefficient σ_s and the asymmetry factor g are still required to determine the scattering distribution as well as emission. The following section reviews thermotical calculation and the empirical estimation method.

(a) Rayleigh scattering coefficient.

Rayleigh (1899) scattering is attributed to Lord Rayleigh who was the first to explain the colour of the sky in exploring molecular scattering. The scattering coefficient for Rayleigh scatterers is proportional to the inverse fourth power of the radiation wavelength as shown as Equation 2-18.(Siegel, 2001, Elim et al., 2009)

$$\sigma_s = \frac{2\pi^5}{3}\frac{d^6}{\lambda^4}\left(\frac{n^2-1}{n^2+2}\right)^2 \tag{2-18}$$

For incident unpolarized radiation, the phase function of this Rayleigh scattering is independent of the azimuthal angle ϕ as Equation 2-19. The phase function for Rayleigh scattering was already shown graphically in Figure 2.31a. For Rayleigh scattering, the scattered energy is symmetric with respect to the direction of the incident radiation and has both the forward and backward scattering lobes.

$$\Phi_R(\boldsymbol{s}\cdot\boldsymbol{s}') = \frac{3}{4}(1+\cos^2\theta) \tag{2-19}$$

(b) Mie calculation

The exact scattering solution for dielectric spherical particle with a homogenous optical property and smooth surface under a plane wave was derived by Mie (1908), which is a complete mathematical–physical theory of the scattering of electromagnetic wave. It embraces all possible ratios of the particle radius to wavelength, differing from the Rayleigh scattering (Eremin, 2005).

This solution is derived from the solution of the vector Helmholtz equation, the magnetic harmonics, and electric harmonics. As a result, a group of coefficients, a_n, b_n, c_n, and d_n are obtained to determine the scattering. Among this, the a_n and b_n are applied for the scattered far field of scattering and Mie scattering efficiency whereas c_n, and d_n determine the internal field (Mätzler, 2002). By use these coefficients, the scattering cross section can be determined as well as the asymmetry parameter g_{Mie}, which indicates the average cosine of the scattering angle θ. (Detailed introduction of the functions is in the Chapter 3, section 3.4.6 p159)

(c) Empirical method

Apart from the theoretical method, there are empirical equations to estimate the absorption and scattering coefficients, especially for porous titanium catalysts. Romero et al. (1997) reported that the absorption coefficient and the scattering coefficient of UV light can be related to the catalyst loading, as Equation 2-20 and Equation 2-21.

$$a = 0.2758W_{cat} \tag{2-20}$$

$$\sigma_s = 3.598W_{cat} \tag{2-21}$$

These equations have been widely used in the simulation of the radiation intensity in slurry reactors (Boyjoo et al., 2014, Pareek et al., 2003, Brandi et al., 2000, Pareek, 2005) and the inlet loading was applied to determine the optical properties of the mixture. Wang et al. (2019) take the local concentration of particles as the catalyst loading. It shows that the inlet catalyst loading overestimates the absorption and the scattering coefficients, resulting less incident radiation. This result also implies the better performance of the tubular reactor with swirl induced.

2.6.5 Methods to Solve the Radiation Transfer Equation (RTE)

As the properties of materials are determined, the RTE can be solved via numerical method. Generally, there are three widely used strategies, series expansion and moment methods, discrete ordinates methods, and Monte Carlo methods.(Siegel, 2001)

Many methods for the solution of the differential form of the RTE are based on moment methods, and these are often combined with using a series expansion of the intensity along a particular direction vector. The series is then truncated to some small number of terms, resulting in final formulations that are mathematically and numerically tractable. There are several models compared in this section including the diffusion model, spherical harmonics expansion (P-N) model, simplified PN (SP-N) model, and M-N model where the N is the order of the expansion. Among various derivatives, the first order of general Spherical Harmonics (P-N) method denoted by P-1 model and the Rosseland diffusion model are included by the ANSYS fluent 19.0. (Siegel, 2001, Fluent, 2018)

The discrete ordinates method (DO method) is an extension of a more restricted method (the two-flux method) proposed independently by Schuster (1905) and Schwarzschild (1906) for studying radiative transfer in stellar atmospheres. Chandrasekhar extended the two-flux method in 1960 to include anisotropic scattering and made it applicable to multidimensional geometries.(Chandrasekhar, 2013) When the solid angle about a location is divided into more than the two hemispheres, each assumed with uniform intensities as used in the two-flux method, the method is known as the discrete ordinates, S_N, or multi-flux method (Chandrasekhar, 2013, Lathrop, 1966). This is also provided by the ANSYS fluent 19.0.(Fluent, 2018)

Monte Carlo method utilizes a statistical simulation to determine the behaviour of a system. It was applied to radiative transfer among surfaces without an intervening participating medium. (Siegel, 2001) By extending the Monte Carlo model developed for surface-to-surface exchange, it is possible to account for a large variety of effects in radiating media. This can be done without resorting to the simplifying assumptions that are often necessary for numerical solutions based on direct numerical solution of the RTE. However, this approach did not be provided by the fluent to simulate the radiation transfer. Therefore, this approach was not reviewed in this thesis and the other two methods was firstly reviewed and applied to the simulation.

González et al. (2008) compared DO and M1 methods for a particular 2D square domain with and without coupling to other heat transfer modes. Further, Planck mean opacity was modelled for an inhomogeneous aluminium plasma. They show that for this particular case, both methods were quite accurate near the source in comparison with an analytical solution for the radiative equilibrium problem.

Tencer and Howell (2013) and Tencer (2014) have carried out comparisons of predictions from DO, P-N, and SP-N over a wide range of scattering albedo and optical thickness for various 1- and

2D geometries. The general conclusions are that the DO methods are highly accurate in problems without ray-effect-inducing discontinuities. For problems with such features, the large number of ordinate directions required to mitigate the ray-effect oscillations may make the discrete ordinates methods computationally intractable. Relative errors were determined solution is used as the benchmark for comparison (Tencer, 2013). These results show that the DO method is reliable and applicable to determine the radiation field in the photoreactor (Pareek et al., 2008, Wang et al., 2019).

2.7 Reaction Simulation

2.7.1 Mechanisms of Solid-state photochemistry

The kinetics of the traditional chemistry is regarded as flowing the rate law and increasing the temperature is the most used method to accelerate reactions. The temperature leads to a significant reduction on the reaction time. The relationship between the temperature and the kinetics is described by the Arrhenius equation (equation 2-23), where k is rate constant, T is temperature, and E_a is activation energy.

$$r = k[M]^a[N]^b \tag{2-22}$$

$$k = A \cdot e^{-\frac{E_a}{RT}} \tag{2-23}$$

Another overcoming the energy barrier for the reaction is the participation of photons. Photons can be selectively absorbed by the starting material. The kinetics of the photon-driven reaction are observed that strongly dependent on the photon flux or the incident radiation intensity, which is described as

$$k = \alpha \cdot I^{\beta} \tag{2-24}$$

Where α is a constant depending on the reaction type, and the β is a constant depending on photon flux (Bloh, 2019).

As shown in the Figure 2.32, for low light intensities (<around 200−250 W·m^{-2}), β is equal to 1.0 indicating a linear increase of the reaction rate constant with increasing light intensities (region A). This value can be larger than 1 depending on the reaction mechanism. For the two-photon excitation, the value of β is 2 (Benedict and Coppens, 2009).

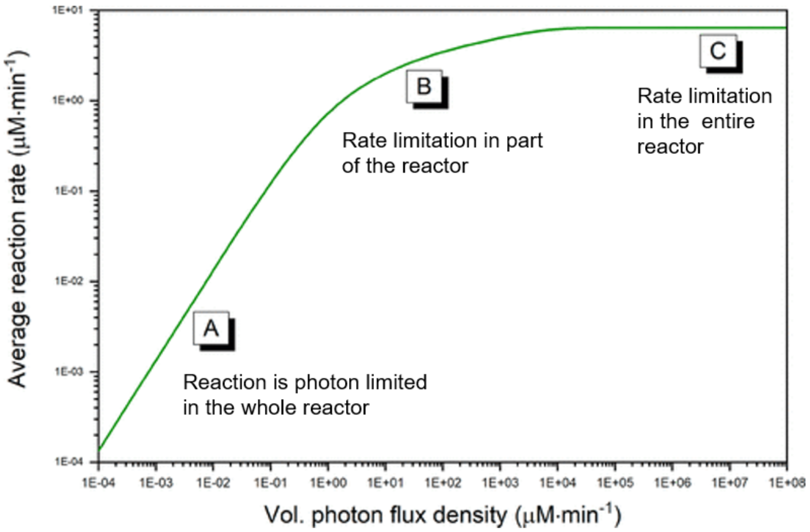

Figure 2.32 General relationship between light intensity and the reaction rate in the solution. (Bloh, 2019)

With increasing light intensity, the β is reduced gradually (region B) due to the exceeding photons in some part of the reactor, or in other words unequal distribution of the reactant to the photons.

At a certain moment, a further increase in light intensity will not result in an enhancement of the reaction rate. The reaction becomes ultimately independent of the photon flux ($\beta = 0$) (region C). At this point, the photocatalyst is constantly active and the reaction medium is completely saturated with photons. Additional photons will not be productively absorbed anymore.

Notably, it can be easily understood that the linear part of this correlation can be extended by increasing the catalyst loading (or by increasing the concentration of the photon absorbing species). These important insights have their repercussions on the energy efficiency of the photochemical process, and it is therefore important to carefully balance the solid loading with the light intensity both in amount but also on the distribution.

Photochemical reaction rates typically can be carried out at room temperature and readily tuned by simply varying the light intensity. From a safety perspective, photochemical reactions can be easily quenched by switching off the light.

Compared to the photochemical reaction in the solution whose rate is controlled by the temperature and the radiation intensity, the solid-state photochemistry is more likely follow the rules of topochemistry due to the intermolecular force form the solid crystal structure. The kinetics of the solid-state chemistry follow four mechanisms which are (a) nucleation and nuclei growth, (b) geometrical contraction, (c) diffusion, and (d) reaction.

(a) Nucleation and nuclei growth

The kinetics of many solid-state reactions have been described by nucleation models. These reactions include crystallization, crystallographic transition, adsorption, hydration, and desolvation.

Crystals have varying local energies from imperfections, including point defects, impurities, edges, cracks, surfaces, and dislocations. These imperfections provide sites for solid state reactions where the activation energies are minimized. Solid-state reactions start at these sites and then develop, which called the nucleation and nuclei growth. In this mechanism, there are three models based on different assumptions, including power law, the JMEAK equation, and autocatalytic model.

- *Power law*

Nucleation was classified to two groups, single stepped and multi-stepped. A general form to describe this mechanism was presented in 1945 (Bagdassarian, 1945). This equation was derived by the probability method. It describes the nucleation and nucleus growth assuming that the multiple steps have the same probability to succeed for each single step, and the growth rate are constant show as follows (Equation 2-25)

$$\alpha^{1/n} = kt \tag{2-25}$$

where n is a constant affected by the probability and the number of the growth dimensions. This model does not consider the growth constrains and it is usually applied to analysis the acceleratory period of a kinetic curve.

- *JMAEK Equation*

A famous model, JMAEK (Johnson–Mehl–Avrami–Erofeev–Kolmogorov) equation was first derived by Kolmogorov in 1937 and popularized by Avrami from 1939 to 1941 (Avrami, 1939, Avrami, 1940, Avrami, 1941), which gave Equation 2-26.

$$\alpha = 1 - \exp[-kt^n]$$

2-26

Where α is the conversion fraction, k is a rate constant, t is the reaction time, and n is a dimension factor. This equation describes the nuclei generation and growth under the restrictions of ingestion and coalescence (Luiggi Agreda, 2015).

- *Autocatalytic Models*

In homogeneous kinetics, autocatalysis occurs when the products catalyse the reaction; this occurs when the reactants are regenerated during a reaction in what is called "branching". The reactants will eventually be consumed, and the reaction will enter a "termination" stage where it will cease. A similar observation can be seen in solid-state kinetics. Autocatalysis occurs in solid-state kinetics if nuclei growth promotes continued reaction due to the formation of imperfections such as dislocations or cracks at the reaction interface. Termination occurs when the reaction begins to spread into material that has decomposed (Jacobs, 1997). Prout and Tompkins (1945) derived an autocatalysis model for the thermal decomposition of potassium permanganate which produced considerable crystal cracking during decomposition (Equation 2-27).

$$\ln \frac{\alpha}{1-\alpha} = kt + c$$

2-27

(b) Geometrical Contraction

These models assume that nucleation rapidly occurs on the surface of the reactant, which is applicable to interfacial reactions. As a result, the rate of the reaction is controlled by the progress of the interface to the centre of the particle. Based on these assumptions, formula was derived (Carstensen, 1974a) to describes the contraction of cylindrical (area), spherical or cubical (volume) particles. Equation 2-28 and Equation 2-29 represents the contracting surface and volume, respectively. This model has been verified in the dehydration of calcium oxalate monohydrate (Liqing and Donghua, 2004)

$$1-(1-\alpha)^{\frac{1}{2}}=kt \tag{2-28}$$

$$1-(1-\alpha)^{\frac{1}{3}}=kt \tag{2-29}$$

(c) Diffusion

One of the major differences between solid-state reaction and solution reaction is the mobility of the reactant molecules. They are available already to react with each other in the solution system, whereas the solid-state reaction occurs between the lattices or with molecules that must permeate into lattices. This permeation is limited and most likely to rely on the lattice defect (Welch, 1955).

A product layer may increase where the reaction rate is controlled by the movement of the reactants to or products from the reaction interface. Solid-state reactions are not usually controlled by mass transfer except for a few reversible reactions or when large evolution or consumption of heat occurs. Diffusion usually plays a role in the rates of reaction between two reacting solids, when reactants are in separate crystal lattices (Brown, 1980).

Wyandt and Flanagan (1992) have shown that the desolvation of sulfonamide-ammonia adducts follows diffusion models. A correlation was found between calculated desolvation activation energies of the ammonia adducts and the sulfonamide’s intrinsic acidity. This finding was attributed to an acid-base-type interaction between the sulfonamide (acid) and ammonia (base) in the solid state. The $\mathrm{p}_{\mathrm{K_a}}$ of the drug was found to inversely relate to the strength of the ammonia-drug interaction, which in turn affected desolvation activation energy.

Jander (1927) used the parabolic law to define the thickness of the reaction zone and obtained an equation to describe the kinetics controlled by the diffusion with the assumption that the particle shape does not affect the diffusion. When the parabolic law is applied to the simplest equation, it can describe the one-dimensional diffusion.

$$\alpha^2 = kt \tag{2-30}$$

$$\left(1 - (1-\alpha)^{\frac{1}{3}}\right)^2 = kt \tag{2-31}$$

Ginstling and Brounshtein (1950) have shown that the Jander model is oversimplified and valid at low conversion values. They proposed another model which can be derived from the Fick's law to present the reaction kinetics controlled by diffusion.

$$1 - \frac{2}{3}\alpha - (1-\alpha)^{\frac{2}{3}} = kt \tag{2-32}$$

By using the Ginstling-Brounshtein approach, this equation can be promoted to two-dimensional diffusion.

$$\big((\alpha)\ln(1-\alpha)\big) + \alpha = kt \tag{2-33}$$

An interesting phenomenon was found that the diffusion can be also described by the modified JMEAK model, where n becomes 1.5, 2, and 2.5 representing one-dimensional, two-dimensional, and three-dimensional diffusion respectively (Perez-Maqueda et al., 2003).

$$-\ln(1-\alpha) = (kt)^n \tag{2-34}$$

(d) Reaction order

Order-based kinetics models are similar to the reaction occurring in the solution. The reaction rate is proportional to the concentration of the substrate raised to a power which is the reaction order (n).

$$\frac{d\alpha}{dt} = k(1-\alpha)^n \tag{2-35}$$

Lopes et al. (2005) have shown that decomposition of gadolinium (III) complexes follows a zero-order model. Thermal oxidation of porous silicon (Pap et al., 2004) and desorption of 2-phenylethylamine from silica surfaces were shown to follow a first-order model (Carniti et al., 2005).

2.7.2 Kinetics of Solid-state Photoreaction for Reactor Design

The strict structure of the crystalline provides a better selectivity of the solid-state photoreaction, but also limits the movement of the reactant movement, which affects the reaction rate. Thus, many solid-state photochemical reactions are controlled by mechanism of topochemistry, especially the nucleation and nuclei growth.

Perez-Maqueda et al. (2003) found the kinetic of the 2+2 photodimerization of cinnamic acid follow the JMAK equation, which are describes both the nucleation, nucleus growth and the diffusion. Meanwhile, this model and its modification (Equation

2-36) are also used to describe kinetics of many photochemical reactions (Benedict and Coppens, 2009, Park et al., 2018), where A and B represents the importance of different of different mechanisms.

$$\alpha = 1 - B \cdot e^{-k_B t} - A \cdot e^{-k_A t^n} \tag{2-36}$$

However, these models only provide the relationship between the conversion and the reaction time, which is inadequate for the solid-state photoreactor design especially for continuous operation. The relationship between the light intensity and the reaction rate are required for the design both to maximize the use of the photons and to prevent over-irradiation. It presents a strong positive correlation between the photon flux and the reaction rate in the photochemistry in solution before the critical point of photon flux (Figure 2.32 region A and region B), while there is still a lack of study on this correlation in solid-state photochemical reactions. The correlation for solution reaction cannot be applied directly because many of the solid-state photochemical reaction follows the solid-state reaction mechanisms. Therefore, experimental data and theoretical derivation of kinetics for the solid-state photoreactions are important for the reactor design.

A few of the research presents a correlation between the photon flux and the reaction rate for solid-state photoreaction. Benedict and Coppens (2009) studied the kinetics of SCSC two-photon photodimerization of cinnamic acid. They found that the kinetics of the reactions follow two-photon exiting mechanisms at a wavelength of 532 nm and the conversion fit the JMAK expression. This research also shows that the rate constant at the exponential is proportional to the photon flux within the low conversion region (smaller than 20%).

Hu et al. (2014) traced the reaction mechanism of photocyclodimerization with the help of in-situ X-ray diffraction snapshotting technic. Meanwhile, kinetics at different light intensity by controlling the distance from the light source to the solid sample are also presents. It shows that at 12.95 and 37.55 mw/cm^2, and the corresponding reaction rate constants are 7.14 x 10^{-3} and 12.5 x 10^{-3} min^{-1}. This implied that the reaction rate constant has a similar trend as the reaction in the solution, which are reaction rate increased with increasing photon flux till the turning point.

There is a model also showing the connection between reaction rate and the radiation intensity, obtained from the quantum yield which is the shown as Equation 2-37. In this equation, I is the light intensity, ϕ is the quantum yield and a is the absorption coefficient.(Pariani et al., 2011)

$$r = I\phi a \tag{2-37}$$

However, the quantum yields of reactions were not commonly report. Meanwhile, it is a measured value and determined by the reaction rate. Any energy loss process such as inelastic scattering or fluorescence, or the radiation conversion to heat reduces this value. It is an important value to assess the performance of the reactor, but it is not accurate to determine the reaction rate. Therefore, a detailed kinetic model is required to calculate the reaction rate from various affecting factors.

2.7.3 Species Transport Equation

To simulate the reaction situation inside the reactor, the species transport equation is a good tool for determining describing convection, diffusion, and reaction sources for each component species.(Fluent, 2018) The key feature of this equation is to determine the diffusion term and the convection term especially in the solution. These terms determine the limiting factor whether the reaction is rate controlled or diffusion controlled. It was widely applied to study mass transfer from phase to phase caused by reactor designs (Ngamsidhiphongsa et al., 2020) and additional structures such as membrane (Barnoon et al., 2022) or stirrer (Mishra et al., 2023).

Depending on whether the fluid participate the reaction, the form of the species transport equation is different. For crystal-to-crystal reactions such as solid-state photodimerization, the mass transfer between phase can be ignored. This reaction only occurred in the solid phase, so the movement of the species was the same as the result from the phase. However, the reaction field was determined in the species transport framework.(Fluent, 2018) It need to be adapted if the crystal to crystal reactions were performed in the simulation.

2.8 Conclusion and Research Gap

Photochemical reactions have a great potential to produce valuable molecules in a greener path. The solid-state photochemistry was gradually concerned by researchers due to its high selectivity and its unique products, which increase the atom economy or even shorten the synthesis route. Although there are many well-designed photoreactors which solved problems from the attenuation effect of the photon transfer, fouling and clogging are still problems in handling the solid in the reactors. Meanwhile, the settlement of the solid result in the uneven distribution of light and retention time, which further leads to over-irradiation and production of the by-product.

Swirl pipe has the potential to solve these problems in the particle conveying in the tube. The main mechanism is using tangential force to bring particles to annular movement. This tangential force performed well in the pipe cleaning, and it was also applied to some photoreactors for mixing. These implied that the induction of swirling flow could solve the problem of pipe failure and uneven distribution.

To study the performance of the swirl pipe, the numerical method was preferred first. It can provide more detailed analytical results which is difficult to obtained, such as light intensity distribution and particle distribution. These distributions are important which is the primary dependent variable after the induction of the swirl pipe. These models have been applied widely in different fields and verified with good accuracy. However, the boundary conditions are very important to affect the accuracy. The simulation needs to be carefully set, as shown in Chapter 3.

Chapter 3 Numerical Methodology

3.1 Introduction

Computational fluid dynamics or CFD is a branch of fluid mechanics, combining of modern fluid mechanics, numerical mathematics, and computer science. It can analyse systems involving fluid flow, heat transfer and associated phenomena by computational simulation. This technic is quite powerful and able to solve many research or industrial problem. By using CFD, it can save time and the cost of producing new designs. It is a good method to research when the experimental method is limited. This project plans to perform simulation first and then to build up a rig relied on the simulation result. The relationship between the flow boundary condition and particle distribution was studied as well as that between particle distribution and absorbed radiation.

The CFD simulation models include several sections, for instance geometry model, govern models, solution methods. The geometry model is often created by 2D or 3D drawing software such as AutoCAD, Solidworks, or create it in the mesh creation software (ICEM) directly. The mesh creation cut the geometric volume into small cells. These cells provide co-ordinates of vertices and the centre of the cells acting as the calculation region and position. Thus, different mesh creations on the geometry model results in different convergence times and accuracies of the simulation results.

The govern models are equations describing how the flow field, radiation field, and reaction field change with the given boundary condition or material properties. Direct numerical simulation is a method solve the govern equation directly, but this method is extremely time consuming and high standard hardware required. Then, these govern equations are simplified with different assumptions to meet different requirements of different scenarios. For example, at category of multiphase models, Euler-Euler approaches regard particles as a special fluid while the Euler-Lagrange take these particles as mass point. The former is good at simulation their bulk movement while the latter performs better on particle tracking. Therefore, the model selection is essential to meet the specific requirements of the simulation for this swirl-induced photoreactor. The comparison and selection of models and the detailed introduction of the models are presented in the corresponding section (3.3, 3.4, and 3.5).

To determine the multiple fields, accurate boundary conditions are required to maximize to fit the designed experiment. This boundary condition constrains the govern equations leading to the determined field are accord with the set scenario. In this chapter, the general boundary conditions are introduced while the detailed individual boundary conditions are listed at corresponding section.

Difference scheme is the key method to discrete and solve the govern differentiation equations. Different order of schemes provides different degree of precision to the solution of the certain model. however not all the difference schemes can be applied to all case. For example, overly diffusive schemes such as the first order upwind or power law scheme should be avoided, because they may unduly damp out the energy of the resolved eddies. Corresponding suitable scheme used in this these is presented and compared in their model section respectively. The stability and the precision are the standard to assess the scheme.

3.2 Swirl Pipe and Transition Creation, and Mesh construction

3.1.1 Introduction

Ganeshalingam (2002) tested various cross sections of pipe (3, 4, 5 and 6 lobed) and concluded, based on the evaluation criteria of Swirl Effectiveness the ratio of the swirl intensity produced to the pressure loss) loss), that the 4-lobed cross-section was most effective at swirl generation. He recommended a P:D ratio of 8 and 400mm of length as optimal for the 4-lobed pipe, namely the swirl-inducing pipe. Later, Ariyaratne (2005) designed a transition pipe which provides a gradual transition from circular to lobed cross-section and vice versa and connected it either prior to the 400mm length swirl-inducing pipe as the entry transition or after it as the exit transition. The transition pipe was found to increase swirl induction at the exit of the swirl pipe and reduce pressure losses. Li et al. (2015) improved the efficiency of the cleaning-in-place procedure with the swirl pipe and showed that the β transition and shorter (200mm) swirl-inducing pipe have a good performance in the cleaning process. In this thesis, the optimized swirl pipe by Li was firstly applied as the swirl inducer. This section demonstrates the calculation of the simulation domain following the process from geometry calculation, and geometry creation, to mesh creation and adaption. Then, the simulations are performed on the built mesh.

3.2.1 Geometry Configuration

The inner wall of the swirl-induced pipe was displayed in the Figure 3.1. This pipe consists of a full swirl section and two transition pipes. This calculation and configuration are listed as follows.

Transition pipes

The general cross-section of the transition pipes is displayed at Figure 3.1 b. The pink circle indicates the circular core, the dash area is the total lobe area. The calculation is based on this geometry. The key parameters include the radius of the circular core radius for intermediate stage of transition pipe R, the radius of the lobe r, the length of intermediate x_i, and the local twist degree of the swirl transition θ_i.

- **Calculation of R, circular core radius for intermediate stage of transition pipe**, **and the radius of the lobe** r.

One of key parameter of the transition pipe is the degree of the angle γ, which increases from 45° to 90° in a given number of increments (N_{inc}) as lobes develop. This changing angle γ (in arc) changes the radius of the lobe (r) and the distance between the lobe centre and the origin O (y), but these parameters keep the cross-section area equal for all stages.

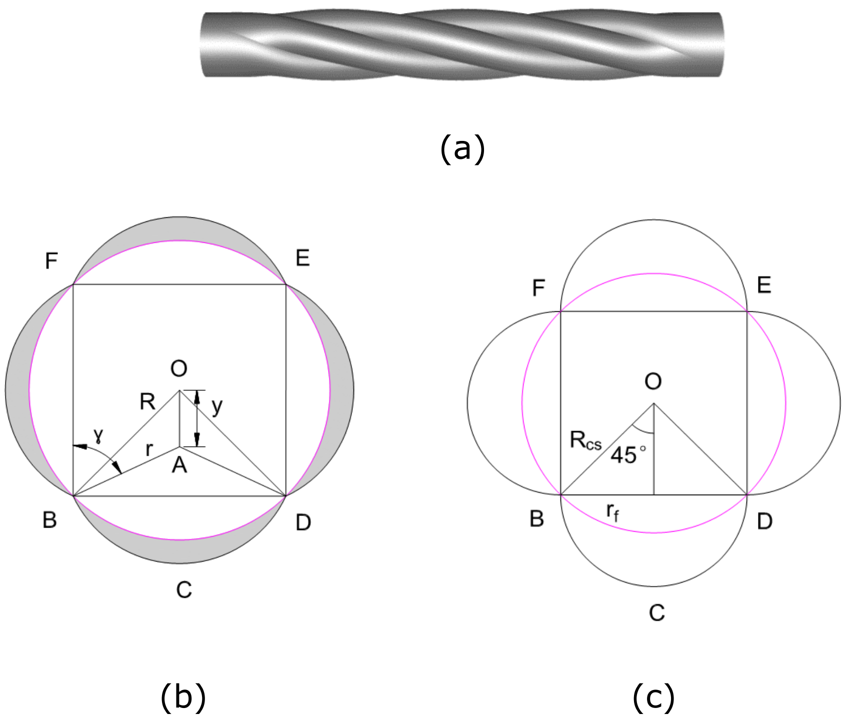

Figure 3.1 inner wall of the swirl pipe (a) and the general cross-section of transition (b) and that of fully swirl pipe (c)

Through the geometrical relationship and then applying the Sine rule in the triangle ABO, y can be determined as

$$y = \frac{1}{\sqrt{2}}\mathrm{R}\left(1 - \frac{1}{\tan\gamma}\right)$$

3-1

At mean time, the area of the segment BCD is calculated as

$$A_{BCD} = r^2\left(\pi\gamma - \frac{1}{2}\sin 2\gamma\right)$$

3-2

Then let $f_1 = \frac{1}{\sqrt{2}}\left(1 - \frac{1}{\tan\gamma}\right)$, $f_2 = \pi\gamma - \frac{1}{2}\sin 2\gamma$

By applying Cosine rule in the triangle ABO,

$$r^2 = \mathrm{R}^2 + y^2 - 2\mathrm{R}y\cos 45°$$

3-3

Replace the f_1 and f_2 into equation 3-3

$$r^2 = \mathrm{R}^2 + f_1^2\mathrm{R}^2 - \sqrt{2}f_1\mathrm{R}^2$$

3-4

At stage 1, where the pipe has no lobe at all, the cross-section area A_{cs} is determined as

$$A_{cs} = \pi \mathrm{R}_1^2 \tag{3-5}$$

Then the changing R for general stage has

$$A_{cs} = 4A_{BCD} + L_{BD}^2 \tag{3-6}$$

$$L_{BD} = \sqrt{2}\mathrm{R} \tag{3-7}$$

Then,

$$A_{cs} = 4r^2 f_2 + 2\mathrm{R}^2 \tag{3-8}$$

Combining equation 3-5 and 3-8

$$\pi \mathrm{R}_1^2 = \mathrm{R}^2\left(4f_2 + 4f_2 f_1^2 - 4\sqrt{2}f_2 f_1 + 2\right) \tag{3-9}$$

Rearrange equation 3-9, then,

$$\mathrm{R} = \mathrm{R}_1\sqrt{\frac{\pi}{4f_2+4f_2f_1^2-4\sqrt{2}f_2f_1+2}} \tag{3-10}$$

- **Determine the intermediate length** x_i,

The lobe area of intermediate for i stage (LA_i) is the difference area between the total cross section area and the centre circle area (figure grey area). It can be expressed as,

$$LA_i = 4fr^2 - (\pi\mathrm{R}^2 - 2\mathrm{R}^2) \tag{3-11}$$

Then the maximum of the LA_i is when the transition is fully developed, noted as LA_{max}. According to the Li et al 2015 and Ariyaratne (2005), β transition pipe performs better than α transition and linear transition. The ratio β represents the degree of the development, where,

$$\beta = \frac{LA_i/(\pi R^2 - LA_i)}{LA_{max}/(\pi R^2 - LA_{max})} \tag{3-12}$$

When $\mathrm{R} = \mathrm{R}_{\mathrm{CS}}$, $LA_i = LA_{max}$.

To avoid discontinuity in the case of a linear relationship, vary lobe area along length as a cosine relationship. Ratio β can now be defined as desired to determine lobe development in transition.

$$\frac{x_i}{L_t} = \frac{\cos^{-1}(1-2\beta)}{\pi} \qquad \text{3-13}$$

Where L_t is the length of the transition pipe.

The equation 3-13 is rearranged and then the β can be expressed as

$$\beta = \frac{1-\cos\left(\frac{\pi x_i}{L_t}\right)}{2} \qquad \text{3-14}$$

Another parameter, transition multiplier n was introduced to control the shape of the geometry, where β was expressed as equation 3-15.

$$\beta = \left[\frac{LA_i/(\pi R^2 - LA_i)}{LA_{max}/(\pi R^2 - LA_{max})}\right]^n \qquad \text{3-15}$$

Then, after combining equation 3-14 and equation 3-15, the position of each intermediate (x) can be determined.

- **Determine the local twist degree of the swirl transition θ_i**

The types of transitions discussed above all have a constant change in twist with respect to the length, namely geodesic helices. Raylor (2000) proposed a brachistochrone helix for a swirl pipe, where the twist has a power law relationship with respect to length ratio.

$$\theta_i = \left(\frac{x_i}{L_t}\right)^t \times \theta \qquad \text{3-16}$$

Where θ is total twist of the swirl transition pipe (deg/m), θ_i is the local twist angle and the index t is the power variable for twist which can be changed to apply an increasing or decreasing helix. When $t < 1$, the helix is faster near the start of the transition while the helix is faster near the end of the transition at $t > 1$.

Full swirl section

The cross-section of the full swirl pipe is displayed in the Figure 3.1 c. The calculation of this fully developed swirl section is a special case of the calculation of the transition, when $\mathrm{R} = \mathrm{R}_{cs}$.

- **Calculate the minimum lobe diameter** $\mathrm{r_f}$

By the equal cross section area, this of circular pipe ($\pi \mathrm{R}_1^2$) is equal to this of the fully developed swirl section. Then, there is

$$4\mathrm{r_f^2} + 2\pi \mathrm{r_f^2} = \pi \mathrm{R}_1^2 \tag{3-17}$$

Rearrange the equation 3-17, the expression of $\mathrm{r_f}$ can be found as equation 3-18

$$\mathrm{R_f} = \sqrt{\frac{\mathrm{R}_1^2}{2+\frac{4}{\pi}}} \tag{3-18}$$

- **Calculate the pipe length by the twist** θ (deg/m).

In this swirl pipe design, one lobe twist 90° using pitch to diameter (P:D) ratio ($\eta = 8$) such that the lobe pattern repeats in the length of the transition. D is the equivalent diameter, which is equal to $2\mathrm{R}_1$. In this case, the $D = 0.01m$. The twist direction was set as negative for clockwise rotation.

$$\theta = \frac{360°}{\eta D} = 4500\ deg/m \tag{3-19}$$

- **Calculate the minimum core radius R_{cs}.**

It is the radius of the circular section of fully developed swirl pipe. it can be easily expressed from the geometrical relationship as equation 3-20

$$\mathrm{R}_{cs} = \frac{\mathrm{r_f}}{\sin 45°} = \sqrt{2}\mathrm{r_f} \tag{3-20}$$

3.2.2 Geometry Creation

Based on the calculation, the configuration of the swirl-pipe was summarized in **Table 3-1**

Table 3-1. The basic information of the transition pipe

Item	**Data**	**Notes**
Lobe number	4	
Total length of transition pipe (L_t), m	0.02	Length of transition based on one lobe twisted 90 degrees
Equivalent diameter (D), m	0.01	
P:D ratio (η)	8	
Type of transition	β	
Transition multiplier (n)	0.5	
Variable helix (t)	1	
Twist (θ), deg/m	4500	
Twist direction	-1	Clockwise

Swirl Pipe Creation

The **transition pipe** was created in a software ICEM using an advanced swept blend feature. The swept blend is a combination between a general blend and a sweep feature in the ICEM. It allows for blending several varying cross sections following a specific trajectory according to the calculation result. An interval of 5 degree for γ was selected. At the start (45°-50°) and the end of the transition pipe (85°-90°), 4 extra intermediates were added into these two sections respectively to build a more accurate transition (Figure 3.2).

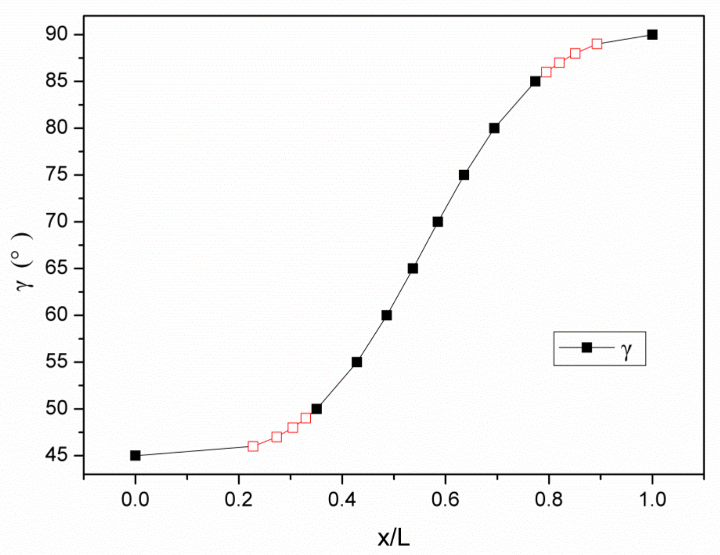

Figure 3.2 γ **versus length for transition pipe, red hollow square represents inserted intermediates afterwards. (Li, 2016)**

After that, the **fully developed swirl pipe** was created. The same swept blend method was adopted in creating the 20mm length, 10mm equivalent diameter swirl inducing pipe, which is half of the full swirl inducing pipe.

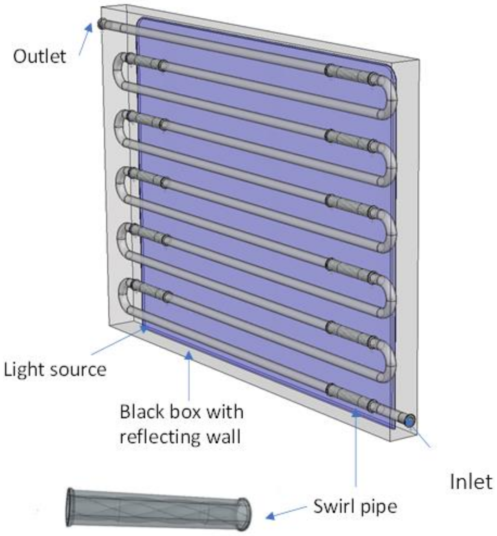

Figure 3.3, Swirl-induced pipe and a proposed reactor structure

Single Unit of the Reactor/Flow Domain Creation

The design of the swirl induced photoreactor is based on the classical model of plug flow reactor. It made of circular transparent pipe inserted with opaque swirl induction pipes at certain locations to induce swirl motion to the solid-air system. The periodical employment of the swirl pipe can maintain the swirl flow for desired length shown in the Figure 3.3. Then, this design can be split into several repeated single unit. This single unit consist of firstly a developing pipe (optional), a swirl-induced pipe and then a transparent pipe, follow the order of the flow direction. The developing pipe is to ensure that the fluid is fully developed. The insertion of the swirl-induce pipe is to generate and to maintain the swirl flow in the following transparent tubing reactor. Because they are repeated unit, one of the units is selected as the object of study.

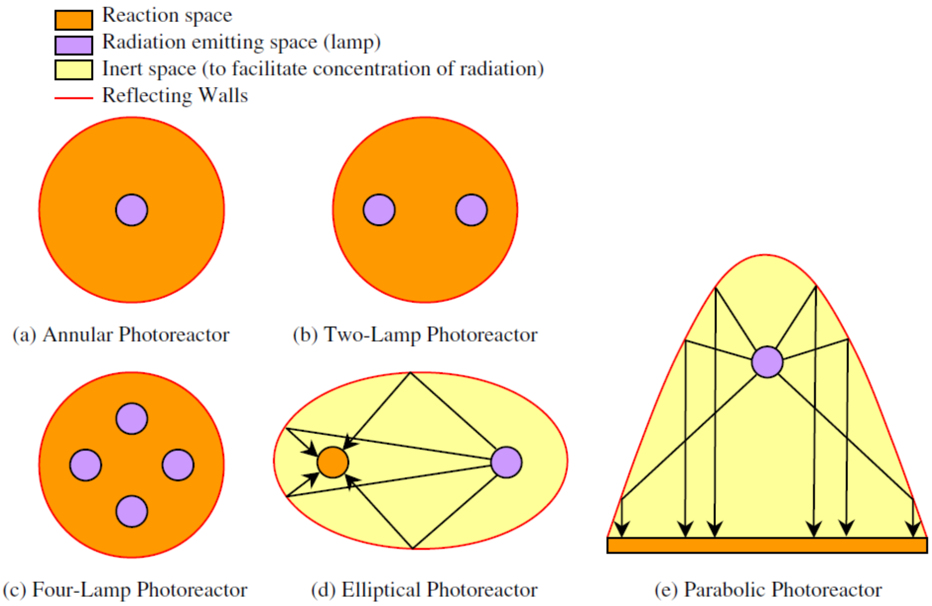

Figure 3.4, Various photochemical reactor configurations.(Pareek et al., 2008)

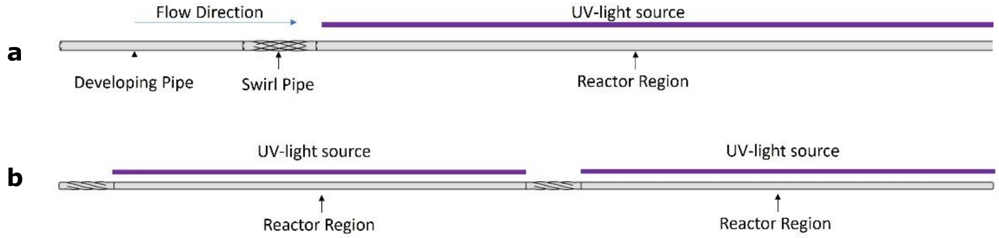

Figure 3.5, geometries and mesh display, a) Geo 1, long pipe, reactor region length L=500D, Geo 2, short pipe, L=60D or Geo 3, middle pipe, L=100D; b) Geo 4, joint pipe: two short pipe connected

The single unit of this reactor is modelled as presented in Figure 3.5, which consists of two circular pipe and a swirl pipe. The first circular pipe with length of 50 diameter (50D) ensures the flow is fully developed before it enters swirl pipe, and the swirl pipe and a downstream circular pipe of XD as the test section. Another set of the model was the repeat of the unit of swirl-pipe and glass pipe (Figure 3.5 b). This set was to show the stability of multi-swirl-tube insertion.

Figure 3.4 indicates a various configuration of photoreactor in terms of the relative position between the reaction space and the light source. Because the tubular reactor was selected as the base inserted with swirl induced pipe, the elliptical arrangement of light source (Figure 3.4 (d)) was firstly applied in this design.

3.2.3 Mesh Creation and Qualification

To model the swirling vortex flow in the reactor, the Eulerian-Eulerian granular fully coupled model was adopted to simulate the hydrodynamics and the mass transfer characteristics in the confined geometry as shown in Figure 3.5. The grid was generated using the software ICEM, and structured mesh are created. This multi blocking strategy can increase the qualities of the cells and then increase the stability, and accuracy of calculation. This blocking allows the mesh to be arranged in a mean of reflecting the geometric character of the domain. Therefore, the flow direction can be maximally orthogonal to the cell surface, which promotes the solution convergence.

At mean time, the refinery of the mesh closed to the wall is important in this simulation. Apart from it is a low-Reynolds number region, it is also the place where the solid reactant gathers and receives photon. These situations require fine cells near wall.

The mesh is qualified by three criteria during the creation, orthogonal quality, aspect ratio and skewness.

- **Orthogonal quality** is computed for cells using the vector from the cell centroid to each of its faces, the corresponding face area vector, and the vector from the cell centroid to the centroids of each of the adjacent cells. The worst cells will have an orthogonal quality closer to 0, with the best cells closer to 1. The minimum orthogonal quality for all types of cells should be more than 0.01, with an average value that is significantly higher.

- **Aspect ratio** is a measure of the stretching of the cell. For highly anisotropic flows, extreme aspect ratios may yield accurate results with fewer cells. Generally, it is best to avoid sudden and large changes in cell aspect ratios in areas where the flow field exhibit large changes or strong gradients. The maximum aspect ratio was 5 at the centre of the calculation domain while it was 20 at near-wall region.
- **Skewness** is defined as the difference between the shape of the cell and the shape of an equilateral cell of equivalent volume. Highly skewed cells can decrease accuracy and destabilize the solution. For example, optimal quadrilateral meshes will have vertex angles close to 90 degrees, while triangular meshes should preferably have angles of close to 60 degrees and have all angles less than 90 degrees. A general rule is that the maximum skewness for a triangular/tetrahedral mesh in most flows should be kept below 0.95, with an average value that is significantly lower. A maximum value above 0.95 may lead to convergence difficulties and may require changing the solver controls, such as reducing under-relaxation factors and/or switching to the pressure-based coupled solver.

Grid sensitivity trial simulation was carried out and it was found that the adoption of a total amount of about 12 million for long pipe (initial test), 6 million cells for middle pipe, 8 million cells for joint pipe and 4 million cells for short pipe/control pipe, were appropriate. Further refining of the mesh has little impact on the simulation results, especially on the radiation field. The mesh of the geometry was created by structured mesh with O-block scheme.

3.3 Multiphase Flow Models

3.3.1 Introduction to the Multiphase Flow Simulation.

Solid particles in this flow reactor are driven by gas or liquid forming pneumatic conveying or slurry flow respectively. These physical phases are applied in a broader sense in multiphase flow system. In this flow, a phase can be defined as an identifiable class of material that has a particular inert response to and interaction with the flow and the potential field where it is immersed. For example, because different-sized particles of the same materials have different dynamic response to the flow field, they are treated as different phases. Therefore, according to the dynamic response, different models are compared and selected, shown in the section 3.3.2.

To describe the effects of the turbulent fluctuations of velocities and scalier equations in a single phase, various closure models can be applied. In comparison to the single-phase flow, a large number of extra terms is required to be calculated in the momentum equations for simulating the multiphase flow and this makes this simulation process complex. These govern equations are displayed at section 3.3.3.

3.3.2 Multiphase Model Selections

The ANSYS Fluent provides two numerical approaches to simulate the momentum exchange between two different phases. They are Euler-Euler approach and Euler-Lagrange approach.

Euler-Lagrange approach treat the fluid phase as continuum by solving the Navier-Stokes equations while the secondary phase is regarded as discrete phase. This dispersed phase is solved by tracking a large number of particles, bubbles or droplet through the flow.

In the Euler-Euler approaches, the different phases are assumed as continua with different volume fraction mathematically. This volume fraction is defined to be a continuous function of space and time. The sum of these fractions for different phases is one because the volume of a phase cannot be occupied by the other one. These equations are closed by providing constitutive relations that are obtained from empirical information or kinetic theory.

Compared to the Euler-Euler approach, the Lagrange method calculate the granular phase individually. This enables these approaches track the movement of the particles. However, it requires that the particle-particle interactions can be neglected and that the dilute second phase occupies a low volume fraction (< 10% is recommend). This approach is not suitable for the swirl-induced reactor design because there is a transition between dispersed and settled condition. This locally settled particle conflict to the Lagrange method.

There are three models are provided by the ANSYS Fluent in terms of Euler-Euler approach, including **Volume of Fraction (VOF)**,

Mixture, and **Eulerian**. These models are suitable for different scenarios with different assumptions.

The **VOF** model is a surface-tracking technique applied to a fixed Eulerian mesh. It is designed for two or more immiscible fluids where the position of the interface between the fluids is of interest. In the VOF model, a single set of momentum equations is shared by the fluids, and the volume fraction of each of the fluids in each computational cell is tracked throughout the domain. Applications of the VOF model include stratified flows, free-surface flows, filling, slug flow, and the motion of large bubbles in a liquid.

The **mixture** model is designed for two or more phases (fluid or particulate). As in the Eulerian model, the phases are treated as interpenetrating continua. The mixture model solves for the mixture momentum equation and prescribes relative velocities to describe the dispersed phases. Applications of the mixture model include particle-laden flows with low loading, bubbly flows, sedimentation, and cyclone separators. The mixture model can also be used without relative velocities for the dispersed phases to model homogeneous multiphase flow. However, this model is not suitable for the rapid change of local volume fraction. Because the different phases are treated as a homogenous entirety and the average properties are applied in the momentum conservation equation, there is a relatively large difference between the simulation result and the reality.

The **Eulerian** model is the most complex of the multiphase models in ANSYS Fluent. It solves a set of n momentum and continuity equations for each phase. Coupling is achieved through the pressure and interphase exchange coefficients. For granular flows, the properties are obtained from application of kinetic theory. The detailed description of the properties and the interaction are selected and displayed in the following corresponding section. Applications of the Eulerian multiphase model includes bubble columns, risers, particle suspension, and fluidized beds.

In conclusion, the Eulerian model is selected to simulate the complex multiphase flow in multiple flow regime involved in the swirl-induced photoreactor. Although this model has to solve a series of equations, it has the most accuracy to tackle the multiple flow regime.

3.3.3 Eulerian Theory and Govern Equations

Mass conservation

The mass conservation equation for single-phase flow is showed as follows.

$$\frac{\partial \rho}{\partial t} + \nabla \cdot (\rho \mathbf{u}) = 0 \qquad 3\text{-}21$$

Where ρ is the density, t is the real time and $\boldsymbol{v}$ is the velocity.

For Eulerian model, the multiphase are all regarded as fractions which occupy the space. Then, the volume of phase q can be described as equation 3-22 and the sum of the volume fraction of every phase is 1(equation 3-23).

$$\mathrm{V}_q = \int_V \phi_q dV \qquad 3\text{-}22$$

where

$$\sum_{q=1}^{n} \phi_q = 1 \qquad 3\text{-}23$$

The effective density of phase q is

$$\hat{\rho} = \phi_q \rho_q \qquad 3\text{-}24$$

In this thesis, phase q includes fluid l and solid s. Therefore, the mass conservation equation for multiphase flow becomes equation 3-25, where $\dot{m}_{ls} - \dot{m}_{sl}$ are the mass transport from the l^{th} to s^{th} and from s^{th} to l^{th}, respectively.

$$\frac{\partial}{\partial t}(\phi_s \rho_s) + \nabla \cdot (\phi_s \rho_s \mathbf{u}_s) = \sum(\dot{m}_{ls} - \dot{m}_{sl}) \qquad 3\text{-}25$$

Momentum

For single phase, the momentum conservation equations are expressed as equation 3-26.

$$\frac{\partial}{\partial t}(\rho \boldsymbol{v}) + \nabla \cdot (\rho \mathbf{u}\mathbf{u}) = -\nabla p + \nabla \cdot (\,\bar{\bar{\tau}}\,) + \rho \boldsymbol{g} + \boldsymbol{F} \qquad 3\text{-}26$$

where

$$\bar{\bar{\tau}} = \mu \left[(\nabla \mathbf{u} + \nabla \mathbf{u}^T) - \frac{2}{3} \nabla \cdot \mathbf{u} \bar{\bar{I}} \right] \qquad 3\text{-}27$$

Where $\bar{\bar{\tau}}$ is the tensor of the stress, μ is the molecular viscosity, and the $\bar{\bar{I}}$ is the unit tensor, and the second term at the right-hand side is the volume dilation.

A multi-fluid granular model to describe the flow behaviour of fluid-solid mixture. The solid-phase stresses are derived by making an analogy between the random particle motion arising from particle-particle collisions and the thermal motion of molecules in a gas, considering the inelasticity of the granular phase. As is the case for a gas carrier, the intensity of the particle velocity determines the stresses, viscosity, and pressure of the solid phase. The kinetic energy associated with the particle velocity fluctuations is represented by a pseudothermal or granular temperature which is proportional to the mean square of the random motion of particles.

Then, the conservation of momentum for the s^{th} solid phase is

$$\begin{aligned}\frac{\partial}{\partial t}(\phi_s\rho_s\mathbf{u}_s) + \nabla\cdot(\phi_s\rho_s\mathbf{u_s}\mathbf{u_s}) = {} & -\phi_s\nabla\mathrm{p} - \nabla\mathrm{p_s} + \nabla\bar{\bar{\tau}}_s + \phi_s\rho_s\boldsymbol{g} \\ & + \textstyle\sum_{l=1}^{N}(K_{ls}(\mathbf{u_l}-\mathbf{u_s}) + \dot{m}_{ls}\mathbf{u_{ls}} - \dot{m}_{sl}\mathbf{u_{sl}}) \\ & + \left(\boldsymbol{F_s} + \boldsymbol{F_{lift,s}} + \boldsymbol{F_{vm,s}} + \boldsymbol{F_{td,s}}\right)\end{aligned} \quad \text{3-28}$$

$$\bar{\tau} = \phi_s\mu_s(\nabla\boldsymbol{v}_s + \nabla\boldsymbol{v}_s^T) + \phi_s\left(\lambda_s - \tfrac{2}{3}\mu_s\right)\nabla\cdot\boldsymbol{v_s}\bar{\bar{I}} \quad \text{3-29}$$

where the μ_s and λ_s are the shear and bulk viscosity of phase and the $\bar{\bar{I}}$ is the unit tensor. The expressions of these two viscosities are shown in the Equation 3-44 the Equation 3-47 respectively.

where the $\mathrm{p_s}$ is the s^{th} solids pressure, $K_{ls} = K_{sl}$ is the momentum exchange coefficient between fluid or solid phase l and solid phase s, N is the total number of phase, and $\boldsymbol{F_s}$, $\boldsymbol{F_{lift,s}}$, $\boldsymbol{F_{vm,s}}$, and $\boldsymbol{F_{td,s}}$ are the body forces, which are external body force, lift force, virtual mass force and turbulent dispersion force respectively. These forces are introduced in section 3.3.4, multiphase interaction.

Energy conservation

For the conservation of energy in the Eulerian multiphase model, a separate enthalpy equation can be written for each phase (Equation 3-30).

$$\begin{aligned}&\frac{\partial}{\partial t}(\phi_s\rho_s h_s) + \nabla\cdot(\phi_s\rho_s\mathbf{u_s}h_s) \\ &\qquad = \phi_s\frac{\partial\mathrm{p}_s}{\partial t} + \bar{\bar{\tau}}_s\colon\nabla\mathbf{u_s} - \nabla\cdot\vec{q}_s + S_s + \sum_{p=1}^{N}(Q_{ls} + \dot{m}_{ls}h_{ls} - \dot{m}_{sl}h_{sl})\end{aligned} \quad \text{3-30}$$

Where h_q is the specific enthalpy of the q^{th} phase, $\vec{q}_q$ is the heat flux, S_s is the source term including heat input and heat generation. Q_{ls} is the intensity of heat exchange between the fluid and solid phase. h_{ls} is the interphase enthalpy. Here, the heat exchange between phases complies with the local balance conditions $Q_{ls} = -Q_{sl}$ and $Q_{ss} = 0$.

3.3.4 Multiphase Interactions

One of the complexities to describe the multiphase flow is the various interaction among different phases. This section is going to introduce these interactions and models to describe them, including fluid-solid exchange coefficient, solid-solid exchange coefficient (Optional), lift force virtual mass force and turbulence dispersion force. At mean time, these interactions are also selected to fit the simulation.

Fluid-solid exchange coefficient

The momentum exchange between different phase is based on the value of the exchange coefficient. The fluid-solid exchange coefficient can be written in the following general form as equation 3-31.

$$K_{fs} = \frac{\phi_s \rho_s f}{\tau_s} \tag{3-31}$$

where f is defined differently for different drag force model described below, and τ_s, the particulate relexation time, is defined as,

$$\tau_s = \frac{\rho_s d_s^2}{18\mu_l} \tag{3-32}$$

where d_s is the diameter of particles of phase s.

There are several exchange-coefficient models f including a drag function (C$_D$) that based on the solid Reynolds number (Re$_s$) such as Gidaspow model, Wen and Yu model, Syamlal-O'Brien model, and Huilin-Gidaspow model, which are provided by ANSYS fluent.

The Syamlal-O'Brien model is appropriate when the shear stresses are obtained according to Syamlal et al, and its parameterized form is restricted to use in gas-solid flows where the primary gas phase is incompressible and where the solid is the Geldart group B particles.

Wen and Yu model is recommended for dilute system, while the Gidaspow model combined the Wen and Yu model with the Ergun equation with switch at $\phi_s = 0.8$. This step change makes this model are suitable for fluidized beds. The Huilin-Gidaspow model provided a smoother switch when the solid volume fraction is less than 0.2. According to the initial test, volume fraction of particles in the swirl-induced reactor reach to 0.4 locally. According to the particle's movement inside the reactor and the properties, Huilin-Gidaspow model was selected to fit the complex distribution of the particles.

The smooth switcher is equation 3-33, and it switch the exchange coefficient form Wen-Yu ($K_{sl-Wen\&yu}$) at low solid volume fraction (equation 3-35) to Ergun ($K_{sl-Ergun}$) at packed particle regime (equation 3-37).

$$K_{fs} = \psi K_{fs-Ergun} + (1-\psi) K_{fs-Wen\&Yu}$$

3-33

$$\psi = 0.5 + \frac{\arctan\left(262.5(\phi_s - 0.2)\right)}{\pi}$$

3-34

$$K_{fs-Wen\&Yu} = \frac{3}{4} C_D \frac{\phi_s \phi_l \rho_l |\mathbf{u}_s - \mathbf{u}_l|}{d_s} \phi_l^{-2.65}$$

3-35

$$C_D = \frac{24}{\phi_l Re_s}\left[1 + 0.15(\phi_l Re_s)\right]^{0.687}$$

3-36

$$K_{fs-Ergun} = 150\,\frac{\phi_s(1-\phi_l)\mu_l}{\phi_l d_s^2} + 1.75\,\frac{\rho_l \phi_s |\mathbf{u}_s - \mathbf{u}_l|}{d_s}$$

3-37

Solid-solid exchange coefficient

The solid-solid exchange coefficient K_{ss} has the following form (equation 3-38). When there are different Eulerian solid phases (with different particle sizes) set, this solid-solid exchange coefficient is calculated.

$$K_{ss} = \frac{3(1+e_{ls})\left(\frac{\pi}{2}+C_{fr,ls}\frac{\pi^2}{8}\right)\phi_s\rho_s\phi_l\rho_l(d_l+d_s)^2 g_{0,ls}}{2\pi\left(\rho_l d_l^3+\rho_s d_s^3\right)}|\mathbf{u}_l - \mathbf{u}_s|$$

3-38

- e_{ls}=the coefficient of restitution
- $C_{fr,ls}$= the coefficient of friction between the l^{th} and the s^{th} solid phase particles
- d_l= the diameter of the particles of solid l
- d_s= the diameter of the particle of solid s
- $g_{0,ls}$= the radial distribution coefficient

Lift force

For multiphase flow, the lift force affects the motion of the secondary phase particles, droplets, or bubbles. These lift force acts due to the velocity gradient in the primary phase flow field. This effect is more significant on large particles. The model in the ANSYS Fluent assumes that the particles diameter is much small than the interparticle spacing. Thus, the packed bed and very small particle are not suggested to activate this model. Due to the particle distribution that particles are loosely packed closed to the wall by the flowing carrier and the relatively small diameter applied (200 nm – 2 μm), the lift force on the particles were ignored in this simulation.

Virtual mass force

For multiphase flows, virtual mass effect occurs when a secondary phase obviously accelerates relative to the primary phase l. When a particle accelerates relative to the surrounding fluid, there is a secondary flow around it. Therefore, it consumes the extra work for generating this secondary flow. The inertia of the primary phase mass encountered by the accelerating particles exerts a "virtual mass force" on the particles. The virtual mass force is defined as equation 3-39. From this equation, there is a "virtual mass" attached on the particles, which equals to the half mass of the displaced fluid.

$$\mathbf{F}_{\mathrm{vm}} = 0.5\phi_s\rho_l\left(\frac{d_l\mathbf{u}_l}{dt} - \frac{d_s\mathbf{u}_s}{dt}\right) \tag{3-39}$$

Where the term

$$\frac{\mathrm{d_l}(\Phi)}{dt} = \frac{\partial(\Phi)}{\partial \mathrm{t}} + (\mathbf{u}\cdot\nabla)\Phi$$

The virtual mass force $\mathbf{F}_{\mathrm{vm}}$will be added to the right-hand side of the momentum for both phases ($\mathbf{F}_{\mathrm{vm,p}} = -\mathbf{F}_{\mathrm{vm,q}}$)

This model then is significant to liquid-solid system and gas-solid system at the high-speed nozzle. Therefore, this model was applied in the liquid-solid system.

Brownian Force

The Brownian force describing the effect of random motion of small particles in a fluid medium. For sub-micron particles, the effects of the Brownian motion are significant. The performance of this force is the diffusion of the molecules or the dispersion of the small particles in the suspension. This force is intended to statistic system or laminar flow. When the flow regime becomes turbulent, the dispersion would be determined by the turbulent dispersion force

Turbulent Dispersion Force

For multiphase turbulent flow, using the Eulerian model, the turbulent dispersion accounts for the interphase turbulent momentum transfer. The turbulent dispersion force act as a turbulent diffusion in the dispersed flows. For example, for a boiling flow in a heated vertical pipe, vapour is generated on heated wall surfaces. Their turbulent dispersion force plays a crucial role in driving the vapour away from the vicinity of the wall to towards the centre of the pipe, which is similar to the movement pattern of blowing settled particles.

The turbulent dispersion force arises from averaging the interphase drags term. For a dispersed phase, p, and a continuous phase, q, the turbulent drag is modelled as equation 3-40.

$$K_{sl}\left(\tilde{\boldsymbol{v}}_s - \tilde{\boldsymbol{v}}_q\right) = K_{pq}\left(\boldsymbol{v}_p - \boldsymbol{v}_q\right) - K_{pq}\boldsymbol{v}_{dr} \tag{3-40}$$

The term at left side is the instantaneous drag. The first term on the right-hand side, $(K_{pq}(\boldsymbol{v}_p - \boldsymbol{v}_q))$ appears in the equation and represents the mean momentum exchange between the two phases. K_{pq} is the interphase exchange coefficient, and $\boldsymbol{v}_p$ and $\boldsymbol{v}_q$ are the mean phase velocity vectors. The second term, $K_{pq}\boldsymbol{v}_{dr}$, is referred to as the turbulent dispersion force (Equation 3-41). $\boldsymbol{v}_{dr}$ is the drift velocity and accounts for the dispersion of the secondary phases due to transport by turbulence fluid motion. This drift velocity is shown in Equation 3-97 later (p143), which describes the turbulence in multiphase flow. $f_{td,limit}$ is a factor that can be used to impose a limiting function on turbulent dispersion force.

$$\boldsymbol{F}_{td,q} = -\boldsymbol{F}_{td,p} = -f_{td,limit}K_{pq}\boldsymbol{v}_{dr} \tag{3-41}$$

ANSYS Fluent provides a standard limiting function as the equation as

$$f_{td,limit}(\phi_p) = \max\left[0, \min\left(1, \frac{\phi_{p,2}-\phi_p}{\phi_{p,2}-\phi_{p,1}}\right)\right]$$

where $\phi_{p,1} = 0.3$ and $\phi_{p,2} = 0.7$ by default.

3.3.5 Multiphase Properties

There are extra properties of the flow involved in the multiphase system. This section mainly focuses on packing limit, solid pressure, radial distribution function, solid shear stress, and granular temperature. Some of these properties are real but the others are created to describe the multiphase flow behaviour.

Packing limits

The packing limit is a nature of solid particles according to the shape. It is not a fixed quantity, and it may change according to the number of the particles present within a given volume and the diameter of the particles. When the small particles occupy in the space between larger particles. In this thesis, the packing limit is assumed as 0.5.

Solid pressure

A solid compressible regime is when solid volume fraction is lower than the packing limit. For granular flow in the solid compressible regime, a solid pressure is calculated independently and used for the pressure gradient term, ∇p_s in the granular phase momentum equation. A Maxwellian velocity distribution is used for the particles so that a granular temperature is introduced into the model both in the expression of solid pressure and viscosity. The solid pressure consists of a kinetic term and a second term due to particle collisions.

$$p_s = \phi_s \rho_s \Theta_s + 2\rho_s (1 + e_{ss}) a_s^2 g_{0,ss} \Theta_s \tag{3-42}$$

where e_{ss} is the restitution for particle collisions, $g_{0,ss}$is the radial distribution function, and the Θ_s is the granular temperature.

Granular temperature is proportional to the kinetic energy of the fluctuating particle motion. The function of radial distribution is to control the compressibility of the solid distribution, from the compressible with $\phi < \phi_{max}$ the incompressible condition with $\phi = \phi_{max}$.

Radial distribution function

The radial distribution function g_0 is a correction factor that the probability of collisions between grains when the solid granular phase become dense. This function may also be interpreted as the nondimensional distance between spheres.

$$g_0 = \frac{s + d_p}{s} \tag{3-43}$$

For one solid phase, $g_0 = \left[1 - \left(\frac{\alpha_s}{\alpha_{s,max}}\right)^{\frac{1}{3}}\right]^{-1}$ e to the particle size was assumed as a constant (not vary in a large range) the only one solid phase was set. Otherwise, additional phase should be set for presenting the variation of the solid diameter.

Solid shear stresses

The solid stress tensor contains shear and bulk viscosities arising from particle momentum exchange due to translation and collision. It includes collisional ($\mu_{s,col}$), kinetic ($\mu_{s,k}$), and the optional frictional part, to give the solid shear viscosity. The frictional part accounts for the viscous-plastic transition that occurs when particles of a solid phase reach the maximum solid volume fraction. According to the pre-simulation, the maximum of the volume fraction that they reach is about 0.3, which still has distance to the packing limit.

$$\mu_s = \mu_{s,col} + \mu_{s,k} \tag{3-44}$$

- Collisional viscosity

The collisional part of the shear viscosity is described by

$$\mu_{s,col} = \frac{4}{5}\phi_s \rho_s d_s g_{0,ss}(1 + e_{ss})\left(\frac{\Theta_s}{\pi}\right)^{\frac{1}{2}}\phi_s \tag{3-45}$$

- Kinetic viscosity

There are two models provided to describe the kinetic viscosity in the ANSYS Fluent, Syamlal et al and Gidaspow. Considering the model matching, Gidaspow was selected to determine the kinetic viscosity (Equation 3-46).

$$\mu_{s,k} = \frac{10\rho_s d_s\sqrt{\Theta_s\pi}}{96\phi_s(1+e_{ss})g_{0,ss}}\left[1+\frac{4}{5}g_{0,ss}\phi_s(1+e_{ss})\right]^2\phi_s$$

3-46

Bulk viscosity

The solids bulk viscosity accounts for the resistance of the granular particles to compression and expansion. It has the following form from Lun et al. (1984).

$$\lambda_s = \frac{4}{3}\phi_s^2\rho_s d_s g_{0,ss}(1+e_{ss})\left(\frac{\Theta_s}{\pi}\right)^{\frac{1}{2}}$$

3-47

Granular temperature

The granular temperature Θ_s for the s^{th} solid phase is proportional to the kinetic energy of the particles random motion and the expression of this is Equation 3-48.

$$\Theta_s = \frac{1}{3}u_{s,i}u_{s,i}$$

3-48

In the equation, $u_{s,i}$ represents the i^{th} component of the solid velocity in the Cartesian coordinate system. This is defined as an ensemble average of the particles' random velocity within a finite volume and time period (Chapman and Cowling, 1990, Ding and Gidaspow, 1990).

The transport equation of this granular temperature is Equation 3-49. The first term of this equation at the right-hand side means the generation of energy by the solid stress tensor. k_{Θ_s} is the diffusion coefficient, and then $k_{\Theta_s}\nabla\Theta_s$ is the diffusion of energy. γ_{Θ_s}

is the collisional dissipation rate of energy and ϕ_{ls} is the energy exchange between l^{th}fluid or solid phase and the s^{th} solid phase.

$$\frac{3}{2}\left[\frac{\partial}{\partial x}(\rho_s\phi_s\Theta_s)+\nabla(\rho_s\phi_s\mathbf{u}_s\Theta_s)\right] = \left(-p_s\overline{\overline{I}}+\overline{\overline{\tau}}_s\right):\nabla\mathbf{u}_\mathrm{s}+\nabla\cdot\left(k_{\Theta_s}\nabla\Theta_s\right)-\gamma_{\Theta_\mathrm{s}}+\phi_{ls} \tag{3-49}$$

The term $k_{\Theta_s}\nabla\Theta_s$ contained in equation 3-49 describing the diffusive flux of granular energy, and then the diffusion coefficient $k_{\Theta_s}$was determined by Equation 3-50 provided by Gidaspow et al. (1991)

$$k_{\Theta_s}=\frac{150d_s\rho_s\sqrt{\Theta_s\pi}}{384(1+e_{ss})g_{0,ss}}\left[1+\frac{6}{5}\phi_s g_{0,ss}(1+e_s)\right]^2+2\rho_s\phi_s^2 d_s(1+e_{ss})g_{0,ss}\sqrt{\frac{\Theta_s}{\pi}} \tag{3-50}$$

The collisional dissipation of energy γ_{Θ_s} represents the rate of energy dissipation within the s^{th} solids phase due to collisions between particles. This term is represented by the expression derived by Lun et al. (1984)

$$\gamma_{\Theta_\mathrm{s}}=\frac{12\left(1-e_{ss}^2\right)g_{0,ss}}{d_s\sqrt{\pi}}\rho_s\phi_s^2\Theta_s^{\frac{3}{2}} \tag{3-51}$$

The transfer of the kinetic energy of random fluctuation in the particle velocity.

$$\phi_{ls}=-3K_{ls}\Theta_\mathrm{s} \tag{3-52}$$

For a granular phase s, the shear force at the wall was written as equation 3-53.

$$\boldsymbol{\tau}_s=-\frac{\pi}{6}\sqrt{3}C\frac{\phi_s}{\phi_{s,max}}\rho_s g_0\sqrt{\Theta_s}\boldsymbol{U}_{s,p} \tag{3-53}$$

where, $\boldsymbol{U}_{s,p}$ is the particle slip velocity parallel to the wall, C is the specularity coefficient between the particle and the wall, which is

0.6 (Johnson and Jackson, 1986), $\phi_{s,max}$ is the volume fraction for the particles at maximum packing, and g_0 is the radial distribution function that is model dependent.

The general boundary condition for the granular temperature at the wall can be expressed by Equation 3-54.

$$q_s = \frac{\pi}{6}\sqrt{3}C\,\frac{\phi_s}{\phi_{s,max}}\rho_s g_0\sqrt{\Theta_s}\boldsymbol{U}_{s,p}\cdot\boldsymbol{U}_{s,p} - \frac{\pi}{4}\sqrt{3}\,\frac{\phi_s}{\phi_{s,max}}(1-e_{sw}^2)\rho_s g_0\Theta_s^{\frac{3}{2}} \tag{3-54}$$

3.3.6 Multiphase Turbulence models

To describe the effects of turbulent fluctuations of velocities in multiphase flow, a large number of terms is added to the single-phase model, which makes this simulation complex. ANSYS Fluent provides three types of models that are compatible with the multiphase flow to describe the turbulence, including $k-\varepsilon$, $k-\omega$, and the Reynolds stress method (RSM). Considering the accuracy and the CPU consumption, $k-\omega$ SST model was selected at the beginning.

$k-\omega$ model is one of the two-equation turbulence models and in the fluent, this standard and SST model are based on the Wilcox $k-\omega$ model. This model modified the low-Reynolds number effect, compressibility and the shear flow spreading, but it is sensitive to the solution of the values of k and ω outside the shear layer.

There are three ways to treat the multiphase flow, including mixture, disperse, and a model called per-phase. The mixture model is applicable for separated phase (e.g., stratified phase) or the density ratio between different phases is close to 1.

In contrast, the dispersed turbulence model is the appropriate model for the dilute granular phases flow in a continuous phase. In this model, fluctuating quantities can be given in terms of the mean characteristics of the continuous phase and the ratio of the particle relaxation time and eddy particle interaction time. However, it is not compatible with the solid-state photoreaction. The species transfer equation was solved in the secondary phase, while this dispersed turbulence model does not solve the conservation equations in this phase resulting in the loss of equation closure.

The most general multiphase turbulence model solves a set of k and ω equations for each phase called per-phase model. This model is appropriate when the turbulence transfer among the phases is important. Although the per-phase model is more complex, the individual determination is more suitable to treat the changing particle distribution from dispersed, annular and the settled state.

Equations for SST $k-\omega$ model

The $k-\omega$ model is an empirical model based on model transport equations for the turbulence kinetic energy (k) and specific dissipation rate (ω) or called turbulence frequency, and the SST $k-\omega$ model with the per-phase treatment was shown as follows.

$$\omega = \frac{\varepsilon}{k} \tag{3-55}$$

$$\frac{\partial(\phi_q \rho_q k_q)}{\partial t} + \nabla \cdot \left(\phi_q \rho_q \boldsymbol{U}_q k_q\right) = \nabla \cdot \left(\phi_q \Gamma_k \nabla k_q\right) + \phi_q G_{k,q} - \phi_q Y_{k,q} + \phi_q S_{k,q} + M_q \tag{3-56}$$

$$\frac{\partial(\phi_q\rho_q\omega)}{\partial t}+\nabla\cdot(\phi_q\rho_q\boldsymbol{U}_q\omega)=\nabla\cdot(\phi_q\Gamma_\omega\nabla\omega)+\phi_qG_{\omega,q}-\phi_qY_{\omega,q}+\phi_qS_{\omega,q}+\phi_qD_{\omega,\mathrm{q}}+C_3M_q \tag{3-57}$$

In these equations, ω is the specific dissipation rate, ε is the dissipation rate, ϕ_q,ρ_q, μ_q and $\boldsymbol{U}_q$ is the volume fraction, density, and the viscosity of the phase q. C_3 is a constant, which is specified by Equation 3-58. Γ is the **effective diffusivity**.G, Y, D_ω, M,and S_ω are **the turbulence production**, **turbulence dissipation**, **cross-diffusion** term, **phase interaction term** and the user-defined term.

$$C_3=\tanh\left|\frac{v}{u}\right| \tag{3-58}$$

where v is the component of the flow velocity parallel to the gravitational vector and u is the component of the flow velocity perpendicular to the gravitational vector. In this way, C_3 will become 1 for buoyant shear layers for which the main flow direction is aligned with the direction of gravity. For buoyant shear layers that are perpendicular to the gravitational vector, will become zero.

- **Effective diffusivity**, Γ

The effective diffusivities for the SST $k-\omega$ model are presented as follows, where σ_k and σ_ω are the turbulent Prandtl number for k and ω respectively.

$$\Gamma_k=\mu_q+\frac{\mu_{t,q}}{\sigma_k} \tag{3-59}$$

$$\Gamma_\omega=\mu_q+\frac{\mu_{t,q}}{\sigma_\omega} \tag{3-60}$$

The turbulent viscosity μ_t is computed as equation 3-61, while the turbulent Prandtl number is determined by equation 3-62 equation

3-63 respectively. In this equation, S is the strain rate magnitude. F_1 and F_2 are the blending function, given by

$$\mu_t = \frac{\rho_q k}{\omega} \frac{1}{\max\left[\frac{1}{\alpha^*}, \frac{SF_2}{a_1 \omega}\right]} \tag{3-61}$$

$$\sigma_k = \frac{1}{\frac{F_1}{\sigma_{k,1}} + \frac{(1-F_1)}{\sigma_{k,2}}} \tag{3-62}$$

$$\sigma_\omega = \frac{1}{\frac{F_1}{\sigma_{\omega,1}} + \frac{(1-F_1)}{\sigma_{\omega,2}}} \tag{3-63}$$

$$\mathrm{F}_1 = \tanh(\Phi_1^4) \tag{3-64}$$

$$\Phi_1 = \min\left[\max\left(\frac{\sqrt{k}}{0.09\omega y}, \frac{500\mu}{\rho y^2 \omega}\right), \frac{4\rho k}{\sigma_{\omega,2} D_\omega^+ y^2}\right] \tag{3-65}$$

$$F_2 = tanh(\Phi_2^2) \tag{3-66}$$

$$\Phi_2 = \max\left[\frac{2\sqrt{k}}{0.09\omega y}, \frac{500\mu}{\rho y^2 \omega}\right] \tag{3-67}$$

$$D_\omega^+ = \max\left[\frac{2\rho}{\omega \sigma_{\omega,2}} \frac{\partial k}{\partial x_j} \frac{\partial \omega}{\partial x_j}, 10^{-10}\right] \tag{3-68}$$

In these y is the distance to the next surface and D_ω^+ is the positive portion of the **cross-diffusion term** modification.

The coefficient α^* damps the turbulent viscosity causing a low-Reynolds number correlation.

$$\alpha^* = \alpha_\infty^* \left(\frac{\alpha_0^* + \frac{Re_t}{R_k}}{1 + \frac{Re_t}{R_k}}\right) \tag{3-69}$$

where,

$$Re_t = \frac{\rho k}{\mu \omega} \tag{3-70}$$

$$\alpha_0^* = \frac{\beta_i}{3} \tag{3-71}$$

where β_i and R_k are constant and they are collected at the end of this section.

- **Cross-diffusion term**, D_ω

The SST $k-\omega$ model is based on both the standard $k-\omega$ model and the standard $k-\varepsilon$ model. To blend these two models together, the standard $k-\varepsilon$ model has been transformed into equations based on k and ω, which leads to the introduction of a cross-diffusion term defined as

$$D_\omega = 2(1-F_1)\rho\frac{1}{\omega\sigma_{\omega,2}}\frac{\partial k}{\partial x_j}\frac{\partial \omega}{\partial x_j} \qquad 3\text{-}72$$

High Reynolds number form, $\alpha^* = \alpha^*_\infty = 1$

- **Turbulence Production**, G

Turbulence production of kinetic energy G_k is defined as

$$G_k = -\rho\overline{u_i'u_j'}\frac{\partial u_j}{\partial x_i} \qquad 3\text{-}73$$

To evaluate G_k in a manner consistent with the Boussinesq hypothesis,

$$G_k = \mu_t S^2 \qquad 3\text{-}74$$

where S is the modulus of the mean rate of strain tensor, defined as follows.

$$S \equiv \sqrt{2S_{ij}S_{ij}} \qquad 3\text{-}75$$

The mean strain rate was defined as

$$S_{ij} = \frac{1}{2}\left(\frac{\partial u_j}{\partial x_i} + \frac{\partial u_i}{\partial x_j}\right) \qquad 3\text{-}76$$

Turbulence production of specific dissipation rate G_ω is defined as

$$G_\omega = \frac{\alpha}{v_t}G_k \qquad 3\text{-}77$$

where G_k is given by equation

the coefficient α

$$\alpha = \frac{\alpha_\infty}{\alpha^*}\left(\frac{\alpha_0 + Re_t/R_\omega}{1 + Re_t/R_\omega}\right) \qquad 3\text{-}78$$

where

$$\alpha_\infty = F_1\alpha_{\infty,1} + (1 - F_1)\alpha_{\infty,2} \qquad 3\text{-}79$$

$$\alpha_{\infty,1} = \frac{\beta_{i,1}}{\beta_\infty^*} - \frac{\kappa^2}{\sigma_{\omega,1}\sqrt{\beta_\infty^*}} \qquad 3\text{-}80$$

$$\alpha_{\infty,2} = \frac{\beta_{i,2}}{\beta_\infty^*} - \frac{\kappa^2}{\sigma_{\omega,2}\sqrt{\beta_\infty^*}} \qquad 3\text{-}81$$

Where R_ω, α^*,and Re_t are constant displayed at the end of this section as well as the Appendix.

- **Turbulence Dissipation** Y

The term Y_k represents the dissipation of turbulence kinetic energy, and Y_ω means the dissipation of ω.

$$Y_k = \rho\beta_\infty^* k\omega \qquad 3\text{-}82$$

$$Y_\omega = \rho\beta_i\omega^2 \qquad 3\text{-}83$$

where

$$\beta_i = F_1\beta_{i,1} + (1 - F_1)\beta_{i,2} \qquad 3\text{-}84$$

- **Phase interaction**

For per phase model, the phase interaction is important for turbulence develop.

$$M = \sum_{l=1}^{N} K_{pq}\left(C_{pq}k_l - C_{qp}k_q\right) - \sum_{l=1}^{N} K_{pq}\left(\boldsymbol{U}_p - \boldsymbol{U}_q\right)\cdot\frac{\mu_{t,p}}{\phi_p\sigma_p}\nabla\phi_p + \sum_{l=1}^{N} K_{pq}\left(\boldsymbol{U}_p - \boldsymbol{U}_q\right)\cdot\frac{\mu_{t,q}}{\phi_q\sigma_q}\nabla\phi_q \qquad 3\text{-}85$$

Where σ is the surface tension of the corresponding phase.

The terms C_{pq} and C_{qp} can be approximated as

$$C_{pq} = 2, C_{qp} = 2\left(\frac{\eta_{pq}}{1+\eta_{pq}}\right) \qquad \text{3-86}$$

The η_{lq} is the ratio between two characteristic times, the time scale of the energetic-turbulent eddies $\tau_{t,pq}$ and the characteristic particle relaxation time connected with inertial effects acting on a dispersed phase p, $\tau_{F,pq}$.

$$\eta_{pq} = \frac{\tau_{t,pq}}{\tau_{F,pq}}$$

3-87

$$\tau_{t,pq} = \frac{2C_\mu}{3\omega_q\sigma_1\sqrt{1 + C_\beta\xi_\tau^2}}$$

3-88

$$C_\beta = 1.8 - 1.35\cos^2\theta$$

3-89

Where θ is the angle between the mean particle velocity and the mean relative velocity.

$$\xi_\tau = \frac{\left|\boldsymbol{U}_p - \boldsymbol{U}_q\right|}{\sqrt{\frac{2}{3}k_q}}$$

3-90

$$\tau_{F,pq} = \frac{\rho_p d_p^2}{18\mu_c f\left(Re, \phi_q\right)}\left(1 + \frac{C_{VM}\rho_q}{\rho_p}\right)$$

3-91

The $f\left(Re, \phi_q\right)$ is the drag coefficient, which can be determined by combining equation 3-31, 3-32, 3-33, 3-34, 3-35, 3-36, and 3-37. C_{VM} is the coefficient of the virtual mass force, which is 0.5 as default. σ_1 is a model constant, which is 1.

- **Turbulence Interaction Models**

When using a turbulence model in a Eulerian multiphase simulation, Fluent provides models describing the influence of the dispersed phase on the multiphase turbulence equations. The influence of the dispersed phases is represented by source terms $S_{k,q}$ and $S_{\omega,q}$. For the $k-\omega$ models with Per Phase turbulence model, Simonin et al. model (1990) is the only choice.

The term $S_{k,q}$ is derived from the instantaneous equation of the continuous phase and takes the following form, where N represents the number of secondary phases,

$$S_{k,q} = C_s\phi_q \sum_{p=1}^{N} K_{pq}\boldsymbol{v}_{pq} \cdot \boldsymbol{v}_{dr} \tag{3-92}$$

For the dispersed phase

$$S_{k,p} = C_s\phi_p K_{pq}\boldsymbol{v}_{pq} \cdot \boldsymbol{v}_{dr}\ , p = 1 \dots N \tag{3-93}$$

Turbulence dissipation sources for all phases are computed as Equation 3-94.

$$S_{\omega,r} = C_3\omega_q S_{k,q} \tag{3-94}$$

C_s is a model constant. It is 1 by default. k_{pq} is the covariance of the velocities of the continuous phase q and the dispersed phase p, calculated from equation 3-96, $\boldsymbol{v}_{pq}$ is the relative velocity. _$\boldsymbol{v}_{dr}$ is the drift velocity, calculated from equation 3-97.

$$k_p = k_q\left(\frac{\eta_{pq}}{1+\eta_{pq}}\right) \tag{3-95}$$

$$k_{pq} = 2k_q \left(\frac{\eta_{pq}}{1 + \eta_{pq}} \right)$$

3-96

$$v_{dr} = -D_{pq} \cdot \left(\frac{\nabla \phi_p}{\phi_p} - \frac{\nabla \phi_q}{\phi_q} \right)$$

3-97

$$D_{t,pq} = \frac{1}{3} k_{pq} \tau_{t,pq}$$

3-98

Where k_q is the kinetic energy of the continuous phase q, where D_{pq} is assumed is a scaler and determined by equation 3-98.

3.3.7 Enhanced Wall Treatment of SST $k - \omega$ Model

The physical quantities (temperature, velocities, and pressure etc.) in the flow field calculated by the finite volume method are linear. If these quantities have a great gradient, finer mesh is required to analysis the change. The quantities near the wall changes sharply due to the boundary layer formed and the Reynolds number of this layer varies from laminar region to turbulent region (Figure 3.6). This means that typical turbulent model is not suitable for calculate the flow near the wall and finer mesh should be constructed closed to the wall.

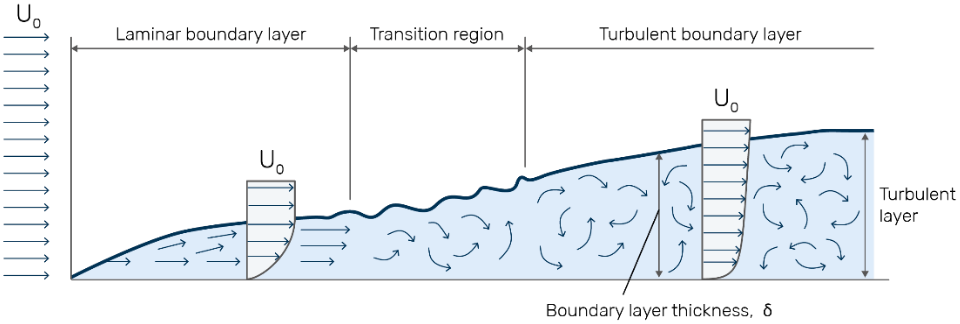

Figure 3.6, Hydrodynamic boundary layers

Newton law of viscosity are shown as Equation 3-99.

$$\frac{\tau_w}{\rho} = -\nu \left(\frac{\partial U}{\partial y}\right)_{y=0}$$

3-99

Enhanced Wall Treatment for Momentum

The standard wall function uses empirical equations to skip the laminar regime closed to the wall, while for all $k-\omega$ based model, the enhanced wall function is applied to treat the near-wall flow. This treatment archives a single wall law for the entire wall region by a blending function, which blending the linear and logarithmic law of the wall. it was suggested by Kader (1981) as 3-100 .

$$u^+ = e^{\Gamma} u^+_{lam} + e^{\frac{1}{\Gamma}} u^+_{turb}$$

3-100

In this equation, the blending function Γ is given by Equation 3-101 where $a = 0.01$ and $b = 5$.

$$\Gamma = \frac{a(y^+)^4}{1 + by^+}$$

3-101

Similarly, the general equation for derivative $\frac{du^+}{dy^+}$ is Equation 3-102.

$$\frac{du^+}{dy^+} = e^{\Gamma} \frac{du^+_{lam}}{dy^+} + e^{\frac{1}{\Gamma}} \frac{du^+_{turb}}{dy^+}$$

3-102

The enhanced wall functions were developed by smoothly blending the logarithmic layer formulation with the laminar formulation. The enhanced turbulent law-of-the-wall for compressible flow with heat transfer and pressure gradients has been derived by combining the approaches of F.White and Christoph (1971) and Huang et al. (1993) as Equation 3-103.

$$\frac{du^+_{turb}}{dy^+} = \frac{1}{\kappa y^+} [S'(1 - \beta u^+ - \gamma(u^+)^2)]^{\frac{1}{2}}$$

3-103

$$S' = \begin{cases} 1 + \alpha y^+ & \text{for } y^+ < y_s^+ \\ 1 + \alpha y_s^+ & \text{for } y^+ \geq y_s^+ \end{cases} \tag{3-104}$$

and

$$\alpha \equiv \frac{\nu_w}{\tau_w u^*}\frac{dp}{dx} = \frac{\mu}{\rho^2 (u^*)^3}\frac{dp}{dx}$$

3-105

$$\beta \equiv \frac{\sigma_t q_w u^*}{c_p \tau_w T_w} = \frac{\sigma_t q_w}{\rho c_p u^* T_w}$$

3-106

$$\gamma \equiv \frac{\sigma_t (u^*)^2}{2 c_p T_w}$$

3-107

where y_s^+ is the location at which the log-law slope is fixed. By default, $y_s^+ = 60$ (Figure 3.7). The coefficient α in Equation 3-103 represents the influences of pressure gradients while the coefficients β and γ represent the thermal effects. Equation 3-103 is an ordinary differential equation and ANSYS Fluent will provide an appropriate analytical solution. If α, β, and γ all equal 0, an analytical solution would lead to the classical turbulent logarithmic law-of-the-wall.

The laminar law-of-the-wall is determined from the Equation 3-108.

$$\frac{du_{lam}^+}{dy^+} = 1 + \alpha y^+$$

3-108

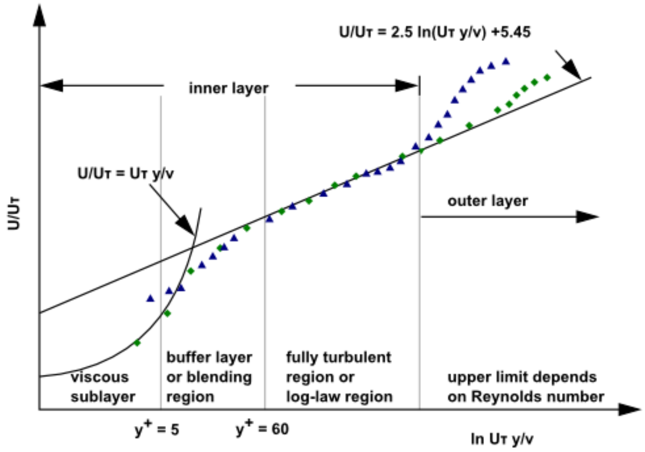

Figure 3.7, Subdivisions of the Near-Wall Region

After integration,

$$u^{+}_{lam} = y^{+}\left(1 + \frac{\alpha}{2} y^{+}\right)$$

3-109

The ω-equation can be integrated through the viscous sublayer without the need for a two-layer approach. This feature can be utilized for a y^{*}-insensitive wall treatment by blending the viscous sublayer formulation and the logarithmic layer formulation based on y^{*}.

Enhanced Wall Treatment for Turbulence

The wall boundary conditions for the k equation in the $k-\omega$ models are treated in the same way as the k equation is treated when enhanced wall treatments are used with the $k-\varepsilon$ models. This means that all boundary conditions for wall-function meshes will correspond to the wall function approach, while for the fine meshes, the appropriate low-Reynolds number boundary conditions will be applied.

The wall boundary conditions for the k and ω are expressed as Equation 3-110 and Equation 3-111, where n is normal to the boundary.

$$\frac{\partial k}{\partial n} = 0 \tag{3-110}$$

$$\frac{\partial \omega}{\partial n} = 0 \tag{3-111}$$

Moreover, the centroid value of k in the cell adjacent to the solid wall (k_w) is specified as Equation 3-112, while ω at wall (ω_w) is specified as Equation 3-113.

$$k_w = \frac{(u^+)^2}{\sqrt{\beta_\infty^*}} \tag{3-112}$$

$$\omega_w = \frac{\rho (u^*)^2}{\mu} \omega^+ \tag{3-113}$$

Analytical solution can be given for both the laminar sublayer and the logarithmic region.

$$\omega_{lam}^+ = \frac{6}{\beta_i (y^+)^2} \tag{3-114}$$

$$\omega_{turb}^+ = \frac{1}{\sqrt{\beta_\infty^*}} \frac{du_{turb}^+}{dy^+} \tag{3-115}$$

Therefore, a wall treatment can be defined for the ω-equation, which switches automatically from the viscous sublayer formulation to the wall function, by the blending function (Equation 3-116).

$$\omega^+ = \sqrt{(\omega_{turb}^+)^2 + (\omega_{lam}^+)^2} \tag{3-116}$$

3.3.8 Model Constants

$\sigma_{k,1} = 1.176$, $\sigma_{\omega,1} = 2.0$,$\sigma_{k,2} = 1.0$,$\sigma_{\omega,2} = 1.18$,$a_1 = 0.31$,$\beta_{i,1} = 0.075$, $\beta_{i,2} = 0.0828$, $\alpha_\infty = 0.52$, $\alpha_\infty^* = 1$, $\alpha_0 = \frac{1}{9}$, $\beta_\infty^* = 0.09$, $R_\beta = 8$, $R_k = 6$, $R_\omega = 2.95$, $\zeta^* = 1.5$, $M_{t0} = 0.25$, $\kappa = 0.41$, $C_\mu = 0.09$.

3.4 Radiation Models

3.4.1 Introduction to Radiation transfer

Radiation transfer is the phenomena that energy is transferred in the form of electromagnetic radiation. The propagation of radiation through a medium is affected by absorption, emission, and scattering processes. The equation of radiative transfer describes these interactions mathematically.

3.4.2 Radiation Transfer Equation

For reactor design, whose characteristic length is much higher than the radiation of the light wavelength, there is a macroscope balance on the radiation of a finite volume at certain wavelength (λ). The intensity of the light I, which depends on position $\boldsymbol{r}$ and direction $\boldsymbol{s}$, is changed due to the following mechanism.

$$\frac{dI_\lambda(\boldsymbol{r},\boldsymbol{s})}{ds} = -W_a + W_e - W_{in} + W_{out}$$

3-117

The loss due to the absorption (W_a) and the out-scattering (W_{out}) result in the radiation loss in this controlled volume.

$$W_a = a_\lambda I(s, \Omega)$$ 3-118

$$W_{out} = \sigma_s I(s, \Omega)$$ 3-119

The gain in the controlled cell in light intensity due to the in-scattering W_{in} and emission W_e are presented as Equation 3-120 and Equation 3-121 respectively.

$$W_{in} = \frac{1}{4\pi}\sigma_\lambda \int_{4\pi} \Phi(\boldsymbol{s} \cdot \boldsymbol{s}') I_\lambda(\boldsymbol{r}, \boldsymbol{s}') d\Omega'$$

3-120

$$W_e = a_\lambda n^2 \frac{\sigma T^4}{\pi}$$

3-121

where there σ_s and a_λ is the scattering coefficient and the absorption coefficient with unit m^{-1}, respectively. $\Phi(\boldsymbol{s} \cdot \boldsymbol{s}')$ is the phase function. The value of it is 1 for isotropic scattering. $\boldsymbol{s}$ is the direction vector, $\boldsymbol{s}'$ is the scattering direction vector, and $\boldsymbol{r}$ is the position vector. n is the refractive index, σ is Stefan-Boltzmann constant, Ω' is the solid angle, T is the local temperature. Thus, the radiation transport equation becomes Equation. 3-122.

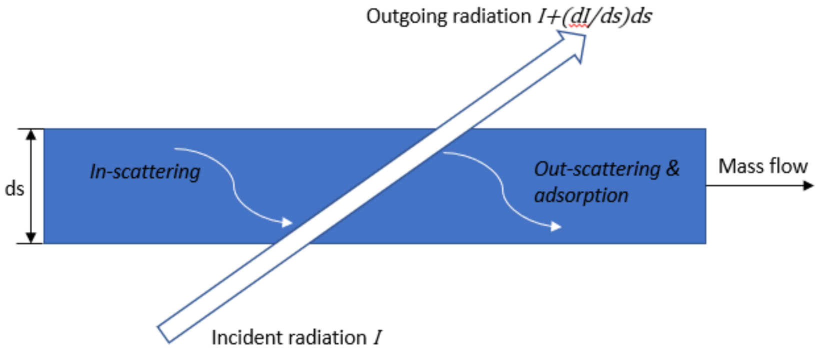

Figure 3.8, Radiation balance schematic diagram

$$\frac{dI_\lambda(\boldsymbol{r},\boldsymbol{s})}{ds} = a_\lambda n^2 \frac{\sigma T^4}{\pi} - a_\lambda I_\lambda(\boldsymbol{r},\boldsymbol{s}) - \sigma_\lambda I_\lambda(\boldsymbol{r},\boldsymbol{s}) + \frac{1}{4\pi}\sigma_\nu \int_0^{4\pi} \Phi(\boldsymbol{s}\cdot\boldsymbol{s}') I_\lambda(\boldsymbol{r},\boldsymbol{s}) d\Omega'$$

3-122

However, the scattering normally is not the isotropic scattering. For nanoparticles, the scattering model follows different scattering model.

3.4.3 Energy Conservation Equation

The conservation equation of energy for multiphase flow is Equation 3-123.

$$\frac{\partial}{\partial t}(\phi_q \rho_q h_q) + \nabla\cdot(\phi_q \rho_q \mathbf{u}_q h_q) = \phi_q \frac{\partial p_q}{\partial t} + \bar{\tau}_q : \nabla \mathbf{u}_q - \nabla \mathbf{q}_q + Q_R + Q_r + \sum_{p=1}^{n} (Q_{pq} + \dot{m}_{pq} h_{pq} - \dot{m}_{qp} h_{qp})$$

3-123

where h_q is the specific enthalpy of t he q^{th} phase, $\boldsymbol{q}_q$ is the heat flux. The Q_R and Q_r represents the source term from the production of the chemical reaction and converted from the radiation. The Q_{pq} intensity of heat exchange between the $p^{th}$and q^{th} phase.

3.4.4 Discrete Ordinates (DO) Method

Since the ANSYS Fluent was selected as the framework to determine the fields inside the reactor, models provided in this software were firstly considered. The DTRM, the P-1, Rosseland, surface to surface (S2S), and DO radiation models are offered. Based on the ANSYS Fluent Theory guide (Fluent, 2018) as well as the literature review, a summarized comparison was displayed as follows.

The DTRM Model

- It is a relatively simple model, and its accuracy can be increased by increasing the number of rays.
- Wide range of optical thicknesses.
- It assumes that all surfaces are diffuse – all reflections are isotropic with respect to the solid angle.
- It assumes that grey radiation was implemented.
- The spectral emissivity at wall is constant to each bend.
- Solving large number of rays is CPU-intensive.
- The effect of scattering in not included.
- Not compatible with non-conformal interfaces, sliding meshes, and parallel processing.

The P-1 Model

- It is easy to solve with little CPU demand that the RTE (Equation 3-122) is regarded as a diffusion equation (compared to the **DTRM** model).
- The effect of scattering is considered.
- It performs well on combustion (large optical thickness)

- Grey-band model is applied to simulate the current implementation, either grey radiation or non-grey radiation.
- It assumes that all surfaces are diffuse as the **DTRM** model.
- There may be a loss of accuracy, depending on the complexity of the geometry, if the optical thickness is small.
- It tends to over-predict radiative fluxes from localized heat sources or sinks.

The Rosseland Model

- It does not solve an extra transport equation for the incident radiation.
- Only applicable for optically thick media (>3).
- Not available for the density-based solver.

Surface to Surface (S2S) Model

- Good for modelling the enclosure radiative transfer without participating media.
- A much faster time per iteration compared to DTRM and DO model.
- It assumes that grey radiation was implemented.
- It assumes all surfaces are diffuse.
- The storage and memory requirements increase very rapidly,
- It cannot be used to model participating radiation problems.

The DO Model

- It spans the entire range of optical thicknesses.
- It also allows the solution of radiation at semi-transparent walls.
- Computational cost is moderate for typical angular discretizations, and memory requirements are modest.
- The non-grey implementation is compatible with which the grey implementation of the DO model can be used. Thus, it is possible to include scattering, anisotropy, semi-transparent media, and particulate effects.
- Grey-band model is applied to simulate the current implementation, either grey radiation or non-grey radiation.
- The non-grey implementation can be used on participating media with a spectral absorption coefficient.

From this comparison, the DO method is suitable for a variety of scenarios, including wide optical thicknesses, from problem of surface-to-surface radiation to participating radiation as well as radiation at the semi-transparent wall. Meanwhile, the computational cost is cost is moderate for typical angular discretization, and memory requirements are modest. Therefore, the DO method was selected to solve the RTE.

The discrete ordinates (DO) radiation model solves the radiative transfer equation (RTE) for a finite number of discrete solid angles, each associated with a vector direction $\boldsymbol{s}$ fixed in the global Cartesian system (x, y, z). The resolution of this method can be fitted by the angular discretization, analogous to choosing the number of rays for the DTRM. Unlike the DTRM, however, the DO model does not perform ray tracing. Instead, the DO model transforms RTE (Equation 3-122) into a transport equation for radiation intensity in the spatial coordinates. The DO model solves for as many transport equations as there are directions $\boldsymbol{s}$. The solution method is identical to that used for the fluid flow and energy equations.

Two implementations of the DO model are available in ANSYS Fluent: uncoupled and (energy) coupled. The uncoupled implementation is sequential in nature and uses a conservative variant of the DO model called the finite-volume scheme, and its extension to unstructured meshes. In the uncoupled case, the equations for the energy and radiation intensities are solved one by one, assuming prevailing values for other variables. Alternatively, in the coupled ordinates method, the discrete energy and intensity equations at each cell are solved simultaneously, assuming that spatial neighbours are known. The advantage of using the coupled approach is that it speeds up applications involving high optical thicknesses and/or high scattering coefficients. Such applications slow down convergence drastically when the sequential approach is used. However, the reactant applied is not a high optical thick material, the uncoupled scheme was applied in this thesis.

DO Model Equations

The DO model considers the radiative transfer equation (RTE) in the direction $\boldsymbol{s}$ as a field function. Thus, this vector equation written as Equation 3-124, which is a general form.

$$\nabla \cdot (I(\boldsymbol{r}, \boldsymbol{s})\boldsymbol{s}) + (a + \sigma_s) I(\boldsymbol{r}, \boldsymbol{s}) = a_\lambda n^2 \frac{\sigma T^4}{\pi} + \frac{\sigma_s}{4\pi} \int_0^{4\pi} I(\boldsymbol{r}, \boldsymbol{s}') \Phi(\boldsymbol{s} \cdot \boldsymbol{s}')\, d\Omega' \tag{3-124}$$

Because the reactant is the grey body, this model can be converted into the grey-band model, the spatial intensity can be written as

$$\nabla \cdot (I_\lambda(\boldsymbol{r}, \boldsymbol{s})\boldsymbol{s}) + (a_\lambda + \sigma_s) I_\lambda(\boldsymbol{r}, \boldsymbol{s}) = a_\lambda n^2 I_{b\lambda} + \frac{\sigma_s}{4\pi} \int_0^{4\pi} I_\lambda(\boldsymbol{r}, \boldsymbol{s}') \Phi(\boldsymbol{s} \cdot \boldsymbol{s}')\, d\Omega' \tag{3-125}$$

where λ is the wavelength, a_λ is the spectral absorption coefficient, and $I_{b\lambda}$ is the black body intensity given by the Planck function. The scattering coefficient, the scattering phase function, and the refractive index n are assumed independent of wavelength.

To solve this equation and find the radiation field, which is the distribution of the radiation distribution, there are some properties and functions to be figured out, including the phase function for scattering absorption, and scattering coefficient. How to determine these functions and parameters are stated in the section 3.4.5 and 3.4.6 respectively.

Resolution of the model

Each octant of the angular space 4π at any spatial location is discretized into $N_\theta \times N_\phi$ solid angles of extent ω_i, called control angles. The angles θ and ϕ are the polar and azimuthal angles respectively and are measured with respect to the global Cartesian system (x, y, z) as shown in Figure 3.9. The θ and ϕ extents of the control angle, $\Delta\theta$ and $\Delta\phi$, are constant. In three-dimensional calculations, a total of $8N_\theta N_\phi$ directions are solved.

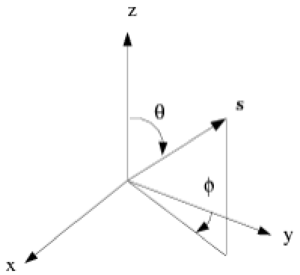

Figure 3.9, Angular Coordinate System

When Cartesian meshes are used, it is possible to align the global angular discretization with the control volume face, as shown in Figure 3.10 (a). For generalized unstructured meshes, however, control volume faces do not in general align with the global angular discretization, as shown in Figure 3.10 (b), leading to the problem of control angle overhang. Essentially, control angles can straddle the control volume faces, so that they are partially incoming and partially outgoing to the face. Figure 3.10 (c) shows a 3D example of a face with control angle overhang.

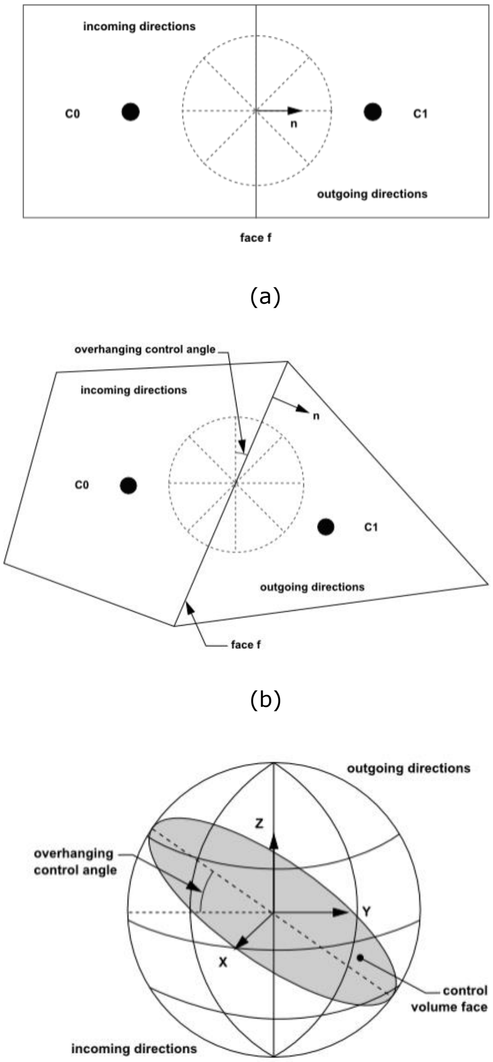

(a)

(b)

(c)

Figure 3.10, Face (a) without Control Angle Overhang and (b) with Control Angle Overhang and (c) 3D form.

The control volume face cuts the sphere representing the angular space at an arbitrary angle. The line of intersection is a great circle. Control angle overhang may also occur as a result of reflection and refraction. It is important in these cases to correctly account for the overhanging fraction. This is done using pixelation. Each overhanging control angle is divided into pixels, as shown in Figure 3.11.

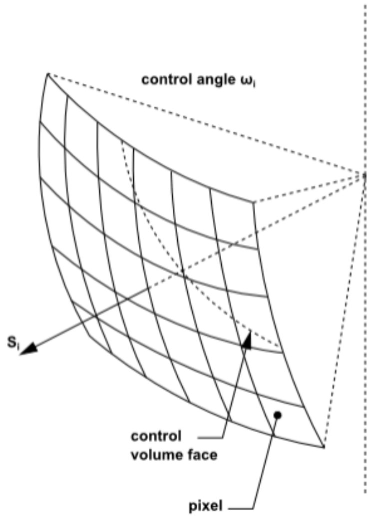

Figure 3.11, Pixelation of Control Angle

The energy contained in each pixel is then treated as incoming or outgoing to the face. The influence of overhang can therefore be accounted for within the pixel resolution. ANSYS Fluent recommends that the default pixelation of 1×1 is usually sufficient for problems involving grey-diffuse radiation. For problems involving symmetry, periodic, specular, or semi-transparent boundaries, a pixelation of 3×3 is recommended. According to Wang et al. (2019), 5x5 and 3x3 are selected as they used in the simulation, for higher resolution.

3.4.5 The Delta-Eddington Phase Function

The scattering of a plane wave by a homogeneous sphere is best described by Mie's formulation of Maxwell's equations. The diversified Mie theory can be used for the entire realm of particle sizes, ranging from Rayleigh scattering (small spheres) to very large spheres where geometric optics and Fraunhofer diffraction apply. But, for practical applications, Mie theory is used for the intermediate size particle theory, where the radius a of the sphere is of the same order as the wavelength λ of the incident radiation. This is challenging to numerically solve the RTE problem accurately when the particle size increase to geometrical scattering which is highly forward-peaked scattering. At mean time the multiple scattering is also different from the single particles. Therefore, a delta-Eddington phase function was applied to estimate the direction of scattering (Han et al., 2017).

The delta-Eddington phase function uses a two term Legendre polynomial expansion of the actual phase function plus a Dirac delta term to account for forward scattering. For the cosine (μ_0) of the angle of scatter between the incident direction $\boldsymbol{s}$ and scattered direction $\boldsymbol{s}'$, the phase function becomes Equation 3-127.

$$\mu_0 = \boldsymbol{s} \cdot \boldsymbol{s}' \tag{3-126}$$

$$\Phi_{\delta E}(\mu_0) = 2f\delta(1-\mu_0) + (1-f)(1+3g'\mu_0) \tag{3-127}$$

where,

$$f = \frac{1}{2}\int_{-1}^{1} \Phi(\mu_0) P_2(\mu_0) d\mu_0 \tag{3-128}$$

$P_2(\mu_0)$ is the second term of Legendre polynomial in the Lorenz–Mie scattering phase function $\Phi(\mu_0)$ calculation, which is $P_2(\mu_0) = \frac{1}{2}(3\mu_0^2 - 1)$.

$$g' = \frac{g-f}{1-f} \tag{3-129}$$

where

$$g = \frac{1}{2}\int_{-1}^{1} \mu_0 \Phi(\mu_0)\, d\mu_0 \tag{3-130}$$

where, g' is asymmetry factor, and the f is the fraction of forward scattering.

By requiring that the second moment of $\Phi(\mu_0)$ agree with the second moment of the Henyey-Greenstein phase function it can be expressed as Equation 3-131 (Joseph et al., 1976).

$$f = g^2 \tag{3-131}$$

Although the multiple scattering differs from the single scattering, it was assumed to estimate the multiple scattering due to the fine mesh was used at the dense packed region. Therefore, Mie theory was applied to obtain the scattering field for different particle sizes.

3.4.6 Absorptions and Scattering Properties Estimation

Absorption coefficient

The absorption coefficient α describes how a chemical species absorbs radiation and thereby attenuates, at a certain wavelength. This property can be measured via UV-Visible spectroscopy, and then the local volumetric rate of energy absorption (LVREA) can be determined. From the absorption spectrum of the reactant, the absorbance at light with a given wavelength λ (A_λ) can be obtained. Then the absorption coefficient can be determined by Equation 3-132 based on the Beer-Lambert law. This property can be also expressed as transmittance (T_λ), and it can be also converted to absorbance as Equation 3-133.

$$a_\lambda = \frac{A_\lambda}{cl} \tag{3-132}$$

$$A_\lambda = -\log_{10} T_\lambda \tag{3-133}$$

Scattering coefficient

The Mie theory is a mathematical-physical theory of the scattering of electromagnetic waves by a homogenous spherical particle. It adopts all size parameters, which is the ratio of the particle radius to wavelength. Thus, in this paper, the Mie scattering theory was applied to calculate the parameters related to the scattering according to the range of size parameter. Based on the Eddington phase function (Equation 3-127), the scattering coefficient, asymmetric factor, and the forward scattering fraction factor are required to be determined. These three parameters are related to the Mie scattering calculation parameter a_j and b_j as follows,

$$a_j = \frac{\bar{n}^2\psi_j(\bar{n}\xi)\left[x\psi_j(\xi)\right]' - \mu_1\psi_j(\xi)\left[\bar{n}\xi\psi_j(\bar{n}\xi)\right]'}{\bar{n}^2\psi_j(\bar{n}\xi)\left[x\varsigma_j^{(1)}(\xi)\right]' - \mu_1\varsigma_j^{(1)}(\xi)\left[\bar{n}\xi\psi_j(\bar{n}\xi)\right]'} \quad \text{3-134}$$

$$b_j = \frac{\mu_1\psi_j(\bar{n}\xi)\left[x\psi_j(\xi)\right]' - \psi_j(\xi)\left[\bar{n}\xi\psi_j(\bar{n}\xi)\right]'}{\mu_1\psi_j(\bar{n}\xi)\left[x\varsigma_j^{(1)}(\xi)\right]' - \varsigma_j^{(1)}(\xi)\left[\bar{n}\xi\psi_j(\bar{n}\xi)\right]'} \quad \text{3-135}$$

$$\bar{n} = n + i\kappa_i \quad \text{3-136}$$

where $\bar{n}$ is the total refractive index of the spherical particle, $\xi = \kappa a$ is the size parameter. In this equation, $\kappa = \frac{2\pi}{\lambda}$ is the wave number. The functions $\psi_j(z)$ and $\varsigma_j^{(1)}(z)$ are spherical Bessel functions of order j (j =1, 2, …) and of the given argument $z = \xi$ or $\bar{n}\xi$ respectively and primes represent their derivatives.

The scattering efficiency Q_{sca} is defined as follows and it can be determined from a_j and b_j.

$$Q_{sca} = \frac{\sigma_{sca}}{\pi a^2} \quad \text{3-137}$$

$$Q_{sca} = \frac{2}{\xi^2}\sum_{j=1}^{\infty}(2j+1)\left(\left|a_j\right|^2 + \left|b_j\right|^2\right) \quad \text{3-138}$$

$$j_{max} = \xi + 4\xi^{\frac{1}{3}} + 2 \quad \text{3-139}$$

$\mathcal{R}(m)$ means the real part of a complex m, and n_{max} is the estimation of the maximum element of the sum.

$$Q_{sca}\langle cos\theta\rangle = \frac{4}{\xi^2}\left\{\sum_{j=1}^{\infty}\frac{j(j+2)}{j+1}\mathcal{R}\left(a_j a_{j+1}^* + b_j b_{j+1}^*\right) + \sum_{j=1}^{\infty}\frac{2j+1}{j(j+1)}\mathcal{R}\left(a_j b_j\right)\right\}$$ 3-140

$$g = \langle cos\theta\rangle = \frac{Q_{sca}\langle cos\theta\rangle}{Q_{sca}}$$ 3-141

The element of the amplitude scattering matrix are of interest as well,

$$S_1 = \sum_{j=1}^{\infty}\frac{2j+1}{j(j+1)}\left(a_j\pi_j + b_j\tau_j\right)$$ 3-142

$$S_2 = \sum_{j=1}^{\infty}\frac{2j+1}{j(j+1)}\left(a_j\tau_j + b_j\pi_j\right)$$ 3-143

where,

$$\begin{cases}\pi_j = \frac{dP_j^l(\cos\theta)}{d\theta}\\ \tau_j = \frac{P_j^l(\cos\theta)}{\sin\theta}\end{cases}$$ 3-144

Here, P_j are the Legendre coefficients of the j^{th} order.

$$P_j(\cos\theta) = \sum_{i=0}^{\left[\frac{j}{2}\right]}(-1)^i\frac{(2j-2i)!}{2^k i!(j-i)!(j-2i)!}(\cos\theta)^{j-2i}$$ 3-145

$$S_{11} = \frac{1}{2}\left[|S_2|^2 + |S_1|^2\right]$$ 3-146

The phase function in terms of scattering angle is the obtained as

$$\Phi(\theta) = \frac{1}{Q_{sca}}\frac{S_{11}(\theta)}{\xi^2}$$ 3-147

Mätzler (2002) developed a full MATLAB code for Mie scattering calculations, then it was applied to estimate the properties of the solid particles.

3.4.7 Cell Zone and Boundary Conditions for Radiation Field

To simulation the complete radiation field, from the light source to particles, large calculation domains are required at the outside of the reactor, from the light source to the reactor wall as showed in the Figure 3.4 (d). To simplify the calculation in a primary step, the radiation behaviour at this region was ignored. The light source and the reflecting wall were arranged elliptical type. The incident radiation flux was assumed constant around the glass wall. This

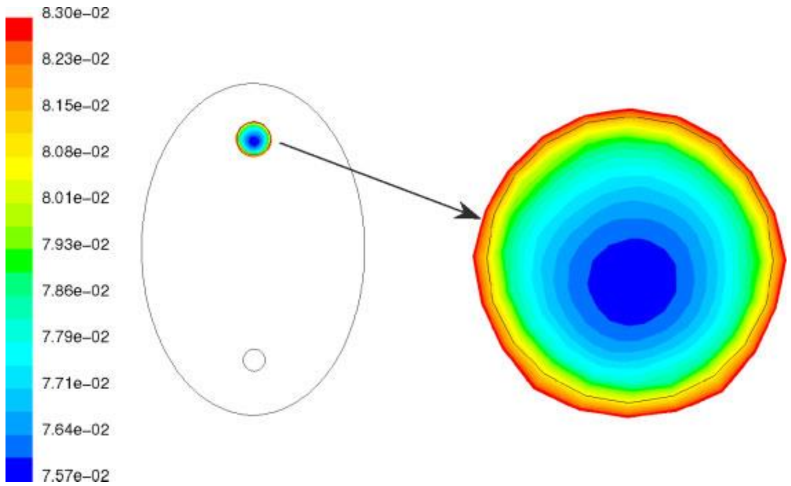

Figure 3.12, Contours of light intensity (einstein m^{-2} s^{-1}**) in an elliptical photoreactor (ellipse major axis = 30 cm, minor axis = 20 cm, reacting tube diameter = 6 cm, lamp diameter = 4 cm, lamp emission power = 0.03** einstein m^{-2} s^{-1}**).(Pareek et al., 2008)**

assumption is reasonable according to Pareek et al. (2008) based on Figure 3.12.

The glass wall was treated as a semi-transparent exterior wall while the swirl pipe was treated as metal opaque wall. This setup was considered based on the experimental verification. There are several casted metal swirl pipes with various dimension, which are going to establish the photoreactor.

Figure 3.13 shows the general case of an irradiation beam applied to an exterior semi-transparent wall with zero thickness and a non-zero absorption coefficient for the material property. An irradiation flux passes through the semi-transparent wall from outside the computational domain into the adjacent fluid medium a. The transmitted radiation can be refracted and dispersed specularly and diffusely, depending on the refractive index (1.3 for glass) and the diffuse fraction of the glass.

Note that there is a reflected component q_{irrad} of when the refractive index of the wall n_b is not equal to 1, as shown in the Figure 3.13.

Which type of the transmitted and reflected radiant energy at the semi-transparent wall was described by the diffuse fraction f_d. If this fraction is equal to 1, all of the radiant energy propagates purely diffusely at the wall, while it is purely specular when the fraction is 0.

Whether the glass wall is diffuse or specular reflector is depending on the material and the surface condition of the reflecting wall of the reactor shown in the Figure 3.3. Because the space inside the dark box, except that inside the tube where particles flow, was ignored, a large amount of input radiation comes from the reflection of the wall. In this research, the glass wall was assumed

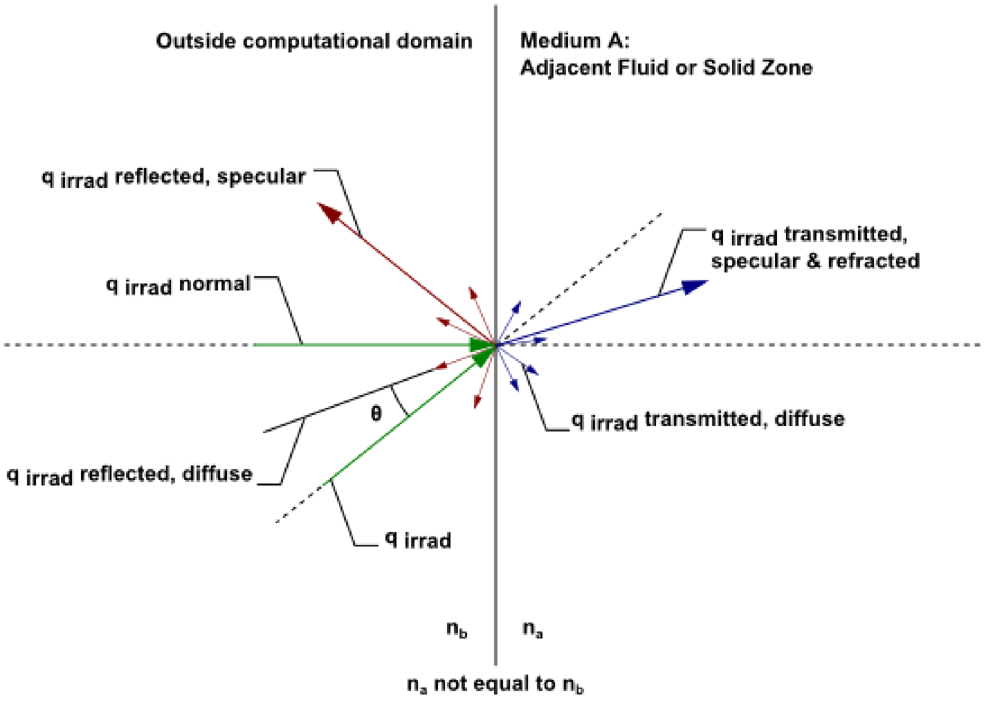

Figure 3.13, DO Irradiation on External Semi-Transparent Wall

as totally diffused in terms of transmitting and reflecting radiant energy. This assumption was based on the following reasons. Firstly, the absorbance of the reactant is relatively low. Therefore, the light can transport through the reactor and then reflected back into the system. Due to the scattering behaviour and the changing particle distribution, the directions of the reflected radiation are chaotic. At mean time, the flatness of the metal wall may not be even, which also results in the diffused incident radiation.

For a purely diffuse case, the interfacial reflectivity $r(\boldsymbol{s})$ is assumed independent of $\boldsymbol{s}$, and equal to the hemi-spherically averaged value r_d. For $n = \frac{n_a}{n_b} > 1$, $r_{d,b}$ are given by Equation 3-148.

$$r_{d,b} = \frac{1}{2} + \frac{(3n+1)(n+1)}{6(n+1)^2} + \frac{n^2(n^2-1)^2}{(n^2+1)^3}\ln\left(\frac{n-1}{n+1}\right) - \frac{2n^3(n^2+2n-1)}{(n^2+1)(n^4-1)} + \frac{8n^4(n^4+1)}{(n^2+1)(n^4-1)}\ln(n) \qquad 3\text{-}148$$

$$r_{d,a} = 1 - \left(\frac{1-r_{d,b}}{n^2}\right) \qquad 3\text{-}149$$

The boundary intensity for all outgoing directions on side of the interface is given by

$$I_{w,b} = \frac{r_{d,b}q_{in,b}+\tau_{d,a}q_{in,a}}{\pi} \qquad 3\text{-}150$$

$$I_{w,a} = \frac{r_{d,b}q_{in,b}+\tau_{d,b}q_{in,b}}{\pi} \qquad 3\text{-}151$$

where,

$$q_{in,a} = -\int_{4\pi} I_{w,a}\,\boldsymbol{s}\cdot\boldsymbol{n}d\Omega,\ \ \boldsymbol{s}\cdot\boldsymbol{n} < 0 \qquad 3\text{-}152$$

$$q_{in,b} = -\int_{4\pi} I_{w,b}\,\boldsymbol{s}\cdot\boldsymbol{n}d\Omega,\ \ \boldsymbol{s}\cdot\boldsymbol{n} < 0 \qquad 3\text{-}153$$

When medium b is external to the domain as in the case of an external semi-transparent wall, $q_{in,b}$ is the boundary condition inputs, specified in the boundary condition list. The refractive index of the external medium is assumed to be 1, which is air. Then the

There is an additional flux beyond that is applied when the radiation wall boundary condition was applied. This external flux at the semi-transparent wall is computed as Equation 3-154.

$$Q_{ext} = \varepsilon_{ext} \sigma T_{rad}^4 \tag{3-154}$$

The fraction of the above energy that will enter the domain depends on the transmissivity of the semi-transparent wall under consideration. This energy is distributed across the solid angles, which is similar to the diffuse semi-transparent wall.

Incident radiation can also occur on external semi-transparent walls. Refer to the previous discussion on interior walls for details since the radiation effects are the same.

The irradiation beam is defined by the magnitude, beam direction, and beam width. The irradiation magnitude is specified in terms of an incident radiant heat flux (w/m^2). Beam width is specified as the solid angle over which the irradiation is distributed (that is, the beam θ and ϕ extents). The default beam width in ANSYS Fluent is 1×10^{-6} degrees which is suitable for collimated beam radiation. Lastly, beam direction was discussed before.

3.5 Reaction Models

3.5.1 Introduction

The solid-state reaction field was simulated by the species conservation coupled with the finite-rate volumetric reaction model. This model can describe the convections, diffusion, and reaction source for each species components.

3.5.2 Species Conservation

Equation 3-155 is the conservation equation for chemical species. The local mass fraction Y_i, through the solution of a convection-diffusion equation for the i^{th} species.

$$\frac{\partial}{\partial t}(\rho Y_i) + \nabla \cdot (\rho \mathbf{u} Y_i) = -\nabla \cdot \boldsymbol{J}_i + R_i + S_i \tag{3-155}$$

where the R_i is the net rate of the production of the species i from the chemical reaction and the S_i is the rate of creation by addition or any other defined source. An equation of this form will be solved for $N - 1$ species where N is the total number of fluid phase chemical species in the system. $\boldsymbol{J}_i$ is the mass transfer rate.

3.5.3 Laminar Framework

Because the studied type of the solid-state photochemistry is the single -crystal-to-single-crystal (SCSC) reaction, there is no mass transfer between carrier and the reactant particles. Then, it cannot be affected by the turbulence. Therefore, the laminar framework was selected to simulate reaction, where effect of turbulent fluctuations can be ignored.

This laminar framework includes mass diffusion $\boldsymbol{J}_i$ in laminar flows (Equation 3-156) and the laminar finite-rate model (Equation 3-157).

$$\boldsymbol{J}_i = -\rho D_{i,m} \nabla Y_i - \frac{D_{T,i} \nabla T}{T} \tag{3-156}$$

where $D_{i,m}$ is the mass diffusion coefficient for species in the mixture and $D_{T,i}$ is the thermal diffusion coefficient.

The reaction rates that appear as source terms in Equation 3-155 are computed in ANSYS Fluent. The laminar finite-rate model was selected as basic framework for SCSC solid-state photoreaction. This framework using the Arrhenius kinetic expressions to affect the reaction rate.

$$R_i = M_{w,i} \sum_{r=1}^{N_R} \hat{R}_{i,r}$$

3-157

where $M_{w,i}$ is the molecular weight of species i and $\hat{R}_{i,r}$ is the Arrhenius molar rate of production/consumption of species i in reaction.

Equation 3-158 considers the r^{th} reaction in a general form. $\mathcal{M}_i$ represents the symbol donating the i species. N is the number of chemical species in the system. $\nu'_{i,r}$ and $\nu''_{i,r}$ are stoichiometric coefficient for reactant i and product i in the reaction r respectively, while $k_{f,r}$ and $k_{b,r}$ are the forward and backward rate constant respectively.

$$\sum_{i=1}^{N} \nu'_{i,r} \mathcal{M}_i \underset{k_{b,r}}{\overset{k_{f,r}}{\rightleftharpoons}} \sum_{i=1}^{N} \nu''_{i,r} \mathcal{M}_i$$

3-158

In this thesis, the SCSC reaction was regarded as irreversible. The general form of the irreversible reaction rate for species i is displayed as Equation 3-159.

$$\hat{R}_{i,r} = \left(\nu''_{i,r} - \nu'_{i,r}\right)\left(k_{f,r} \prod_{j=1}^{N} \left[C_{j,r}\right]^{\eta'_{j,r}+\eta''_{j,r}}\right)$$

3-159

$$k_f = A_r T^{\beta_r} e^{-\frac{E_A}{RT}}$$

3-160

where, $C_{j,r}$ is the molar concentration of species j in reaction r (kmol/m^3), $\eta'_{j,r}$ and $\eta''_{j,r}$ are the rate exponent for reactant and product species j in reaction r respectively.

Equation 3-160 determines the rate constant for reaction r from the Arrhenius expression. A_r is the pre-exponential factor, β_r is the temperature exponent, E_r is the activation energy for the reaction and R is the ideal gas constant.

3.5.4 Limitation and Further Model Building

The laminar framework is the most realistic model available in the ANSYS Fluent to determine the field of the reaction rate for SCSC reaction. However, it cannot express the relationship between the light intensity of the reaction rate.

One of the core problems to be solved in this project is study how particle distribution affects the radiation field which determine reaction rate field further. Then, the relationship between the light intensity of the reaction rate is important. However, there is no full study on the kinetics of SCSC reaction. Therefore, a model building of SCSC reaction was performed in the Chapter 5 to find the relationship.

3.6 Boundary Conditions

3.6.1 Operating Conditions and Materials

The operating conditions allow the user to set the operating pressure, include the effects of gravity and specify other operating variables. Following the FLUENT documentation, the 0 ambient pressure was used which would minimise errors due to the small pressure drop across the flow domain compared to atmospheric pressure. The gravity acting on the negative y axis at 9.81 m/s^2 was included. The operating density was not specified, thus permitting the solver to calculate it by averaging over all cells.

There are four types of materials are involved in this simulation, including the opaque swirl pipe, transparent reactor section, flow carrier fluid and reactant. The opaque swirl pipe was made of stainless steel, while the transparent reactor section was made of glass. What material are used for the fluid and the solid particles are specified in the specific case. In this reactor design, air and water were selected as the carrier, while the titanium oxide (TiO_2) and the cinnamic acid were selected as the solid materials. The properties of them are listed in the Table 3-2.

The fluid carrier was set as the primary phase while the solid reactant was set as the secondary phase. The secondary phase was set as granular phase. The models to describes the properties of the granular flow was described in the section 3.3. The packing limit of the solid particle was set as 0.5 (volume fraction).

3.6.2 Inlet Boundary Condition

At the inlet, a uniform mean flow velocity boundary condition was firstly applied, which are normal to the boundary. For the uniform flow, the solid particle was set the same velocity as the fluid. The volume fraction of the solid particle was set constant as well for the uniform entry. The turbulence of the inlet flow was specified in terms of the hydraulic diameter and the turbulence intensity. In this case, the hydraulic diameter equals the diameter of the pipe, while the turbulence intensity is determined as the ratio of the root-mean-square of the velocity fluctuation (Equation 3-161).

$$I = 0.16 \times Re^{-\frac{1}{8}} \tag{3-161}$$

$$Re = \frac{\rho \bar{u} D}{\mu_f} \tag{3-162}$$

where Re is the Reynolds number, $\bar{u}$ is the average velocity of the corresponding phase, D is the hydraulic diameter, and the μ_f is the viscosity of the fluid. Different velocity and different materials are applied, then the turbulence intensities for different cases are determined and displayed at corresponding section.

Apart from the uniform inlet condition, user-defined inlets are also applied. In these conditions, the flow conditions are written as profiles of velocities at different directions. At mean time, the turbulence of this inlet is the described by the turbulence kinetic energy and the specific dissipation rate, which can be also described by the profile. The distribution of the particles was also filled in the inlet boundary condition by the same method.

3.6.3 Outlet Boundary Condition

A pressure outlet boundary condition with zero uniform static pressure was imposed at the outlet of the computational model. This boundary condition results in a better rate of convergence when backflow occurs during iteration. The turbulence was specified in terms of intensity and hydraulic diameter at the outlet in the same way as the inlet.

3.6.4 Wall Boundary Condition

The pipe walls were specified as being stationary and no slip walls to match the simulation conditions. The no slip condition for viscous fluids is that at a solid boundary, the fluid will have zero velocity relative to the boundary.

The wall roughness of the development section and the test section was set by specifying the roughness height (h), as 1.237×10^{-6} m which is the same value as the measured roughness of transparent

Perspex pipes used in the experimental rig. The roughness was measured employing a surface roughness tester. The internal surface roughness of the swirl pipe was specified as 9×10^{-6}m which is the measured roughness of the stainless-steel swirl pipe produced through investment casting. The two roughness values are small enough that the walls can be considered as hydraulically smooth (Li, 2016).

The light source was set as the wall boundary condition as the photons enter this system through the transparent pipe. According to the design of the design of the full reactor and the assumptions, the diffused radiation was set as constant. The detailed constant was specified at the corresponding section.

3.7 Solution Formulation

3.7.1 Solver and Pressure-velocity Coupling Scheme

To solve a fluid flow numerically, ANSYS FLUENT allows user to choose one of the two numerical methods: pressure-based solver and density-based solver. However, the density based solve is incompatible with the multiphase model, then the pressure-based solver was selected.

Two algorithms exist under the pressure-based solver for single phase in ANSYS FLUENT: a segregated algorithm and a coupled algorithm. In the segregated algorithm the governing equations are solved sequentially, segregated from one another, while in the coupled algorithm the momentum equations and the pressure-based continuity equation are solved in a coupled manner. In general, the coupled algorithm significantly improves the convergence speed over the segregated algorithm; however, the memory requirement for the coupled algorithm is more than the segregated algorithm.

For Eulerian multiphase calculations, ANSYS Fluent can solve the phase momentum equations, the shared pressure, and phasic volume fraction equations in a coupled and segregated fashion. When solving the equations in a segregated manner, ANSYS Fluent uses the phase coupled SIMPLE (PC-SIMPLE) algorithm (Vasquez, 2000) for the pressure-velocity coupling. PC-SIMPLE is an extension of the SIMPLE algorithm (Patankar, 1980) to multiphase flows. The velocities are solved coupled by phases, but in a segregated fashion. This is attained by effectively transforming the total continuity into a shared pressure. It has been successfully implemented and solves a wide range of multiphase flows.

One of the fundamental problems is that the resulting matrix is not symmetric and that the continuity constraint may contribute to a zero-diagonal block, making the solution difficult to obtain. One way to circumvent this problem is to use direct solvers, but these are too expensive for large industrial cases. In addition, we need to avoid a zero diagonal, resulting from the continuity constraint, and like the segregated solver, we need to construct a pressure correction equation. In multiphase, we also have the additional problem of the vanishing phase, which for the coupled solver is important to ensure some continuity in the coefficients. Like the Coupled, a Rhie and Chow type of scheme is used to calculate volume fluxes and to provide proper coupling between velocity and pressure, thereby avoiding unphysical oscillations.

The Coupled scheme solves all equations for phase velocity corrections and shared pressure correction simultaneously (Ghobadian and Vasquez, 2007). These methods incorporate the lift forces, and the mass transfer terms implicitly into the general matrix. This method works very efficiently in steady state situations, or for transient problems when larger time steps are required.

3.7.2 Discretization Scheme

Steady-State Iterative Algorithm

A steady-state calculation was selected as the studied example for reactor design. The governing equations for the pressure-based solver do not contain time-dependent terms when the steady-state is applied. For steady-state flows, control-volume-based discretization of the steady-state transport equation in each control volume becomes Equation 3-163, where ρ is the density, $\boldsymbol{v}$ is the velocity vector, $\boldsymbol{A}$ is the surface vector, Γ_Φ is the diffusion coefficient of scaler Φ, $\nabla\Phi$ is the gradient of Φ, and S_Φ is the source of Φ per unit volume. According to this equation, those govern equations were solved according to different discretization scheme.

$$\oint \rho\Phi\boldsymbol{v}\cdot d\boldsymbol{A} = \oint \Gamma_\Phi \nabla\Phi \cdot d\boldsymbol{A} + \int_V S_\Phi dV \tag{3-163}$$

The under-relaxation of variables is used in all cases for some material properties, in the NITA solver for solution variables, and in the pressure-based coupled algorithm where this explicit under-relaxation is used for momentum and pressure.

Because of the nonlinearity of the equation set being solved by ANSYS Fluent, it is necessary to control the change of Φ. This is typically achieved by under-relaxation of variables (also referred to as explicit relaxation), which reduces the change of Φ produced during each iteration. In a simple form, the new value of the variable Φ within a cell depends upon the old value, Φ_{old}, the computed change in Φ, $\Delta\Phi$, and the under-relaxation factor, α, as follows:

$$\Phi = \Phi_{\text{old}} + \alpha\Delta\Phi \tag{3-164}$$

The under-relaxation of equations, also known as implicit relaxation, is used in the pressure-based solver to stabilize the convergence behaviour of the outer nonlinear iterations by introducing selective amounts of Φ in the system of discretized equations. This is equivalent to the location-specific time step.

$$\frac{a_p\Phi}{\alpha} = \sum_{nb} a_{nb}\Phi_{nb} + b + \frac{1-\alpha}{\alpha} a_p\Phi_{old} \tag{3-165}$$

Spatial Discretization

In the Finite-Volume Method, the computational domain is divided into a finite number of elements known as control volumes by the regular and irregular arrangement of nodes, known as the mesh. Flow parameters are resolved around these nodes, so that the fluid flow can be described mathematically by specifying its velocity at all points in space and time.

ANSYS FLUENT, by default, stores discrete values (e.g. pressure, velocities and turbulence) of the scalar at the cell centres. However, face values are required for the convection terms and must be interpolated from the cell centre values. This is achieved through an upwind scheme. Upwinding means that the face value is derived from quantities in the cell upstream, or “upwind” relative to the direction of the normal velocity.

- **Upwind advection schemes**

ANSYS FLUENT provides several upwind advection schemes for momentum, kinetic energy, specific dissipation rate, energy, discrete ordinates, and species: first-order upwind, second-order upwind, power law, QUICK and third-Order MUSCL scheme.

In the first-order upwind scheme, quantities at cell faces are determined by assuming that the cell centre values of any field variable represent a cell-average value and hold throughout the entire cell. Therefore, when first-order upwinding is selected, the face value is set equal to the cell-centre value of in the upstream cell.

When second-order upwind scheme is used, the higher-order accuracy quantities at cell faces are achieved through a Taylor series expansion of the cell-centred solution about the cell centroid. The face value is the sum of the cell-centred value and the product of its gradient in the upstream cell multiplies the displacement vector from the upstream cell centroid to the face centroid.

The power-law discretization scheme interpolates the face value of a variable using a solution the same as to a one-dimensional convection-diffusion equation. QUICK (Quadratic Upstream Interpolation for Convection Kinetics) type schemes are based on a weighted average of second-order-upwind and central interpolations of the variable. The third-Order MUSCL scheme was conceived from the original MUSCL (Monotone Upstream-Centred Schemes for Conservation Laws) by blending a central differencing scheme and second-order upwind.

ANSYS FLUENT states that, when flow is aligned with the mesh, the numerical diffusion will be naturally low; a first-order scheme yields better convergence without any significant loss of accuracy. However, when flow is not aligned with the mesh, the first-order convective discretization increases numerical discretization error. The second-order scheme generally obtains more accurate results especially for complex flows. In summary, while the first-order discretization generally yields better convergence than the second-order scheme, it generally will yield less accurate results, especially on triangular/tetrahedral meshes.

The QUICK and third-order MUSCL discretization schemes may provide better accuracy than the second-order scheme for rotating or swirling flows. In general, the second-order scheme is sufficient and the QUICK and third-order MUSCL schemes will be applied to meet higher accuracy for specific value (e.g. volume fraction of particles). The power law scheme will generally yield the same accuracy as the first-order scheme.

- **Pressure interpolation schemes**

Similarly, the face values of pressure are computed from the cell values adopting pressure interpolation schemes. The ones available in ANSYS FLUENT, when pressure-based solver is used, include: second-order, body-force-weighted, and the PRESTO! (PREssure STaggering Option) scheme.

The second-order scheme reconstructs the face pressure in the manner used for second-order accurate convection terms. This scheme may provide some improvement over the standard and linear schemes, but it may have some trouble if it is used at the start of a calculation and/or with a bad mesh. This method is not applicable for porous medium and the use of the VOF (Volume of Fluid) or mixture model for multiphase flow.

The body-force-weighted scheme computes the face pressure by assuming that the normal gradient of the difference between pressure and body forces is constant. This works well if the body forces are known a priori in the momentum equations (e.g., buoyancy and axisymmetric swirl calculations).

Generally, for problems involving large body forces, the body-force-weighted scheme is recommended. While for flows with high swirl numbers, high-Rayleigh-number natural convection, high-speed rotating flows, flows involving porous media, and flows in strongly curved domains, the PRESTO! scheme is recommended.

3.7.3 Convergence Judgment

The iterative process is repeated until the change in the variable from one iteration to the next becomes so small that the solution can be considered converged. There are no universal metrics for judging convergence; however, it is common to require the scaled residuals to be in the order of 10^{-3} to 10^{-4} or less for convergence.

However, the residuals of continuity stay at a high value sometimes for multiphase flow especially, with unchanged residuals for other monitored terms. In mean meantime, a pseudo convergence often happens for steady-state multiphase flow that processing data (volume fraction was advancing) shows an approximately constant at a low value. Therefore, the residual was not the single criterion.

In this thesis, the convergence was judged by three criteria, residual, imbalance of important scalar (e.g. mass) and the value change at important surface (e.g. Area-average pressure at inlet surface). When requirements (listed as follows) are all met, this calculation is regarded as convergent.

- The residual is smaller than 10^{-4}.
- The imbalance of the important scalar is smaller than 1%.
- The monitored value keeps constant or fluctuates around a value for 200 iterations.

3.8 Conclusions

In conclusion, the full setup was listed in the Table 3-2. In this summary, the overall settings are all displayed including properties, measured value, selected models, solution schemes and constants. Some of the boundary condition set-up is depending on the specific cases and these studied data were specified individually at where discussed.

Table 3-2 Summary of the full set-up

General setting	
	Gravity: -9.81 at y direction
Materials setup	
Materials – fluid	Air • Density = 1.225 kg/m^3 • Viscosity = 1.7894 e^{-5} kg m^{-1}s^{-1} Water • Density =998 kg kg/m^3 • Viscosity =0.001 kg m^{-1}s^{-1} Powder-cinnamic acid • Density = 1248 kg m^{-3} • Reference temperature =298K • Absorption coefficient = user-defined • Scattering coefficient = user-defined • Scattering phase function: delta-Eddington • delta-Eddington constant: refer to Chapter 6 • Refractive Index = 1.55

	Titanium Oxide (TiO_2) • Density = 3500 kg m^{-3} • Reference temperature =298K • Absorption coefficient = user-defined • Scattering coefficient = user-defined • Scattering phase function: isotropic • delta-Eddington constant: refer to Chapter 6 • Refractive Index = 1.55
Materials – solid	GLASS • Refractive Index = 1.3 STAINLESS STEEL
Model setup	
Multiphase model	Eulerian-Eulerian Number of Eulerian Phase = 2 Volume fraction Parameter’s formulation: implicit
Carrier	
• Primary phase	Air or water
Solid Phase	
• Secondary phase	Granular mode Diameter: 200 nm~5 μm Granular viscosity model: Gidaspow Granular bulk viscosity model: lun-et-al Granular temperature: algebraic Solid pressure: lun-et-al Radial distribution: lun-et-al Elasticity modulus: Derived Packing limit = 0.5
Phase Interaction	Virtual mass modelling: on Drag force: Huilin-Gidaspow model. Turbulence dispersion: Simonin Turbulence interaction: Simonin-et-al Restitution coefficient=0.9
Viscous model	k-ω SST Low Re correlation Per-Phase turbulence multiphase model Model constant refers to Chapter 3 Section 3.3.8

Radiation model	DO model: 5x5 $\theta \times \phi$ Division 3x3 $\theta \times \phi$ Pixels Solar load: off Energy Iteration per Radiation Iteration:10
Reaction model	The Finite-Rate Volumetric reaction rate model Laminar framework with user-defined function Specified at Chapter 3
Boundary conditions	Inlet: Velocity inlet • Fluid velocity: specified individually. • Powder velocity: specified individually. • Volume fraction: specified individually. Turbulence specification method: turbulence intensity & Hydraulic diameter Turbulence intensity follows Equation 3-161 Hydraulic diameter =1 cm Outlet: Pressure outlet • Gauge pressure=0 Pa Reactor Wall: Stationary wall • Roughness height = 1.237×10^{-6} m • Thermal conditions: radiation • External emissivity = 0.98 • External radiation temperature = 298K • BC type = semi-transparent • Diffuse irradiation = specified individually • Diffusion fraction = 1 SWIRL PIPE: Stationary wall • Roughness height = 9×10^{-6}m • Thermal: off • BC type: Opaque • Internal emissivity =1 • Diffuse fraction=0.05 DEVELOPING PIPE: Stationary wall • Roughness height =1.237×10^{-6} m • Thermal conditions: off • BC type: Opaque

	• Internal emissivity =1 • Diffuse fraction=0.05
Solver	Pressure-based Absolute velocity formulation Transient and Steady simulation depending on the trial.
Solution methods	Phase Coupled SIMPLE Scheme Spatial Discretization: Gradient: Least Squares Cell Based Pressure: PRESTO! Volume fraction: QUICK Momentum: Second order upwind Turbulence Kinetic Energy: Second order upwind Specific Dissipation Rate: Second order upwind Energy: Second order upwind DO: Second order upwind Species: Second order upwind

Chapter 4 Characteristics of Multi-phase Swirl Flow

4.1 Introduction

To design a flow photoreactor for solid-state reaction, the characteristics of the multiphase swirl flow were first studied, in terms of its performance on hydrodynamics and particle distribution. This chapter presents a CFD simulation of the swirl-induced flow through a horizontally placed four-lobed swirl pipe. The steady state $k-\omega$ SST model with the Eulerian multiphase model was applied to determine the flow. The analysis was focused on the variation of flow parameters downstream of the swirl pipe as this is the region for the photoreaction.

The performance of swirl pipe was studied by comparison with the circular pipe without swirl induced. Different particle distributions were applied in the inlet conditions of these both geometries, including uniform, settled and semi-settled particles.

Tangential velocities, pressure drop, swirl intensity at the reactor region were studied. Meanwhile the particle distribution was also analysed. The research focus about these characteristics was on studying the potential of the swirl flow on the redistribution of the particles, which construct a basic concept of the multiphase swirl flow.

4.2 Simulation Set-up

The numerical method, turbulence models and wall functions used, the meshing method, the solver parameters and the solution convergence criterions employed were the same as used in the section 3.7.3. The geometry of the simulation was shown in the Figure 4.1.

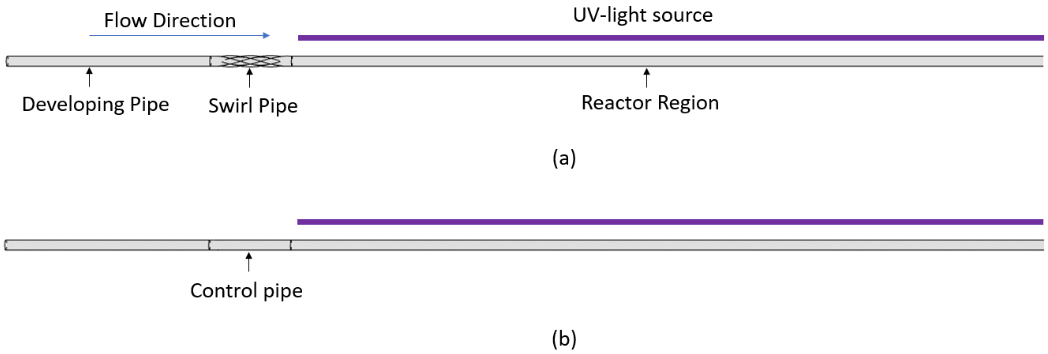

(a)

(b)

Figure 4.1 Configuration of (a) Geo.1, long pipe. Length of reaction region, L=500D, and (b) Geo.5 control pipe, with the same arrangement as Geo.1 where the swirl pipe was replaced by a circular pipe for comparison.

In the inlet condition of the simulation, the velocity of 12 m/s and the volume fraction of 0.004275 cinnamic acid with the diameter of 5μm were first applied. The turbulence intensity was obtained via Equation 3-161 p169 and the hydraulic diameter was 10 mm. The simulation was performed on Geo.1 and Geo.5. This inlet condition is named entry 1 (E1).

The inlet spatial distribution of the particles affects the performance of the swirl pipe reactor. The uniform entry (E1) is an ideal condition from the storage of the raw material, while the more common condition is that particles settle at bottom of the pipe. Meanwhile, when the reaction rate is slow, the long retention time results in this common sedimentation as well. Therefore, to study the ability of the re-distribution of particles, the inlet condition of settled particles had to be set.

However, it is difficult to describe the settled condition directly. Thus, writing a profile and reading it as the inlet condition was applied to create a settled inlet condition. A profile cut from the close end (490D with the indication at Figure 4.2) at the first trial, E1, was set as the inlet condition of the second trial (E2), where particles deposit at bottom of the pipe. Similarly, the inlet condition of Entry 3 (E3) was set from the profile at the 150D of the Entry 2 with a similar statement. This selection is based on the result of E1 both for long pipe and control pipe shown in the Figure 4.8. This profile cutting provides a uniform entry, settled entry as well as the partially settled entry (Figure 4.3), and the average value for these three entries was listed in the Table 4-1.

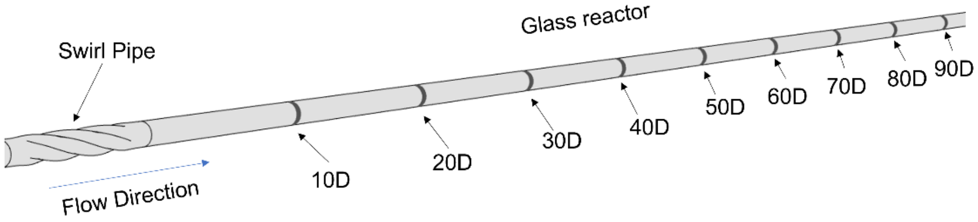

Figure 4.2 Indication of the postion at the downstream swirl pipe.

Table 4-1 displayed the boundary conditions of each inlet. For E1, the inlet condition was estimated by the hydraulic diameter and the turbulence intensity (in section 3.6.2). The slight difference in the velocities, kinetic energy and the dissipation rate shows that the variable of these different entries is controlled in the particle distribution. Because the settled inlet was cut from the close end of the outlet in the uniform case E1, the numbers of the particles (shown as volume fraction of solid) of E2 and E3 were much larger than that in E1 due to the accumulation from settlement.

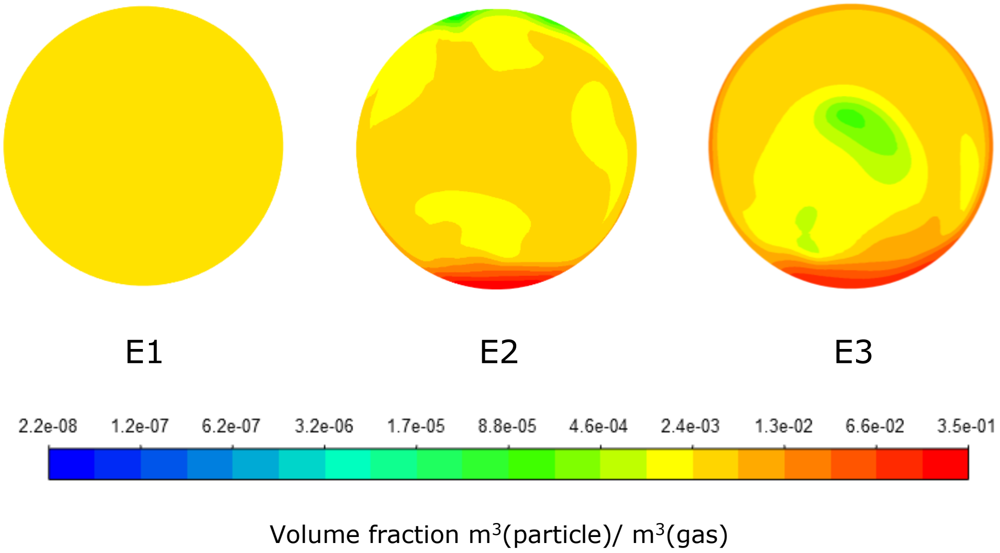

Figure 4.3 Particle distribution of the different entry condition. E1 is uniform, E2 is settled, and E3 is semi-settled.

Table 4-1 Area-weighted average value of each entry condition

Item	E1	E2	E3
Volume fraction (m^3/ m^3)	0.004275	0.006704	0.006023
Gas velocity (m/s)	12	12.07	12.08
Particle velocity (m/s)	12	12.01	11.99
Kinetic energy(m^2/s^2)	/	1.53	1.84
Specific Dissipation rate (s^{-1})	/	2485.56	2578.57

4.3 Characteristics of Velocity Field

The swirl effect cannot always sustain in the reactor, and it dissipate at a certain distance downstream depending on the inlet condition (Li 2016). The streamline gives a general presentation of the swirl flow shown as in the Figure 4.4. It illustrates a spiral movement with decreasing rotation rate. This phenomenon implies that the retention time is slightly increased due to the twisted flow path.

Based on this characteristic, the swirl pipe can be installed in series or parallel to meet the requirement according to the reaction rate, which is the conceptual design of the reactor (shown as in the

Figure 3.3, Swirl-induced pipe and a proposed reactor structure). Therefore, the basic characteristics are required to be studied such as the effective length of the swirl flow regime. The swirl was assessed by the tangential velocity and pressure drop which are highly related to the reactor design.

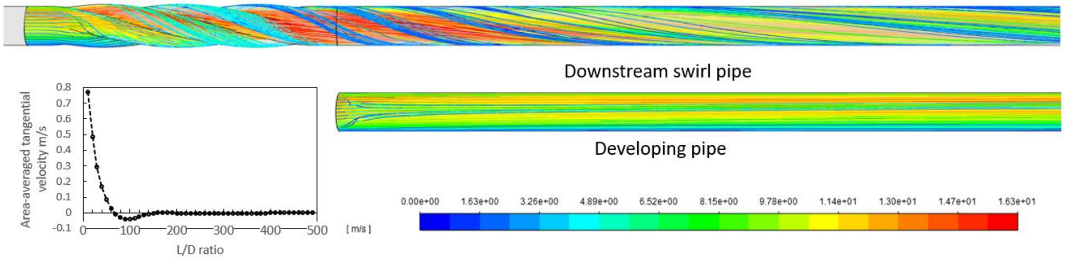

Figure 4.4 Comparison between streamlines with and without the swirl pipe along the reactor, downstream swirl pipe for E2 entry on Geo.1.

4.3.1 Tangential Velocity

Swirling flow is a type of fluid flow that has both axial and tangential velocity components. The tangential velocity is the velocity component that is perpendicular to the axis of rotation and parallel to the circular path of the fluid particles. It affects the pressure distribution, vortex formation, mass transfer, and mixing characteristics of the swirling flow.

As shown in Figure 4.5, the vectors show that a vortex was formed caused by the swirl pipe. This vortex rotates anti-clockwise and start decaying at about 50D length after the swirl pipe where there are vectors moves opposite near the wall. With the tangential velocity decreasing (Figure 4.6), it cannot afford a sufficient the centripetal force, and the interaction between particles and gas carrier compel the flow downward following the movement of particles at right hand side. This movement shifts the centre of the vortex to the left, and another vortex forms to make up the rest space. This new vortex grows up, and it still cannot afford to drag particles up due to the weaker tangential velocities. As a result, these two vortexes form a convection finally after they are balanced.

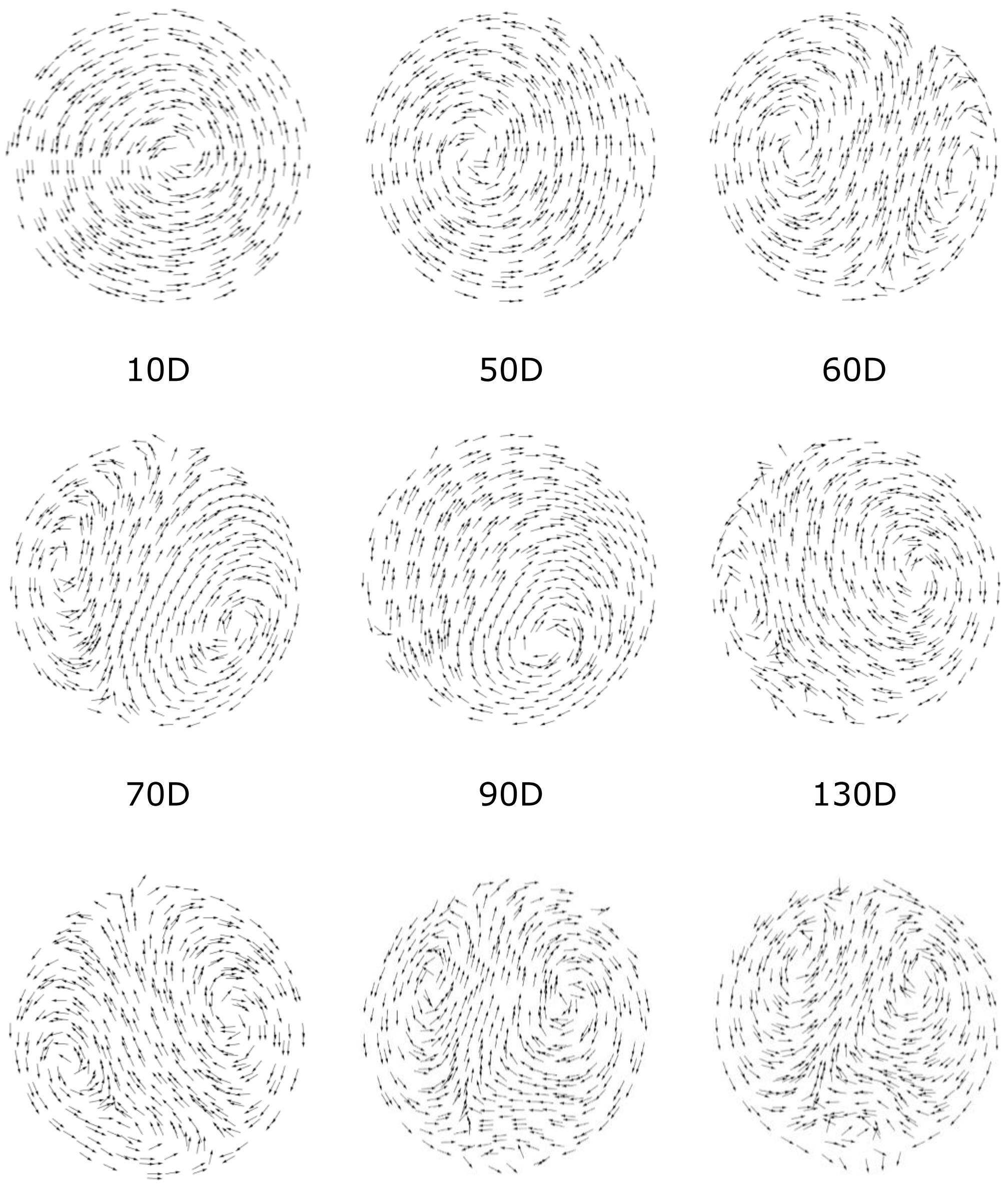

10D 50D 60D

70D 90D 130D

150D 270D 400D

Figure 4.5 Direction vectors of the flow at the x-y plane (cross-section plane) at a different positions for the E2 case and the flow direction (z-axis), is perpendicular to the page and out of the page.

错误!未找到引用源。 zoom in the tangential velocity in the region between 50D to 150D, where minus tangential velocity appears. The tangential velocities for the settled E2 and the semi-settled E3 decrease and touch zero point about 67D while they increase at turning point is about 95D and reach zero at bout 150D. The first zero point represents that the intensity of the swirl is not strong enough to afford the circular motion. This point for E1 case comes later because some of the particles flows following the centre line, which is less affected by the tangential velocity. Therefore, this velocity can afford sufficient centrifugal force for longer. The E2 case shows a lower valve of the tangential velocity while the other two cases show a similar minimum value. The smaller value of the tangential velocity, the more reverse circular movement. This lower value means that the particles is less re-distributed. The second zero point implies that the convection is formed, and it is basically balanced where the swirl effect is totally disappeared and the most of particles settles.

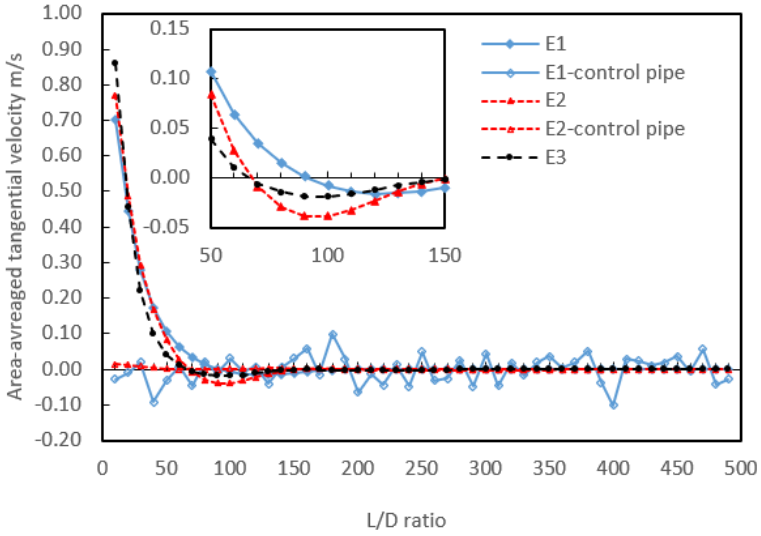

Figure 4.6 Area-averaged tangential velocity along the reactor

4.3.2 Pressure Drop

Pressure is the force applied to a unit area of surface. In a dynamic system, pressure typically is defined using three terms, the static pressure, the dynamic pressure and the total pressure. The static pressure can be identified for every point in a body of fluid, regardless of whether the fluid is in motion or not. The dynamic pressure is associated with the velocity or the flow of the fluid. The total pressure is the sum of the static pressure and the dynamic pressure.

For the current flow system where the circular and swirl pipe have a constant cross-sectional area, the dynamic pressure is constant throughout the system for a given flow velocity. The static pressure was used to understand the flow behaviour within the top horizontal section of the rig that was modelled. The pressure drop along the reactor was shown in the Figure 4.7. It is obvious that the pressure drop is related to the particle distribution. With the particle settles, the pressure drop increase. Meanwhile the swirl flow also caused the pressure drop. From this figure, the gradient is increasing at the outlet of the swirl pipe (or beginning of the reaction region) caused by the strong swirl as well as the particle distribution.

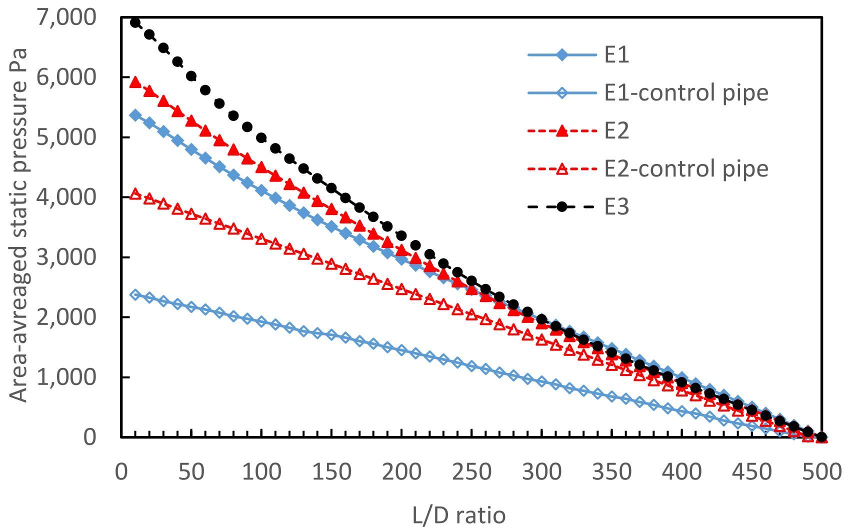

Figure 4.7 area-averaged static pressure along the reactor

4.4 Characteristics of Particle Distribution

The particle distribution was analysed in two aspects, particle loading (in terms of volume fractions) and the relative position of the particles. The area average of particle volume fraction on cross section was applied to analyse the axial distribution, while the relative position on the cross-section area was displayed by the contours of the volume fraction.

4.4.1 Particle Distribution along Reactor

Figure 4.8 shows the volume fraction of the particles along the reactor. This diagram shows the potential that the swirl effect has the potential to concentrate the particles. Compared to the control pipe, the particle concentration in the swirl pipe has obvious higher level. This increase of volume fraction results from the swirl, which twists the flow path shown in the Figure 4.4. This diagram of streamlines represents the mass flux increased when the particles entrained by air. This volume fraction increase shows a potential that more light energy can be absorbed according to the Beer-

Lambert law (increasing concentration in the Equation x). Thus, the swirl can improve the light absorption and the detailed discussion between the particle distribution and the radiation field are shown in the Chapter 6.

Compared the different entry condition, the uniform entry (E1) forms a ‘tick’ shape along the reactor. With the swirl decaying, the flow of particles entrained by air become straight gradually. After that, particles settle and then form an accumulation along the reactor. While for the settled entry (E2) and the semi-settled entry (E3), there is no obvious accumulation after 250D, for they have been compressed. An interesting observation is that the semi-settled entry (E3) performs much better than E2, in terms of gettering particles. This difference would be analysed in the section 4.4.2.

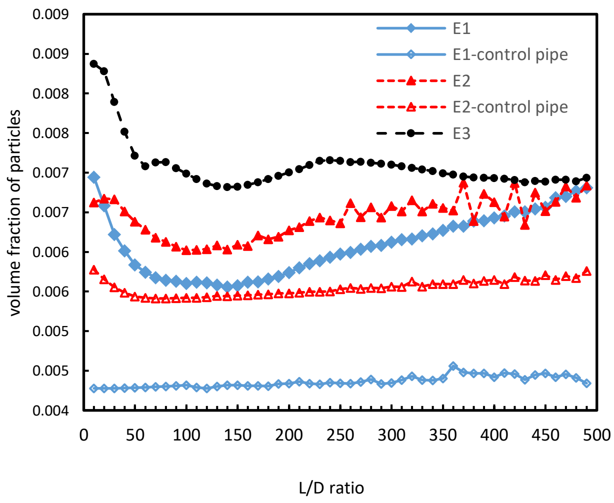

Figure 4.8 Area-averaged volume fraction of cross-section along the reactor for different entry

Furthermore, the settled section (>500D) would also affect the flow field at the swirl section (~0D-50D). Due to the settlement, the diameter of the pipe was reduced and then more energy required to push the particles forward. Because the swirling flow at the exit of the reactor, the manifestation of the extra energy becomes more compressed swirl. If the motion curve of the particles was approximately regarded as a helix with increasing b in the $z(t)$ (Equation 4-1), the compressed swirl means a lower b value. This compressed swirl carries more particles in in the swirl section and leading a better performance (analysed in the Chapter 6).

$$\begin{cases} x(t) = R_i \cos(t) \\ y(t) = R_i \sin(t) \\ z(t) = bt \end{cases} \tag{4-1}$$

As shown in the Figure 4.8, there are more particles stay in the settled section, which is another reason that more particles flow in the swirl section. This result also implies that the swirl pipe in series may improve the performance of upstream flow. This point of view was verified in the Chapter 7 by change the geometry of the calculation domain.

4.4.2 Particle Distribution along the Reactor

The characteristics of the multiphase flow downstream of the swirl pipe was firstly studied by visualizing the particle distribution into the contour plots at the cross-sectional planes. The E2 entry condition was selected as the example because of the important fluctuating phenomenon as well as to show the performance of the swirl-pipe at the fully settled particles as inlet condition. The geometry of the case was long pipe (Geo.1).

Figure 4.10 illustrates the contour of the dispersed cinnamic acid crystalline distribution. In this diagram, the colour map was shown in log scale to display more details. It presents the change of the volume fraction at various planes along the downstream pipe under the joint effect of gravity and centrifugal force. This flow has been divided into three sections, namely swirl section, decay section and settled section.

This contour exhibits 4 regions in the cross-sectional planes where particles are concentrated attributing to the four lobed geometry of the swirl pipe. This is especially prominent in the planes just downstream of the swirl pipe, named as the swirl section. Compared to the inlet particle distribution, the settled particles are lifted and entrained to the near wall region under the swirl effect. The problem of the settlement can be improved by this redistribution to an annually flow.

With the increasing downstream distance to around 50D, the particles merge and form an arc distribution along the pipe wall. At this point, the particles start to settle to the lower part of the cross-sectional plane. This is because the tangential velocity cannot afford all the particles to move circularly as the swirl dissipates, and then the gravity start to dominate the particle movement at x-y plane.

The signal of transformation from the decay to the settled section is when the particle settles at the bottom of the pipe, which is at about 100D. Although they swing slightly along the pipe wall based on inertia, the majority of the particles stay in the bottom segment of the pipe, forming a stratified or heap flow (fluctuating concentration at Figure 4.8). The contours of the cross section at this region were displayed in the Figure 4.9. It shows a gentle rise and fall of a pile of particles, caused by the convection at the cross-section plane shown in the Figure 4.5.

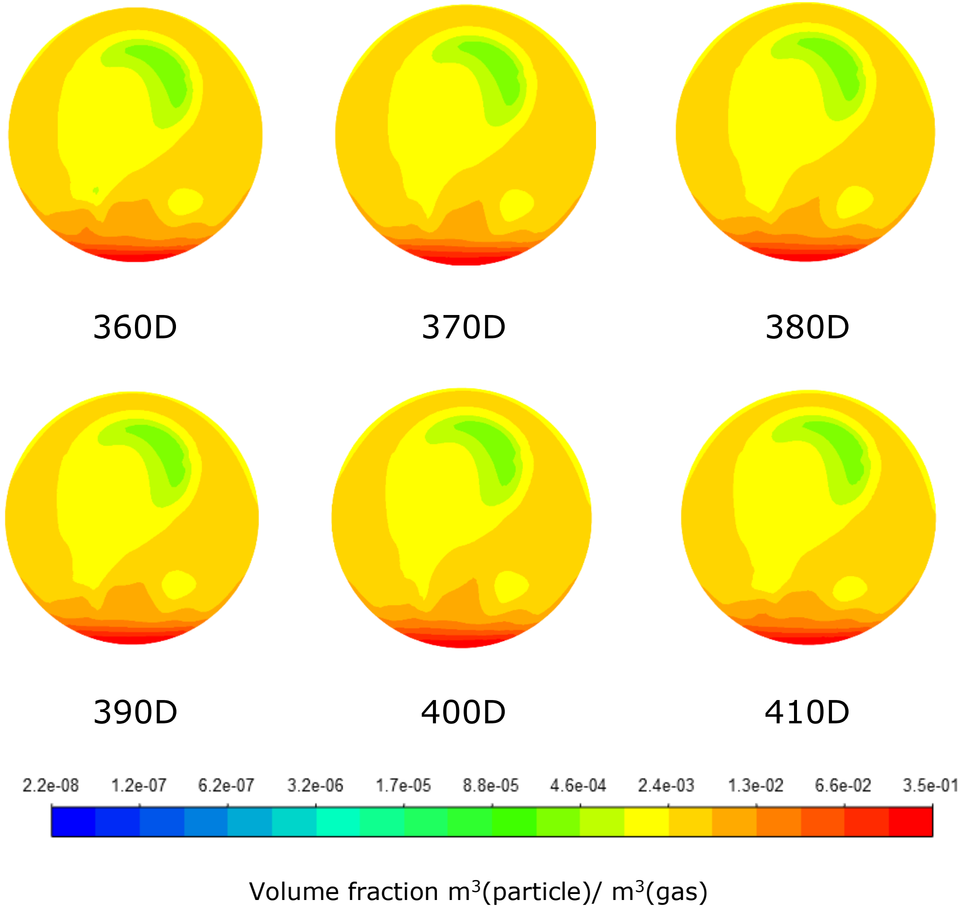

Figure 4.9 contrours of particle distribution in terms of volume fraction at settled flucturating region. The entry condition is E2 at Geo.1 long pipe.

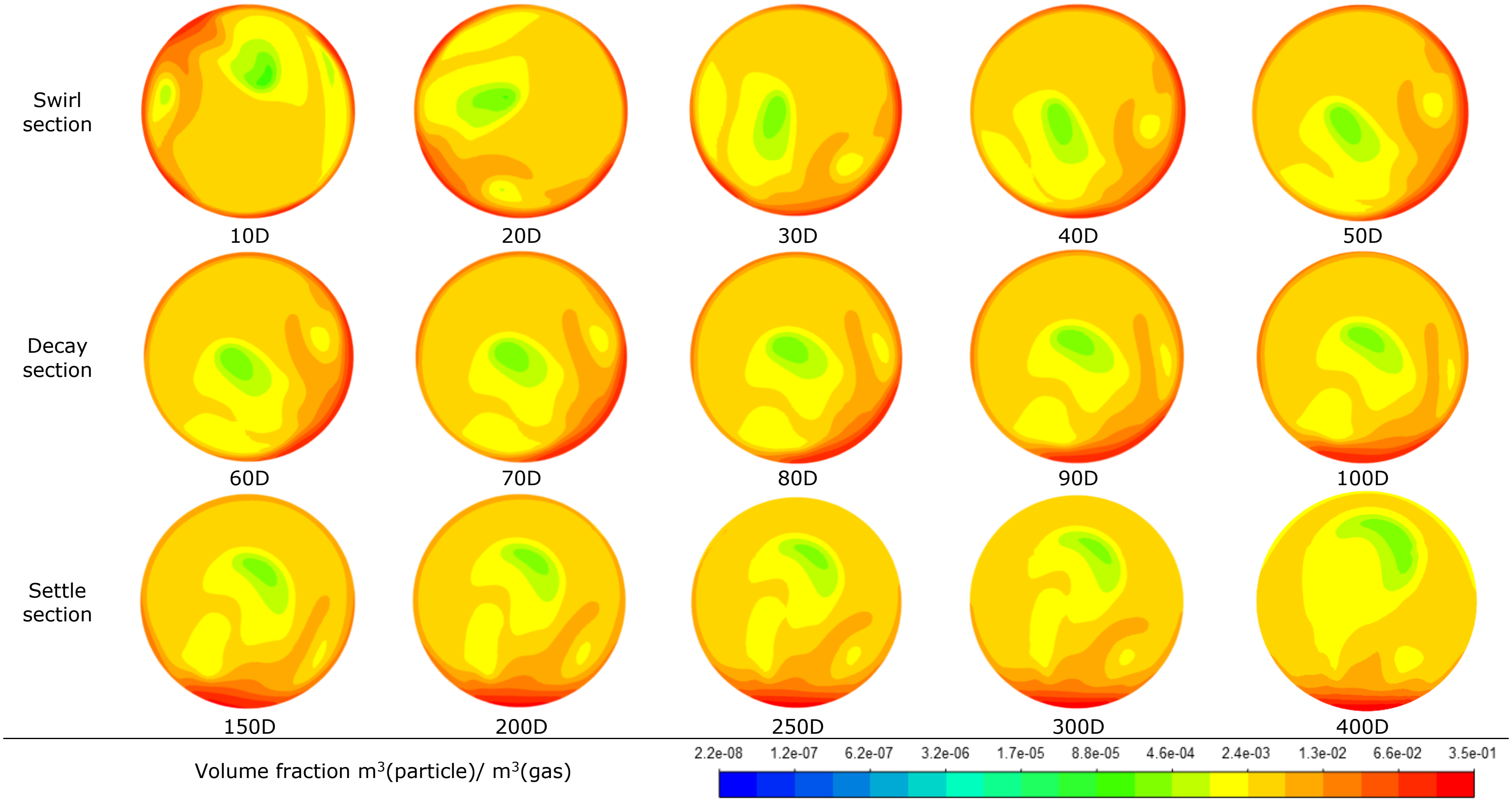

Figure 4.10 contrours of particle distribution along the . The entry condition is E2 at Geo.1 long pipe.

4.4.3 Particle Distribution Cross-section in Different Entry Condition

Figure 4.8 represents a large diffence of area-averaged particle volume fraction at the exit of the swirl pipe among different entry conditions. To analyse this difference, the profiles of that were cut and then compared in the Figure 4.11. Generally, the particles are more concentrated closer to the wall with more times of passing through the swirl inducing pipe. Meanwhile the swirl cannot afford enough centrifugal force to particles to pass the middle point at right-hand side (point of three o’clock) at about 50D (for E1 case, rotational symmetry was obviously broken at 50D). This is accordance with the vectors shown in the Figure 4.5.

E1 is the constant entry, so some particles are flowing at the centre line where swirl is less likely affect particles. As a result, there are certain amount of particles staying around the centre line of the reactor (windmill shape).

For E2 and E3 cases, the overall distribution has a similar mode. Compared to the E2, particles in the E3 are more concentrated near the wall, where the particles are more easily affected by the swirl flow. From the contour of E3 at 30D, part of the particles passes the highest point of the circle, resulting in a peak during 60D-100D shown in Figure 4.8 (p191). These particles keep decaying swirl flow caused by turbulent dissipation and gravity.

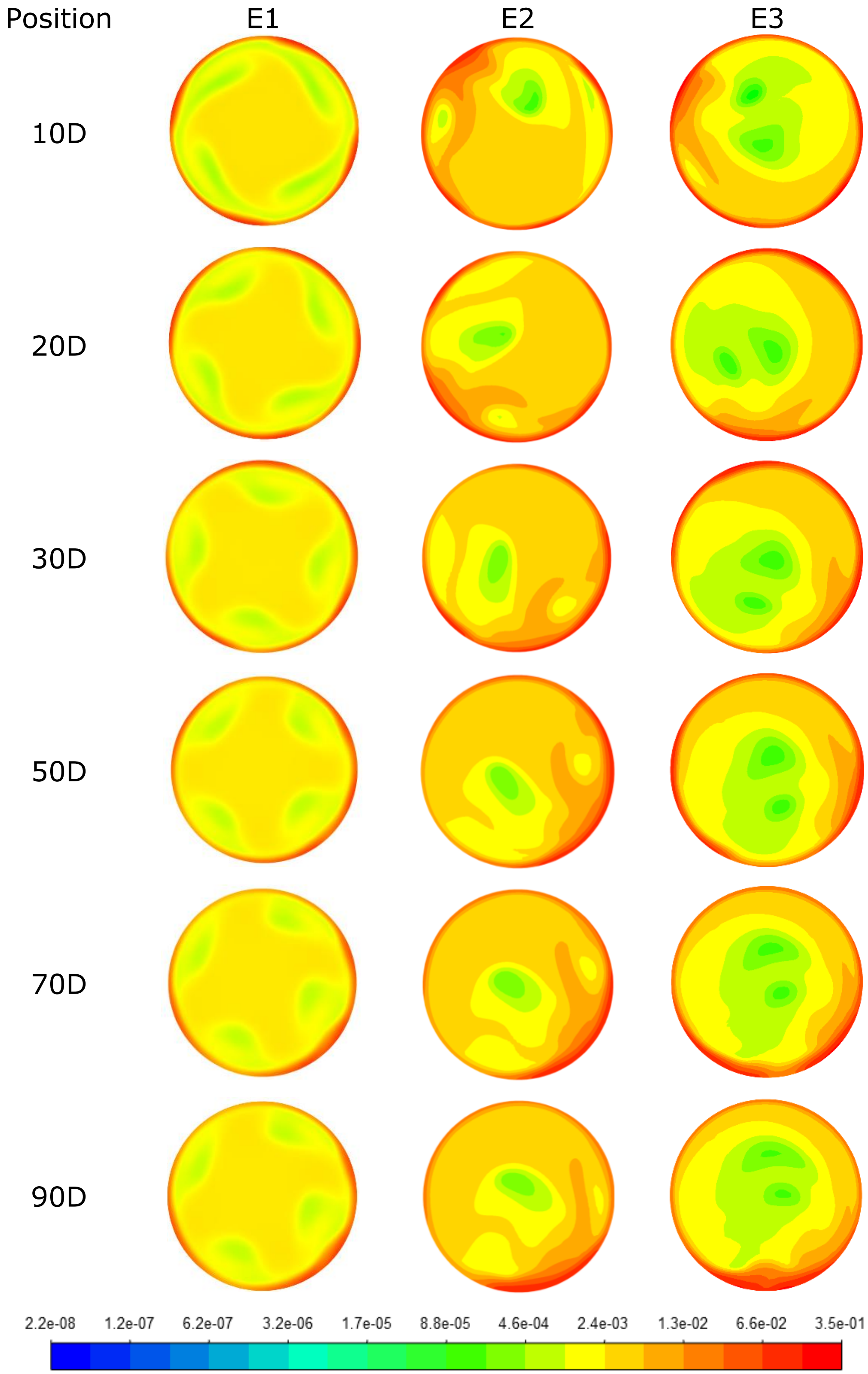

Figure 4.11 Comparison of particle distribution among different entry conditions during the swirl region. (Colour bar represents the volume fraction of the particle.)

After that, particles cannot pass the highest point of the pipe and then settle. This better performance, in terms of redistribution of particles, may result from the initial condition that the particles are not fully settled (Figure 4.3), in which more particles are easier to pass the highest point of the circle.

4.5 Conclusion

This chapter showed a general characteristics of the swirl flow. It shows the changes of the tangential velocities and pressure loss along the reactor with different entry conditions. It shows that the semi-settled entry has the best performace in gathering solid while it comsume the most energy among these three entries. The reason of this phenomenon was analysed in terms of the axial velocity, tangential velocity as well as the initial particle distribution. After that, the particle distributions along the reactor were displayed and compared by contours of volume fraction of the particles. They presented that particles prefer move forward closed to the wall, and the mass fluxs were increased due to the swirl. They are all good signal for photoreactor design according to the Beer-Lambert law. It also showed the ability of the redistribution under the induction of swirl pipe. The settled particles moved in circule under the effect of the tangential velocities and then move forward smoother. This is contribute to the reduction of the hydraulic failure.

Chapter 5 Chemical Reaction Kinetics and Derivation

5.1 Introduction

To design a solid-state photoreactor, a model to describe the reaction kinetics is required. It can translate complex steps of solid-state photo reaction mathematically to a rate equation. There are many models proposed from the theoretical mechanistic assumptions for solid-state reactions. Models for homogeneous photoreaction, are also well-developed based on both theoretical and empirical methods. However, it is a problem to combine them and build a new model to describe the reaction rate of solid-state photochemistry under different reaction conditions.

The [2+2] photocycloaddition of cinnamic acid was selected as the example to evaluate the swirl-induction reactor, which is the typical representative of solid-state reaction following the top chemical principle (Inkinen et al., 2015, Panda and Naumov, 2018, Pandolfi et al., 2021, Benedict and Coppens, 2009, Bertmer et al., 2006, Fonseca et al., 2009, Fonseca et al., 2008, Fonseca et al., 2012). Schmidt (1971) reported the reaction performs a good selectivity on the specific isomer in the α -crystal than that in the liquid solution. The wide application of this photodimerization includes mechanism study in chemistry and valuable molecule synthesis (Sommerwerk et al., 2016, Takada, 2023). This reaction has been better studied and there are experimental results reported. These studies provide a good understanding of the mechanism of this solid-state reaction.

5.2 Models and Mechanisms

5.2.1 Homogeneous Photochemistry

In classical homogeneous (solution or gas phase) kinetics, the reaction rates are described as the product of the rate constants and reactant concentration powered to the reaction order, known as rate law. This rate constant can be used to express the progress of the reaction, and it is normally investigated by changing the temperature, pressure, or reactant/product concentration.

Many elementary steps are relevant for a typical photochemical reaction mechanism (Table 5-1) (Pandolfi et al., 2021). The reaction sequence is started by the absorption of photon hv by a cinnamic acid (CA) molecule (Stark–Einstein law), step 1. The excited cinnamic acid may be quenched by collisions ($\mathrm{CA}* + M \rightarrow \mathrm{CA} + M$) or by spontaneous emission of a photon hv' ($\mathrm{CA}* \rightarrow \mathrm{CA} + hv'$), where this emitted photon has a different wavelength or a different propagation direction from the original one. This quenching process is described in step 2. $\mathrm{CA}*$ may also react with a photon and then emit both photons (stimulated emission–saturation) or become further excited (two-photon absorption), but these processes can usually be neglected at moderate photon densities (light intensity) (Hippler, 2003) except especial design (Benedict and Coppens, 2009). Additional competing elementary reactions are collision-induced emission, intersystem crossing, phosphorescence, internal conversion, or triplet–triplet absorption (Berry et al., 1980). The excited cinnamic acid may then undergo a competitive reaction with another cinnamic acid molecule, step 3, forming an unstable intermediate. This intermediate either return to the exited cinnamic acid and cinnamic acid, step 4 or form the product truxillic acid, step 5. The net reaction of this [2+2] photodimerization is step 6. In these elementary reactions, the k is not constant. The temperature and solution environment such as catalyst and solvent can help the reaction process.

Table 5-1. Simplified [2+2] Photodimerization of Cinnamic acid Mechanism

Elementary steps	Reaction*	Rate law**
1	$\mathrm{CA} + hv \xrightarrow{k_1} \mathrm{CA}*$	$r_1 = k_1[hv][\mathrm{CA}]$
2	$\mathrm{CA}* \xrightarrow{k_2} \mathrm{CA}$	$r_2 = k_2[\mathrm{CA}*]$
3	$\mathrm{CA}* + \mathrm{CA} \xrightarrow{k_3} \mathrm{Int}$	$r_3 = k_3[\mathrm{CA}*][\mathrm{CA}]$
4	$\mathrm{Int} \xrightarrow{k_4} \mathrm{CA}* + \mathrm{CA}$	$r_4 = k_4[\mathrm{Int}]$
5	$\mathrm{Int} \xrightarrow{k_5} \mathrm{TA}$	$r_5 = k_5[\mathrm{Int}]$
6	$2\mathrm{CA} \rightarrow \mathrm{TA}$	

*CA, $\mathrm{CA}*$, Int, TA, *in this table, represent cinnamic acid, excited state cinnamic acid, intermediate, and truxillic acid respectively.* k *are rate constants for corresponding elementary reactions.*

***Brackets denote the concentration of the corresponding species,* r *are reaction rates.*

From this table, the concentration of the reactant (CA), exited reactant $(\mathrm{CA}*)$, intermediate(excimer) (Int), and the product (TA) can be determined by the following equation. The coefficient 2 in equation 5-1 represents that a mole of the reaction requires 2 moles for step 1 reaction, and this coefficient can be a part of k_1.

$$\frac{d[\mathrm{CA}]}{dt} = -2k_1[hv][\mathrm{CA}] + k_2[\mathrm{CA}*] - k_3[\mathrm{CA}][\mathrm{CA}*] + k_4[\mathrm{Int}] \tag{5-1}$$

$$\frac{d[\mathrm{CA}*]}{dt} = 2k_1[hv][\mathrm{CA}] - k_2[\mathrm{CA}*] - k_3[\mathrm{CA}][\mathrm{CA}*] + k_4[\mathrm{Int}] \tag{5-2}$$

$$\frac{d[\mathrm{Int}]}{dt} = k_3[\mathrm{CA}][\mathrm{CA}*] - k_4[\mathrm{Int}] - k_5[\mathrm{Int}]$$

5-3

$$\frac{d[\mathrm{TA}]}{dt} = k_5[\mathrm{Int}]$$

5-4

Assuming steady state condition, $\frac{d[\mathrm{CA}*]}{dt} = \frac{d[\mathrm{In}]}{dt} = 0$ is reached and then the concertation of the intermediate species (Equation 5-5 and Equation 5-6). Then, substituting the Equation 5-5 and Equation 5-6, and $[hv] = I_v$ into Equation 5-1, then the Equation 5-7 was obtained.

$$[\mathrm{Int}] = \frac{k_3[hv]}{k_4 + k_5}[\mathrm{CA}][\mathrm{CA}*]$$

5-5

$$[\mathrm{CA}*] = \frac{k_1[hv](k_4 + k_5)[\mathrm{CA}]}{k_2(k_4 + k_5) + k_3k_5[\mathrm{CA}]}$$

5-6

The net rate law was displayed as Equation 5-7, where $K = \frac{k_2(k_4+k_5)}{k_3k_5}$, k_1-k_5 are corresponding rate constant of each elementary reaction as shown in the Table 5-1, and $[C]$ is the concentration of the cinnamic acid. Based on this kinetic equation, the reaction rate is proportional to the light absorbed, I_v, which is equal to $[hv]$. This proportional relationship means that the reaction rate can be improved by increasing the energy absorption.

$$\frac{d[\mathrm{CA}]}{dt} = -\frac{2k_1I_vk_3k_5[\mathrm{CA}]^2}{k_2(k_4 + k_5) + k_3k_5[\mathrm{CA}]} = -2k_1I_v\frac{[\mathrm{CA}]^2}{K + [\mathrm{CA}]}$$

5-7

The reaction appears of pseudo second order if the concentration of the cinnamic acid $[\mathrm{CA}] \ll K$. Instead for $[\mathrm{CA}] \gg K$, a pseudo first order reaction is obtained, and this means a very small k_2 and/or a large k_3.

5.2.2 Solid-state Reaction

Compared to the traditional homogeneous photoreaction, the solid-state has a higher selectivity due to its intermolecular force. This solvent-free process makes it greener, which is more environmentally friendly. This technic can be also applied to stereochemistry or chiral molecule design due to its high selectivity.

However, if this reaction occurs in the solid state, the chemical environment is completely different. Although its intermolecular force in the solid structure increases the selectivity, it also limits the reaction rate. At mean time, it is sensitive to the temperature. The increasing temperature changes the structure of the solid, and then reducing the selectivity further. The regular method in the homogenous environment becomes invalid to increase the reaction rate. Therefore, Equation 5-7 is required to be considered in the solid environment.

The solid-state reaction normally operates at the isothermal condition and based on mechanistic assumption, models are divided into four types, nucleation, geometrical contraction, diffusion, or reaction-order model. In this section, the former three assumptions are introduced as the reaction-order model was described in the Chapter 2

(a) Nucleation

Imperfections of crystals, including impurities, point defects, edges, surface, and dislocations, generate fluctuating local energies (Boldyrev, 1986). These imperfects produce sites for reactions as the activation energies are minimized at these places. Therefore, the nucleation occurs at these places, called nucleation sites

(Jacobs and Tompkins, 1955, Burnham et al., 2004). With the reaction proceeding, the nuclei grow up gradually.

This mechanism is commonly applied in the describe crystallization, crystallographic transition, decomposition, adsorption, hydration, and desolvation.

(b) Geometrical contraction

When nucleation occurs rapidly on the surface of the crystal, the rate of degradation is controlled by the resulting reaction interface progress toward the centre of the crystal. Depending on crystal shape, there are contracting cylinder (contracting area) or contracting sphere/cube (contracting volume) models describing this mechanism (Carstensen, 1974b).

(c) Diffusion

One of the other major differences between homogeneous and heterogeneous kinetics is the mobility of constituents in the system. While reactant molecules are usually readily available to one another in homogeneous systems, solid-state reactions often occur between crystal lattices or with molecules that must permeate into lattices where motion is restricted and may depend on lattice defects. However, for the SCSC transformation, diffusion may not be the key mechanism that reactant molecules are packed tightly in the lattice.

5.3 Model Construction

The model deviation was based on several proposed reaction mechanisms. These mechanisms include the kinetic of photoreaction as well as that of the solid-state reactions such as nucleation and nuclei growth. This model deviation is adapted from Khawam and Flanagan (2006)

5.3.1 Nucleation

The Nucleation is the formation of a new product truxillic acid phase at relative reactive point in the lattice of reactant. The rate of this mechanism is assumed single-step or multi-step (Jacobs and Tompkins, 1955).

Single-step nucleation assumes the nucleation and its growth happens at a single step. N nuclei are formed at the potential site N_0, and the rate of this at the equivalent light intensity I_i with n-photon mechanism can be described simple first order process as Equation 5-8.

$$\frac{dN}{dt} = k_N I_i (N_0 - N)$$

5-8

where

$$I_i = I_v^d$$

5-9

Separating the variable and integrating Equation 5-8 give Equation 5-10 with the limitation $0 < N < N_0$.

$$N = N_0 (1 - e^{-k_N I_i t})$$

5-10

In the Equation 5-9, the I_v represents the volumetric incident radiation and d here is the mechanism of the excitation (1=one-photon or 2=two photon excitation, which means that the excitation of a reactant requires d photons).

After differentiating equation 5-10, it gives the exponential rate of nucleation.

$$\frac{dN}{dt} = k_N I_i N_0 e^{-k_N I_i t}$$

5-11

When k_N is small, the exponential factor in equation 5-11 becomes 1 and then this equation becomes Equation 5-12.

$$\frac{dN}{dt} = k_N I_i N_0$$

5-12

When k_N is large, the rate of nucleation is very high. It shows that nucleation occurs at all nucleation sites rapidly.

$$\frac{dN}{dt} = {}^{\mathrm{o}}$$

5-13

Multistep nucleation assumes that this nucleation process consists of several steps (40). Accordingly, the formation of the truxillic acid nuclei forms a strain in previous cinnamic acid lattice. These small aggregates of truxillic acid unstable, and the strain from this formation cause them to revert to cinnamic acid.

This strain can be overcome if a critical number (m_c) of truxillic acid nuclei are formed. Therefore, two types of nuclei can be defined: germ and growth nuclei. A germ nucleus is sub-microscopic with truxillic acid molecules below the critical number ($m < m_c$), which will either revert back to reactant cinnamic acid or grow to further state, a growth nucleus. At this state, truxillic acid molecules exceeding the critical number ($m > m_c$) of crystal allowing further growth. Therefore, a germ nucleus must accumulate a number of product molecules, before it is converted to a growth nucleus.

A rate constant (k_i) represents the addition of individual molecules in a nucleus up to p molecules ($n < p$) is assumed to be constant. After p molecules have been accumulated ($n \geq p$), the rate constant (k_g) for further nucleus growth by addition of further molecules is a constant as well. It is assumed that the rate of nucleus growth k_g is higher than that of nucleus formation k_i.

This process is firstly described by Bagdassarian (1945) based on an assumption that each event has a same rate or probability k_i for required β successive events to form the growth nucleus, shown as Equation 5-14, where $D = \frac{N_0 k_i^{\beta}}{\beta!}$.

$$N = \frac{N_0 (k_i t)^{\beta}}{\beta!} = D t^{\beta} \tag{5-14}$$

Allnatt and Jacobs (1968) provided a more general deviation process with different nucleation rates for each step, which completed this equation by using mathematical induction. They specified the event as the number of the product molecules required to form a nucleus. Therefore, the Equation 5-14 can be adapted to Equation 5-15.

$$N = \frac{N_0 (k_i I_i t)^{\beta}}{\beta!} = D (I_i t)^{\beta} \tag{5-15}$$

By differentiation, Equation 5-16 was obtained, representing the power law of nucleation Allnatt and Jacobs (1968).

$$\frac{dN}{dt} = D\beta I_i^{\beta} t^{\beta-1}$$

5-16

Table 5-2 displays a summary of different types of numerical models for nucleation, including single step and multiple steps. Based on these equations, the model of nuclei growth is then developed.

Table 5-2. Different numerical model of nucleation rate

Nucleation rate		Differential form	Integration form
		$\frac{dN}{dt}$	N
Single Step	Exponential	$k_N I_i N_0 e^{-k_N I_i t}$	$N_0(1 - e^{-k_N I_i t})$
	Linear	$k_N I_i N_0$	$k_N I_i N_0 t$
	Instantaneous	o	N_0
Multiple Step	Power law	$D\beta I_i^{\beta} t^{\beta-1}$	$D(I_i t)^{\beta}$

5.3.2 Total Volume of Nuclei

The nuclei growth rate ($G(x)$) can be expressed by the size of the nuclei. The nuclei grow rate usually is a function of radius of the nuclei(Jacobs and Tompkins, 1955, Galwey and Brown, 1999). The growth rate at a tiny radius is different from the that at larger radius. At this submicroscopic structure, the low growth rate is due to the instability of a nuclei with tiny radius (germ nuclei), due to the possible reversion to the cinnamic acid. Then, the radius $r(t, t_0)$ of a stable nucleus at time t can be expressed as Equation 5-17, where t_0 is the formation time of nucleus.

$$r(t, t_0) = \int_{t_0}^{t} G(x)dx$$

5-17

Apart from the radius of the nuclei, two other significant parameters are considered in nuclei growth, growth dimension (λ) and nuclei shape (σ). Then, the volume of an individual nuclei ($v(t)$) can be expressed as Equation 5-18, from a stable nucleus formed at time t_0 to time t. In this equation, λ represents the number of the growth dimension (λ equals 1, 2, or 3) and σ is the shape factor, (for example, 1 for cube and $4\pi/3$ for sphere).

$$v(t) = \sigma[r(t, t_0)]^{\lambda}$$

5-18

Equation 5-18 provides the volume occupied by a single nucleus and then the total volume occupied by all nuclei ($V(t)$) can be calculated. It can be determined by combining nucleation rate (dN/dt) and growth rate ($v(t, t_0)$) equations while accounting for different initial times of nucleus growth (t_0):

$$V(t) = \int_{0}^{t} v(t) \left(\frac{dN}{dt}\right)_{t=t_0} dt_0$$

5-19

5.3.3 Growth Rate of the Nuclei

In the Equation 5-17, a variable, nuclei growth rate ($G(x)$), was proposed. Traditionally in solution, the growth rate of the nuclei depending on two mechanisms, the surface reaction, and the monomer diffusion to the surface, where surface represents the surface of the nuclei or the interphase between truxillic acid and cinnamic acid.

For the solid-sate photoreaction, due to the stronger intermolecular force, it is hard to diffuse as it in liquid or gas. Diffusion do happen in the crystal lattice, including substitutional and interstitial diffusion. However, the reactant molecules are tightly packed, and the size of each molecule are comparative, which the substitutional diffusion is the only possible mechanism for molecule movement in the lattice. This substitutional movement is negligible compared to the reaction mechanism in the nuclei growth process because growth is near the nuclei with tight package so that the photochemical reaction does not require molecule far away from the nuclei. At mean time, the changing radius of the nuclei create the different strains provides different driving force near the boundary between truxillic acid and cinnamic acid. This strain promotes the reaction more likely to occur at the interface of the nuclei. Therefore, the diffusion process is ignored in this deviation.

Then the growth rate, controlled by the reaction can be written as equation 5-20 referring to the proportional relationship between the light intensity and the reaction rate, where unit of I_i is Einstain m^{-2}s^{-1}.

$$G(x) = k_G I_i \tag{5-20}$$

5.3.4 Power Law Model

To describe the complex nucleation process, the power law was applied. Then substituting the Equation 5-16, Equation 5-17, and

Equation 5-18, into the Equation 5-19, then the Equation 5-21 is obtained. Then, substituting Equation 5-20 into the Equation 5-21, the Equation 5-22 is obtained, which is the full expression of the total volume of nuclei.

$$V(t) = \int_0^t \sigma[r(t, t_0)]^\lambda \left(D\beta I_i^\beta t^{\beta-1}\right) dt_0$$

$$= \int_0^t \sigma\left(\int_{t_0}^t G(x)dx\right)^\lambda \left(D\beta I_i^\beta t^{\beta-1}\right) dt_0$$

5-21

$$V(t) = \int_0^t \sigma\left(k_G I_i (t - t_0)\right)^\lambda \left(D\beta I_i^\beta t^{\beta-1}\right) dt_0$$

5-22

By using the binomial theorem and then integrating it, Equation 5-22 becomes Equation 5-23.

$$V(t) = \sigma k_G^\lambda D\beta I_i^{\beta+\lambda} \int_0^t (t - t_0)^\lambda t_0^{\beta-1} dt_0$$

$$= \sigma k_G^\lambda D\beta I_i^{\beta+\lambda} t^{\beta+\lambda} \left(1 - \frac{\lambda\beta}{\beta+1} + \frac{\lambda(\lambda-1)}{2!}\frac{\beta}{\beta+2} \dots\right)$$

5-23

Let $D' = D\beta\left(1 - \frac{\lambda\beta}{\beta+1} + \frac{\lambda(\lambda-1)}{2!}\frac{\beta}{\beta+2} \dots\right)$, $n = \beta + \lambda$ (known as Avrami exponent), then, Equation 5-24 was obtained.

$$V(t) = \sigma k_G^\lambda D' I_i^n t^n$$

5-24

$V(t)$ is all volume growth of the crystalline, and it is proportional to the reaction progress α' (conversion) without the consideration of restriction of the growth.

$$\alpha' = V(t)/V_0$$

5-25

Where V_0 is the initial volume of the crystal.

$$\alpha' = \frac{\sigma k_G^\lambda D'}{V_0} I_i^n t^n$$

5-26

If $k = \left(\sigma k_G^\lambda D'/V_0\right)^{1/n}$, the conversion can be expressed as

$$\alpha' = (kI_i t)^n$$

5-27

This model does not consider the constrain during the nuclei growth, and it can be applied to analysis the acceleratory period of the solid-state reaction at beginning (Khoj et al., 2013).

5.3.5 Modified JMEAK Model

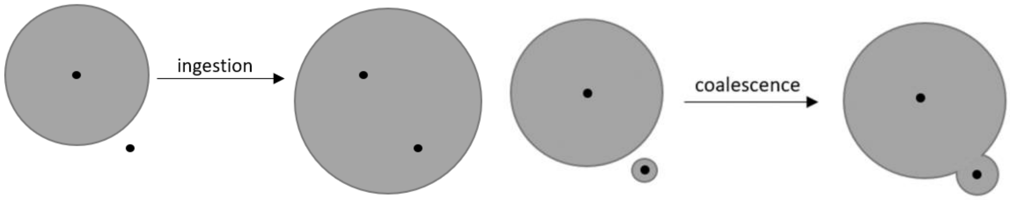

Figure 5.1 Two types of nuclei growth restrictions. Black points represent nucleation sites, the grey areas are nuclei growth regions, and the dark grey border represents the interface between nuclei and the reactant.

There are 2 types of nuclei growth restrictions, ingestion, and coalescence (Figure 5.1). Ingestion represents that the potential nuclei sites are eliminated by the other growing nuclei, while the coalescence means the loss of interface between cinnamic acid and the truxillic acid when reaction zones of two or more growing nuclei merge. Then, real growth rate would be lower than $V(t)$ when the conversion reaches the critical point where these two restrictions.

$$N_1(t) = N_0 - N(t) - N_2(t)$$

5-28

Then an expression, related to the number of the nuclei sites, was shown in the Equation 5-28, where N_0 is the total number of possible site of nuclei growth, $N_1(t)$ is the real number of nuclei exist at time t, $N_2(t)$ is the ingested site and $N(t)$is the activated site at time t.

Avrami 44 obtained the extent conversion fraction α' which is related to the actual conversion α.

$$d\alpha' = \frac{d\alpha}{(1-\alpha)}$$

5-29

After integration of Equation 5-29, the Equation 5-30 can be obtained. Then, the relation between of the conversion and the time is expressed as Equation 5-31.

$$\alpha' = -\ln(1-\alpha)$$

5-30

$$-\ln(1-\alpha) = (kI_i t)^n$$

5-31

Rearranging Equation 5-31, then a modified JMEAK model can be obtained as Equation 5-32.

$$\alpha = 1 - \exp[-(kI_i t)^n]$$

5-32

From this deviation, the net solid state reaction rate, based on nucleation and nuclei growth, has a positive relationship to the light intensity, either controlled by the reaction rate or diffusion.

5.3.6 Standardization for species transport

Because this relationship cannot be fit into the species conservation, it should be converted to the form $\frac{d\alpha}{dt}$. Meanwhile, the expression of $\frac{d\alpha}{dt}$ cannot be a function of t, because the time treatment of this simulation is steady state with $\frac{d\Phi}{dt} = 0$. Therefore, the time t can be canceled by differentiation after separating the index n from t.

Rearranging Equation 5-31,

$$[-\ln(1-\alpha)]^{\frac{1}{n}} = kI_i t$$

5-33

Differentiation

$$d\left\{[-\ln(1-\alpha)]^{\frac{1}{n}}\right\} = kI_i dt$$

5-34

Using the method of substitution, let $x = \ln(1-\alpha)$, then $dx = \frac{1}{\alpha-1} d\alpha$

$$d\left[(-x)^{\frac{1}{n}}\right] = kI_i dt$$

5-35

Because $n > 0$ and $0 \le \alpha < 1$, $x < 0$ and then $-x > 0$. Then Equation 5-35 becomes

$$-\frac{1}{n}(-x)^{\frac{1-n}{n}} dx = \frac{1}{n(1-\alpha)}(-\ln(1-\alpha))^{\frac{1-n}{n}} d\alpha = kI_i dt$$

5-36

Finally, the rate of the reaction, in terms of the conversion, can be expressed as Equation 5-37.

$$\frac{d\alpha}{dt} = nkI_i(1-\alpha)[-\ln(1-\alpha)]^{\frac{n}{1-n}}$$

5-37

5.4 Model Validation

The model is hard to validate by determine the exact same model constant. Apart from the particle size and the light intensity mentioned in this model, temperature, crystal arrangement, energy of radiation (wavelength), the environment of the solid (Pandolfi et al., 2021), and the absorption cross section (Easley et al., 2020) all affect the both rate constant as well as the Avrami exponent.

Overall, this solid-state [2+2] photodimerization was described by the JMEAK model by many researchers listed in Table 5-3, which has the same form accordant with the modified JMEAK model shown in Equation 5-32. Meanwhile, the relationship between the reaction rate and the intensity of the light is accordant with the verified model from Easley et al. (2020) for a similar photodimerization as well as the experimental result from Benedict and Coppens (2009). Therefore, this derived model is reliable generally. In this section, the validation was based on the mechanism and the data, and the corresponding data and reference are listed in Table 5-3.

5.4.1 JMEAK Model Coefficient

Although JMEAK model was applied to describe the kinetic of the solid-state photodimerization, researchers used different form of the JMEAK model of Equation 5-38 or Equation 5-39, where k is the rate constant in different form and the n is the Avrami exponent. This exponent was regarded as having an integer value between 1-4, which reflects the growth dimension of the nuclei.

$$\alpha = 1 - \exp(-kt^n) \tag{5-38}$$

$$\alpha = 1 - \exp[-(kt)^n] \tag{5-39}$$

When $n = 4$, the nuclei grow linearly in a 3-Ds (sphere), which represents the nucleation is homogenous that the product phase appear randomly in the original crystalline. Their growth terminates at their point of mutual contact, which is coalescence shown in the Figure 5.1. When $n = 3$, 2-D growth occurred in a disks or plate with fixed thickness, in the form of radial growth. After that, if $n = 2$, it is the case of 1-D linear growth in the shape of a rod (Fonseca et al., 2008). Finally, if $n = 1$, the reaction rate is likely controlled by nucleation with limited growth space.

Initially, nucleation may be random, and growth unhindered, leading to high values for n (3 or 4). Once the nucleation sites are consumed, the formation of new particles will cease. Furthermore, if the distribution of nucleation sites is non-random, then the growth may be restricted to 1 or 2 dimensions.

From Table 5-3, even for the same α type arrangement (Figure 5.2), the exponents are different from 0.9-1.6, which did not show a classical integer-exponent. This may be caused by the continuum of possible starting points for the nucleation and growth according to Equation 5-24. Meanwhile, the hybrid growth dimension may also affect this exponent. This variation shows that the exponent of the JMAK model is related to the site distribution and the amount of them. Meanwhile, the growth rate may also affect the growth directions/dimensions.

Table 5-3 JMEAK coefficient for solid state photodimerization of cinnamic acid and its derivatives.

n /	k ** (min^{-1})	Size	Type of cinnamic acid* /	Reference
1.43±0.08	6.7±3.7x10^{-5}(s^{-1}) 0.00402±0.00222	~175x175 x87.5 μm ***	α	(Benedict and Coppens, 2009)
1.12±0.08	0.00105±0.0002 (s^{-1}) 0.063±0.0012 (TGA)	Fine particles	α	(Panda and Naumov, 2018)
1.12±0.08	0.00045±0.00008 (s^{-1}) 0.027±0.0048 (^{1}H-NMR)		α	
0.9	0.00266 (s^{-n}) 0.289	5x5x0.5 mm^3	α	(Inkinen et al., 2015)
1.66±0.1	0.019± 0.004	100−500 μm sieved	α	(Bertmer et al., 2006)
0.98 ± 0.11	0.0082 ± 0.0007		*o*-methoxy-α	(Fonseca et al., 2009)
2.22 ± 0.11	0.0193 ± 0.0003		*o*-ethoxy-α	
0.87±0.11	0.007		β	(Fonseca et al., 2008)
0.79 ± 0.11	0.033 ± 0.002		*o*-bromo-β	(Fonseca et al., 2012)
0.80 ± 0.13	0.017 ± 0.001		*m*-bromo- β	
0.69 ± 0.03	0.156 ± 0.002		*p*-bromo-β	
1.8	**	/	*p*-sulfonate-α	(Kumar et al., 2020)
1	0.03~0.264 (h^{-1}) 0.0005~0.0044	/	4-amino-α	(Pandolfi et al., 2021)

o-=ortho-, m-=meta-, and p-=para-. α and β means the crystal arrangement of the cinnamic acid (Figure 5.2). **If not specified, the unit is min^{-1}, otherwise it is the original data from the corresponding source (grey). * 150-200μm edge and 75-100 μm thick.*

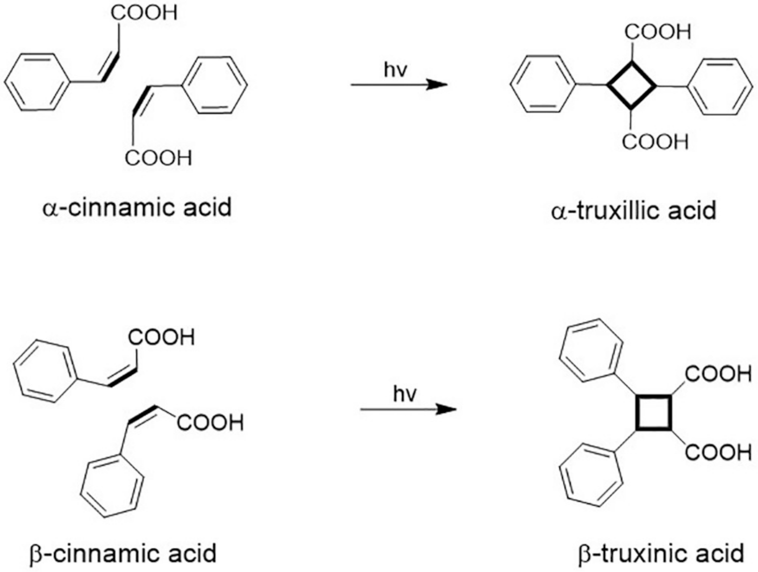

Figure 5.2 Two variants of trans-cinnamic acid and their Photodimerization products (required to be adapted)(Fonseca et al., 2008).

Cinnamic acid in Bertmer et al. (2006), Panda and Naumov (2018), and Benedict and Coppens (2009) are all fine particles. They have more surface, representing more sites at the surface. At mean time, the surfaces provide more strains to inner molecules, that creates more sites. Although Bertmer et al. (2006) did not mention the shape of the cinnamic acid, the continuing work fund that the α-cinnamic acid crystals consisted of laths varying between 1–2 mm in their largest dimension (Fonseca et al., 2008), which is more easier growth in the 1-D. In this high respect ratio crystal, the exponent n equals 1.66 closer to 2. On the other hand for plate shape crystal from Benedict and Coppens (2009), due to the lower reaction rate caused by the two-photon excitation mechanism. In the microscope, a single nucleus may grow in a 3 dimension, while in macroscope, its growth relatively rapid stops due to the mutual contact and the growth behaviour is more likely to trend to be controlled by nucleation, compared to that from Bertmer et al. (2006).

Interestingly, a much larger slide cinnamic acid was created by Inkinen et al. (2015). The exponential is close to 1 represent a heterogenous 1-D linear growth with an initially fixed number of nuclei. This is caused by the different radiation source. They used X-ray as the photon source rather than the UV. This lower value compared to the UV experiment may be caused by the high penetration depth of X-rays as well as process of valence excitations. It is dominantly created as a secondary process, initiating a more homogenous dimerization of the sample. Although a much larger starting material was applied, a much larger rate constant, 0.289 min^{-1} was obtained due to the high energy of the X-ray.

Conversely, Benedict and Coppens (2009) use 532 nm photon flux to exam the two photon-excitation mechanism while the commonly used wavelength is broad radiation from 280 to 400 (Bertmer et al., 2006, Fonseca et al., 2012, Fonseca et al., 2009, Fonseca et al., 2008) or 365 nm (Panda and Naumov, 2018, Pandolfi et al., 2021, Nguyen and Al-Mourabit, 2016, d'Agostino et al., 2016). This two photon-excitation requires two photons to excite the cinnamic acid. Although they claimed that the lower energetic radiation wave had better penetration in the crystalline, the lowest reaction rate (0.00402±0.00222 min^{-1}) in this table for α-cinnamic acid was obtained as well.

Except the data from Inkinen et al. (2015) and Benedict and Coppens (2009), the other two case, from Panda and Naumov (2018) and Bertmer et al. (2006) used the similar condition.

Unfortunately Panda and Naumov (2018) did not provide enough essential conditions such as the shape and the size of the particle so that the comparison was hard to perform. At least, the rate constant is at the similar level, which are 0.063 min^{-1} from TGA, 0.027 min^{-1} from ^{1}H NMR (which are the same material tested by different technic) and 0.019 min^{-1}. This phenomenon described above also implies that the nuclei growth is controlled by the photoreaction rather than the diffusion mechanism (Equation 5-20).

These analyses are in accordance with the deviation process. From the deviation process (isothermal operation), the full expression for the overall rate constant is shown as Equation 5-40 from Equation 5-14, Equation 5-24, and Equation 5-27.

$$k = \left[\sigma k_G^{\lambda} \frac{N_0}{V_0} \frac{\beta k_i^{\beta}}{\beta!} \left(1 - \frac{\lambda\beta}{\beta+1} + \frac{\lambda(\lambda-1)}{2!} \frac{\beta}{\beta+2} \dots\right)\right]^{1/n} \tag{5-40}$$

From this equation, the rate factor is affected by the shape (σ), growth rate (k_G) and its growth dimension (λ), number of the sites in a unit volume (N_0/V_0), and the rest term representing the overall rate constant of the nucleation.

Other examples in Table 5-3 shows the photo dimerization of β-cinnamic acid, as well as the derivatives of the cinnamic acid with corresponding arrangement. This data shows that the kinetics of the photoreaction is the distance between the vinylic carbons of the two reacting cinnamic acid molecules, which is clearly larger in the case of β-cinnamic acid (4.015 Å (Abdelmoty et al., 2005) compared to that of 3.591 Å (Enkelmann et al., 1993) for α-cinnamic acid). Therefore, larger movements of atoms adjacent to the reaction centre are required for the photoreaction to take place, potentially leading to a slower rate. For example, if these movements were more severe in one of the cases this could lead to a slower reaction rate.

5.4.2 Radiation Relationship

An important relationship in this thesis required is that between the reaction rate and the light intensity. The main variable in this flow domain is the involvement of the swirl pipe, which is essentially the change of the particle distribution in the reactor. This distribution affects the light field by the attenuation effect of the photon transmission. Therefore, the light field is not even in the reactor and the relationship between light intensity and the reaction rate is the first step to link the reaction field and the radiation field.

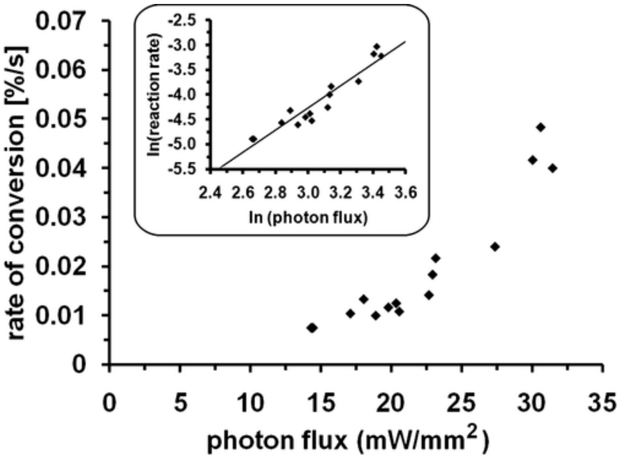

Figure 5.3 Plot of the rate of photoconversion of α-trans-cinnamic acid to α-truxillic acid as a function of 532 nm photon flux incident on (010). Inset: ln−ln plot. The slope of the fitted line is 2.24 ± 0.18. (Benedict and Coppens, 2009)

Figure 5.3 shows the result from the (Benedict and Coppens, 2009). This relationship can be expressed as Equation 5-41 derived from Equation 5-37, and Equation 5-9 (p205).

$$\ln\left(\frac{d\alpha}{dt}\right) = \ln nkX + \ln I_i = d\ln I_v + \ln nkX \tag{5-41}$$

This result shows that the $d = 2.24 \pm 0.18$, which is approximately 2, conformed to the two photon-excitation process. It also proves this derivation.

Hu et al. (2014) also did an experiment on the SCSC transformation of (E)-1,2-di(pyridin-4-yl)ethane (bpe), which underwent a [2+2] cycloaddition on exposure to the UV irradiation. The reaction kinetic was tested under light intensity of $12.95\, mw/cm^2$ and $37.55\, mw/cm^2$ and k in JMAK model were obtained as $7.14 \times 10^{-3} min^{-1}$ and $12.55 \times 10^{-3} min^{-1}$ respectively. It shows that there is a positive correlation between light intensity and the rate constant. If substituting these data into the Equation 5-32, two comparable k can be obtained (0.55 and 0.33). As discussed before, this k is related to many parameters. A possible reason for the higher light intensity with lower k is the temperature. The light intensity was controlled by the distance between the light source and the reactant. A higher radiation with shorter distance result in a possible higher temperature, where solid structures are more likely to be broken. Unfortunately, there are only 2 experiment was performed, which are not enough to show a clear relation.

5.5 Conclusion and Further Validation

In this thesis, the modified JMEAK model for solid-state photochemistry was verified partially and qualitatively. Only examples for [2+2] photodimerization was applied to show the consistency of mathematic model and the experimental data. The application of this model needs more data from other solid-state photochemistry. In addition, the effect of the temperature was not considered in this model.

However, these data confirmed a relative relation among the reaction rate and those variables mentioned in the Equation 5-40, in a direct or an indirect way. Meanwhile, the positive relationship between the intensity of the radiation and the reaction rate was clearly shown, which is sufficient in this thesis to convert the requirement from the higher reaction rate to the higher intensity of photon flux.

To validate this model completely, a large amount of experimental data and corresponding controlling operating condition and parameters mentioned are required. These experiments are required to be well designed to keep the other variable constant.

Chapter 6 Radiation Distribution in The Swirl Pipe Reactor

6.1 Introduction

This chapter presents a computational fluid dynamics model of the swirl flow that is induced in a fluid flow passing through the horizontally mounted optimized four-lobed 400mm length swirl pipe. The steady state CFD model based on the Eulerian- Eulerian multiphase model, $k-\omega$ SST turbulence model, and DO model approach provides time-averaged properties of the swirl flows. Analysis will focus on the particle's distribution and the radiation field.

The intensity of the incident radiation and the absorbed light were analyzed in the flow direction and the cross-section with different entry condition. Special attention is paid to the relationship between the particle distribution and the energy absorbed, where the higher absorbed energy accelerates the reaction rate.

The particles distribution was discrete to angular and radial distribution, and factors was built to describe them. These numerical results indicate that the swirl pipe has the potential to improve the energy absorption by spread the particle to a broader and concentrated ring-like shape. A rough correlation was constructed to assess the particle distribution under the exposure of the light with the elliptic arrangement.

Apart from the different entry condition, the reactor arrangement and the particle size were also tested to validate the statement what is the key parameter affecting the performance of the reactor. Meanwhile the results from these simulations were also applied to verify the correlation, which would be an important assessment in the next Chapter of the boundary condition of the flow filed.

6.2 Simulation Set-up

The commercial CFD software ANSYS Fluent 19.0 was employed to carry the numerical study. The multiphase flow was simulated with the numerical method, turbulence models, multiphase models, and wall functions, the meshing method, the solver parameters, and the solution convergence criteria described in Chapter 3.

The different geometry configuration is illustrated at Figure 6.1. A detailed description of the simulation geometry is covered in section 3.2 There are four arrangements of the swirl pipe and the circular pipe in this chapter. The Geo.1, named as long pipe, consist of a developing pipe, a swirl pipe, and a transparent pipe for reaction. The transparent pipe was 500D long (L=5m with diameter of 1cm, L/D=500). The Geo.3 has the same arrangement with the Geo.1, but the length of the transparent pipe was 60D, named as short pipe. The Geo.5 arrangement has the same arrangement as the Geo.1, Geo.2 and Geo.3, but the swirl pipe was replaced by a circular pipe with the same length and the same equivalent diameter. Lastly, the Geo.4 joint pipe consists of two connecting Geo.3 short pipe. This geometry was designed to test the stability of the swirl flow.

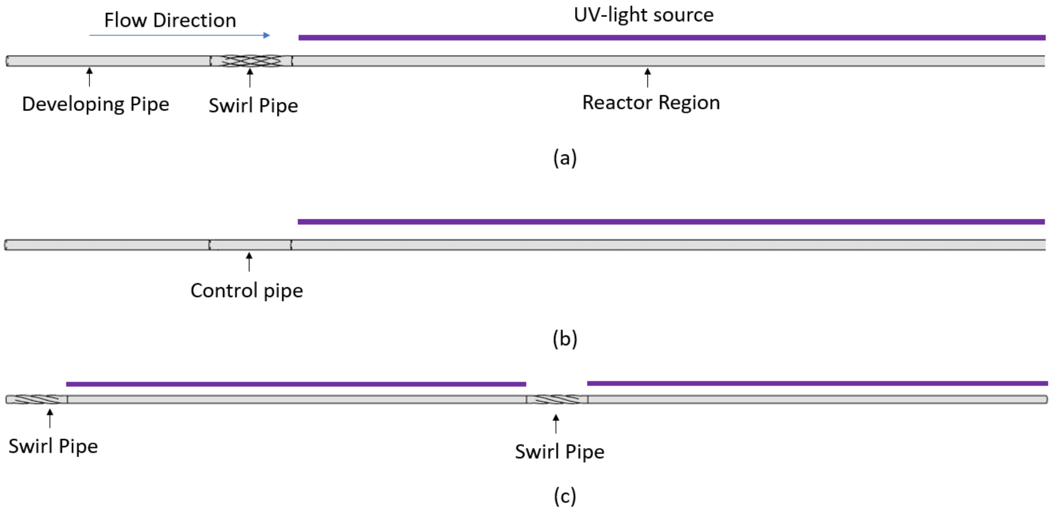

Figure 6.1 Geometries, (a) Geo.1, long pipe, reactor region lenth L=500D or middle pipe Geo.2, L=100D Geo.3, or short pipe, L=60D, ; (b) Geo.5, control pipe, with same lenth as Geo.1 or Geo.2 for comparism (c) Geo.4, joint pipe:two short pipe connected.

The first trial (E1) of this simulation was set as the uniform concentration of the cinnamic acid crystalline with a volume fraction of 0.004275. This dilute particle phase was to simplify the modelling that the heat of reaction can be ignored. The inlet velocity of air and solid was set at 12m/s in the z-axis direction. A 20 w/m^2 diffused radiation with a wavelength of 375 nm was assumed as wall radiation flux at the glass straight pipe as described in Chapter 3, while the swirl-induction pipe and the developing pipe were set opaque.

The inlet spatial distribution of the particles affects the performance of the swirl pipe reactor. The uniform entry is an ideal condition, while the more common condition is that particles settle at bottom of the pipe. When the reaction rate is slow, especially solid-state reaction, the long retention time results in this common sedimentation. It is difficult to describe the settled condition so that a profile cut from the close end at the first trial (490D) was set as the inlet condition of the second trial (E2), where particles deposit at bottom of the pipe. Similarly, the inlet condition of Entry 3 (E3) was set from the profile at the 150D of the Entry 2 with a similar statement. This selection is based on the result in entry 1 showed in the Chapter 4.

6.3 Characteristic of Radiation Distribution

6.3.1 Assessment Format

An accurate estimation of light intensity distribution is essential for a reliable design of photoreactors. According to Equation 5-37, the reaction rate is positively related to the intensity of the radiation.

The LVREA ($E_v(s)$) at any point is given by Equation 6-1, where $I_v(s)$ is the intensity of the incident light and the a_v is the volumetric absorption coefficient, which is $a_v = ca$. From this equation, the higher volumetric absorption coefficient and the higher incident radiation makes the higher LVREA.

$$E_v(s) = a_v I_v(s) \tag{6-1}$$

Another important factor is defined as the specific radiant energy absorbed (Equation 6-2). It represents the energy absorbed per mass of the particles.

$$E_m(s) = \frac{E_v(s)}{\phi_s \rho_s} \tag{6-2}$$

6.3.2 Radiation along the Downstream of the Swirl Pipe

E1, E2, and E3 were performed as the entry condition in the Geo.1 long pipe. As shown in Figure 6.2, the incident radiation decreases to the same level, when the particle settled to the bottom of the pipe (The basic particle distribution characteristics are described in Chapter 4 section 4.4 p190). During the swirl fully developed flow regime and the decaying regime, there is an obvious increase (~5%) in terms of the incident radiation. This means that light is easier pass through the particles and enter the system.

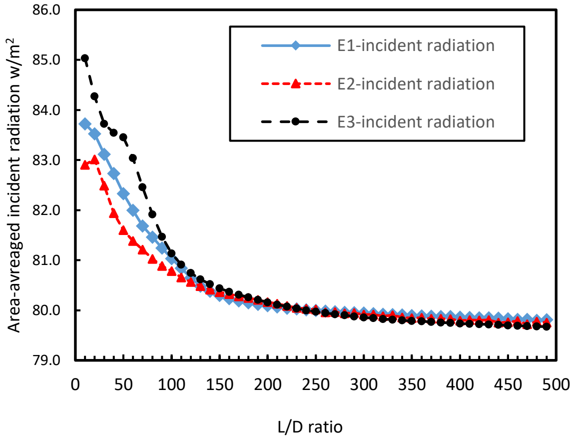

Figure 6.2 Incident radiation over long pipe at different entry condition.

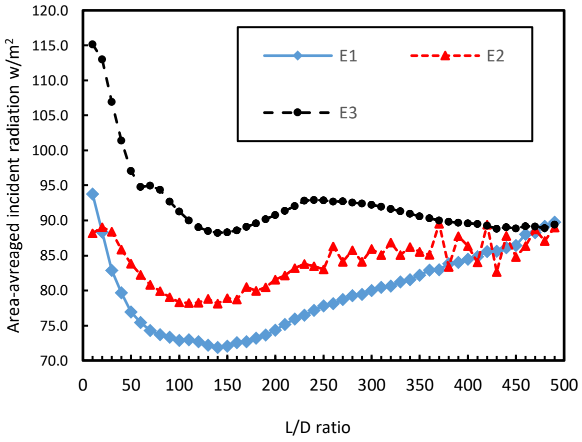

Figure 6.3 LVREA over long pipe at different entry condition.

Figure 6.3 shows the LVREA along the reactor, which is an important criterion to assess the performance of the photoreactor. Generally, there is a similar trend as that in the incident radiation, in the swirl regime. According to the expression of LVREA

(Equation 6-1), the difference between the incident light and the LVREA comes from the volumetric absorption coefficient in the limited volume. The molar absorption coefficient is a nature of a species that cannot be changed by the swirl, and then the concentration is the key factor cause this difference. Referring to the Figure 4.8, which describes the area-averaged concentration along the reactor, there is a more similar trend. The more detailed explanation about difference from different entry condition on the radiation was presents in the section 6.4. The interesting fluctuating LVREA around 250D-500D makes this case as an example for detailed analysis.

6.3.3 Cross-section of Radiation Distribution

Figure 6.4 displays the incident radiation distribution profile along the reactor for E2 case, which is a fully settled entry. It shows that the incident radiation is highly related to the particle distribution. It is more evenly distributed when its position closer to the just outlet of the swirl pipe, where particles form a roughly ring shape. This distribution perpendicular to the direction of light, cutting the rays of radiation. With particles merging and settling gradually at the bottom of the pipe, the radiation distribution follows the change of the particle distribution, focus on where bottom of the pipe. When the solid fully settles at positions from about 250D to the end of this reactor, a weak electromagnetic shielding was formed by concentrated particle with a higher extinction effect. There is a small region with lower incident radiation behands the shield, while the majority of the particles distributed in a segment rather than the layer of the shield. This unmatched distribution prevents a certain amount of the light penetrating in the centre of the pile of the particles.

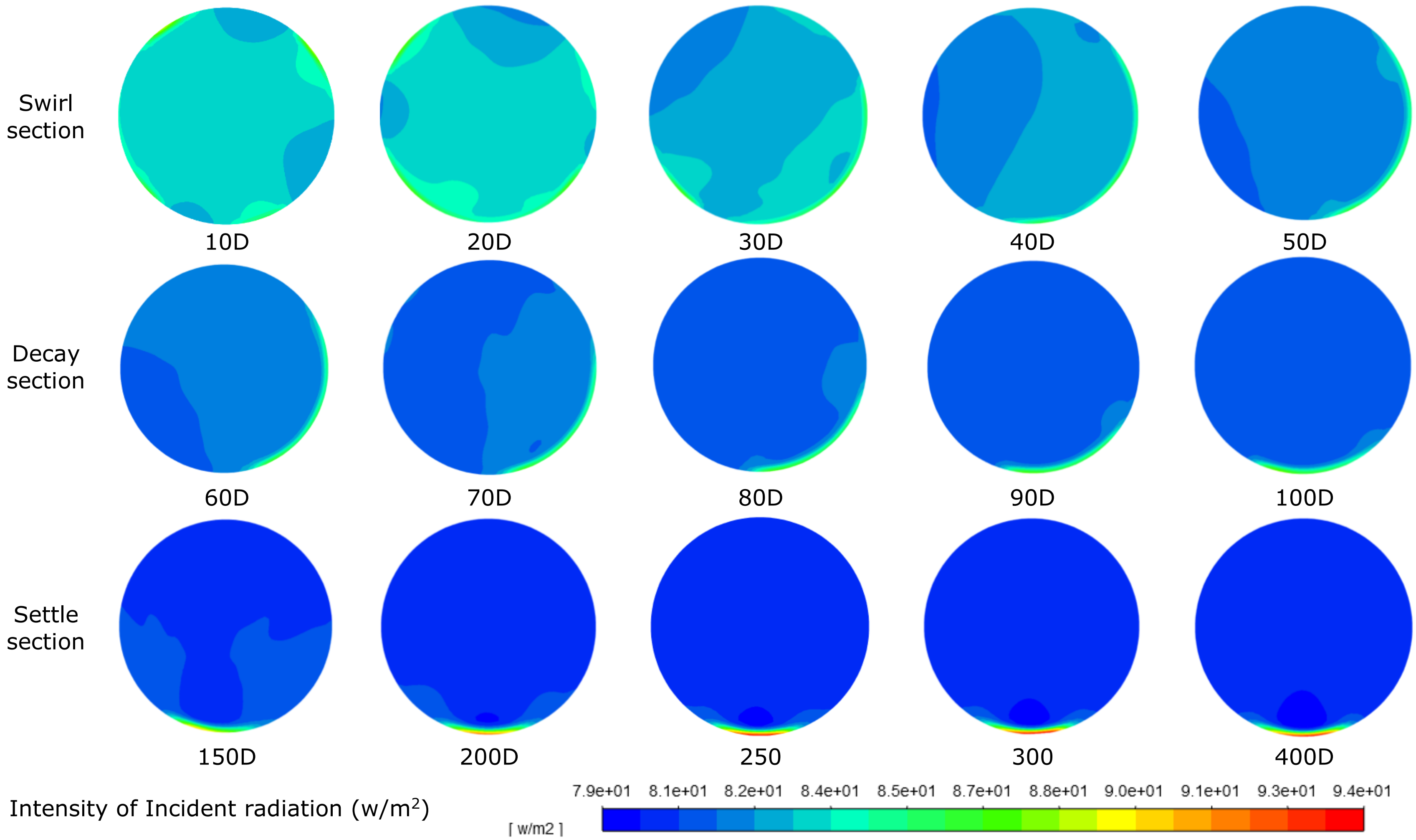

Figure 6.4 Distrubtion of incident radiation in the E2-Geo 1 simulation.

6.4 Correlation between Particle Distribution and Radiation Distribution

6.4.1 Introduction

LVREA has a positive relationship to the reaction rate, which is widely used to assess the performance of the photoreactor. Sufficient exposure of the substrates under light field can maximize the reaction rate. How to increase the LVREA is one of the key factors in this reactor design. Based on the weak electromagnetic shielding effect caused by the settled particle, this induced swirl has the potential to increase the enhance the light absorption.

The Figure 6.5 illustrates the relationship between the LVREA and volume fraction of the particles. It shows that the absorption of the light is proportional to the number of particles generally. This figure is also a validation that the predicted linear trend is in accordance with the Beer Lambert law. From the figure, the increase of the volume fraction of the solid leads to the utilization rate of radiation energy.

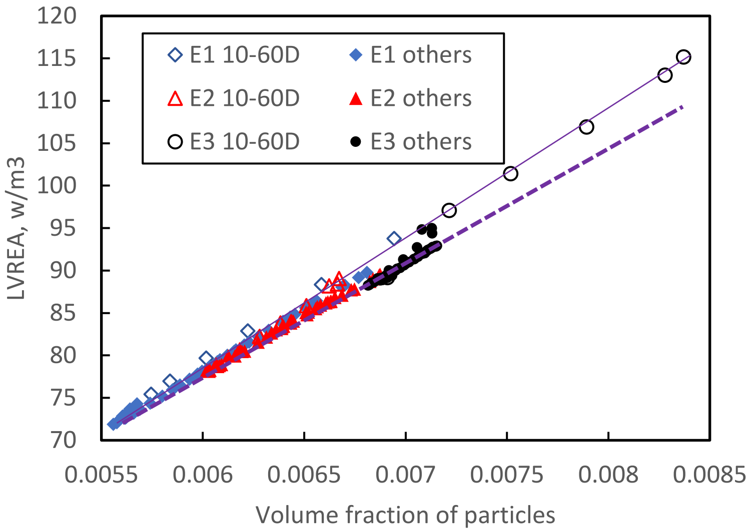

Figure 6.5 Relationship between the area-weighted average of volume fraction and LVREA. E1, E2 and E3 are different entry condition.

Meanwhile, it is worth to notice that some of the point shift up from the line or has a higher slope in other words in the duration 10D to 60D at the vicinity just downstream of the swirl pipe. This higher slope represents more radiation absorbed in the reactor over this duration.

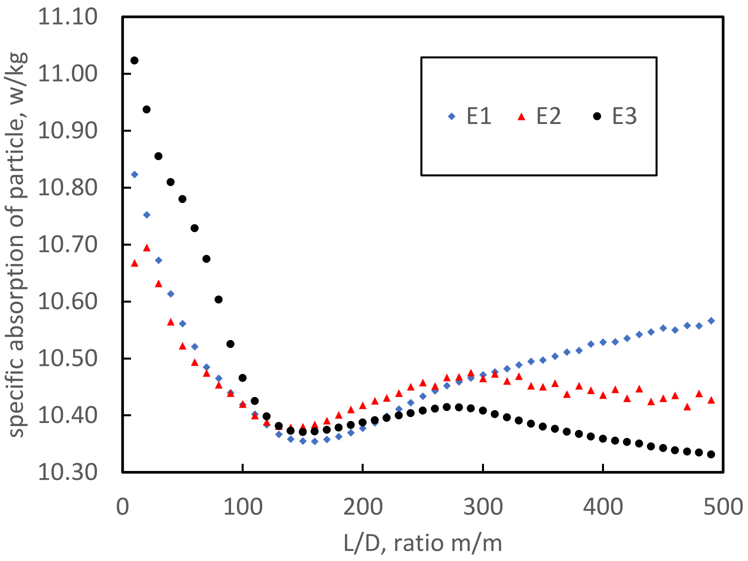

Figure 6.6 specific radiation absorbed over long pipe at different entry condition.

To present this characteristic clearly, the specific radiation absorption of the particle (energy per weight) was calculated and showed in Figure 6.6, which illustrates that with the increase of L/D ratio. The swirl effect dissipates, and this specific absorption of cinnamic acid crystal decreases gradually from the exit to about 150D where swirl effect is decaying. In this figure, the specific absorption of the particle for entry condition of E1 and E2 has the similar trend except the point at around 270D after which The E1 condition keeps increasing the specific absorption while the that of E2 drops. Compared with these entries E1 and E2, the E3 condition dramatically higher from the outlet of the swirl pipe to about 150D, followed with similar trend to the E2. This trend has the consistency with the change of the particle distribution. Hence, the relationship between the radiation field and the particles was assessed in terms of the concentration and the geometrical distribution.

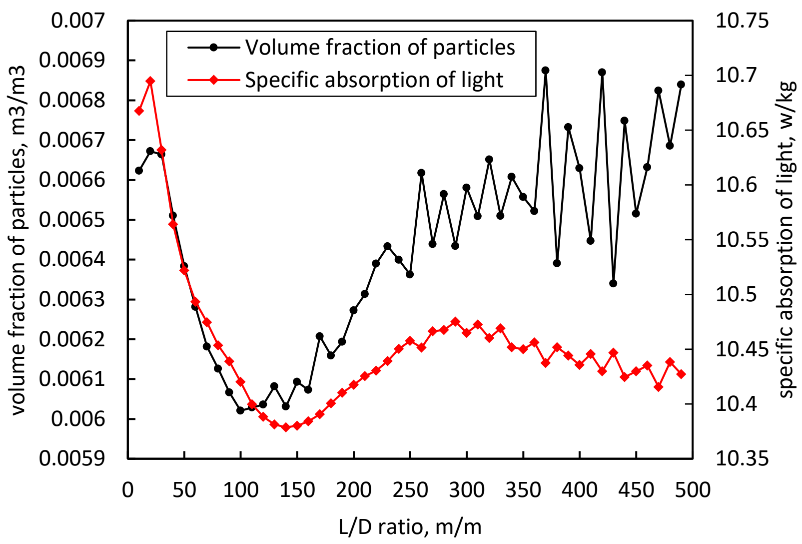

Figure 6.7 A comperision between the area-weighted average of the volume fraction and the specific absorption of the light,

The E2 case was selected as an example to show the association between the specific absorption and the volume fraction of the particle (Figure 6.7). At the region with sufficient swirl effects, the particles have the similar tend as the decreasing particle concentration along the pipe due to the loosing path of the flow. When the particles start accumulating, this absorption increase to the peak point at about 270D. After this point, this specific absorption drops slowly, while the amount of the particles dramatically increases with fluctuation forming a heap flow. At this region, the local maximum of the particle accumulation corresponds the local minimum of the specific absorption, indicating that the specific absorption is impeded by the particle accumulation. This opposition is caused by the accumulation of the particles in the region with less incident radiation and the particles in the centre of a pile formed from the heap flow receive less light absorbed or scattered by outer layer particles.

6.4.2 Effect of Particle Distribution on LVREA

To find the better solid spatial distribution feature for receiving radiation, the profiles of the cross-sectional planes at 10D, 50D, 70D, 150D, 270D, 400D were selected as the samples for analysis. Among these points, 10D, 50D, 150D and 270D are the turning points whereas the 70D and 400D are the place existing difference on absorption. Apart from the point mentioned above, 10D is closest to the exit of the swirl pipe where has best swirl strength and 50D is the location where the strength of the swirl cannot provide the sufficient tangential velocity to the particles for the circular movement.

When extending the Beer-Lambert law, the maximum absorbed radiation occurs at the particle distribution perpendicular to the incident light ray in analogy with motion cutting magnetic induction line in Faraday's law of electromagnetic induction. Because the arrangement of the light source and the reactor was elliptic Figure 3.4, the radiation was penetrated to the reactor evenly towards to the centre. Therefore, the distribution of the particle was analysed in terms of the radial distribution and the angular distribution as shown in the Figure 6.8.

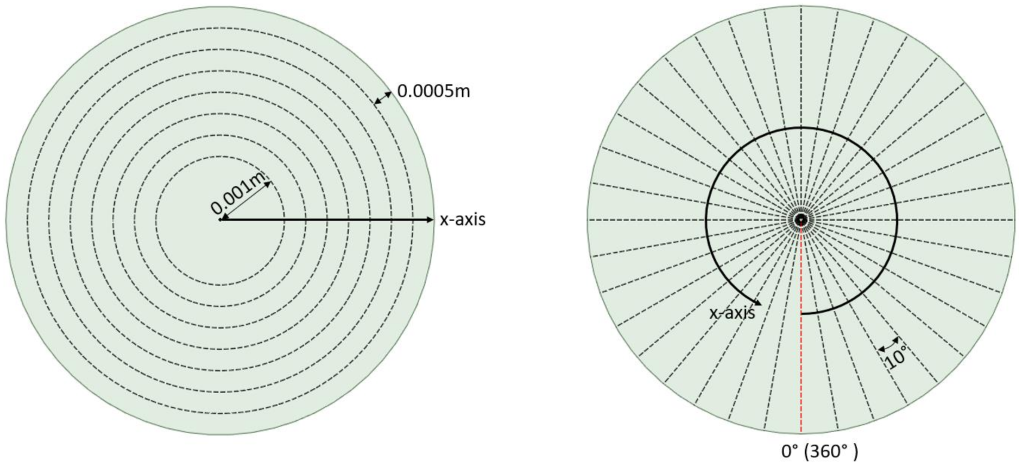

(a) (b)

Figure 6.8, Indication of the rule of the classification, (a) radial position and (b) angular position.

Figure 6.9 displays the radial distribution of the cinnamic crystal at the position. Basically, in terms of radial direction, as the particles were driven to the wall under the inertia force from the swirl firstly, they are concentrated far away from the centre of the pipe. At the location 10D of the swirl pipe, the case with E3 inlet configuration has the particles distributed closest to the wall, followed by that with E2 and E1, and this feature stands for the whole glass reactor. This characteristic is result from the multiple and periodical compress towards to the wall if the flow for the E1, E2 and E3 configuration are regard as the result of a series of the swirl pipe. However, according to the Beer-Lambert law, the radiation absorption should have been negatively proportional to the distance to the wall, while the radiation absorbed for E2 is lowest among these three cases. Therefore, there is another criterion to assess this particle geometrical distribution.

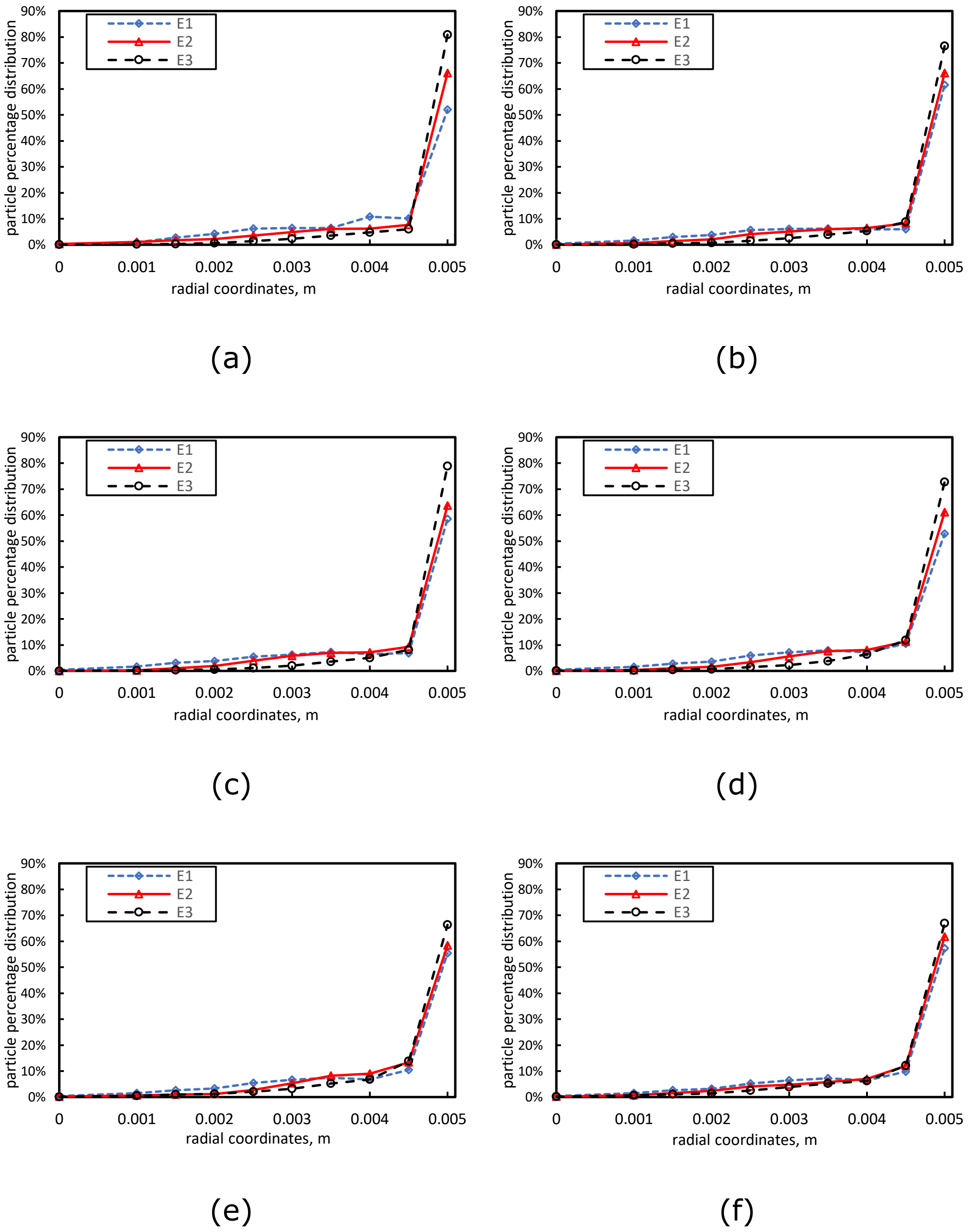

Figure 6.9, Percentage particle distribution at radial direction. (a)10D, (b)50D, (c)70D, (d)150D, (e)270D, (f)400D. The total radius of the circular pipe was 0.005m

The angular distribution is applied to assess this distribution showed in Figure 6.10 at those selected position. This idea comes from the polar system. If these suspended particles are regarded as a disconnected ring or arc, a sharper peak represents shorter equivalent arc length or smaller the equivalent arc angle. Then, a sum of the degrees called coverage that all peaks occupied represents the equivalent angles to assess the angular distribution. This normalized angular distribution reveals the reason why the absorption of E2 case is less than that of E1. Although the distance of particles for E2 is closer to the wall, the radial distribution of the particles for E2 at these positions have sharper peaks or less total angle these peaks occupied.

Meanwhile, this angular distribution diagram presents some detail for better understating of this swirl induced reactor. At place of 10D, it shows that there are four peaks formed due to the geometry of four lobes, among different entry condition, although they are sharp or broad. At position of 50D and 70D (Figure 6.10b, Figure 6.10c), these peaks for all entry condition move closed to about 45^{o} (anticlockwise to the vertically downward line). Due to the anti-clockwise twist swirl pipe, this diminishing tangential velocity of the air blows the particles to rotate a certain angle as a result of confrontation with gravity. Among these three cases, the particles of the E2 case merges faster than that of the other two, and this is also a prove of lower absorption of radiation. Due to the constant distributed inlet condition in the E1, peaks for this case have a similar height and width. This also implies that the complete swirl pipe may not be suitable for the reactor design that four pile of the particles would be settled to the bottom of each lobe.

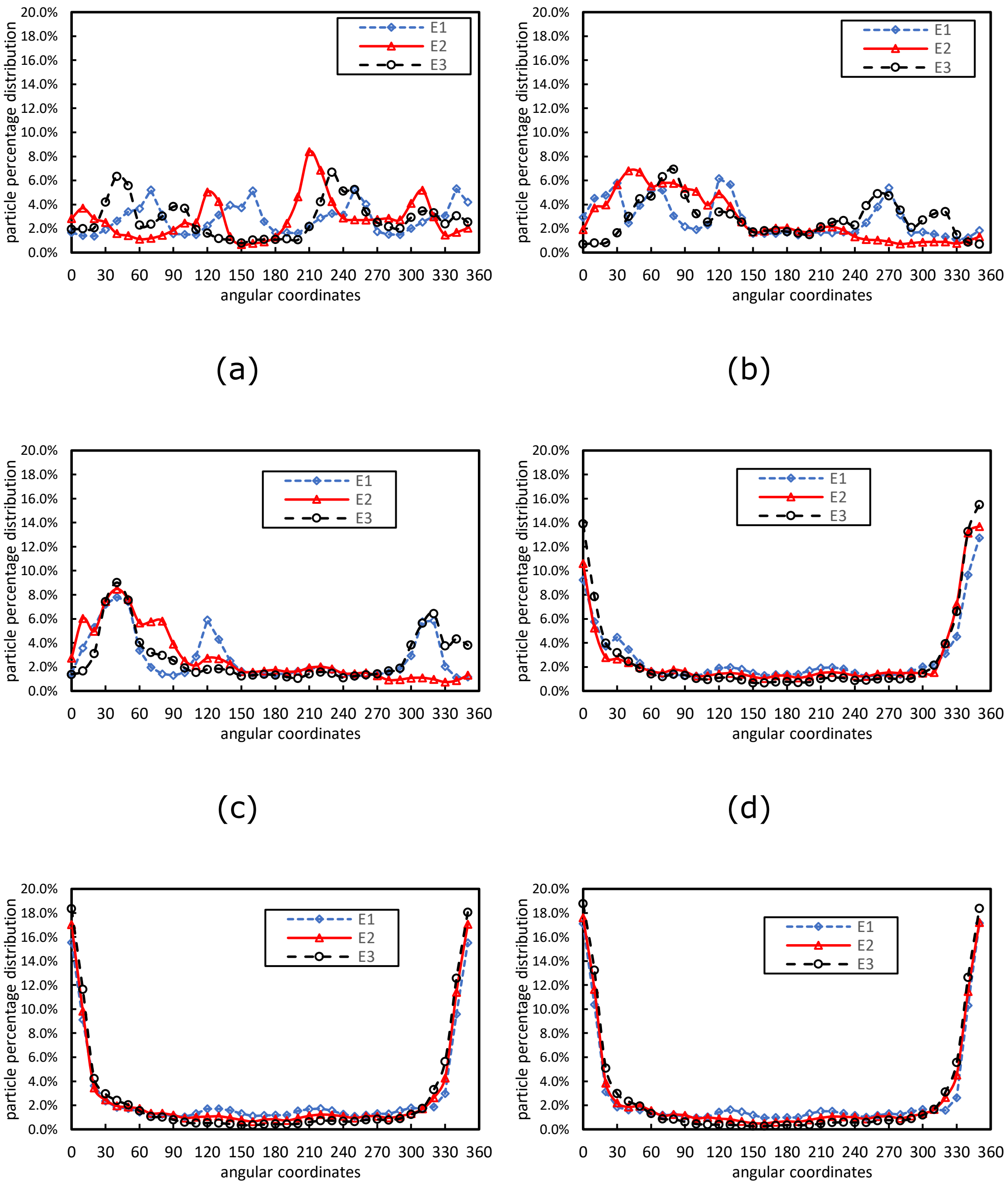

(a)

(b)

(c)

(d)

(e)

(f)

Figure 6.10, percentage particle distribution at angular direction at Geo.1 long pipe. (a)10D, (b)50D, (c)70D, (d)150D, (e)270D,(f)400D. The 0°(360 °) is at the -y axis direaction and the rotation direaction is anti-clockwise. The particle distrimution is discreted by sum up the tatal particles in every 10 °, and normalized.

Figure 6.10d, e, and f show the angular distribution for the settled crystal. With the swirl fully disappeared, portions of the particles settle to the pipe bottom layer by layer, resulting in the increased particle level. Afterwards, the particles firstly fall closed to the wall and then establish the shield which has higher extinction coefficient, which is corresponding to the increasing (about from 150D to 270D) and then decreasing specific radiation absorption (after 270D) respectively for E2 and E3 cases. By contrast, the specification absorption of the E1 case keep increase after 270D. Reflected in the angular distribution, this increase is caused by two prominent two short peaks in the region from 90° to 240° for the condition E1, which expend the arc length to receive radiation. These two peaks are formed by a certain number of particles flowing follow the centreline of the pipe which is blown up by the convection. There are particles because of the uniform entry condition for E1 and they are not affected by the swirl as there is no swirl effect in the vicinity of the centreline of the pipe. Thus, the most ideal distribution of the particle is the annular flow, which forms a thin layer of the particles to facilitate sufficient light absorption.

6.4.3 Define the Particle Distribution

The distribution of solids affects the absorption of light based on previous analysis in terms of the concentration and spatial distribution. However, it is difficult to describe a non-even distribution of particles at a cross-section area downstream of the swirl pipe and relate this distribution to the radiant absorption and boundary conditions. Therefore, in this section, the particle distribution information was analysed at cross-sectional planes along the downstream pipe by defining three factors, namely the radial factor, the angular factor and the position factor.

The idea of this summarization is to convert the image information of particle distribution into a statistical problem by analysing all the volume fractions of the solid phase at a cross-section area as a group of data. These characteristic numbers were designed to assess the distribution of these particles at different downstream planes in terms of the radial and angular distribution and the place where the major particles are. The factors defined are as below.

Radial factor

Radial factor (x) is defined as a fraction. The numerator is the average value of production of local volume fraction ϕ_i and its corresponding radius r_i. This factor represents how close the particles are to the pipe wall. It increases when the particles move to the wall with the assumption that all particle flows forward without accumulation. The denominator ϕ is the volume fraction of the cross-section area and the radius of the pipe R. The denominator is to eliminate the effect of the particle concentration to show the equivalent relative radial position of particles. The range of this factor is from 0 to 1. With particles moving to the wall, the value of this ratio is closer to 1.

$$x = \frac{\sum \overline{\phi_i r_i}}{\phi R} \tag{6-3}$$

Figure 6.11 (a) shows the radial factor along the reactor for different entry conditions. It is in accordance with the result shown in the Figure 6.9**.** This diagram shows the distance of the particles to the wall more intuitively with the dissipating swirl at different entry conditions. Besides the comparison of the distance to the pipe wall among different entry conditions, the radial factor shows the change of this distance inside the case as well. Meanwhile, it can quantify this distance for the reactor design. From the exit of the swirl pipe, the radial factors for these three cases reduce more (E1 and E2) or less (E2). The turning points are at about 150D and then they start to increase due to the falling. Except for the obviously and steadily increasing radial factor for the E1, those of the others are slightly increased till about 290D and then decrease, which is identified with the specific radiation absorption.

Angular factor

The reciprocal of a relative standard deviation is defined as the angular factor. It is applied to assess the angular distribution of the particles with the discrete volume fraction by $\delta\phi/\delta\theta$ in each cross-section area where $\delta\theta = 10°$. Smaller angles were also tested, but some of the information would be hidden after the calculation of deviation due to the fluctuation of particle distribution discrete at a small angle. When this deviation increases, it represents the coverage of the arc is small. The reciprocal was applied for the consistency of the monotonicity of the value and the coverage.

$$\mathrm{s} = 1 \Big/ \mathrm{RSD}\left(\frac{\delta\phi_i}{\delta\theta}\right) \tag{6-4}$$

This factor along the pipe was calculated and displayed in Figure 6.11 (b). This value represents the total angle of the arc. It shows that the swirl pipe can redistribute the particles to a relatively broad angle for about 50D. The angular factor of E1 presents a much higher value than the other because particles are spread more evenly, while the angular factor of E2 and E3 are at comparable levels because their entry configuration is settled particles. Between these two cases, the angular distribution of E3 keeps a stable value for 50D and then decrease while the value for the E2 case decreases from the 20D, with a peak at 100D caused by the rough translation along the pipe wall mentioned before. This decreasing degree of the arc results in its lowest radiation absorption.

Position factor

These two factors describe the distribution separately. Although this split helps the understanding of the relationship between the particle distribution and the radiation and absorption, they do not provide an overall view of the particle distribution. Then, the position factor is defined to describe the particle distribution as follows, which describes the particle distribution affected by two component forces.

$$p = \frac{\overline{\phi_i r_i} + \overline{\phi_i y_i}}{\phi} \tag{6-5}$$

where p is the position factor (m) at a certain cross-section of the reactor, ϕ_i is the local phase volume fraction at point i, r_i is the local radius at point i, ϕ is the volume fraction of the cross-section area and y_i is the vertical coordinates at the same axis of gravity.

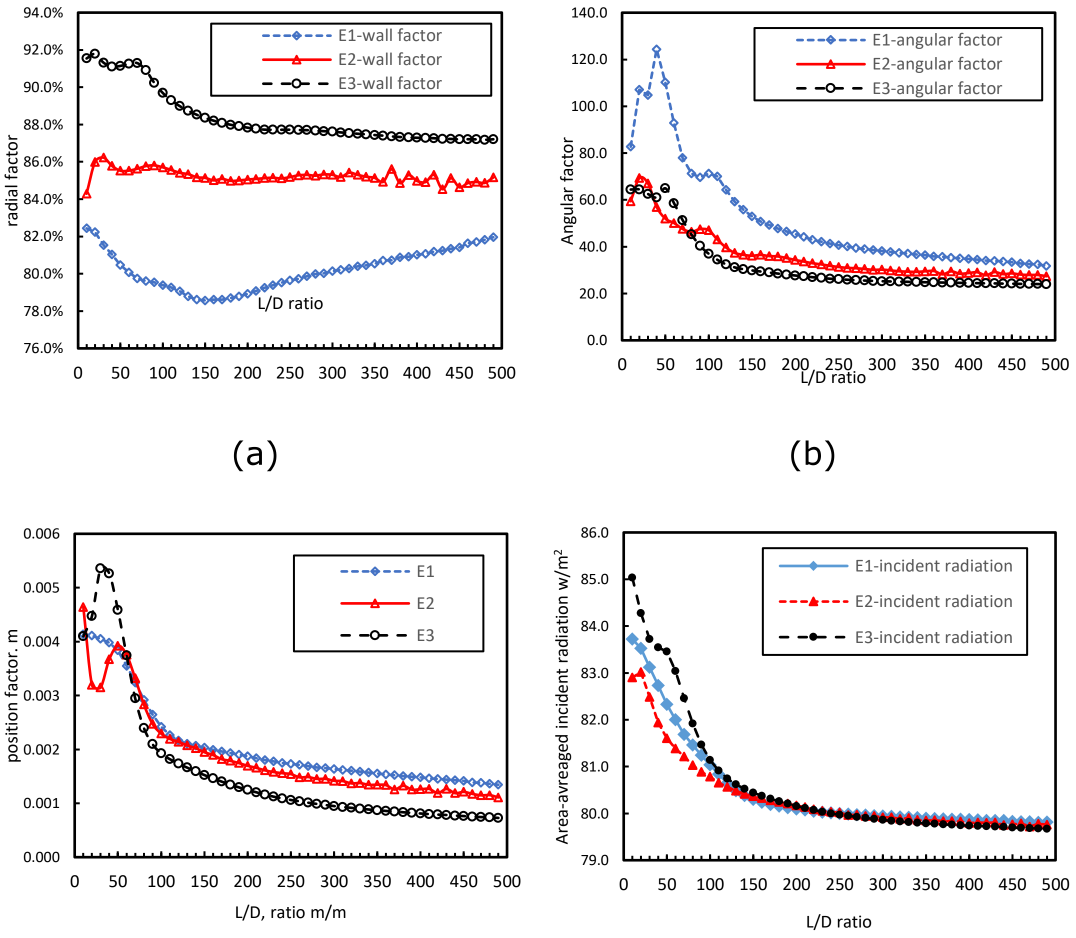

(a) (b)

(c) (d)

Figure 6.11 Defined factors, (a) radial factor, (b) angular factor and (c) position factor, change along the reactor for different entry particle distribution in Geo.1 long pipe. (d) incident radiation

The first term $\overline{\phi_i r_i}$ of the position factor represents the extent to which particles are concentrated near the wall, which is the same as the numerator of the axial factor. This describes the particle distribution affected by centrifugal force at the cross-sectional (x-y) plane. By contrast, the second term $\overline{\phi_i y_i}$ describes the motion of particles affected by gravity, which signifies the parabolic settling movement along the pipe axis at the y-z plane. When particles form a perfect ring-shaped distribution in the cross-sectional planes at the reaction region due to the swirl effects, the value of the second term approaches 0 due to the offset between the value at +y and -y coordinates. With the effect of gravity and the decay of the swirl intensity, the particles settle and move to the -y coordinates region. This phenomenon reflected in equation 26 is the reduction of the attitude of $\overline{\phi_i y_i}$ gradually. The sum of these two terms presents the position where the particles are.

Figure 6.11 (c) shows the position factor change along the pipe. The position factor for E1 displays three regions with clear boundaries of three slopes. Due to the even entry condition, the particles in the upper and lower semicircle of the pipe are neutralized. However, the settled particle cannot be redistributed evenly immediately. The position of the major particles takes a heavier proportion in the calculation of the position factor. Thus, the position factor of the cases E2 and E3 implies the reason why E2 has lower absorption in terms of boundary condition. Generally, the majority of the particles do not pass the highest point, resulting in the movement being more like a swing at the lower semicircle of the pipe rather than a circular motion. On the contrary, the majority of the particles pass the highest point with a high peak at about 30D-40D of position factor. Although the swirl is on the decline, these particles keep expanding under gravity rather than the centrifugal force so that the angular factor of this case keep a higher level and last longer than that of the E2. This explanation can be also verified via the contours of particle distribution of these three cases at 30D shown in the Figure 6.12, where particles in the E3 trend to the upper semicircle whereas the lower semicircle for the E2 case.

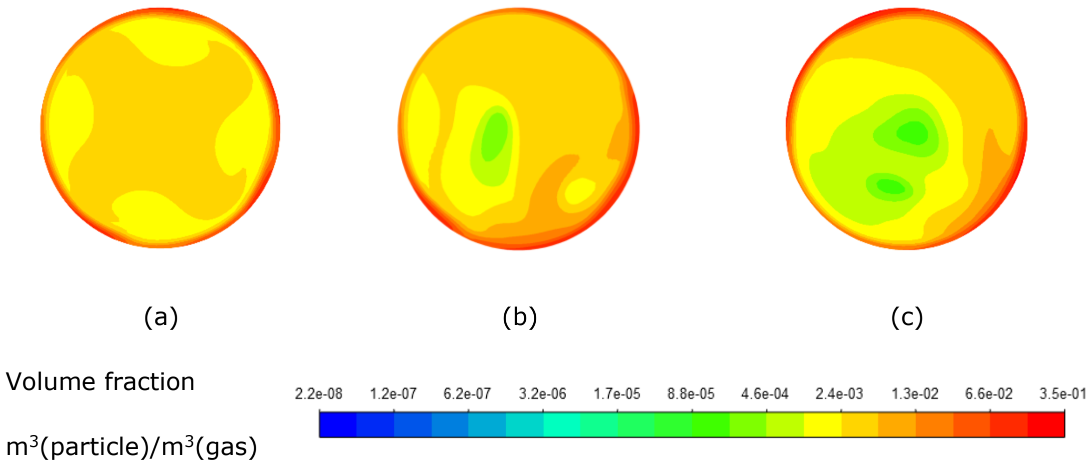

(a) (b) (c)

Figure 6.12 coutours of the particles volume fraction for (a)E1 (b)E2 (c)E3 entry condition.

Figure 6.11 illustrates the incident radiation, which changed based on both the angular and the radial distribution with the same initial boundary radiation input. To design a better-performed reactor, increasing more incident radiation is the right way to increase the efficiency of using the radiation as the absorption coefficient of the radiation is a constant for fixed material at a certain wavelength of the radiation. This increase of the incident radiation at the swirl region means that the light is more easily transferred from the annular distribution than the settled particle. It also implies that this distribution reduces the energy loss via scattering.

To observe the relationship between the distribution factors and the radiation absorption, a correlation between the them were displayed in Figure 6.13 (points after 150D were eliminated). Figure 6.13(a) shows a generally increasing tread with increasing angular factor, while different entry gives a different slop. By contrast, the increasing mode caused by the radial factor (Figure 6.13(b)) like parallel lines for different entry. The possible reasons are (a) different initial solid loadings, (b) related points (each entry is a process and points in the process are affect each other, e.g. overlap of incident light point) and (c) degree of compression (voidage of particles).

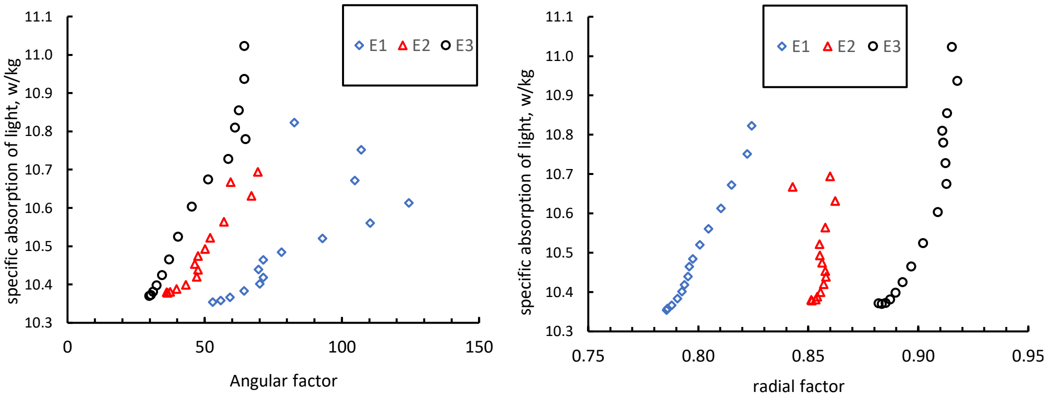

(a) (b)

Figure 6.13 Correlation between specific absorption of light and distribution factors. (a) angular factor and (b) radial factor.

6.5 Effect of the Reactor Arrangement

The multiphase flow field downstream of the swirl pipe varies as the swirl decays suggesting that the swirl pipe only impacts a certain effective distance. To keep the effect of the swirl, various swirl-straight pipe combinations are examined to provide insights into the more complete design of the reactor. The three combinations are long pipe, short pipe and joint pipe.

The swirl effect starts to disappear at about 50D based on the result of a long pipe. Based on this data and an extra 10D longer to ensure the flow for calculation accuracy, a short pipe with a length of 60D was created to examine the performance. The comparison in terms of the radiation absorption between the long pipe and the short pipe is displayed in Figure 6.14. Compared to straight pipe, swirl-induced pipe combined with the long pipe, short pipe, and joint pipe can concentrate particles to the place where they can receive more light. The swirl flow can compress the solid flow at the flow direction so that the movement path of the particle increases, and solids stay longer time at a strong swirl section. It presents a significant difference between them for the same E3 entry condition and the only difference is the length of the reactor. Based on the variable, the settlement of the particle at the far end of the glass pipe may result in this difference. This accumulation at the bottom of the long pipe creates a partial blockage environment which requires higher pressure to ensure the flow. This higher pressure provides more energy to the particles and makes the majority of them flow to the highest point, which results the higher radiation absorption.

This difference implies that the pressure difference may improve the performance of the reactor. Meanwhile, this short pipe cannot be used singly, especially for slow proceeding solid-state photoreaction. Thus, it may suggest that the next swirl pipe connected in series has a positive effect on the straight pipe. Then, the joint pipe which is two connected swirl-straight units was built and tested on how the swirl pipe affects the upstream flow field. Figure 6.14a also displays the performance of the joint pipe reactor. It shows a slightly better absorption of radiation than that for short pipe due to the effect of the downstream swirl pipe on the upstream glass pipe.

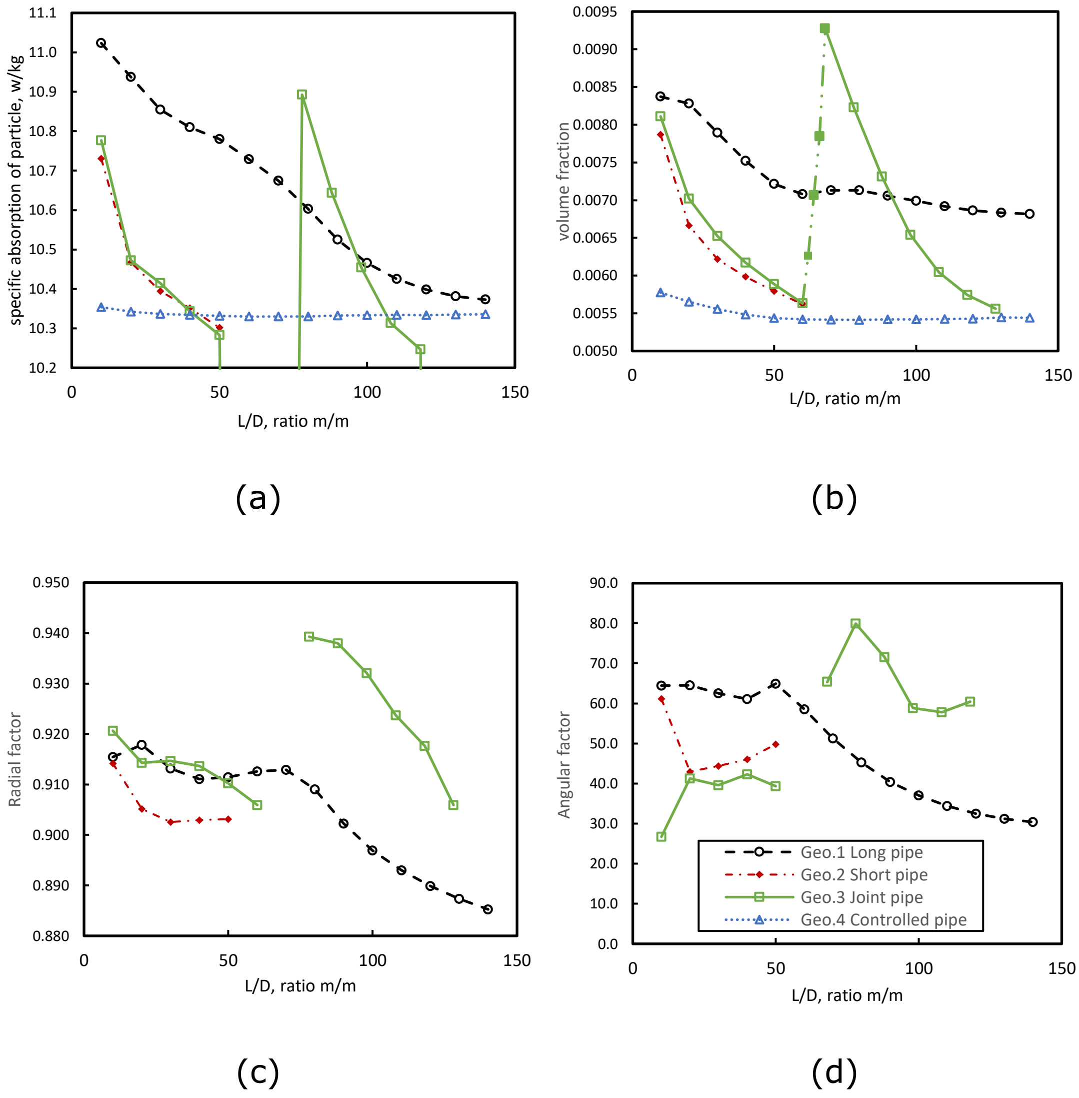

(a)

(b)

(c)

(d)

Figure 6.14 Specific absorption of particles(a), particle volume fraction (b) and the spatial distribution characterized by the radial factor (c) and the angular factor (d) along the glass pipe under different geometries. For the Joint pipe, the point marked with a solid green square represents they are inside the swirl pipe. The gap is due to the stainless steel swirl pipe.

Figure 6.14b displays that the particle volume fraction changes and the LVREA changes along the pipe in these tested geometries. Due to a transition between straight and swirl pipe, the flow can smoothly go through the swirl pipe. Therefore, there is a slight increase of pressure drop caused by the swirl pipe. This increase promotes the movement of the particles to a better distribution for radiation absorption. At mean time that this diagram shows a better continuity for short and joint pipe without settlement formation. The volume fraction at outlet of each glass pipe for the joint pipe keep the same, which presents a stabile particle flow.

Although the total LVREA of the long pipe is higher than that for joint pipe due to the higher concentration of the particle, it has the risk of over-irradiation and pipe blockage for the dead zone created by the settlement.

Figure 6.14c and d represent that the swirl pipe in series can improve the performance in terms of the particle distribution with the increasing number of swirl pipe. Obviously, the addition of swirl pipe can further push the particles to the pipe wall till the volume fraction to the packing limit. Apart from the increase of absorption of radiation from the E1 case to E3 case, the joint pipe shows a higher both in term of radial factor and angular factor. Meanwhile, the frequent application at proper position can help the spread of the particles to a broader angle resulting in a higher angular factor.

These two diagrams also validate the defined factor to a certain degree. The short pipe has the similar radiation arrangement with the joint pip. The higher radial factor but the lower angular factor of the joint pipe results in a similar performance of the specific radiation absorption. Then, the joint pipe has a better performance in terms of LVREA due to the higher volume fraction according to the relationship in the section 4.2. However, although the second glass pipe has a higher radial factor and a higher angular factor, the specific absorption of this section is not comparable with that of the long pipe due to the radiation arrangement. The superposition effect of the light makes the long pipe with the continues light source has higher absorption because it receives a more complete incident radiation. On the contrary, the discrete light source provides a weak incident radiation at the place neighbouring the stainless-steel swirl pipe, leading to lower specific absorption rate.

6.6 Effect of the Particle Size

The radiation transfer equation is mainly affected by the absorption coefficient, scattering properties, temperature, and the initial light intensity. Due to the low absorption coefficient of the cinnamic acid and the slow reaction rate, the heat from the radiation and the reaction can be ignored which can affect both the flow field and the radiation. Thus, the isothermal operation is a reasonable assumption in this simulation. Therefore, the scattering properties of crystalline is one of the possible reasons that affect the absorption of the light as the absorption coefficient is a nature of a molecule.

The scattering coefficient is affected by the particle size. Based on the ratio of particle size and the wavelength of the radiation (a), the scattering coefficient can be divided into Raleigh scattering (a <<1), Mie scattering (a is about 1) and geometric scattering (a >>1). This scattering coefficient can be determined by exactly Mie calculation in the Chapter 3 Section 3.4.6 (p159). Considering that the nanocrystalline was commonly used in solid-state photochemistry (Park et al., 2018, Hernández-Linares et al., 2015) and that the mode switches from Mie scattering to geometric scattering, the particle size was selected as 200 nm to 5μm shown in the Table 1. Meanwhile, apart from the properties of the scattering, different particle sizes affect not only the flow field through the momentum exchange coefficient but also the reaction rate.

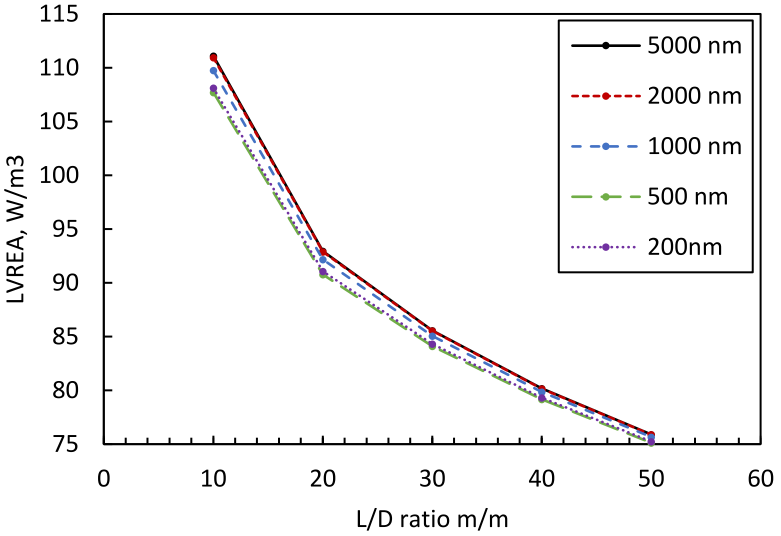

Figure 6.15 Relationship between the LVREA in the swirl section under different particle size

To avoid the particle distribution affecting radiation field under different particle size, the flow field of case at short pipe with E3 entry condition and 5μm particle size was fixed and the radiation distribution under this distribution was calculated by one-way calculation. Thus, the flow field can be regarded as independent to the radiation. In this paper, five different particle sizes were tested, and the parameters for each test are summarised in Table 6-1.

Table 6-1 Mie scattering calculation.

Diameter of the particle	Parameter number	Scattering efficiency	Asymmetric factor	Forward fraction weighting factor
d (nm)	x	Q_{sca}	g	f
5000	34.41	2.129	0.7814	0.6106
2000	17.21	1.282	0.7203	0.5188
1000	8.602	2.787	0.6197	0.3840
500	3.441	4.411	0.7268	0.5282
200	1.721	1.464	0.6143	0.3773

Overall, the light scattering of the particles with different size has a little effect on the LVREA. Apart from the annular distribution of the particles reduce the radiation loss, the main reduction caused form the particle scattering properties. Figure 6.15 displays the absorption of the light for different particle size. Apart from the 500nm particle, the LVREA increase with the increasing particle size. For this special case, their diameter is comparable to the wavelength of the radiation, which is 365nm. This comparable size results in the radiation act as a photon rather than the electronic wave, so that the radiation absorption is reduced by higher scattering loss. When the particle sizes increase and enters the region of geometric scattering, the effect of the scattering is almost the same (2000nm-5000nm).

6.7 Conclusion

In this chapter, a swirl-induction pipe was attempted to address the existing sedimentation problems in a multiphase flow photoreactor for solid state reactions. The air-particle flow field induced by the swirl induction pipe and the particle distribution caused by this flow was numerically investigated with the Eulerian-Eulerian approach k-ω turbulent model. At mean time, the relationship between radiation absorption and the particle distribution was studied with the DO model.

The effect of the particle’s distribution in the angular and radial co-ordinates on the absorption of the radiation was described in detail, as well as that of the particle loading caused by the compression of the swirl flow. Generally, the swirl pipe promoted an even spread particles distribution to the downstream, forming an annular flow with a relatively compact layer, minimized the loss of the radiation caused by scattering. This swirl tube can form a particle flow with four streams due to the geometry. When these four streams of particle merge together with settlement process, the specific absorption of the particles decrease to a constant level. Although this swirl induced pipe cannot form a perfect spread particle flow, it can still increase the coverage and the distance to the pipe wall. Meanwhile, particles are concentrated due to the twisted path caused by the swirl flow, resulting in the increase of LVREA, improving the performance of the tubular reactor.

According to the those stated phenomena, radial, angular and position factor are defined to assess the spatial distribution of the particles. These factors describe the distribution mathematically in terms of the distance to the reactor wall, total angle of the discrete arc and the place of the majority of particles respectively. They can explain the relationship between the particle distribution and the radiation performance.

A comparison between different geometric arrangement of the reactor was performed to assess the performance of the reactor. It shows that the swirl induced pipe can increase both the LVREA and the specific radiant absorption of the particles periodically. The swirl pipe in series can gradually increase the radial and angular factor, improving the absorption of the light. At mean time, it can provide continuous swirl so that the settlement and the dead zone can be reduced effectively.

It also shows that there is a large gap to optimize the reactor, in terms the boundary condition for instance, gas speed, length of the glass pipe, particle size and radiation flux. How to increase the radial factor and the angular factor are the key step to improve the performance of the reactor. It shows a large potential to build a suitable continuous flow reactor for solid state photoreaction.

This study provides insight on what is good spatial distribution of the particles via this swirl pipe. By using the swirl pipe, the solid-state photoreaction can proceed in a continuous flow system. It helps the development of the research of the solid-state photoreaction and provide a possibility for industrial production. This process enjoys the superiorities of solid-state photoreaction including the mild reaction condition, high selectivity, solvent-free and green energy source. Meanwhile, the application of the solid-state photoreaction has the potential to a shorter or even new route for organic synthesis of valuable molecules.

Chapter 7 Flow Field Simulation

7.1 Introduction

This chapter presents a computational fluid dynamics model of the swirl flow that is induced in a fluid flow passing through the horizontally mounted optimized four-lobed 400mm length swirl pipe. The steady-state CFD model based on the Eulerian- Eulerian multiphase model, and $k-\omega$ SST turbulence model provide time-averaged properties of the swirl flows. The analysis focused on how the inlet boundary condition affects the particle distribution under the effect of the swirling pipe.

In this chapter, the variables to which are paid attention include initial velocities, particle load, particle size, initial particle distribution, and flow carrier. Meanwhile, the effect of the turbulence force and the length of the geometry were discussed in this chapter. Under the change of these variables, how the angular and radial distribution of the particles were analysed in terms of the related factor and then the radiation absorption can be estimated from them according to the correlation displayed in the last chapter. How the swirl pipe affects this distribution was also discussed in terms of velocity components.

A dimensionless analysis was performed to analyse the relationship between these inlet boundary conditions and the particle distribution factors along the downstream swirl pipe. A rough model was constructed via this analysis, and it was initially verified by the simulated data. By this equation, the performance of this swirl-induced photoreactor for solid-state reaction can be estimated, which is important to the reactor design.

7.2 Simulation Set-up

The commercial CFD software ANSYS Fluent 19.0 was employed to carry out the numerical study. The multiphase flow was simulated with the numerical method. Models including turbulence models, multiphase models, wall functions, the meshing method, the solver parameters, and the solution convergence criteria are described in Chapter 3.

Different inlet condition was applied, including the initial velocities, particle loading, particle size, entry condition, and different flow media (with different solids). For dilute pneumatic conveying, Hall (2012) provided a range including the particle loading and the gas speed, which is from 700-1000m/min (11.67m/s-16.67m/s) with mass ratio of solid to gas up to 15. According to this suggestion, the initial velocity was set as from 11 to 17m/s and the solid loading set from 1 to 20. Different particle sizes were also tested for they are used in the different literature. They affect not only the reaction rate based on the sites but also the flow field by the momentum exchanges. Different particle distribution at the inlet condition was also tested as the initial result shows that the semi-settled inlet performs better than the fully settled and uniform particle distribution.

The geometry used in this chapter includes a short pipe (L=60D) and a middle pipe (L=100D) with the consideration that different initial velocities change the position of the turning point between the swirl region and the decay region.

7.3 Result and Discussion

From the previous discussion, a proper particle distribution can improve the absorption rate of light radiation. This improvement can further increase the reaction rate. Therefore, in the reactor design, how the inlet condition affects the particle distribution is significant to study. In this section, the results were displayed in terms of independent variables.

Generally, the movement of the particles is mainly driven by these two interactions, the drag force and the turbulent dispersion force. They are highly related to the stokes number (Equation 7-1, same as Equation 2-5, p47). It shows that the force is related to the particle density, diameter, initial velocity, fluid viscosity and the characteristic length. Meanwhile, the initial conditions are important such as the initial position of the particles, geometry of the reactor and particle loading. In this section, the geometry, initial velocity, loading and the entry condition were analysed as the variable.

$$St = \frac{\rho_p d_p^2}{18\mu_f} \cdot \frac{u_0}{l_0}$$

7-1

7.3.1 Geometry

The geometry or dimension of the reactor is an important part of reactor design. Typically, the design equation provides the essential volume of the reactor and the ratio between the height/length and diameter was determined by pressure drop or geometric stability. In this design, the photoreactor was modified based on the tubular reactor by inserting one or more swirl pipes. Apart from the geometry of the swirl pipe (the twist angle and PD ratio), the length of the glass tube is important to use the swirl effectively as it is related to the radiation absorption.

In this section, the length of the transparent pipe was concerned. The same position was checked for different length of the length of the pipe with different arrangements. Figure 7.1 shows the area-averaged volume fraction along the pipe in different geometry. It presents that the induction of the swirl pipe increases the residence time of particles. The length of the glass pipe was set around the swirl section (60D), decay section (100D), and settled section (500D).

Compared to particles in the short pipe, those gather more in the middle pipe and long pipe, which implies that the retention time is longer in the middle and the long pipe. This is caused by the settlement of the particles. This settlement generates a higher pressure drop and compresses the swirl so that the mass flux is increased for the length longer than the decay lasts.

Considering the effect of geometry at the end, the joint pipe (two L=60D swirl-straight pipes connected) was also tested to show how the swirl pipe affected the particles in the last straight pipe. The performance of the short pipe was similar to that of the joint pipe which has a slightly higher volume fraction or higher retention time. This is caused by the pressure drop of the next swirl pipe to be overcome.

Although this higher retention time means a better use of the space and a higher rate of absorption of the light, the settlement of the particle is still a problem. From a previous study, the swirl pipe can handle the settled particle by the redistribution, but the increasing solid flow flux may result in a stronger light attenuation leading to a less uniform light distribution.

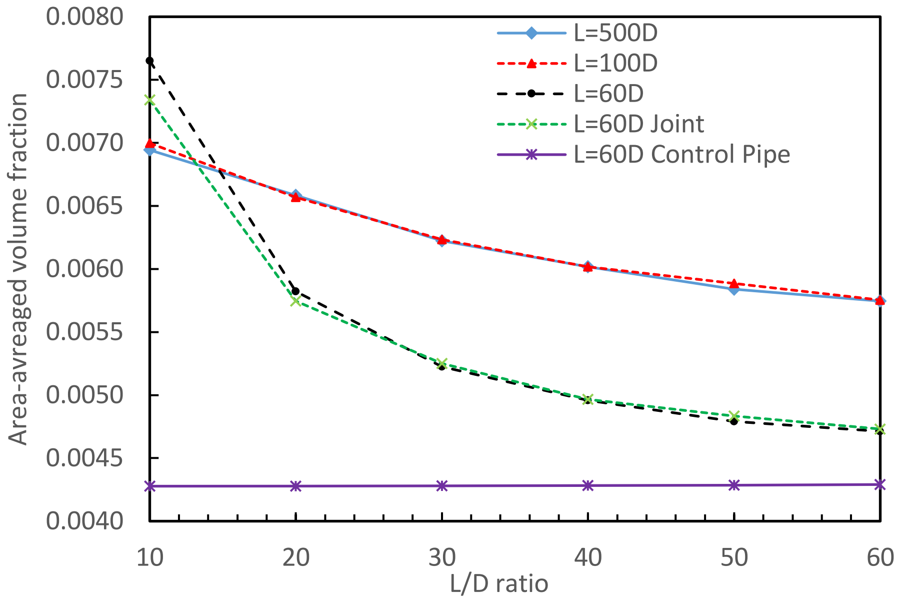

Figure 7.1 Particle distribution along the pipe in different reactors at the swirling section. (uniform inlet, particle loading=4.17, velocity=12m/s)

7.3.2 Initial velocity

Different inlet velocity provides different tangential velocities, which generate different centrifugal forces to the particles. This difference results in changes in the particle distribution in the reactor. In this section, the characteristics of the distribution were analysed in terms of axial distribution, radial distribution and angular distribution under the change of the tangential velocity.

The minimum tangential velocity of the swirl pipe provided is required larger than the minimum velocity for circular motion at the highest point. The minimum velocity for the circular motion can be determined by $u_{min} = \sqrt{gR}$, where R is the radius of the circle (which is the radius of the pipe in this case) and g is the gravity. In this $R = 0.005\,\mathrm{m}$ pipe, the minimum velocity for the circular motion was about $0.22\mathrm{m/s}$.

In this section, different inlet velocity was applied in the uniform entry where the gas velocity and particle velocity are equal. The solid load was 4.17 and the diameter of the particle was 5$\mathrm{\mu m}$.

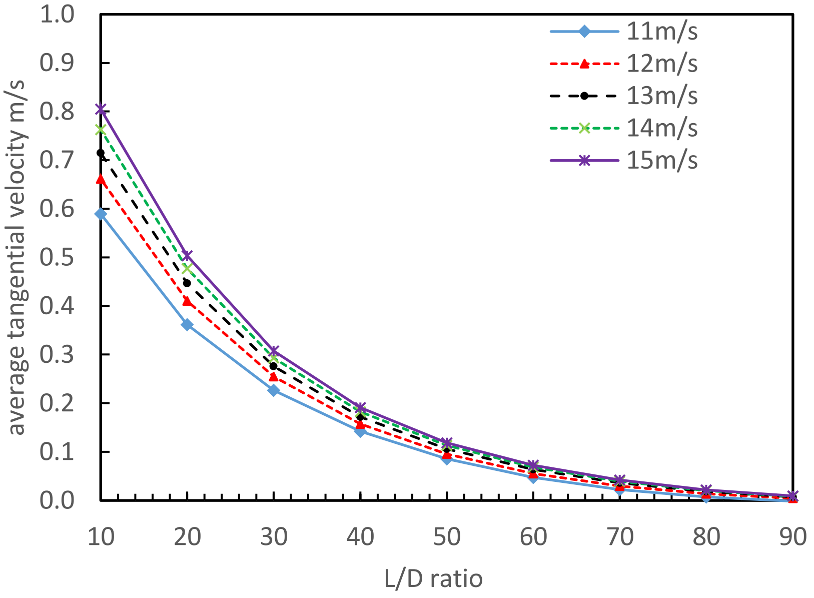

Figure 7.2 Tangential velocity distribution along the pipe under different initial velocities.

Figure 7.2 displays the tangential distribution along the pipe, from this figure, the tangential velocity was dropped down to the minimum velocity for the circular motion at about 50D. When particles are at the highest point with this velocity, they keep moving in a circle.

Figure 7.3 shows the average particle fraction along the reactor under different initial velocities. From this figure, the mass flux was increased with decreasing inlet velocity. There is an intersection at around 50D under this inlet speed. When the initial velocity is more than 13 m/s, the effect of accumulation is limited.

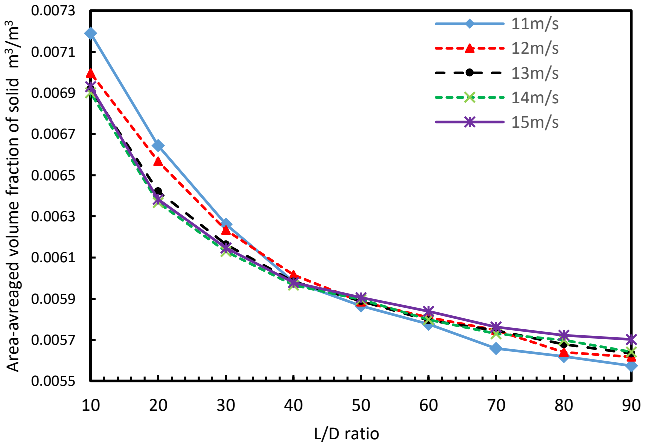

Figure 7.3 Particle distribution along the pipe under different initial velocities.

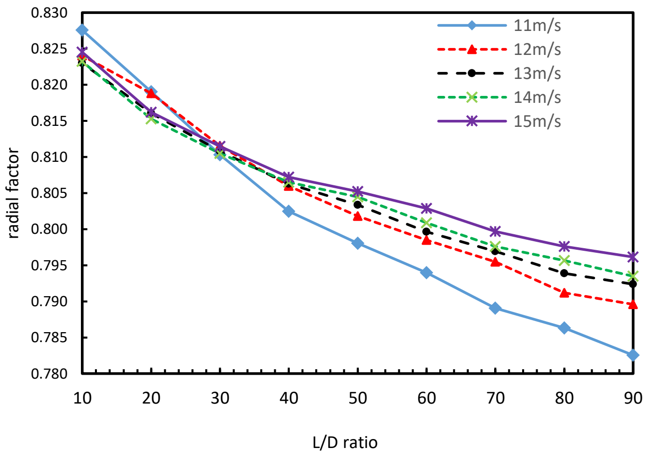

Figure 7.4 Radial distribution at different cross-section areas

The radial distribution displays a similar trend as shown in Figure 7.4. Apart from the initial velocity of 11m/s which has a sharper decrease, particles in the reactor have similar wall factors. The particles with 12m/s have a slightly higher wall factor. This is because more particles are accumulated in the larger ring. After the 30D, the case with higher speed has a higher wall factor. This was caused by the less press between the intergranular gap. The higher speed in the small channel between particles results in a higher pressure from the bulk gas and then keeps forming a compact layer of particles.

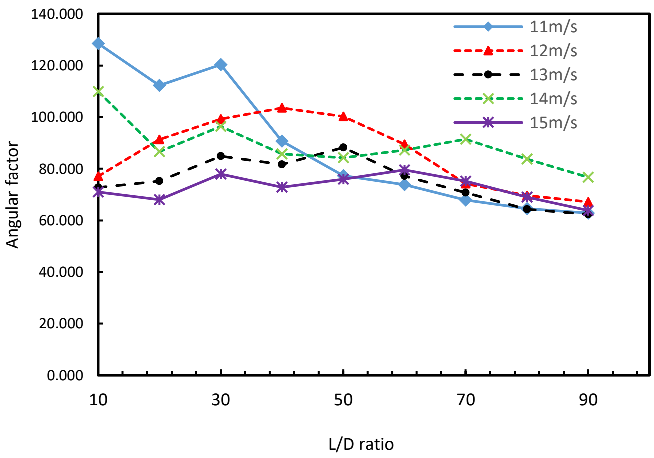

Figure 7.5 Angular distribution at different cross-section areas at different initial velocities.

Figure 7.5 shows that initial velocities have less effect on the angular distribution of the particles when they meet the requirement of the circular motion. When the speed is large enough, the angular factor can be regarded as a constant. The higher velocity has a lower angular factor because the less retention time results in the particle at the middle line having less chance to be affected by the swirl. The velocity of 11 m/s has an apparent decrease as the critical point appears earlier according to the tangential velocity.

In general, the inlet velocity has less effect on the particle distribution once it meets the basic requirement. In this case, 12 m/s may be the best choice as particles can be well redistributed and the energy consumption is acceptable.

7.3.3 Particle load

Compared to the initial velocity, the particle load has a greater effect on the distribution. From the value of these two variables, the change of the velocity is less than 100%, while the particle load is changed in multiples. The higher particle load requires more energy to convey. Meanwhile, the thicker layer of the particles affects the light absorption as well.

The Fluent requires a volume fraction as the phase concentration, so the particle loading was converted from 0.97, 2.03, 4.17, 8.27, 15.19, 19.69 to volume fractions of 0.001, 0.0021, 0.0043, 0.0085, 0.0155, 0.02 respectively. 12m/s gas velocity was used in this uniform entry with a diameter of 5 μm particles.

With the particle loading increasing, the tangential velocities provided became less (Figure 7.6). Gas at the same inlet condition cannot afford increasing particle load as more energy is required to support the motion of the particles. This led to the shortened swirl section as the critical point of minimum tangential velocity (0.22 m/s) appeared earlier.

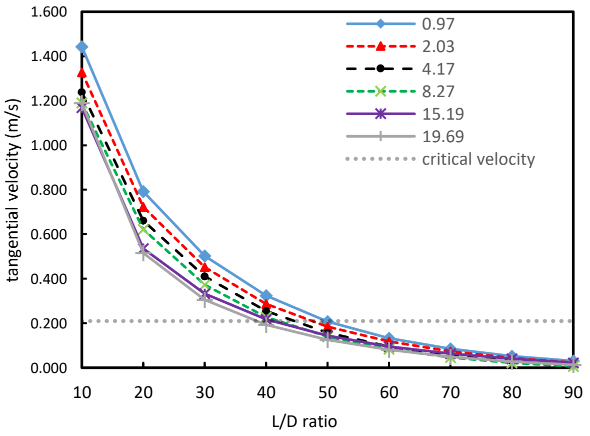

Figure 7.6 tangential velocity along the reactor under different particle load

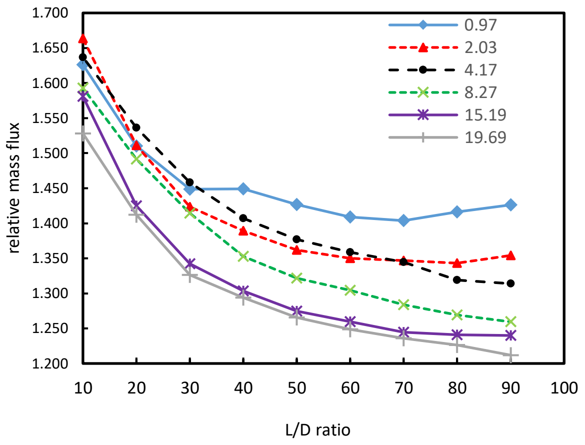

Figure 7.7 Mass change along the reactor under different particle load

Because the concentrations of the particle differ from these cases, the change of the mass flow was assessed by the relative mass flux, which is the ratio of the local area-averaged volume fraction over the initial volume fraction. This relative mass flux shows the mass change along the reactor based on different solid loading (Figure 7.7). From this figure, the mass is easier to accumulate in the reactor for lower solid loading. The mass flux reaches a peak at about 20D and then drop down rapidly. The rate of this drop down become flat at around 50D. It was worth noting that the loading of 4.17 shows a higher relative mass flux than that of 0.97 and 2.03 during the swirl section 20-40D. This may be caused from the higher tangential velocity provided in the lower loading.

The radial factors of these cases were shown in Figure 7.8. It shows that the lower particle loading has a higher factor. The increase of the particle loading results in a thicker ring of the particle distribution. With the thickness of the ring increasing, the average diameter of the ring is reduced, and then the extinction coefficient is increased as the light was absorbed and scattered by more particles. This phenomenon was also shown in the radial factors. This fact can still illustrate how these particles are closed to the glass wall in terms of determining the absorption of the light.

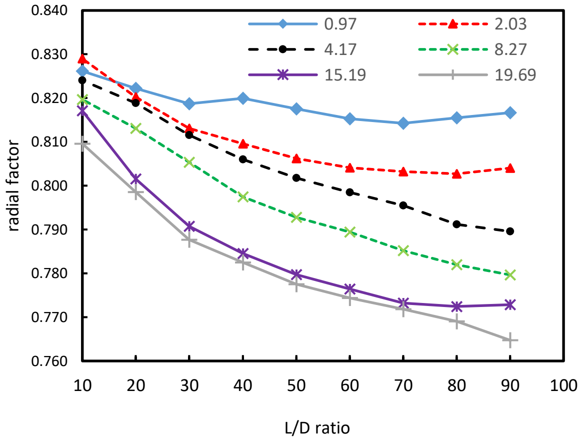

Figure 7.8 Radial factor along the reactor under different particle load

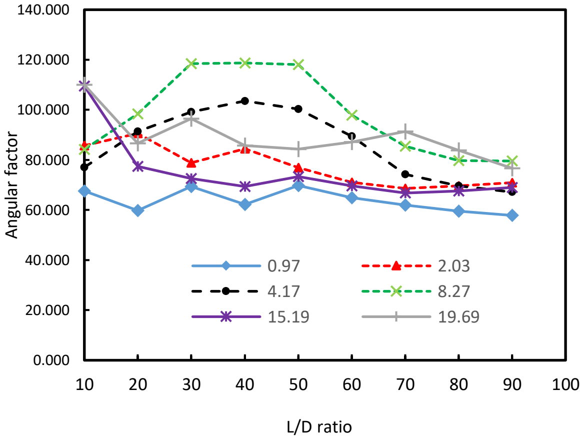

Figure 7.9 Angular factor along the reactor under different particle load

The angular distribution affected by the particle load is no longer linear as the radial factor. For the small loading in the Figure 7.9, the change is not obvious, while for the large loading, they are drop down early and then keep constant. For solid loading of 4.17 and 8.27, there is an obvious expand to the circle and then settled. Considering the accumulation effect of the swirl pipe, the solid loading of 4.17 was selected to provide more space for increasing particles.

7.3.4 Entry Condition

Profiles from 30D to 200D was cut from the E3 (described in Chapter 4) and they are applied as the inlet of the swirl pipe (as the second swirl pipe in the Geo.4 Joint pipe). They include swirl section (30D-50D), decay section (60-100D), and the settled section (150D and 200D). The main differences between them are particle distribution and the velocity distribution. The initial conditions of these profiles are listed as follows: the average velocity at the inlet was 12m/s; the diameter of the particle was 5μm and the loading was 4.17.

Figure 7.10 illustrated the tangential velocity under these entries. In general, the change of tangential velocities for them are almost the same. However, the similar tangential velocity gives different particle distributions.

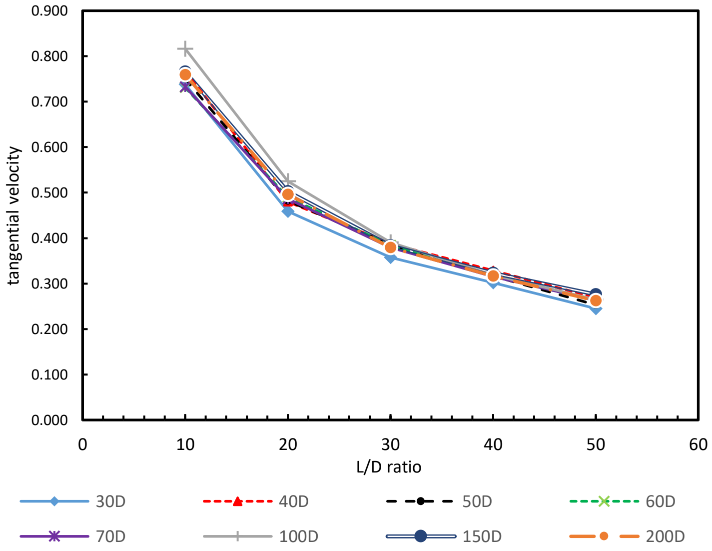

Figure 7.10 tangential velocity along the reactor under different entry condition (particle distribution)

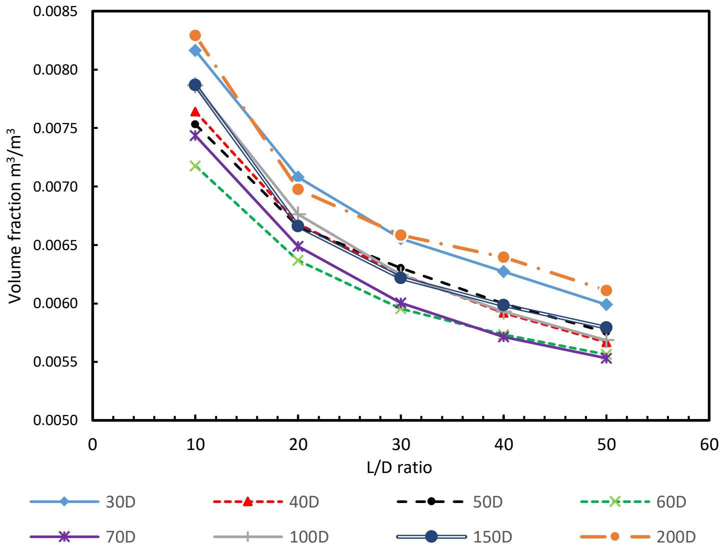

Figure 7.11 Particle concentration along the reactor under different entry condition (particle distribution)

The particle distribution along the pipe was shown in the Figure 7.11. The concentration of the particle was separated into three different level. The highest concentrated were the case at inlet 150D and 200D, which are the settled entry. After that, the swirl entry gives the downstream particle distribution a middle accumulation. This cause by a second centrifuge and particles are more likely flow close to the wall. Therefore, particles in the decay region has a lowest accumulation as particles are loosen from the swirl and some of them flow on the centre line of the pipe (it is the easiest place to escape from the tube where has the highest gas velocity).

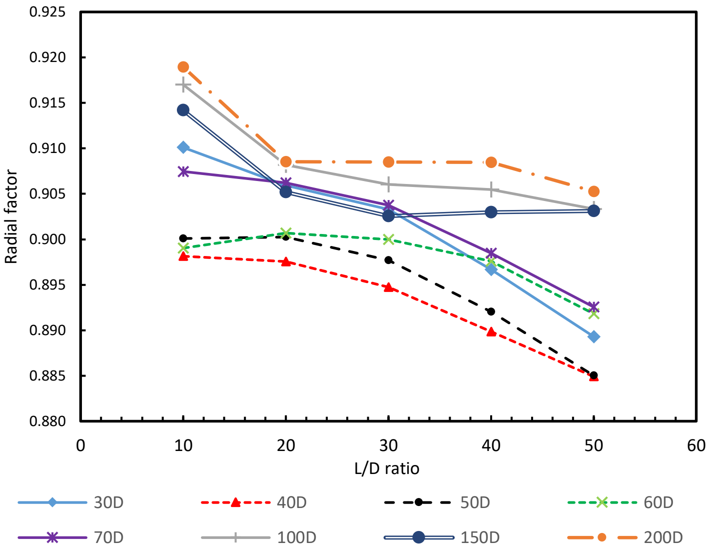

Figure 7.12 Radial factor along the reactor under different entry condition (particle distribution)

In terms of the radial distribution of the solid particles, the radial factor illustrates a decreasing trend (Figure 7.12). Generally, the change of them can be divided into two shape. The first type is parabolic and they appear in the case with inlet distribution from 30D to 70D. In this group, the two highest cases are 30D and 70D. The formation of them are different. The case with 30D inlet was caused by the secondary compress of a strong swirling particle flow, while the settlement of the particle leads to a thicker layer of the particles which resulting a higher radial factor of the 70D inlet case. After that, the case 60D occupies a middle place and the last two curves have this shape shown in the case with 40D and 50D inlet. This decrease between the 30D case and 70D case is because part of the particles falls to the region near the centre of the pipe where a weaker swirl generated. Similarly, the radial factor is high when the particles fully settled at the inlet as case 100D-200D, which forms another shape of the curve. This shape implies particles are gathered (loose packed) and thrown to the highest point while parts of them are limited to the highest point due to the packing limit. These particles rotated falls to a smaller circle (close to the centre) and contributing to a smaller radial factor at about 20D.

It was proved by the angular factors shown in the Figure 7.13 as higher angular factor represents a more even distribution. The angular factor of then shows that the semi-entry 70D has a high angular distribution that decay helps the spread to form a thin layer of particles.

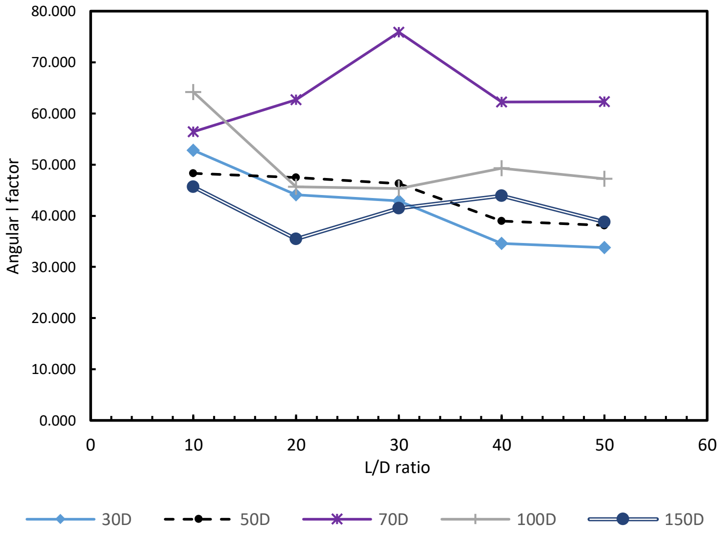

Figure 7.13 Angular factor along the reactor under different entry conditions (particle distribution)

7.4 Conclusion

In this chapter, a swirl-induction pipe was attempted to address the existing sedimentation problems in a multiphase flow photoreactor for solid state reactions. The air-particle flow field induced by the swirl induction pipe and the particle distribution caused by this flow was numerically investigated with the Eulerian-Eulerian approach SST k-ω turbulent model. Different inlet boundary conditions were tested and compared.

The length of the glass pipe was determined based on the combination of the entry distribution and the geometry. The point at the middle of the decay section (about 70D) should be connected to the next the swirl pipe. Thus, the settlement can be reduced meanwhile a better particle layer would be formed. The velocity is about 12m/s and the best solid loading is about 4.17.

Chapter 8 Discussion

8.1 Summary of the Key Findings

Solid-state photochemical reactions have many advantages in terms of high selectivity. The currently used photoreactors have limitations on the solid-state chemistry in managing solid and controlling the light. The absence of a suitable reactor limits the development of solid-state photochemistry. This thesis focuses on four main research problems in designing a suitable photoreactor for solid-state reactions. In this thesis, we found that:

- The insertion of the swirl pipe redistributes the particle distribution downstream of the swirl pipe and helps the continuous movement of particles.
- The redistribution of particles improves the absorption of radiation from the light.
- The relationship between the absorption of the light and the reaction rate was theoretically derived.
- There is an optimum region of the initial conditions giving a better performance.

8.2 Interpretations and Implications

8.2.1 CFD Simulation

This investigation was based on the numerical simulation method, which is a cost-effective approach to obtain information that cannot captured by experiment. In this research, it seems that the induction of the swirl pipe is the main variable, but it is the particle distribution caused by the swirl flow in fact. The change of the particle distribution affected the radiation distribution by changing the extinction coefficient of light. The particle distribution can be observed by taking photo from high-speed camera while the radiation distribution is hard to be measured. Therefore, this method is helpful for better understanding about how this swirl pipe works. The accuracy of the model was initially tested and the result was similar to what shown in the literature. Because the content of the test is not related to design of the reactor, they are not included in this thesis.

8.2.2 Reaction kinetics

To design a reactor for solid-state photoreactions, the kinetics or the reaction rate is significant. The most popular model used to describe the reaction rate of solid-state photochemistry was the JAMK model. As it was originally used for the solid-state chemical reaction, there is no light intensity in the expression but it is important for photochemical reactor design. Besides, another expression was also commonly used base on the definition of the quantum yield for photochemistry in solution. Although this equation connects the reaction rate and the light intensity, this equation is not applicable for solid-state reactions for two reasons. Firstly, it does not consider the effect of the solid structure. Therefore, the quantum yield can describe the average efficiency of the light for the reaction, but it cannot be applied reversely to described the relationship between light and the reaction rate. On the other hand, the instantaneous quantum yield is hard to be measured accurately for reactions in solid state, so that there is no enough information reported about the quantum yield for solid state reactions.

This derivation in the Chapter 5 combined the mechanism of the solid-state reaction and that of the photochemistry. This expression was derived from the cites of the particles. It shows that the reaction rate was related to the concentration of the particle as well as the light intensity during the reaction process controlled by the nucleation and nuclei growth. Apart from these, the expression for isothermal reaction shows that the reaction rate also related to the particle properties, including the shape and the density of the sites. This model was verified by other researchers results. It shows that how this process is controlled by the solid-state mechanism and the light intensity, and it is a modification to describe the kinetics of solid-state photochemistry.

8.2.3 Radiation field

The radiation field was affected by the extinction coefficient. This coefficient was widely measured by the Bear-lambert law, with the assumption that the media for light transport was uniform. This coefficient was changed according to the particle properties and their distribution. As the particle optical properties is the nature of the chemical, the distribution was regarded as the object of research.

Compared to the straight pipe (controlled pipe) which results in the uniform distribution (ideal) and the settled distribution, the ring distribution of the particles has higher radial factor and angular factor at mean time. This characteristic of the ring distribution makes the particles receive more uniform radiation. This distribution lead to a higher extinction coefficient close to the edge of the circle (cross-section area) and it was reduced from the wall to the centre of the circle. When the highest radiation intensity meets the highest extinction coefficient all around the pipe wall, the radiation intensity was also reduced with the decreasing coefficient, and then forming a relatively uniform distribution. This phenomenon was accordant with the Bear-Lambert law.

In this research, the distribution of the particle was separated into angular distribution and radial distribution. These two component distribution was defined by angular factor and radial factor respectively. The increase of radial factor means more particle gather closed to the wall, while the decrease of the angular factor represents that the particles separate more evenly to each angle. According to the result in the Chapter 6 section 6.4 (p231), the combination of them is able to describe the relationship between the particle distribution and the radiation distribution. However, this correlation was not expanded to a large range limited to the properties of the reactant. More data are required to prove the feasibility of it for a broader application.

This is a new trial to us a statistic method to convert the ring distribution into two numbers. These intermediate indicators show the mechanism how the swirl works on improving the radiation absorption. By using these two factors, the performance of the reactor can be more easily estimated as there are various boundary conditions affecting the radiation absorption. Meanwhile this estimation can reduce the computation consumption where calculating the radiation field occupy.

Focusing on the specific case of the [2+2] photocycloaddition of the cinnamic acid, the absorption of the light in this swirl-induced reactor can be increased up to 5% than that in straight pipe. Although it is not large enhancement for small-scale production, it can save a large amount of energy after scale up. In addition, cinnamic acid is a semi-transparent material with 70% transmittance at wavelength at 365 nm. This imply that there still are margins of the performance of this swirl induced reactor.

8.2.4 Flow field

- Research pathway and initial condition selection

In fact, the TiO_2 was firstly selected as the solid particles at the beginning of this research, as there are empirical equations of the absorption coefficient and the scattering coefficient. Meanwhile, it was also applied in simulation of the slurry tank photoreactor. It was a good choice to start with a simpler material.

Water-TiO_2 system was initially tested considering that this system is more easily validated by assembling a similar rig. The particle was set to a diameter of 200 nm and a concentration of 1g/L (uniform distribution), with the liquid velocity from 1 m/s to 3 m/s. However, it is hard to redistribute the particles due to the strong following features. Therefore, to build a ring separation, air-TiO_2 system was tested afterwards.

TiO_2 was tested and compared at the same condition as the cinnamic acid. The LVREA of ring distribution can be up to about 4 times higher than the uniform distribution, and about 20% higher than the settled distribution. The difference between these two solid materials shows that the performance of the reactor depends on the extinction coefficient of the material and shows that the potentials of this reactor.

The reason why TiO_2 was not selected as the example to characterize this reaction is the fast reaction rate for the photocatalytic reaction with gas, which the stationary solid may be the better choice based on the literature review. Meanwhile, the characteristics of this swirl-induced reactor is more suitable for solid-state reactant than catalyst.

Table 8-1 Stokes numbers of particles at different initial condition

Media	Velocity of fluid (m/s)	Stokes number			
		Titanium catalyst		Cinnamic acid	
		d_p=200nm	d_p=2μm	d_p=200nm	d_p=2μm
Water	1	0.04	0.39	0.01	0.14
(μ_g=1cp)	2	0.08	0.78	0.03	0.28
	3	0.12	1.17	0.04	0.42
Air	12	25.93	259.26	9.24	92.44
(μ_g=0.012cp)	13	28.09	280.86	10.01	100.15
	14	30.25	302.47	10.79	107.85
	15	32.41	324.07	11.56	115.56

Stokes number, $St = \frac{\rho_p d_p^2 u_0}{18\mu_g L}$, ρ_p is the density of particles, d_p is the diameter of particles, u_0 is the velocity of fluid, μ_g is the viscosity of the fluid and L is the characteristic length.

Considering the application of this reactor, the cinnamic acid was selected as example to show the performance of the reactor. Compared to the titanium catalyst, the organic solid has lower density. The titanium catalyst has a density of about 3500 kg/m^3

while that of cinnamic acid is about 1248 kg/m^3. By studying the Stokes number of the system, which is a dimensionless number describing the behavior of particles suspended in a flow, the general performance of the reactor can be estimated. Table 8-1 shows the Stokes number of each system. According to the physical meaning of this number, when this number is much larger than 1, the particles detach from a flow especially where the flow decelerates suddenly. Therefore, when particles conveyed by gas meet the twisting wall of the swirl pipe where the velocity of the flow decrease, particles are more easily gathering in the place close to the wall. This results in a better performance of solid-gas system than that of solid-liquid.

The change of media also changes the models used. When air was applied as the transport media, the stokes number increased to much than one. This implies that the turbulence dispersion force is no longer affect the movement of the particle apparently.(Zhang et al., 2024)

Apart from the perspective of Stokes numbers, the tangential velocity is also a parameter to assess the performance of the system. The swirl pipe can provide water without particles the maximum tangential velocity. From previous study, the maximum tangential velocity of water system was just higher than the critical velocity at the exit of the swirl pipe (0D) when the inlet velocity was 1.5 m/s. For even inlet velocity at 3m/s, the tangential velocity can last higher than the critical velocity for only 30D, where it is very high speed of water in industry with lower cost performance (Li, 2016). This also shows that water may not be a good start for this reactor design.

- Characteristics of the downstream flow of swirl pipe

The much higher absorption of the light of titanium catalyst in swirl pipe system than that in straight pipe (uniform entry) drew the attention as well. It implies that the selection of the reference may be inappropriate, as uniform distribution of the particle is ideal. Therefore, the different initial conditions in terms of the particle distribution was tested and shown in the Chapter 4. This chapter shows the basic characteristics of this system under different entry condition and the downstream particle distribution was mainly studied. The result showed that the swirl pipe can handle solid effectively even for settled condition. Meanwhile, combined the result of the flow and the relationship between the particles distribution and the radiation distribution in Chapter 6, the semi-settled entry performed better. It implies that when multiple swirl pipes were applied to the system as a part of the reactor, the length of the circular pipe between two swirl pipes was the better at about 60D-150D. This is important in reactor design. Other boundary conditions were discussed in last chapter.

- An attempt to construct a universal equation

Apart from creating an intermediate to link the flow field and the radiation field, another aims of defining radial factors and the angular factors is to construct a universal model describing the relationship between the boundary condition and these factors and then forming a design equation for this reactor. For this purpose, the dimensionless analysis has been attempted to fitting and then to find an equation. The Buckingham Π theorem is a key theorem in dimensional analysis. This theorem states that if there is a physically meaningful equation involving a certain number n of physical variables, then the original equation can be rewritten in terms of a set of $\mathrm{p} = \mathrm{n} - \mathrm{k}$ dimensionless parameters Π_1, Π_2, ..., Π_p constructed from the original variables. (Here k is the number of physical dimensions involved; it is obtained as the rank of a particular matrix.) Variables including particle diameter (L), particle speed (LT^{-1}), particle density (ML^{-3}), mass flow rate (MT^{-1}), length from the exit of swirl pipe (L), pipe diameter (fluid characteristic length) (L), fluid speed (LT^{-1}), fluid viscosity ($ML^{-1}T^{-1}$), and fluid density (ML^{-3}) were regarded related to radial factor (L) and angular factor (L^{-2}), and symbols in the bracket represent the length (L), mass (M) and time (T). By establishing several dimensionless numbers from these variables and these two factors, and then doing the logarithm of the production of these dimensionless numbers, the equation was initially formed by fitting the simulation data.

However, this result was considered unreliable as the particle distribution is dependent on the system, while it is hard to describe the change of the system by numbers. For example, when the length of the straight pipe increases from decay region to settled region, the stream lines are compressed due to the equivalent reduce of the diameter. This change is hard to be described and quantified in an equation and then this plan was abandoned. Possibly, if more data, whether they are experimental or computational, are obtained, this could be a way to simplify the process in design the reactor.

8.3 Significance

Generally, the invention of this reactor can increase the radiation absorption of solid particles. This can increase the reaction rate and improve the energy efficiency. The performance of this system shows that it has the potential to scale up for larger production for solid-state photochemical reactions. It can handle the settled particle and reduce the formation of the dead zone, which results in a continuous and controllable photoreactor.

Further, a well-established system of the swirl-induced reactor can promote the development of solid-state photochemistry, which has a high selectivity under mild reaction conditions. In addition, the unique product of solid-state photochemistry can shorten the route of synthesis, which can reduce the cost of production. This solvent-free process reduces the use of the organic solvent, which is more environment friendly.

8.4 Limitations

There is a few of limitation on this research in terms of the methodology, sample selections and workload.

Due to the large span of the particle concentration of the particles, the Eulerian model was selected to calculate the multiphase distribution, so that the retention time cannot be directly displayed by a bar chart (retention time vs number of particles) to show the continuity of this system. DDPM (dense discrete phase model) was tried to trace the particles, which can show the retention time intuitively. However, this method requires a large amount of computational resources and it is not stable because of the local high concentration of solid and the interaction among them.

Another limitation on the design of simulation is to design a reactor in practice, so that the result is different from that for studying simple relationship between particles distribution and the radiation absorption. For further studying the relationship between the particle distribution and the radiation, a thin layer of window can be applied to the reactor. By using this design, the effect of superposition of light fields can be eliminated, and the light distribution on the cross-section area and that scattered to the other space can be analyzed. However, this is not the target of this research. This thin window may not appear in a real reactor for solid-state reaction at present stage as the reaction rate has a positive relationship with light absorption. This design with periodically interstitial windows may be applied in the future for other purpose and it can be studied as future work.

Typically, the simulation should have been validated by experiment. To save cost, the initial plan is to design the reactor according to the simulation result. During the simulation, it was found that it is hard to observe the distribution of particle distribution and radiation distribution. The multiphase flow is sensible to the geometry inside pipe so that an insert sensor can change the flow, which prevents the validation. Therefore, the performance of the reactor was assessed by comparing the light absorption with and without the swirl pipe.

The potential of this system was not fully excavated due to the selection of the reactant. This selection was based on the richness of the experimental data to simplify the calculation. However, the transmission of cinnamic acid was about 70% at the setting wavelength, which is quite transparent material. Under this condition, the absorption of the light still has an increase of about 5% compared to settled particle in circular pipe in a lean phase. This number will be increase with less transparent material, which was verified by the performance of titanium catalyst in the system.

Other research factors may also affect the research results, such as the breakage of large particle and granulation of small particles under the shear stress, wear of glass and temperature. The effects of them are ignored during the simulation to simplified the calculation and they can be further studied to observe how they affect the performance of the reactor.

Chapter 9 Conclusion and Future work

9.1 Conclusion

This thesis intends to address the basics of designing the chemical reactor for solid-state photoreactions by the efficiency of CIP procedures in closed processing systems by locally introducing an intensified hydrodynamic force from swirl flow induced by an optimised swirl pipe. This investigation was carried out using a numerical method and covered four main topics: the basic characteristics of the multiphase swirl flow. The following conclusion can be drawn from the investigation.

9.1.1 Basic Characteristics of the Multiphase Swirl Flow

- The general characteristics of the swirl flow were investigated under three representatives of uniform, semi-settled and settled initial particle distribution. It shows that the semi-settled entry performs best in gathering solids while consuming the most energy.
- Particles prefer to move forward close to the wall under the drag of the swirling flow, and this property applies to fully settled particles. This property can solve particle settlement in the reactor and reduce the dead zone formation. This phenomenon allows solid-state photochemistry to operate as flow chemistry.
- The mass fluxs were increased due to the swirl so that the aborption of the light is going to be improved according to the Beer-Lambert Law.

9.1.2 Chemical Kinetics Derivation

- The modified JMEAK model was derived theoretically to adapt for solid-state photochemistry. It was verified partially and qualitatively as the number of data is limited.
- It was clearly shown that the increasing intensity of the radiation accelerates the reaction rate, which is sufficient in this thesis to convert the requirement from the higher reaction rate to the higher intensity of photon flux. This simplified the simulation as reaction simulation is difficult in involving multiple variables and less stability of calculation.

9.1.3 Radiation

- Particle distribution was separated into radial distribution and the angular distribution. By comparing the radiation absorption and the distribution, it was found that a fully expanded layer of particles close to the pipe wall is the best distribution to receive photons.
- Factors are defined to describe them in these two dimensions, and the results show that the radial factor and the angular factor can well describe the particle distribution. The higher radial factor represents how the particle compacted and closed to the wall while the angular factor shows the angle the particle occupied.
- Compared to the radial factor, the radial factor dominates the absorption of the light. It has a better comparison among different radial factors in a similar solid loading, because a higher concentration of the solid results in a shorter equivalent radius of the ring.
- The increased mass flux increased the LVREA up to twice as much as that of the controlled pipe, and the specific

absorption of photons increased by 5%. This means that the tubular reactor with swirl pipe performs much better in receiving light.

- The increase in the specific absorption of light means the efficiency of the light is increased. This was realized by a cutting (perpendicular) distribution to the light source. This results in a parallel change of extinction coefficient and the incident radiation and then forms a relatively uniform distribution of incident radiation. This is important to a photoreactor to reduce over-irradiation.

9.1.4 Flow Field Simulation

- Different length of the reactors was tested and the result shows that the performances are similar when the length of the glass reactor is longer than the settled.
- The performance of the downstream is depended on the distribution at the inlet. A semi-decaying inlet may be the best choice (70D in this case) to connect to the next swirl pipe.
- The relationship between particle loading, the inlet velocity and the particle distribution is not linear. In this thesis, the best loading is between 4 to 8 while the gas speed is about 12m/s. This value would be varied based on the particle density, particle size, fluid density and fluid viscosity.

9.2 Future work

9.2.1 Reaction Kinetics Verification

- To design a good reactor, the reaction kinetics are important, so that the verification of the model is essential.

In this research, the model was partially verified by limited data from the literature. Although it is sufficient for simplifying the research simulation, it is essential in the reactor design.

- The existing data for the kinetics are only related to the time and dimension index, while the temperature and the radiation intensity are also important. To validate this model completely, a large amount of experimental data is required with wide range of radiation intensity and strict temperature control.

9.2.2 Reactor System Assembly

- Based on the simulation result, the reactor system can be assembled. This construction can validate the simulation result. In this research, the result was only from the simulation. The performance of the reactor is based on the comparison with the straight pipe. However, the real performance still needs to be studied.
- During the design of the system, a difference between simulation and experiment is that experimental data cannot be collected as in simulation. For example, it is hard to find a radiation/particle distribution by using sensors or probes. If the conversion of the was chosen as the target to test, there are a lot of disturbances affecting the result. Thus, it is challenging to build this reactor for design purposes.

9.2.3 Model Optimization

- DDPM (dense discrete phase model) can be still tried to trace the particles, which can show the retention time intuitively.

It can provide another view to study the movement of the particles.

- More parameters may be applied to this model. In this research, the particles were set as cinnamic acid, while the absorption properties can be virtualized to a certain range rather than the set value of the cinnamic acid. Thus, more effective data in a large range can be obtained and then a calibration curve may be created.

Nomenclature

A	Absorbance
A	Area (m^2)
a	Absorption coefficient (m^{-1})
C	Specific coefficient/constant, depending on the subscript
C	Asymmetry coefficient
C_D	Drag coefficient
c	Concentration (mol.m^{-3})
D	Diameter of Pipe (m)
d	Diameter of particles (m)
e_{ls}	Coefficient of restitution between l^{th} phase and s^{th} phase
$\boldsymbol{F}$	Force (with different subscript)
f	Weighting fraction (or factor) of the forward scattering/ forward scattering factor
f	Temperately defined function or factor, normally noted with subscript or locally described.
f_d	Diffuse fraction
G	Turbulence production
g_0	Radial distribution function
g_{Mie}	Asymmetry parameter, determined from Mie calculation
$\boldsymbol{g}$	Gravity (ms^{-2})

g	Asymmetry factor
g'	Asymmetry factor of the truncated phase function
h	Heat transfer coefficient
I	Radiation intensity (energy per area of emitting surface per unit solid angle)
$\bar{\bar{I}}_{2D}$	Second invariant of the deviatoric stress tensor
$\bar{\bar{I}}$	Unit tensor
J	Mass flux; diffusion flux
k	Kinetic energy per unit mass
k	Reaction rate constant
L	Length of the pipe
$\dot{m}$	Mass flow rate (kg.s^{-1})
m	Mass (kg)
n	The (ordinary) refractive index
$\bar{n}$	The complex index of refraction
P_j	Legendre coefficients
p	pressure
p_s	Solid pressure
Q_{sca}	scattering efficiency
Q_{ext}	Extinction efficiency
Re	Reynolds number (dimensionless number)

Re_s	Reynolds number of solid particles (dimensionless number)
R	Core radius for the intermediate stage of transition pipe
r	Radius (m)
$\boldsymbol{r}$	The position vector of radiation
$\boldsymbol{r}$	Position vector
S	Modulus of the mean rate of strain tensor
S	Source term, normally with subscript
S_{ij}	Strain rate tensor
s	Path length (m)
$\boldsymbol{s}$	The direction vector of radiation
St	Stokes number (dimensionless number)
T	Temperature (K)
T	Transmittance (%)
t	Time (s)
$\boldsymbol{U}$	Free stream velocity (ms^{-1})
$\bar{u}$	Average velocity
$\mathbf{u}$	General velocity
u, v, w	Velocity component magnitude at x, y, and z directions respectively; also written with directional subscripts. $(\mathrm{u}_x, \mathrm{u}_y, \mathrm{u}_z)$ (m.s^{-1})

$\boldsymbol{u}, \boldsymbol{v}, \boldsymbol{w}$	Velocity component vector; also written with directional subscripts. $(\mathbf{u}_x, \mathbf{u}_y, \mathbf{u}_z)$
V	Volume (m^3)
W	Work (w)
x	Distance or length
x, y, z	Directions/axis in the Cartesian system
Y	Turbulence dissipation
y^+	Virtual distance

Greek symbols

α	Conversion fraction
α	Constant for different photochemical reactions to determine rate constant
β	Coefficient
β	Probability for multi-stepped nucleation to succeed
γ	Degree
Δ	Change in variable, final value minus initial value (for example, $\Delta\mathrm{p}, \Delta\mathrm{t}, \Delta\mathrm{T}$)
δ	Dirac delta function $\delta(x)$
ε	Dissipation rate
ξ	Size parameter for scattering
η	Ratio with specification

θ	Degree
Θ_s	Granular temperature
κ_i	Imaginary part of the complex index of refraction
κ	Von Kármán constant, 0.4187
λ	Wavelength
μ	Dynamic viscosity
ν	Kinematic viscosity
π	3.14
ρ	Density
$\hat{\rho}_q$	The effective density of phase q
σ	Stefan-Boltzmann constant ($5.669 \times 10^{-8}\, Wm^{-2}K^{-4}$)
σ	Prandtl number
σ	Shape factor
σ	Surface tension
σ_s	Scattering coefficient
Γ	Effective diffusivity
$\bar{\bar{\tau}}$	Stress tensor
τ	Shear stress
τ	Time scale
ϕ	Volume fraction
ϕ	Coefficient with description

ϕ_f	The angle of internal fraction
Φ	General scalar
$\mathit{\Phi}$	Phase function
Ω'	Solid angle
ω	Specific dissipation rate or turbulent frequency (s^{-1})

Subscript

w	wall
k	Kinetic energy
col	Collision
t	Transition pipe
t	Turbulent
fr	Frictional
pq,qp	Transfer from p^{th}(q^{th}) phase to q^{th} (q^{th})phase
q	Phase q
p	Phase p
f	Fluid
s	Solid
dr	drag
i,j,k	element indices, including species, orders,
ω	Specific dissipation rate

λ	At specific wavelength

Abbreviations

SCSC	Single-Crystal to Single-Crystal (reaction)
JMAK model	Johnson-Mehl-Avrami-Kolmogorov model
DO method	Discrete Ordinates Method
RTE	Radiative Transfer Equation
S2S	Surface to Surface
PD (ratio)	Pitch to diameter ratio
LVREA	Local Volumetric Rate of Energy Absorption
DTRM	Discrete Transfer Radiation Model
ee.	enantiomeric excess
ca.	circa
wt%	Weight fraction
dE	The delta-Eddington (dE) phase function
GQ	Galerkin quadrature

Bibliography

1896. Recent Work with Röntgen Rays. *Nature,* 53**,** 613-616.

ABDELMOTY, I., BUCHHOLZ, V., DI, L., GUO, C., KOWITZ, K., ENKELMANN, V., WEGNER, G. & FOXMAN, B. M. 2005. Polymorphism of Cinnamic and α-Truxillic Acids: New Additions to an Old Story. *Crystal Growth & Design,* 5**,** 2210-2217.

ABDIAJ, I., FONTANA, A., GOMEZ, M. V., DE LA HOZ, A. & ALCÁZAR, J. 2018. Visible-Light-Induced Nickel-Catalyzed Negishi Cross-Couplings by Exogenous-Photosensitizer-Free Photocatalysis. *Angewandte Chemie International Edition,* 57**,** 8473-8477.

ABDIAJ, I., HORN, C. R. & ALCAZAR, J. 2019. Scalability of Visible-Light-Induced Nickel Negishi Reactions: A Combination of Flow Photochemistry, Use of Solid Reagents, and In-Line NMR Monitoring. *The Journal of Organic Chemistry,* 84**,** 4748-4753.

AILLET, T., LOUBIERE, K., DECHY-CABARET, O. & PRAT, L. 2014. Accurate Measurement of the Photon Flux Received Inside Two Continuous Flow Microphotoreactors by Actinometry. *International Journal of Chemical Reactor Engineering,* 12**,** 257-269.

AKHLAGHI, M., MOHAMMADI, V., NOURI, N. M., TAHERKHANI, M. & KARIMI, M. 2019. Multi-Fluid VoF model assessment to simulate the horizontal air–water intermittent flow. *Chemical Engineering Research and Design,* 152**,** 48-59.

AKHTARUZZAMAN, KHAN, S., DUTTA, B., KANNAN, T. S., KUMAR KOLE, G. & HEDAYETULLAH MIR, M. 2023. Cocrystals for photochemical solid-state reactions: An account on crystal engineering perspective. *Coordination Chemistry Reviews,* 483**,** 215095.

ALBINI, A. 2016. Photochemistry and Green Synthesis. *Photochemistry: Past, Present and Future.* Berlin, Heidelberg: Springer Berlin Heidelberg.

ALGIFRI, A. H., BHARDWAJ, R. K. & RAO, Y. V. N. 1988. Heat transfer in turbulent decaying swirl flow in a circular pipe. *International Journal of Heat and Mass Transfer,* 31**,** 1563-1568.

ALLNATT, A. & JACOBS, P. 1968. Theory of nucleation in solid state reactions. *Canadian Journal of Chemistry,* 46**,** 111-116.

ALONSO, F., BELETSKAYA, I. P. & YUS, M. 2005. Non-conventional methodologies for transition-metal catalysed carbon–carbon coupling: A critical overview. Part 1: The Heck reaction. *Tetrahedron,* 61**,** 11771-11835.

AMINI, M. & MEMARI, A. M. 2021. CFD-Based Evaluation of Elevated Coastal Residential Buildings under Hurricane Wind Loads. *Journal of Architectural Engineering,* 27**,** 04021014.

ANASTAS, P. T. & KIRCHHOFF, M. M. 2002. Origins, Current Status, and Future Challenges of Green Chemistry. *Accounts of Chemical Research,* 35**,** 686-694.

ANASTAS, P. T. & WARNER, J. C. 1998. Principles of green chemistry. *Green chemistry: Theory and practice,* 29.

ARIYARATNE, C. 2005. *Design and optimisation of swirl pipes and transition geometries for slurry transport.* University of Nottingham.

ASADA, Y., TOKUMOTO, M., AIHARA, Y., OKU, M., ISHIMI, K., WAKAYAMA, T., MIYAKE, J., TOMIYAMA, M. & KOHNO, H. 2006. Hydrogen production by co-cultures of Lactobacillus and a photosynthetic bacterium, Rhodobacter sphaeroides RV. *International Journal of Hydrogen Energy,* 31**,** 1509-1513.

AVRAMI, M. 1939. Kinetics of phase change. I General theory. *The Journal of chemical physics,* 7**,** 1103-1112.

AVRAMI, M. 1940. Kinetics of phase change. II transformation‐time relations for random distribution of nuclei. *The Journal of chemical physics,* 8**,** 212-224.

AVRAMI, M. 1941. Granulation, phase change, and microstructure kinetics of phase change. III. *The Journal of chemical physics,* 9**,** 177-184.

BAGDASSARIAN, C. 1945. *Acta Physicochim,* 20**,** 441.

BAGHBANZADEH, M., GLASNOV, T. N. & KAPPE, C. O. 2013. Continuous-flow production of photocatalytically active titanium dioxide nanocrystals and its application to the photocatalytic addition of n, n-dimethylaniline to n-methylmaleimide. *Journal of Flow Chemistry,* 3**,** 109-113.

BAI, Y., HAO, M., DING, S., CHEN, P. & WANG, L. 2022. Surface Chemistry Engineering of Perovskite Quantum Dots: Strategies, Applications, and Perspectives. *Adv Mater,* 34**,** e2105958.

BAKER, D. W. & SAYRE, C. L. 1974. Decay of swirling turbulent flow of incompressible fluids in long pipes. *In:* AMERICA, I. S. O. (ed.) *Flow: Its Measurement and Control in Science and Industry. Flow measuring devices.* Instrument Society of America.

BALI, T. 1998. Modelling of heat transfer and fluid flow for decaying swirl flow in a circular pipe. *International communications in heat and mass transfer,* 25**,** 349-358.

BARNOON, P., TOGHRAIE, D., MEHMANDOUST, B., FAZILATI, M. A. & EFTEKHARI, S. A. 2022. Numerical modeling of species transport and functional characteristics of a proton exchange membrane fuel cell using an agglomerate model with a multi-phase model. *Energy Reports,* 8**,** 11343-11362.

BAUMANN, M., BAXENDALE, I. R. & LEY, S. V. 2011. The flow synthesis of heterocycles for natural product and medicinal chemistry applications. *Molecular diversity,* 15**,** 613-630.

BAUMANN, M., BAXENDALE, I. R., MARTIN, L. J. & LEY, S. V. 2009. Development of fluorination methods using continuous-flow microreactors. *Tetrahedron,* 65**,** 6611-6625.

BEAVER, M. G., ZHANG, E.-X., LIU, Z.-Q., ZHENG, S.-Y., WANG, B., LU, J.-P., TAO, J., GONZALEZ, M., JONES, S. & TEDROW, J. S. 2020. Development and Execution of a Production-Scale Continuous [2 + 2] Photocycloaddition. *Organic Process Research & Development,* 24**,** 2139-2146.

BENEDICT, J. B. & COPPENS, P. 2009. Kinetics of the Single-Crystal to Single-Crystal Two-Photon Photodimerization of α-trans-Cinnamic Acid to α-Truxillic Acid. *The Journal of Physical Chemistry A,* 113**,** 3116-3120.

BENGTSSON, M. & LAURELL, T. 2004. Ultrasonic agitation in microchannels. *Analytical and bioanalytical chemistry,* 378**,** 1716-1721.

BERRY, R., RICE, S. & ROSS, J. 1980. Chemical kinetics. *Physical Chemistry*.

BERTMER, M., NIEUWENDAAL, R. C., BARNES, A. B. & HAYES, S. E. 2006. Solid-State Photodimerization Kinetics of α-trans-Cinnamic Acid to α-Truxillic Acid Studied via Solid-State NMR. *The Journal of Physical Chemistry B,* 110**,** 6270-6273.

BERTONI, R., LORENC, M., GRABER, T., HENNING, R., MOFFAT, K., LÉTARD, J. F. & COLLET, E. 2016. Cooperative elastic switching vs. laser heating in [Fe(phen)2(NCS)2] spin-crossover crystals excited by a laser pulse. *CrystEngComm,* 18**,** 7269-7275.

BHASKARAN, R. & COLLINS, L. Integration of simulation into the undergraduate fluid mechanics curriculum using FLUENT. 2003 Annual Conference, 2003. 8.755. 1-8.755. 10.

BLANCO-ANIA, D., GAWADE, S. A., ZWINKELS, L. J. L., MAARTENSE, L., BOLSTER, M. G., BENNINGSHOF, J. C. J. & RUTJES, F. P. J. T. 2016. Rapid and Scalable Access into Strained Scaffolds through Continuous Flow Photochemistry. *Organic Process Research & Development,* 20**,** 409-413.

BLOH, J. Z. 2019. A Holistic Approach to Model the Kinetics of Photocatalytic Reactions. *Frontiers in Chemistry,* 7.

BOEK, E. S., LADVA, H. K., CRAWSHAW, J. P. & PADDING, J. T. 2008. Deposition of colloidal asphaltene in capillary flow: experiments and mesoscopic simulation. *Energy & fuels,* 22**,** 805-813.

BOGDAN, A. R., POE, S. L., KUBIS, D. C., BROADWATER, S. J. & MCQUADE, D. T. 2009. The Continuous-Flow Synthesis of

Ibuprofen. *Angewandte Chemie International Edition,* 48**,** 8547-8550.

BOLDYREV, V. V. 1986. Topochemistry of thermal decompositions of solids. *Thermochimica Acta,* 100**,** 315-338.

BOWEN, E. J. & LIND, S. 1946. Chemical Aspects of Light. *The Journal of Physical Chemistry,* 50**,** 490-490.

BOYJOO, Y., ANG, M. & PAREEK, V. 2014. CFD simulation of a pilot scale slurry photocatalytic reactor and design of multiple-lamp reactors. *Chemical Engineering Science,* 111**,** 266-277.

BRANDI, R., ALFANO, O. & CASSANO, A. 2000. Evaluation of radiation absorption in slurry photocatalytic reactors. 2. Experimental verification of the proposed method. *Environmental science & technology,* 34**,** 2631-2639.

BROWN, W. 1980. *Comprehensive chemical kinetics*, Elsevier.

BROWNE, D. L., DEADMAN, B. J., ASHE, R., BAXENDALE, I. R. & LEY, S. V. 2011. Continuous flow processing of slurries: evaluation of an agitated cell reactor. *Organic Process Research & Development,* 15**,** 693-697.

BUGLIONI, L., RAYMENANTS, F., SLATTERY, A., ZONDAG, S. D. A. & NOËL, T. 2022. Technological Innovations in Photochemistry for Organic Synthesis: Flow Chemistry, High-Throughput Experimentation, Scale-up, and Photoelectrochemistry. *Chemical Reviews,* 122**,** 2752-2906.

BURNHAM, A. K., WEESE, R. K. & WEEKS, B. L. 2004. A Distributed Activation Energy Model of Thermodynamically Inhibited Nucleation and Growth Reactions and Its Application to the β−δ Phase Transition of HMX. *The Journal of Physical Chemistry B,* 108**,** 19432-19441.

BUSHUYEV, O. S., FRIŠČIĆ, T. & BARRETT, C. J. 2016. Photo-induced motion of azo dyes in organized media: from single and liquid crystals, to MOFs and machines. *CrystEngComm,* 18**,** 7204-7211.

BYRNE, C., SUBRAMANIAN, G. & PILLAI, S. C. 2018. Recent advances in photocatalysis for environmental applications. *Journal of environmental chemical engineering,* 6**,** 3531-3555.

CALVERT, J. G. & PITTS, J. N. 1966. *Photochemistry*, Wiley New York.

CAMBIÉ, D., BOTTECCHIA, C., STRAATHOF, N. J. W., HESSEL, V. & NOËL, T. 2016. Applications of Continuous-Flow Photochemistry in Organic Synthesis, Material Science, and Water Treatment. *Chemical Reviews,* 116**,** 10276-10341.

CARLONI, A. C. N., CONDE, K. E. D., PANTALEÃO, A. V., AZEVEDO, J. L. F. D. & RADE, D. A. 2022. Validation and analysis of turbulence modeling in pipe elbow under secondary flow conditions. *Journal of the Brazilian Society of Mechanical Sciences and Engineering,* 44**,** 595.

CARNITI, P., GERVASINI, A., BIELLA, S. & AUROUX, A. 2005. Intrinsic and effective acidity study of niobic acid and niobium phosphate by a multitechnique approach. *Chemistry of Materials,* 17**,** 6128-6136.

CARSTENSEN, J. 1974a. Stability of solids and solid dosage forms. *Journal of Pharmaceutical Sciences,* 63**,** 1-14.

CARSTENSEN, J. T. 1974b. Stability of Solids and Solid Dosage Forms. *Journal of Pharmaceutical Sciences,* 63**,** 1-14.

CERONI, P., CREDI, A., VENTURI, M. & BALZANI, V. 2010. Light-powered molecular devices and machines. *Photochemical & Photobiological Sciences,* 9**,** 1561-1573.

CHANDRASEKHAR, S. 1960. Radiative Transfer Dover Publications Inc. *New York*.

CHANDRASEKHAR, S. 2013. *Radiative transfer*, Courier Corporation.

CHAPMAN, S. & COWLING, T. G. 1990. *The mathematical theory of non-uniform gases: an account of the kinetic theory of viscosity, thermal conduction and diffusion in gases*, Cambridge university press.

CHARLES, M., H-S CHEH, C. & H-L. CHU, L. 1971. The flow of "settling" slurries in tubes with internal spiral ribs. *The Canadian Journal of Chemical Engineering,* 49**,** 737-741.

CHATANI, S., KLOXIN, C. J. & BOWMAN, C. N. 2014. The power of light in polymer science: photochemical processes to manipulate polymer formation, structure, and properties. *Polymer chemistry,* 5**,** 2187-2201.

CHEN, C.-Y., YANG, M.-H., YEH, K.-L., LIU, C.-H. & CHANG, J.-S. 2008. Biohydrogen production using sequential two-stage dark and photo fermentation processes. *International Journal of Hydrogen Energy,* 33**,** 4755-4762.

CHEN, D. L., GERDTS, C. J. & ISMAGILOV, R. F. 2005. Using microfluidics to observe the effect of mixing on nucleation of protein crystals. *Journal of the American Chemical Society,* 127**,** 9672-9673.

CHEN, M., LIU, M. & TANG, Y. 2019. Comparison of Euler-Euler and Euler-Lagrange approaches for simulating gas-solid flows in a multiple-spouted bed. *International Journal of Chemical Reactor Engineering,* 17.

CHIZHIK, S., SIDELNIKOV, A., ZAKHAROV, B., NAUMOV, P. & BOLDYREVA, E. 2018. Quantification of photoinduced bending of dynamic molecular crystals: from macroscopic strain to kinetic constants and activation energies. *Chem Sci,* 9**,** 2319-2335.

CHOI, S. M., LEE, G. R., PARK, C. D., CHO, S. H. & LIM, B. J. 2021. Wind load on the solar panel array of a floating photovoltaic system under extreme hurricane conditions. *Sustainable Energy Technologies and Assessments,* 48**,** 101616.

CHOU, Y.-W. & LIAO, C.-C. 2023. Numerical simulation of the pneumatic conveying of dilute particulate flows in a diffuser using Euler-Euler approach. *AIP Conference Proceedings,* 2685.

CHU, K., CHEN, Y., JI, L., ZHOU, Z., YU, A. & CHEN, J. 2022. Coarse-grained CFD-DEM study of Gas-solid flow in gas cyclone. *Chemical Engineering Science,* 260**,** 117906.

CHU, K., WANG, B., XU, D., CHEN, Y. & YU, A. 2011. CFD–DEM simulation of the gas–solid flow in a cyclone separator. *Chemical Engineering Science,* 66**,** 834-847.

CIAMICIAN, G. & SILBER, P. 1901. Chemische Lichtwirkungen. *Berichte der deutschen chemischen Gesellschaft,* 34**,** 2040-2046.

CLARK, C. A., LEE, D. S., PICKERING, S. J., POLIAKOFF, M. & GEORGE, M. W. 2018. UV PhotoVap: demonstrating how a simple and versatile reactor based on a conventional rotary evaporator can be used for UV photochemistry. *Organic Process Research & Development,* 22**,** 595-599.

CLOETE, S., JOHANSEN, S. T. & AMINI, S. 2012. Performance evaluation of a complete Lagrangian KTGF approach for dilute granular flow modelling. *Powder Technology,* 226**,** 43-52.

COLE, J. M. & IRIE, M. 2016. Solid-state photochemistry. *CrystEngComm,* 18**,** 7175-7179.

CONG, W., SHEN, H., CONG, A., WANG, Y. & WANG, G. 2007. Modeling photon propagation in biological tissues using a generalized Delta-Eddington phase function. *Physical Review E,* 76**,** 051913.

CRISENZA, G. E. M. & MELCHIORRE, P. 2020. Chemistry glows green with photoredox catalysis. *Nature Communications,* 11**,** 803.

CUNDALL, P. & STRACK, O. 1979. A discrete numerical model for granular assemblies. Ge´ otechnique 29: 47–65.

D'AGOSTINO, S., SPINELLI, F., BOANINI, E., BRAGA, D. & GREPIONI, F. 2016. Single crystal to single crystal [2+ 2] photoreactions in chloride and sulphate salts of 4-amino-cinnamic acid via solid-solution formation: a structural and kinetic study. *Chemical Communications,* 52**,** 1899-1902.

DE JONG, A. 1923. Constitution of the truxillic and truxinic acids and the action of sunlight on the cinnamic acids and the cinnamic acid salts. *Ber. Dtsch. Chem. Ges. B,* 56**,** 818-8332.

DE LASA, H. I., SERRANO, B. & SALAICES, M. 2005. *Photocatalytic reaction engineering*, Springer.

DEBROUWER, W., KIMPE, W., DANGREAU, R., HUVAERE, K., GEMOETS, H. P. L., MOTTAGHI, M., KUHN, S. & VAN AKEN, K. 2020. Ir/Ni Photoredox Dual Catalysis with Heterogeneous Base Enabled by an Oscillatory Plug Flow Photoreactor. *Organic Process Research & Development,* 24**,** 2319-2325.

DELANEY, E. N., LEE, D. S., ELLIOTT, L. D., JIN, J., BOOKER-MILBURN, K. I., POLIAKOFF, M. & GEORGE, M. W. 2017. A laboratory-scale annular continuous flow reactor for UV photochemistry using excimer lamps for discrete wavelength excitation and its use in a wavelength study of a photodecarboxlyative cyclisation. *Green Chemistry,* 19**,** 1431-1438.

DESIRAJU, G. R. & PARSHALL, G. W. 1989. Crystal engineering: the design of organic solids. *Materials science monographs,* 54.

DING, J. & GIDASPOW, D. 1990. A bubbling fluidization model using kinetic theory of granular flow. *AIChE journal,* 36**,** 523-538.

DONG, Z., WEN, Z., ZHAO, F., KUHN, S. & NOËL, T. 2021. Scale-up of micro- and milli-reactors: An overview of strategies, design principles and applications. *Chemical Engineering Science: X,* 10**,** 100097.

DONNELLY, K. & BAUMANN, M. 2021. Scalability of photochemical reactions in continuous flow mode. *Journal of Flow Chemistry,* 11**,** 223-241.

DOYLE, B. J., GUTMANN, B., BITTEL, M., HUBLER, T., MACCHI, A. & ROBERGE, D. M. 2020. Handling of Solids and Flow Characterization in a Baffleless Oscillatory Flow Coil Reactor. *Industrial & Engineering Chemistry Research,* 59**,** 4007-4019.

DUKE, D. W. & OWENS, J. F. 1982. Quantum-chromodynamic corrections to deep-inelastic Compton scattering. *Physical Review D,* 26**,** 1600-1609.

DÜRR, M., KENTSCH, J., MÜLLER, T., SCHNELLE, T. & STELZLE, M. 2003. Microdevices for manipulation and accumulation of micro- and nanoparticles by dielectrophoresis. *Electrophoresis,* 24**,** 722-31.

EASLEY, C. J., TONG, F., DONG, X., AL-KAYSI, R. O. & BARDEEN, C. J. 2020. Using light intensity to control reaction kinetics and reversibility in photomechanical crystals. *Chemical Science,* 11**,** 9852-9862.

EDMUND, W. S. 1967. Method and apparatus for transporting slurries. Google Patents.

ELIM, H. I., CAI, B., KURATA, Y., SUGIHARA, O., KAINO, T., ADSCHIRI, T., CHU, A.-L. & KAMBE, N. 2009. Refractive Index Control and Rayleigh Scattering Properties of Transparent TiO2 Nanohybrid Polymer. *The Journal of Physical Chemistry B,* 113**,** 10143-10148.

ELIMELECH, M. 1998. *Particle Deposition & Aggregation [electronic resource] : Measurement, Modelling and Simulation,* Burlington, Burlington : Elsevier Science.

ENKELMANN, V., WEGNER, G., NOVAK, K. & WAGENER, K. B. 1993. Single-crystal-to-single-crystal photodimerization of cinnamic acid. *Journal of the American Chemical Society,* 115**,** 10390-10391.

EREMIN, Y. A. 2005. SCATTERING | Scattering Theory. *In:* GUENTHER, R. D. (ed.) *Encyclopedia of Modern Optics.* Oxford: Elsevier.

EVANS, D. A., BRITTON, T. C., DOROW, R. L. & DELLARIA, J. F. 1986. Stereoselective amination of chiral enolates. A new approach to the asymmetric synthesis of .alpha.-hydrazino and .alpha.-amino acid derivatives. *Journal of the American Chemical Society,* 108**,** 6395-6397.

F.WHITE & CHRISTOPH, G. 1971. A Simple New Analysis of Compressible Turbulent Skin Friction Under Arbitrary Conditions. *Technical Report AFFDL-TR-70-133.*

FABRY, D., SUGIONO, E. & RUEPING, M. 2016. Online monitoring and analysis for autonomous continuous flow self-optimizing reactor systems. *Reaction Chemistry & Engineering,* 1**,** 129-133.

FABRY, D. C., SUGIONO, E. & RUEPING, M. 2014. Self-optimizing reactor systems: algorithms, on-line analytics, setups, and strategies for accelerating continuous flow process optimization. *Israel Journal of Chemistry,* 54**,** 341-350.

FERNANDES, M. A. & LEVENDIS, D. C. 2004. Photodimerization of the alpha'-polymorph of ortho-ethoxy-trans-cinnamic acid in the solid state. I. Monitoring the reaction at 293 K. *Acta Crystallogr B,* 60**,** 315-24.

FERNANDES, M. A. & LEVENDIS, D. C. 2016. Photodimerisation of the α′ -polymorph of ortho-ethoxy-trans-cinnamic acid occurs via a two-stage mechanism at 343 K yielding 100% α-truxillic acid. *CrystEngComm,* 18**,** 7363-7376.

FLUENT, A. 2018. User's Guide and Theory Guide, Version 19.0.

FOKEER, S. 2006. An investigation of geometrically induced swirl applied to lean phase pneumatic flows.

FONSECA, I., BAIAS, M., HAYES, S. E., PICKARD, C. J. & BERTMER, M. 2012. Effects of Aromatic Substitution on the Photodimerization Kinetics of β-trans Cinnamic Acid Derivatives Studied with 13C Solid-State NMR. *The Journal of Physical Chemistry C,* 116**,** 12212-12218.

FONSECA, I., HAYES, S. E. & BERTMER, M. 2009. Size effects of aromatic substitution in the ortho position on the photodimerization kinetics of α-transcinnamic acid derivatives. A solid-state NMR study. *Physical Chemistry Chemical Physics,* 11**,** 10211-10218.

FONSECA, I., HAYES, S. E., BLÜMICH, B. & BERTMER, M. 2008. Temperature stability and photodimerization kinetics of β-cinnamic acid and comparison to its α-polymorph as studied by solid-state NMR spectroscopy techniques and DFT calculations. *Physical Chemistry Chemical Physics,* 10**,** 5898-5907.

FRANK, S. E. 1941. Tubular heat exchange apparatus. Google Patents.

FRANK, T. 2008. Fabrication and Assembling of Microreactors Made from Glass and Silicon. *Microreactors in Organic Synthesis and Catalysis.*

FREITAS DE FREITAS, L., VARCA, G. H. C., DOS SANTOS BATISTA, J. G. & BENÉVOLO LUGÃO, A. 2018. An overview of the synthesis of gold nanoparticles using radiation technologies. *Nanomaterials,* 8**,** 939.

FUJII, H., CHIBA, G., YAMADA, Y., HOSHI, Y., KOBAYASHI, K. & WATANABE, M. 2020. A comparative study of the delta-Eddington and Galerkin quadrature methods for highly forward scattering of photons in random media. *Journal of Computational Physics,* 423**,** 109825.

GALWEY, A. K. & BROWN, M. E. 1999. *Thermal decomposition of ionic solids: chemical properties and reactivities of ionic crystalline phases*, Elsevier.

GANESHALINGAM, J. 2002. *Swirl-Induction for Improved Solid-Liquid Flow in Pipes.* PhD, University of Nottingham.

GAROOSI, F., MERABTENE, T. & MAHDI, T.-F. 2022. Numerical simulation of merging of two rising bubbles with different densities and diameters using an enhanced Volume-Of-Fluid (VOF) model. *Ocean Engineering,* 247**,** 110711.

GEMOETS, H. P., SU, Y., SHANG, M., HESSEL, V., LUQUE, R. & NOEL, T. 2016. Liquid phase oxidation chemistry in continuous-flow microreactors. *Chemical Society Reviews,* 45**,** 83-117.

GENZINK, M. J., KIDD, J. B., SWORDS, W. B. & YOON, T. P. 2022. Chiral Photocatalyst Structures in Asymmetric Photochemical Synthesis. *Chemical Reviews,* 122**,** 1654-1716.

GHOBADIAN, A. & VASQUEZ, S. A general purpose implicit coupled algorithm for the solution of eulerian multiphase transport equation. International Conference on Multiphase Flow, Leipzig, Germany, 2007.

GIDASPOW, D., BEZBURUAH, R. & DING, J. 1991. Hydrodynamics of circulating fluidized beds: kinetic theory approach. Illinois Inst. of Tech., Chicago, IL (United States). Dept. of Chemical ….

GIJS, M. A. 2004. Magnetic bead handling on-chip: new opportunities for analytical applications. *Microfluidics and nanofluidics,* 1**,** 22-40.

GINSTLING, A. M. & BROUNSHTEIN, B. I. 1950. The diffusion kinetics of reactions in spherical particles. *The Russian Journal of Applied Chemistry,* 23**,** 1327-1338.

GONZÁLEZ, M., VELARDE, P. & GARCÍA-FERNÁNDEZ, C. First Comparison of Two Radiative Transfer Methods: M_1 and S_n Techniques. Numerical Modeling of Space Plasma Flows, 2008. 91.

GUI, Q.-W., HE, X., WANG, W., ZHOU, H., DONG, Y., WANG, N., TANG, J.-X., CAO, Z. & HE, W.-M. 2020. The clean preparation of multisubstituted pyrroles under metal-and solvent-free conditions. *Green Chemistry,* 22**,** 118-122.

GUO, Y., YANG, X., LI, G., YANG, J., LIU, L., CHEN, L. & LI, B. 2021. Shear turbulence controllable synthesis of aggregated nano-particles using a swirling vortex flow reactor assisted by ultrasound irradiation. *Chemical Engineering Journal,* 405**,** 126914.

GUPTA, A. K., LILLEY, D. G. & SYRED, N. 1984. Swirl flows. *Tunbridge Wells*.

GUTMANN, B., CANTILLO, D. & KAPPE, C. O. 2015. Continuous‐flow technology — a tool for the safe manufacturing of active pharmaceutical ingredients. *Angewandte Chemie International Edition,* 54**,** 6688-6728.

HALL, S. 2012. 15 - Pneumatic Conveying. *In:* HALL, S. (ed.) *Branan's Rules of Thumb for Chemical Engineers (Fifth Edition).* Oxford: Butterworth-Heinemann.

HALSEY, D. 1987. Flowmeters in swirling flows. *Journal of Physics E: Scientific Instruments,* 20**,** 1036.

HAN, W., LONG, F., CONG, W., INTES, X. & WANG, G. 2017. Radiative transfer with delta-Eddington-type phase functions. *Applied Mathematics and Computation,* 300**,** 70-78.

HARTMAN, R. L., NABER, J. R., ZABORENKO, N., BUCHWALD, S. L. & JENSEN, K. F. 2010. Overcoming the challenges of solid bridging and constriction during Pd-Catalyzed C− N bond formation in microreactors. *Organic Process Research & Development,* 14**,** 1347-1357.

HASSAN, I. U., NAIKOO, G. A., SALIM, H., AWAN, T., TABOOK, M. A., PEDRAM, M. Z., MUSTAQEEM, M., SOHANI, A., HOSEINZADEH, S. & SALEH, T. A. 2023. Advances in Photochemical Splitting of Seawater over Semiconductor Nano-Catalysts for Hydrogen Production: A Critical Review. *Journal of Industrial and Engineering Chemistry*.

HENYEY, L. G. & GREENSTEIN, J. L. 1941. Diffuse radiation in the galaxy. *The Astrophysical Journal,* 93**,** 70-83.

HERATH, A., DAHL, R. & COSFORD, N. D. P. 2010. Fully Automated Continuous Flow Synthesis of Highly Functionalized Imidazo[1,2-a] Heterocycles. *Organic Letters,* 12**,** 412-415.

HERNÁNDEZ-LINARES, M. G., GUERRERO-LUNA, G., PÉREZ-ESTRADA, S., ELLISON, M., ORTIN, M.-M. & GARCIA-GARIBAY, M. A. 2015. Large-Scale Green Chemical Synthesis of Adjacent Quaternary Chiral Centers by Continuous Flow Photodecarbonylation of Aqueous Suspensions of Nanocrystalline Ketones. *Journal of the American Chemical Society,* 137**,** 1679-1684.

HERNANDEZ-LINARES, M. G., GUERRERO-LUNA, G., PEREZ-ESTRADA, S., ELLISON, M., ORTIN, M. M. & GARCIA-GARIBAY, M. A. 2015. Large-scale green chemical synthesis of adjacent quaternary chiral centers by continuous flow photodecarbonylation of aqueous suspensions of nanocrystalline ketones. *J Am Chem Soc,* 137**,** 1679-84.

HICKMAN, D. A., WEIDENBACH, M. & FRIEDHOFF, D. P. 2004. A comparison of a batch recycle reactor and an integral reactor with fines for scale-up of an industrial trickle bed reactor from laboratory data. *Chemical engineering science,* 59**,** 5425-5430.

HIPPLER, M. 2003. Photochemical Kinetics: Reaction Orders and Analogies with Molecular Beam Scattering and Cavity Ring-Down Experiments. *Journal of Chemical Education,* 80**,** 1074.

HOFFMANN, N. 2008. Photochemical reactions as key steps in organic synthesis. *Chemical reviews,* 108**,** 1052-1103.

HORIE, T., SUMINO, M., TANAKA, T., MATSUSHITA, Y., ICHIMURA, T. & YOSHIDA, J.-I. 2010. Photodimerization of Maleic Anhydride in a Microreactor Without Clogging. *Organic Process Research & Development,* 14**,** 405-410.

HOWARD, G. 1941. Effects of Rifling on Four-Inch Pipe Transporting Solids. *Transactions of the American Society of Civil Engineers,* 106**,** 135-147.

HSIEH, H.-W., COLEY, C. W., BAUMGARTNER, L. M., JENSEN, K. F. & ROBINSON, R. I. 2018. Photoredox Iridium–Nickel Dual-Catalyzed Decarboxylative Arylation Cross-Coupling: From Batch to Continuous Flow via Self-Optimizing Segmented Flow Reactor. *Organic Process Research & Development,* 22**,** 542-550.

HU, F.-L., WANG, S.-L., LANG, J.-P. & ABRAHAMS, B. F. 2014. In-situ X-ray diffraction snapshotting: Determination of the kinetics of a photodimerization within a single crystal. *Scientific Reports,* 4**,** 6815.

HU, S., WANG, A., LÖWE, H., LI, X., WANG, Y., LI, C. & YANG, D. 2010. Kinetic study of ionic liquid synthesis in a microchannel reactor. *Chemical Engineering Journal,* 162**,** 350-354.

HUANG, P., BRADSHAW, P. & COAKLEY, T. 1993. Skin friction and velocity profile family for compressible turbulentboundary layers. *AIAA journal,* 31**,** 1600-1604.

HUBENY, I. & MIHALAS, D. 2014. *Theory of stellar atmospheres: An introduction to astrophysical non-equilibrium quantitative spectroscopic analysis*, Princeton University Press.

HURTADO, L., SOLÍS-CASADOS, D., ESCOBAR-ALARCÓN, L., ROMERO, R. & NATIVIDAD, R. 2016. Multiphase photo-capillary reactors coated with TiO2 films: Preparation, characterization and photocatalytic performance. *Chemical Engineering Journal,* 304**,** 39-47.

INKINEN, J., NISKANEN, J., TALKA, T., SAHLE, C. J., MÜLLER, H., KHRIACHTCHEV, L., HASHEMI, J., AKBARI, A., HAKALA, M. & HUOTARI, S. 2015. X-ray induced dimerization of cinnamic acid: Time-resolved inelastic X-ray scattering study. *Scientific Reports,* 5**,** 15851.

IRIE, M., FUKAMINATO, T., MATSUDA, K. & KOBATAKE, S. 2014. Photochromism of diarylethene molecules and crystals: memories, switches, and actuators. *Chemical Reviews,* 114**,** 12174-12277.

IRIE, M., FUKAMINATO, T., SASAKI, T., TAMAI, N. & KAWAI, T. 2002. A digital fluorescent molecular photoswitch. *Nature,* 420**,** 759-760.

ISHIMARU, A. 1999. *Wave Propagation and Scattering in Random Media*, John Wiley & Sons.

ISMAIL, N. I., KUANG, S., TANG, Y. & YU, A. 2022. CFD-DEM evaluation of screen types for sand control applications. *Powder Technology,* 404**,** 117496.

JACOBS, P. & TOMPKINS, F. 1955. Chemistry of the solid state. *Surfaces of Solids***,** 91-122.

JACOBS, P. W. M. 1997. Formation and Growth of Nuclei and the Growth of Interfaces in the Chemical Decomposition of Solids: New Insights. *The Journal of Physical Chemistry B,* 101**,** 10086-10093.

JAMALI, A., VANRAES, R., HANSELAER, P. & VAN GERVEN, T. 2013. A batch LED reactor for the photocatalytic degradation of phenol. *Chemical Engineering and Processing: Process Intensification,* 71**,** 43-50.

JANDER, W. 1927. Reaktionen im festen Zustande bei höheren Temperaturen. Reaktionsgeschwindigkeiten endotherm verlaufender Umsetzungen. *Zeitschrift für anorganische und allgemeine Chemie,* 163**,** 1-30.

JIAO, Y., YANG, R., LUO, Y., LIU, L., XU, B. & TIAN, W. 2022. Fulgide Derivative-Based Solid-State Reversible Fluorescent Switches for Advanced Optical Memory. *CCS Chemistry,* 4**,** 132-140.

JOHNSON, P. C. & JACKSON, R. 1986. Frictional–collisional constitutive relations for granular materials, with application to plane shearing. *Journal of Fluid Mechanics,* 176.

JOSEPH, J. H., WISCOMBE, W. J. & WEINMAN, J. A. 1976. The Delta-Eddington Approximation for Radiative Flux Transfer. *Journal of Atmospheric Sciences,* 33**,** 2452-2459.

JUNKERS, T. & WENN, B. 2016. Continuous photoflow synthesis of precision polymers. *Reaction Chemistry & Engineering,* 1**,** 60-64.

KADER, B. A. 1981. Temperature and concentration profiles in fully turbulent boundary layers. *International Journal of Heat and Mass Transfer,* 24**,** 1541-1544.

KALT, P. A., AL-ABDELL, Y. M., MASRI, A. R. & BARLOW, R. S. 2002. Swirling turbulent non-premixed flames of methane: flow field and compositional structure. *Proceedings of the Combustion Institute,* 29**,** 1913-1919.

KARGAR, F. & BALANDIN, A. A. 2021. Advances in Brillouin–Mandelstam light-scattering spectroscopy. *Nature Photonics,* 15**,** 720-731.

KARIMI, A., AL-RASHED, A. A. A. A., AFRAND, M., MAHIAN, O., WONGWISES, S. & SHAHSAVAR, A. 2019. The effects of tape insert material on the flow and heat transfer in a nanofluid-based double tube heat exchanger: Two-phase mixture model. *International Journal of Mechanical Sciences,* 156**,** 397-409.

KARKAS, M. D., PORCO JR, J. A. & STEPHENSON, C. R. 2016. Photochemical approaches to complex chemotypes: applications in natural product synthesis. *Chemical Reviews,* 116**,** 9683-9747.

KAUSHAL, D. R., THINGLAS, T., TOMITA, Y., KUCHII, S. & TSUKAMOTO, H. 2012. CFD modeling for pipeline flow of fine particles at high concentration. *International Journal of Multiphase Flow,* 43**,** 85-100.

KHAN, M., BRUNKLAUS, G., ENKELMANN, V. & SPIESS, H.-W. 2008. Transient States in [2 + 2] Photodimerization of Cinnamic Acid:

Correlation of Solid-State NMR and X-ray Analysis. *Journal of the American Chemical Society,* 130**,** 1741-1748.

KHAWAM, A. & FLANAGAN, D. R. 2006. Solid-State Kinetic Models: Basics and Mathematical Fundamentals. *The Journal of Physical Chemistry B,* 110**,** 17315-17328.

KHOJ, M. A., HUGHES, C. E., HARRIS, K. D. M. & KARIUKI, B. M. 2013. Polymorphism in a trans-Cinnamic Acid Derivative Exhibiting Two Distinct β-type Phases: Structural Properties, [2 + 2] Photodimerization Reactions, and Polymorphic Phase Transition Behavior. *Crystal Growth & Design,* 13**,** 4110-4117.

KIM, D., KWON, Y., CHO, Y., LI, C., CHEONG, S., HWANG, Y., LEE, J., HONG, D. & MOON, S. 2009. Convective heat transfer characteristics of nanofluids under laminar and turbulent flow conditions. *Current Applied Physics,* 9**,** e119-e123.

KIM, T., ZHU, L., MUELLER, L. J. & BARDEEN, C. J. 2012. Dependence of the solid-state photomechanical response of 4-chlorocinnamic acid on crystal shape and size. *CrystEngComm,* 14**,** 7792-7799.

KITAGAWA, D., TANAKA, R. & KOBATAKE, S. 2016. Photoinduced stepwise bending behavior of photochromic diarylethene crystals. *CrystEngComm,* 18**,** 7236-7240.

KITOH, O. 1991. Experimental study of turbulent swirling flow in a straight pipe. *Journal of fluid mechanics,* 225**,** 445-479.

KOBAYASHI, T. & YODA, M. 1987. Modified k-ε Model for Turbulent Swirling Flow in a Straight Pipe : Fluids Engineering. *JSME international journal : bulletin of the JSME,* 30**,** 66-71.

KOCKMANN, N., GOTTSPONER, M. & ROBERGE, D. M. 2011. Scale-up concept of single-channel microreactors from process development to industrial production. *Chemical Engineering Journal,* 167**,** 718-726.

KOCKMANN, N., KASTNER, J. & WOIAS, P. 2008. Reactive particle precipitation in liquid microchannel flow. *Chemical Engineering Journal,* 135**,** S110-S116.

KOLE, G. K. & MIR, M. H. 2022. Isolation of elusive cyclobutane ligands via a template-assisted photochemical [2+ 2] cycloaddition reaction and their utility in engineering crystalline solids. *CrystEngComm,* 24**,** 3993-4007.

KOLE, G. K. & VITTAL, J. J. 2022. Isomerization of cyclobutane ligands in the solid state and solution. *Journal of the Indian Chemical Society,* 99.

KOLMOGOROV, A. N. Dissipation of energy in the locally isotropic turbulence. Dokl. Akad. Nauk. SSSR, 1941a. 19-21.

KOLMOGOROV, A. N. The local structure of turbulence in incompressible viscous fluid for very large Reynolds number. Dokl. Akad. Nauk. SSSR, 1941b. 301-303.

KRALJ, J. G., LIS, M. T., SCHMIDT, M. A. & JENSEN, K. F. 2006. Continuous dielectrophoretic size-based particle sorting. *Analytical chemistry,* 78**,** 5019-5025.

KRYSANOV, S. & ALFIMOV, M. 1982. Ultrafast formation of transients in spiropyran photochromism. *Chemical Physics Letters,* 91**,** 77-80.

KUDO, A. & MISEKI, Y. 2009. Heterogeneous photocatalyst materials for water splitting. *Chemical Society Reviews,* 38**,** 253-278.

KUHN, S., NOËL, T., GU, L., HEIDER, P. L. & JENSEN, K. F. 2011. A Teflon microreactor with integrated piezoelectric actuator to handle solid forming reactions. *Lab on a Chip,* 11**,** 2488-2492.

KUMAR, P. 2016. *Fundamentals and Techniques of Biophysics and Molecular biology*, Pathfinder Publication unit of PAPL.

KUMAR, V., FUSARO, L., APRILE, C., ROBEYNS, K. & GARCIA, Y. 2020. [2 + 2] Photodimerization of Sulfonate Derivative of trans-Cinnamic Acid: Kinetics Study Using Solid State 13C NMR and Hybrid Material Inclusion. *Crystal Growth & Design,* 20**,** 7850-7861.

KUME, A. 2017. Importance of the green color, absorption gradient, and spectral absorption of chloroplasts for the radiative energy balance of leaves. *Journal of Plant Research,* 130**,** 501-514.

LATHROP, K. 1966. Use of discrete-ordinates methods for solution of photon transport problems. *Nuclear Science and Engineering,* 24**,** 381-388.

LAUNDER, B. E. & SPALDING, D. B. 1974. The numerical computation of turbulent flows. *Computer Methods in Applied Mechanics and Engineering,* 3**,** 269-289.

LEE, D. S., AMARA, Z., CLARK, C. A., XU, Z., KAKIMPA, B., MORVAN, H. P., PICKERING, S. J., POLIAKOFF, M. & GEORGE, M. W. 2017. Continuous Photo-Oxidation in a Vortex Reactor: Efficient Operations Using Air Drawn from the Laboratory. *Organic Process Research & Development,* 21**,** 1042-1050.

LEE, D. S., SHARABI, M., JEFFERSON-LOVEDAY, R., PICKERING, S. J., POLIAKOFF, M. & GEORGE, M. W. 2020. Scalable Continuous Vortex Reactor for Gram to Kilo Scale for UV and Visible Photochemistry. *Organic Process Research & Development,* 24**,** 201-206.

LEE, H. S., SINGH, P., THOMASON, W. H. & FOGLER, H. S. 2008. Waxy oil gel breaking mechanisms: adhesive versus cohesive failure. *Energy & Fuels,* 22**,** 480-487.

LEIGHTON, H. 1980. Application of the delta‐Eddington method to the absorption of solar radiation in the atmosphere. *Atmosphere-Ocean,* 18**,** 43-52.

LEY, S. V., FITZPATRICK, D. E., INGHAM, R. J. & MYERS, R. M. 2015. Organic synthesis: march of the machines. *Angewandte Chemie International Edition,* 54**,** 3449-3464.

LI, G. 2016. *Investigation of swirl pipe for improving cleaning efficiency in closed processing system.* University of Nottingham.

LI, G., HALL, P., MILES, N. & WU, T. 2015. Improving the efficiency of 'Clean-In-Place' procedures using a four-lobed swirl pipe: A numerical investigation. *Computers & Fluids,* 108**,** 116-128.

LI, H. & TOMITA, Y. 1994. Characteristics of swirling flow in a circular pipe.

LI, H. & TOMITA, Y. 2000. Particle velocity and concentration characteristics in a horizontal dilute swirling flow pneumatic conveying. *Powder Technology,* 107**,** 144-152.

LI, L., GU, Z., XU, W., TAN, Y., FAN, X. & TAN, D. 2023. Mixing mass transfer mechanism and dynamic control of gas-liquid-solid multiphase flow based on VOF-DEM coupling. *Energy,* 272**,** 127015.

LIANG, Y., ZHANG, X. & MACMILLAN, D. W. 2018. Decarboxylative sp 3 C–N coupling via dual copper and photoredox catalysis. *Nature,* 559**,** 83-88.

LIEBNER, C., FISCHER, J., HEINRICH, S., LANGE, T., HIERONYMUS, H. & KLEMM, E. 2012. Are micro reactors inherently safe? An investigation of gas phase explosion propagation limits on ethene mixtures. *Process Safety and Environmental Protection,* 90**,** 77-82.

LILLIEHORN, T., SIMU, U., NILSSON, M., ALMQVIST, M., STEPINSKI, T., LAURELL, T., NILSSON, J. & JOHANSSON, S. 2005. Trapping of microparticles in the near field of an ultrasonic transducer. *Ultrasonics,* 43**,** 293-303.

LIQING, L. & DONGHUA, C. 2004. Application of iso-temperature method of multiple rate to kinetic analysis. *Journal of thermal analysis and calorimetry,* 78**,** 283-293.

LIU, L., RUAN, L. & TAN, H. 2002. On the discrete ordinates method for radiative heat transfer in anisotropically scattering media. *International Journal of Heat and Mass Transfer,* 45**,** 3259-3262.

LIU, X., LIU, P., LI, H., XU, Z., JIA, L., XIA, Y., YU, M., TANG, W., ZHU, X., CHEN, C., ZHANG, Y., NANGO, E., TANAKA, R., LUO, F., KATO, K., NAKAJIMA, Y., KISHI, S., YU, H., MATSUBARA, N., OWADA, S., TONO, K., IWATA, S., YU, L.-J., SHEN, J.-R. & WANG, J. 2022. Excited-state intermediates in a designer protein encoding a phototrigger caught by an X-ray free-electron laser. *Nature Chemistry,* 14**,** 1054-1060.

LIU, Y., CHEN, Z., ZHANG, Y. & ZHOU, L. 2020. Hydrodynamic Modeling of Swirling Binary Mixture Gas–Particle Flows Using a Second-Order-Moment Turbulence Model. *ACS Omega,* 5**,** 31490-31501.

LOPES, W. S., DA S. MORAIS, C. R., DE SOUZA, A. G. & LEITE, V. D. 2005. Synthesis and non-isothermal kinetic study of the thermal decomposition of gadolinium(III) complexes. *Journal of Thermal Analysis and Calorimetry,* 79**,** 343-347.

LUIGGI AGREDA, N. J. 2015. Kinetic Analysis of Recovery, Recrystallization, and Phase Precipitation in an Al-Fe-Si Alloy Using JMAEK and Sesták–Berggren Models. *Metallurgical and Materials Transactions B,* 46**,** 1376-1399.

LUN, C., SAVAGE, S. B., JEFFREY, D. & CHEPURNIY, N. 1984. Kinetic theories for granular flow: inelastic particles in Couette flow and slightly inelastic particles in a general flowfield. *Journal of fluid mechanics,* 140**,** 223-256.

MAEDA, Y., MINAMI, S., TAKEHANA, Y., DANG, J.-S., AOTA, S., MATSUDA, K., MIYAUCHI, Y., YAMADA, M., SUZUKI, M., ZHAO, R.-S., ZHAO, X. & NAGASE, S. 2016. Tuning of the photoluminescence and up-conversion photoluminescence properties of single-walled carbon nanotubes by chemical functionalization. *Nanoscale,* 8**,** 16916-16921.

MANJAVACAS, A., FENOLLOSA, R., RODRIGUEZ, I., JIMÉNEZ, M. C., MIRANDA, M. A. & MESEGUER, F. 2017. Magnetic light and forbidden photochemistry: the case of singlet oxygen. *Journal of Materials Chemistry C,* 5**,** 11824-11831.

MARCATI, A., SERRA, C., BOUQUEY, M. & PRAT, L. 2010. Handling of polymer particles in microchannels. *Chemical engineering & technology,* 33**,** 1779-1787.

MARCKWALD, W. 1899. Über phototropie. *Zeitschrift für Physikalische Chemie,* 30**,** 140-145.

MÄTZLER, C. 2002. MATLAB functions for Mie scattering and absorption, version 2.

MENGÜÇ, M. & IYER, R. 1988. Modeling of radiative transfer using multiple spherical harmonics approximations. *Journal of Quantitative Spectroscopy and Radiative Transfer,* 39**,** 445-461.

MENTER, F. Zonal two equation kw turbulence models for aerodynamic flows. 23rd fluid dynamics, plasmadynamics, and lasers conference, 1993. 2906.

MENZEL, J. P., NOBLE, B. B., BLINCO, J. P. & BARNER-KOWOLLIK, C. 2021. Predicting wavelength-dependent photochemical reactivity and selectivity. *Nature Communications,* 12**,** 1691.

MIE, G. 1908. Beiträge zur Optik trüber Medien, speziell kolloidaler Metallösungen. *Annalen der Physik,* 330**,** 377-445.

MIKLOS, D. B., REMY, C., JEKEL, M., LINDEN, K. G., DREWES, J. E. & HÜBNER, U. 2018. Evaluation of advanced oxidation processes for water and wastewater treatment–A critical review. *Water research,* 139**,** 118-131.

MISHRA, S., KUMAR, V., SARKAR, J. & RATHORE, A. S. 2023. Mixing and mass transfer in production scale mammalian cell culture reactor using coupled CFD-species transport-PBM validation. *Chemical Engineering Science,* 267**,** 118323.

MO, Y. & JENSEN, K. F. 2016. A miniature CSTR cascade for continuous flow of reactions containing solids. *Reaction Chemistry & Engineering,* 1**,** 501-507.

MOJARRAD, M. S., KESHAVARZ, A. & SHOKOUHI, A. 2013. Nanofluids thermal behavior analysis using a new dispersion model along with single-phase. *Heat and Mass Transfer,* 49**,** 1333-1343.

MONFARED, R. H., NIKNEJADI, M., TOGHRAIE, D. & BARNOON, P. 2022. Numerical investigation of swirling flow and heat transfer of a nanofluid in a tube with helical ribs using a two-phase model. *Journal of Thermal Analysis and Calorimetry,* 147**,** 3403-3416.

MONGEON, S. S., ROBERGE, D. M., BITTEL, M., ELSNER, P. & MACCHI, A. 2016. Liquid–Liquid Mass Transfer in an Oscillatory-Flow

Mesoscale Coil Reactor without Baffles. *Organic Process Research & Development,* 20**,** 733-741.

MOREL, J. 1979. On the validity of the extended transport cross-section correction for low-energy electron transport. *Nuclear Science and Engineering,* 71**,** 64-71.

MOREL, J. E. 1989. Hybrid collocation-Galerkin-Sn method for solving the Boltzmann transport equation. *Nuclear Science and Engineering,* 101**,** 72-87.

MOREL, J. E., WARSA, J. S., FRANKE, B. C. & PRINJA, A. K. 2017. Comparison of two Galerkin quadrature methods. *Nuclear Science and Engineering,* 185**,** 325-334.

MORI, Y. & SAKAI, M. 2021. Development of a robust Eulerian–Lagrangian model for the simulation of an industrial solid–fluid system. *Chemical Engineering Journal,* 406**,** 126841.

MÜLLER, S. T. & WIRTH, T. 2015. Diazo Compounds in Continuous-Flow Technology. *ChemSusChem,* 8**,** 245-250.

NABER, J. R. & BUCHWALD, S. L. 2010. Packed-Bed Reactors for Continuous-Flow C N Cross-Coupling. *Angewandte Chemie,* 122**,** 9659-9664.

NANDWANI, S. K., CHAKRABORTY, M. & GUPTA, S. 2019. Chemical flooding with ionic liquid and nonionic surfactant mixture in artificially prepared carbonate cores: A diffusion controlled CFD simulation. *Journal of Petroleum Science and Engineering,* 173**,** 835-843.

NEJAD, A., VANKA, S., FAVALORO, S., SAMIMY, M. & LANGENFELD, C. 1989. Application of laser velocimetry for characterization of confined swirling flow.

NEWTON, I. 1672. A letter of Mr. Isaac Newton, Professor of the Mathematicks in the University of Cambridge; containing his new theory about light and colors: sent by the author to the publisher from Cambridge, Febr. 6. 1671/72; in order to be communicated to the R. Society. *Philosophical Transactions of the Royal Society of London,* 6, 3075-3087.

NGAMSIDHIPHONGSA, N., PONPESH, P., SHOTIPRUK, A. & ARPORNWICHANOP, A. 2020. Analysis of the Imbert downdraft gasifier using a species-transport CFD model including tar-cracking reactions. *Energy Conversion and Management,* 213, 112808.

NGUYEN, T. B. & AL-MOURABIT, A. 2016. Remarkably high homoselectivity in [2 + 2] photodimerization of trans-cinnamic acids in multicomponent systems. *Photochemical & Photobiological Sciences,* 15, 1115-1119.

NILSSON, A., PETERSSON, F., JÖNSSON, H. & LAURELL, T. 2004. Acoustic control of suspended particles in micro fluidic chips. *Lab on a Chip,* 4, 131-135.

NOËL, T., NABER, J. R., HARTMAN, R. L., MCMULLEN, J. P., JENSEN, K. F. & BUCHWALD, S. L. 2011. Palladium-catalyzed amination reactions in flow: overcoming the challenges of clogging via acoustic irradiation. *Chemical Science,* 2, 287-290.

NORIKANE, Y., TANAKA, S. & UCHIDA, E. 2016. Azobenzene crystals swim on water surface triggered by light. *CrystEngComm,* 18, 7225-7228.

NUIM LABIB, M., NINE, M. J., AFRIANTO, H., CHUNG, H. & JEONG, H. 2013. Numerical investigation on effect of base fluids and hybrid nanofluid in forced convective heat transfer. *International Journal of Thermal Sciences,* 71, 163-171.

OELGEMOELLER, M. 2012. Highlights of photochemical reactions in microflow reactors. *Chemical engineering & technology,* 35, 1144-1152.

OH, Y.-K., SEOL, E.-H., KIM, M.-S. & PARK, S. 2004. Photoproduction of hydrogen from acetate by a chemoheterotrophic bacterium Rhodopseudomonas palustris P4. *International journal of hydrogen energy,* 29, 1115-1121.

OTAKE, Y., NAKAMURA, H. & FUSE, S. 2018. Recent advances in the integrated micro-flow synthesis containing photochemical reactions. *Tetrahedron Letters,* 59**,** 1691-1697.

ÖZGÜR, E., MARS, A. E., PEKSEL, B., LOUWERSE, A., YÜCEL, M., GÜNDÜZ, U., CLAASSEN, P. A. & EROĞLU, İ. 2010. Biohydrogen production from beet molasses by sequential dark and photofermentation. *International Journal of Hydrogen Energy,* 35**,** 511-517.

OZISIK, M. N. 1973. Radiative transfer and interactions with conduction and convection(Book- Radiative transfer and interactions with conduction and convection.). *New York, Wiley-Interscience, 1973. 587 p*.

PAMME, N. 2007. Continuous flow separations in microfluidic devices. *Lab on a Chip,* 7**,** 1644-1659.

PANDA, T. & NAUMOV, P. 2018. Time-Dependent Photodimerization of α-trans-Cinnamic Acid Studied by Photocalorimetry and NMR Spectroscopy. *Crystal Growth & Design,* 18**,** 2744-2749.

PANDOLFI, L., GIUNCHI, A., SALZILLO, T., BRILLANTE, A., DELLA VALLE, R. G., VENUTI, E., GREPIONI, F. & D'AGOSTINO, S. 2021. The impact of solid solution composition on kinetics and mechanism of [2 + 2] photodimerization of cinnamic acid derivatives. *CrystEngComm,* 23**,** 1352-1359.

PAP, A. E., KORDÁS, K., GEORGE, T. F. & LEPPÄVUORI, S. 2004. Thermal Oxidation of Porous Silicon: Study on Reaction Kinetics. *The Journal of Physical Chemistry B,* 108**,** 12744-12747.

PAREEK, V. 2005. Light intensity distribution in a dual-lamp photoreactor. *International Journal of Chemical Reactor Engineering,* 3.

PAREEK, V., CHONG, S., TADÉ, M. & ADESINA, A. A. 2008. Light intensity distribution in heterogenous photocatalytic reactors. *Asia-Pacific Journal of Chemical Engineering,* 3**,** 171-201.

PAREEK, V., COX, S., BRUNGS, M., YOUNG, B. & ADESINA, A. 2003. Computational fluid dynamic (CFD) simulation of a pilot-scale annular bubble column photocatalytic reactor. *Chemical Engineering Science,* 58**,** 859-865.

PARIANI, G., BIANCO, A., CASTAGNA, R. & BERTARELLI, C. 2011. Kinetics of Photochromic Conversion at the Solid State: Quantum Yield of Dithienylethene-Based Films. *The Journal of Physical Chemistry A,* 115**,** 12184-12193.

PARK, J. H., CHUNG, T. S., HIPWELL, V. M., RIVERA, E. & GARCIA-GARIBAY, M. A. 2018. Transient Kinetics and Quantum Yield Studies of Nanocrystalline alpha-Phenyl-Substituted Ketones: Sorting Out Reactions from Singlet and Triplet Excited States. *J Am Chem Soc,* 140**,** 8192-8197.

PATANKAR, S. 1980. Numerical heat transfer and fluid flow, hemisphere, Washington DC. *Publishing Corporation*.

PEEDIKAKKAL, A. M. P. & VITTAL, J. J. 2010. Solid-State Photochemical Behavior of a Triple-Stranded Ladder Coordination Polymer. *Inorganic Chemistry,* 49**,** 10-12.

PEREZ-MAQUEDA, L., CRIADO, J. M. & MALEK, J. 2003. Combined kinetic analysis for crystallization kinetics of non-crystalline solids. *Journal of non-crystalline solids,* 320**,** 84-91.

PETERSSON, F., ÅBERG, L., SWÄRD-NILSSON, A.-M. & LAURELL, T. 2007. Free flow acoustophoresis: microfluidic-based mode of particle and cell separation. *Analytical chemistry,* 79**,** 5117-5123.

PETERSSON, F., NILSSON, A., HOLM, C., JÖNSSON, H. & LAURELL, T. 2005. Continuous separation of lipid particles from erythrocytes by means of laminar flow and acoustic standing wave forces. *Lab on a Chip,* 5**,** 20-22.

POE, S. L., CUMMINGS, M. A., HAAF, M. P. & MCQUADE, D. T. 2006. Solving the Clogging Problem: Precipitate-Forming Reactions in Flow. *Angewandte Chemie International Edition,* 45**,** 1544-1548.

POMBERGER, A., MO, Y., NANDIWALE, K. Y., SCHULTZ, V. L., DUVADIE, R., ROBINSON, R. I., ALTINOGLU, E. I. & JENSEN, K. F. 2019. A continuous stirred-tank reactor (CSTR) Cascade for handling solid-containing photochemical reactions. *Organic process research & development,* 23**,** 2699-2706.

PROUT, E. & TOMPKINS, F. C. 1945. The thermal decomposition of silver permanganate. *Transactions of the Faraday Society,* 42**,** 468-472.

PU, Y., CHEN, J., WANG, W. & ALFANO, R. R. 2019. 11 - Basic Optical Scattering Parameter of the Brain and Prostate Tissues in the Spectral Range of 400–2400nm. *In:* ALFANO, R. R. & SHI, L. (eds.) *Neurophotonics and Biomedical Spectroscopy.* Elsevier.

QUEVEDO, E., STEINBACHER, J. & MCQUADE, D. T. 2005. Interfacial Polymerization within a Simplified Microfluidic Device: Capturing Capsules. *Journal of the American Chemical Society,* 127**,** 10498-10499.

RAEESH, M., DEVI, T. T. & HIROM, K. 2022. Recent Developments on Application of Different Turbulence and Multiphase Models in Sedimentation Tank Modeling—a Review. *Water, Air, & Soil Pollution,* 234**,** 5.

RAMACHANDRAN, V. & FOGLER, H. S. 1998. Multilayer deposition of stable colloidal particles during flow within cylindrical pores. *Langmuir,* 14**,** 4435-4444.

RAMACHANDRAN, V. & FOGLER, H. S. 1999. Plugging by hydrodynamic bridging during flow of stable colloidal particles within cylindrical pores. *Journal of Fluid Mechanics,* 385**,** 129-156.

RAMAMURTHY, V. 1991. *Photochemistry in organized and constrained media*, VCH publishers.

RAMAMURTHY, V. & SIVAGURU, J. 2016. Supramolecular Photochemistry as a Potential Synthetic Tool: Photocycloaddition. *Chemical Reviews,* 116**,** 9914-9993.

RANGANATHAN, P., PANDEY, A. K., SIROHI, R., TUAN HOANG, A. & KIM, S.-H. 2022. Recent advances in computational fluid dynamics (CFD) modelling of photobioreactors: Design and applications. *Bioresource Technology,* 350**,** 126920.

RAYLEIGH, L. 1899. XXXIV. On the transmission of light through an atmosphere containing small particles in suspension, and on the origin of the blue of the sky. *The London, Edinburgh, and Dublin Philosophical Magazine and Journal of Science,* 47**,** 375-384.

RAYLOR, B. 1998. Pipe design for improved particle distribution and improved wear.

RAYLOR, B. 2000. Pipe design for improved particle distribution and improved wear.

READER-HARRIS, M. 1994. The decay of swirl in a pipe. *International journal of heat and fluid flow,* 15**,** 212-217.

REDWOOD, M. D. & MACASKIE, L. E. 2006. A two-stage, two-organism process for biohydrogen from glucose. *International Journal of Hydrogen Energy,* 31**,** 1514-1521.

REN, T., YANG, P., TANG, G., HUANG, X. & MLAWER, E. 2020. Improved δ-Eddington approximation for optically thin clouds. *Journal of Quantitative Spectroscopy and Radiative Transfer,* 240**,** 106694.

RESENDIZ, M. J. E., FAMILY, F., FULLER, K., CAMPOS, L. M., KHAN, S. I., LEBEDEVA, N. V., FORBES, M. D. E. & GARCIA-GARIBAY, M. A. 2009. Radical Reactions with Double Memory of Chirality (2MOC) for the Enantiospecific Synthesis of Adjacent Stereogenic Quaternary Centers in Solution: Cleavage and Bonding Faster than Radical Rotation. *Journal of the American Chemical Society,* 131**,** 8425-8433.

ROBERGE, D. M., DUCRY, L., BIELER, N., CRETTON, P. & ZIMMERMANN, B. 2005. Microreactor Technology: A Revolution for the Fine Chemical and Pharmaceutical Industries? *Chemical Engineering & Technology,* 28**,** 318-323.

ROBINSON, A. W. 1923. Delivery pipe for hydraulic dredging machines. Google Patents.

ROCKLAGE-MARLIANI, G., SCHMIDTS, M. & VASANTA RAM, V. I. 2003. Three-dimensional laser-Doppler velocimeter measurements in swirling turbulent pipe flow. *Flow, Turbulence and Combustion,* 70**,** 43-67.

RODI, W. 1993. *Turbulence models and their application in hydraulics*, CRC Press.

RODRÍGUEZ-VILLARREAL, A. I., TARN, M. D., MADDEN, L. A., LUTZ, J. B., GREENMAN, J., SAMITIER, J. & PAMME, N. 2011. Flow focussing of particles and cells based on their intrinsic properties using a simple diamagnetic repulsion setup. *Lab on a Chip,* 11**,** 1240-1248.

ROMERO, R. L., ALFANO, O. M. & CASSANO, A. E. 1997. Cylindrical photocatalytic reactors. Radiation absorption and scattering effects produced by suspended fine particles in an annular space. *Industrial & engineering chemistry research,* 36**,** 3094-3109.

ROSSO, C., GISBERTZ, S., WILLIAMS, J. D., GEMOETS, H. P. L., DEBROUWER, W., PIEBER, B. & KAPPE, C. O. 2020. An oscillatory plug flow photoreactor facilitates semi-heterogeneous dual nickel/carbon nitride photocatalytic C–N couplings. *Reaction Chemistry & Engineering,* 5**,** 597-604.

ROSTRON, P., GABER, S. & GABER, D. 2016. Raman spectroscopy, review. *laser,* 21**,** 24.

RUTHERFORD, E. 1911. LXXIX. The scattering of α and β particles by matter and the structure of the atom. *The London, Edinburgh, and Dublin Philosophical Magazine and Journal of Science,* 21**,** 669-688.

RYDE, N., KALLAY, N. & MATIJEVIĆ, E. 1991. Particle adhesion in model systems. Part 14.—Experimental evaluation of multilayer deposition. *Journal of the Chemical Society, Faraday Transactions,* 87**,** 1377-1381.

SAFFMAN, P. G. & WHITHAM, G. B. 1970. A model for inhomogeneous turbulent flow. *Proceedings of the Royal Society of London. A. Mathematical and Physical Sciences,* 317**,** 417-433.

SAFIN, D. A., ROBEYNS, K. & GARCIA, Y. 2016. 1,2,4-Triazole-based molecular switches: crystal structures, Hirshfeld surface analysis and optical properties. *CrystEngComm,* 18**,** 7284-7296.

SAIDI, M. S., RISMANIAN, M., MONJEZI, M., ZENDEHBAD, M. & FATEHIBOROUJENI, S. 2014. Comparison between Lagrangian and Eulerian approaches in predicting motion of micron-sized particles in laminar flows. *Atmospheric Environment,* 89**,** 199-206.

SAKAMOTO, M., FUJISTUKA, M. & MAJIMA, T. 2009. Light as a construction tool of metal nanoparticles: Synthesis and mechanism. *Journal of Photochemistry and Photobiology C: Photochemistry Reviews,* 10**,** 33-56.

SAKAMOTO, M., TAKAHASHI, M., SHIMIZU, M., FUJITA, T., NISHIO, T., IIDA, I., YAMAGUCHI, K. & WATANABE, S. 1995. "Absolute" Asymmetric Synthesis Using the Chiral Crystal Environment: Photochemical Hydrogen Abstraction from Achiral Acyclic Monothioimides in the Solid State. *The Journal of Organic Chemistry,* 60**,** 7088-7089.

SAMBIAGIO, C. & NOËL, T. 2020. Flow Photochemistry: Shine Some Light on Those Tubes! *Trends in Chemistry,* 2**,** 92-106.

SCHEFFER, J. R. & XIA, W. 2005. Asymmetric induction in organic photochemistry via the solid-state ionic chiral auxiliary approach. *Organic Solid State Reactions: -/-*, 233-262.

SCHMIDT, G. 1971. Photodimerization in the solid state. *Pure and Applied Chemistry,* 27**,** 647-678.

SCHRIEK, W., SMITH, L., HAAS, D. & HUSBAND, W. 1974. The potential of helically ribbed pipes for solids transport. *Canadian Mining and Metallurgical Bulletin,* 67.

SCHUSTER, A. 1905. Radiation through a foggy atmosphere. *Astrophysical Journal, vol. 21, p. 1,* 21**,** 1.

SCHWARZSCHILD, K. 1906. On the equilibrium of the sun's atmosphere. *Nachrichten von der Königlichen Gesellschaft der Wissenschaften zu Göttingen. Math.-phys. Klasse,* 195**,** 41-53.

SEDELMEIER, J., LEY, S. V., BAXENDALE, I. R. & BAUMANN, M. 2010. KMnO4-Mediated Oxidation as a Continuous Flow Process. *Organic Letters,* 12**,** 3618-3621.

SEDREZ, T. A., SHIRAZI, S. A., RAJKUMAR, Y. R., SAMBATH, K. & SUBRAMANI, H. J. 2019. Experiments and CFD simulations of erosion of a 90 elbow in liquid-dominated liquid-solid and dispersed-bubble-solid flows. *Wear,* 426**,** 570-580.

SEEBERGER, P. H. & BLUME, T. 2007. New avenues to efficient chemical synthesis: emerging technologies.

SENIER, A. & SHEPHEARD, F. G. 1909. CCXIV.—Studies in phototropy and thermotropy. Part I. Arylidene-and naphthylidene-amines. *Journal of the Chemical Society, Transactions,* 95**,** 1943-1955.

SHAH, M., NORRIS, S. E., TURNER, R. & FLAY, R. G. J. 2023. A review of computational fluid dynamics application to investigate tropical cyclone wind speeds. *Natural Hazards,* 117**,** 897-915.

SHAUGHNESSY, K. H. 2009. Hydrophilic ligands and their application in aqueous-phase metal-catalyzed reactions. *Chemical reviews,* 109**,** 643-710.

SHAW, M. H., TWILTON, J. & MACMILLAN, D. W. C. 2016. Photoredox Catalysis in Organic Chemistry. *The Journal of Organic Chemistry,* 81**,** 6898-6926.

SHI, H., YUAN, J. & LI, Y. 2021. The Impact of Swirls on Slurry Flows in Horizontal Pipelines. *Journal of Marine Science and Engineering,* 9**,** 1201.

SHI, X., RONSSE, F., ROEGIERS, J. & PIETERS, J. G. 2019a. 3D Eulerian-Eulerian modeling of a screw reactor for biomass thermochemical conversion. Part 1: Solids flow dynamics and back-mixing. *Renewable Energy,* 143**,** 1465-1476.

SHI, Y.-N., ZHANG, F., CHAN, K. L., LI, W., LIN, H. & DUAN, M. 2019b. An improved Eddington approximation method for irradiance calculation in a vertical inhomogeneous medium. *Journal of Quantitative Spectroscopy and Radiative Transfer,* 226**,** 40-50.

SIEGEL, R. 2001. *Thermal radiation heat transfer*, CRC press.

SINGH, V. & CHARLES, M. 1976. The flow of sand/water slurries in horizontal pipes with internal spiral ribs—effect of rib height. *The Canadian Journal of Chemical Engineering,* 54**,** 249-254.

SOMMERWERK, S., KLUGE, R., STRÖHL, D., HELLER, L., KRAMELL, A. E., OGIOLDA, S., LIEBING, P. & CSUK, R. 2016. Synthesis, characterization and cytotoxicity of new piplartine dimers. *Tetrahedron,* 72**,** 1447-1454.

SPEZIALE, C. G., YOUNIS, B. A. & BERGER, S. A. 2000. Analysis and modelling of turbulent flow in an axially rotating pipe. *Journal of Fluid Mechanics,* 407**,** 1-26.

STEENBERGEN, W. & VOSKAMP, J. 1998. The rate of decay of swirl in turbulent pipe flow. *Flow measurement and instrumentation,* 9**,** 67-78.

STOBBE, H. 1922. Light reactions of the cis-and trans-cinnamic acids. *Ber Dtsch Chem Ges,* 55**,** 2225-2245.

STUDER, A. & CURRAN, D. P. 2016. Catalysis of radical reactions: a radical chemistry perspective. *Angewandte Chemie International Edition,* 55**,** 58-102.

SU, Y., HESSEL, V. & NOËL, T. 2015. A compact photomicroreactor design for kinetic studies of gas - liquid photocatalytic transformations. *AIChE Journal,* 61**,** 2215-2227.

TAKADA, K. 2023. Synthesis of biobased functional materials using photoactive cinnamate derivatives. *Polymer Journal,* 55**,** 1023-1033.

TAKEI, G., KITAMORI, T. & KIM, H.-B. 2005. Photocatalytic redox-combined synthesis of l-pipecolinic acid with a titania-modified microchannel chip. *Catalysis Communications,* 6**,** 357-360.

TENCER, J. The impact of reference frame orientation on discrete ordinates solutions in the presence of ray effects and a related mitigation technique. ASME International Mechanical Engineering

Congress and Exposition, 2014. American Society of Mechanical Engineers, V08AT10A017.

TENCER, J. & HOWELL, J. R. 2013. A multi-source full spectrum k-distribution method for 1-D inhomogeneous media. *Journal of Quantitative Spectroscopy and Radiative Transfer,* 129**,** 308-315.

TENCER, J. T. 2013. Error analysis for radiation transport.

TEPE, A. Ü., YETIŞKEN, Y., UYSAL, Ü. & ARSLAN, K. 2020. Experimental and numerical investigation of jet impingement cooling using extended jet holes. *International Journal of Heat and Mass Transfer,* 158**,** 119945.

TONKIN, R. J. J. 2005. Swirling pipeflow of non-Newtonian and particle-laden fluids.

TSUJI, Y., KAWAGUCHI, T. & TANAKA, T. 1993. Discrete particle simulation of two-dimensional fluidized bed. *Powder technology,* 77**,** 79-87.

TYNDALL, J. 1874. On the Atmosphere as a Vehicle of Sound. *Philosophical Transactions of the Royal Society of London,* 164**,** 183-244.

USUTANI, H., TOMIDA, Y., NAGAKI, A., OKAMOTO, H., NOKAMI, T. & YOSHIDA, J.-I. 2007. Generation and Reactions of o-Bromophenyllithium without Benzyne Formation Using a Microreactor. *Journal of the American Chemical Society,* 129**,** 3046-3047.

VAN HERK, D., CASTAÑO, P., MAKKEE, M., MOULIJN, J. A. & KREUTZER, M. T. 2009. Catalyst testing in a multiple-parallel, gas–liquid, powder-packed bed microreactor. *Applied Catalysis A: General,* 365**,** 199-206.

VASQUEZ, S. A phase coupled method for solving multiphase problems on unstructured mesh. ASME 200 Fluids Engineering Division Summer Meeting, 2000.

VENKATESAN, R., NAGARAJAN, N. R., PASO, K., YI, Y. B., SASTRY, A. M. & FOGLER, H. S. 2005. The strength of paraffin gels formed under static and flow conditions. *Chemical Engineering Science,* 60**,** 3587-3598.

VERSTEEG, H. K. & MALALASEKERA, W. 2007. *An introduction to computational fluid dynamics: the finite volume method*, Pearson education.

WAN, Z., YANG, S., TANG, D., YUAN, H., HU, J. & WANG, H. 2023. Particle-scale modeling study of coaxial jets of gas-solid swirling flow in an industrial-scale annular pipe via CFD-DEM. *Powder Technology,* 419**,** 118307.

WANG, H., QI, H., SUN, X., JIA, S., LI, X., MIAO, T. J., XIONG, L., WANG, S., ZHANG, X., LIU, X., WANG, A., ZHANG, T., HUANG, W. & TANG, J. 2023. High quantum efficiency of hydrogen production from methanol aqueous solution with PtCu–TiO2 photocatalysts. *Nature Materials*.

WANG, J., DENG, B., GAO, J. & CAO, H. 2019. Numerical simulation of radiation distribution in a slurry reactor: the effect of distribution of catalyst particles. *Chemical Engineering Journal,* 357**,** 169-179.

WANG, S., YAO, J., LU, X. & DING, T. 2022. Light-Induced Solid-State Protrusion of Gold Nanowires and Their Derivatives for Sensing Applications. *Advanced Optical Materials,* 10**,** 2102238.

WANG, Y., ZHANG, X., YOU, S. & HU, Y. 2020. One-step electrosynthesis of visible light responsive double-walled alloy titanium dioxide nanotube arrays for use in photocatalytic degradation of dibutyl phthalate. *RSC Advances,* 10**,** 21238-21247.

WEBB, D. & JAMISON, T. F. 2010. Continuous flow multi-step organic synthesis. *Chemical Science,* 1**,** 675-680.

WEINGARTEN, A. 2017. Photochemistry: Electrons clean up by going green. *Nature Reviews Chemistry,* 1**,** 0092.

WELCH, A. 1955. Chemistry of the Solid State. *Chap. IZ, ed. 6y WE Garneq Butterworths, London*.

WILCOX, D. C. 2006. *Turbulence modeling for CFD*, DCW industries La Canada, CA.

WILCOX, D. C. 2008. Formulation of the k-w Turbulence Model Revisited. *AIAA Journal,* 46**,** 2823-2838.

WU, K.-J., NAPPO, V. & KUHN, S. 2015. Hydrodynamic Study of Single- and Two-Phase Flow in an Advanced-Flow Reactor. *Industrial & Engineering Chemistry Research,* 54**,** 7554-7564.

WYANDT, C. M. & FLANAGAN, D. R. 1992. Solid-state non-isothermal kinetics of sulfonamide-ammonia adduct desolvation. *Thermochimica acta,* 196**,** 379-389.

WYSS, H. M., BLAIR, D. L., MORRIS, J. F., STONE, H. A. & WEITZ, D. A. 2006. Mechanism for clogging of microchannels. *Physical Review E,* 74**,** 061402.

XIE, B., ZHU, L., YANG, K., ZHOU, B., HIRAOKA, N., CAI, Y., YAO, Y., WU, C., WANG, E. & FENG, D. 2010. Inelastic x-ray scattering study of the state-resolved differential cross section of Compton excitations in helium atoms. *Physical Review A,* 82**,** 032501.

XU, A., WANG, G., LI, Y., DONG, H., YANG, S., HE, P. & DING, G. 2020. Carbon-Based Quantum Dots with Solid-State Photoluminescent: Mechanism, Implementation, and Application. *Small,* 16**,** 2004621.

YANG, S., WANG, H., WEI, Y., HU, J. & CHEW, J. W. 2020. Particle-scale characteristics of the three distinct regions in the multi-chamber slot-rectangular spouted bed. *Powder Technology,* 360**,** 658-672.

YE, L., ZHOU, L. & LU, Y. 2022. Direct Continuous Synthesis of Oleic Acid-Modified Fe3O4 Nanoparticles in a Microflow System. *Industrial & Engineering Chemistry Research,* 61**,** 4320-4328.

YU, J.-G., GAN, M.-M., BAI, S. & HAN, Y.-F. 2019. Photodriven solid-state multiple [2+ 2] cycloaddition strategies for the construction of polycyclobutane derivatives. *CrystEngComm,* 21**,** 4673-4683.

YUILLE, N. A. 1928. Dredger pipe line. Google Patents.

ZEINY, S., CHERIF, Y. & LASSUE, S. 2023. Analysis of the Thermo-Aeraulic Behavior of a Heated Supply Air Window in Forced Convection: Numerical and Experimental Approaches. *Energies,* 16**,** 3243.

ZHANG, J. 2019. On sampling of scattering phase functions. *Astronomy and Computing,* 29**,** 100329.

ZHANG, X., LIU, Z. & LIU, W. 2012. Numerical studies on heat transfer and flow characteristics for laminar flow in a tube with multiple regularly spaced twisted tapes. *International Journal of Thermal Sciences,* 58**,** 157-167.

ZHANG, X., TIAN, Z. F., CHINNICI, A., ZHOU, H., NATHAN, G. J. & CHIN, R. C. 2024. Particle dispersion model for RANS simulations of particle-laden jet flows, incorporating Stokes number effects. *Advanced Powder Technology,* 35**,** 104345.

ZHOU, J.-W., DU, C.-L. & MA, Z.-L. 2018. Influence of swirling intensity on lump coal particle pickup velocity in pneumatic conveying. *Powder technology,* 339**,** 470-478.

ZIEGENBALG, D., WRIEDT, B., KREISEL, G. & KRALISCH, D. 2016. Investigation of photon fluxes within microstructured photoreactors revealing great optimization potentials. *Chemical Engineering & Technology,* 39**,** 123-134.